Shock-Wave Heating Model for Chondrule Formation: Thermal Evolution of Precursor Dust Particles and Hydrodynamics of Molten Droplets

Hitoshi Miura

January 28, 2006

Abstract

Chondrules are millimeter-sized, once-molten, spherical shaped grains universally contained in chondritic meteorites, which command a majority of meteorites falling onto the Earth. They are considered to have formed from chondrule precursor dust particles in the solar nebula; they were heated and melted through flash heating events in the solar nebula and cooled again to solidify in a short period of time. A shock-wave heating model is one of the most plausible models for chondrule formation. In this thesis, we investigate two themes about the shock-wave heating model for chondrule formation. The former theme is about the dust thermal histories when they meet shock waves generated in the protoplanetary disk. The latter theme is about the hydrodynamics of molten dust particles exposed to the high-velocity rarefied gas flow.

First, we notice the heating rate of the precursor dust particles before they melt in the gas flow. It is known that the precursor dust particles should be heated rapidly enough ($\gtrsim 10^4\,\mathrm{K\,hr^{-1}}$) at a temperature range of $1273 - 1473\,\mathrm{K}$ in order to prevent the isotopic fractionation of sulfur contained in chondrules. In the shock-wave heating model, the gas frictional heating can heat the dust particles rapidly enough in the post-shock region. However, the dust particles can be heated in the pre-shock region by the radiation mainly emitted from the post-shock gas and dust particles. It has not been investigated how the radiation field affects the heating rates of the precursor dust particles. We study the conditions for the rapid heating constraint by numerical simulating the shock-wave heating model taking into account the radiation transfer, and obtain the heating rates of the precursor dust particles for various conditions. We find that the heating rates decreases drastically

if the dust temperatures when the dust particles reach at the shock front, $T_{\rm sf}$, exceed 1273 K. We analytically derive $T_{\rm sf}$ by using the theory of the radiative diffusion and confirmed that the analytic values of $T_{\rm sf}$ well match with the numerical simulations. We conclude that if the optical depth of the pre-shock region is smaller than about $1 - 10$, the isotopic fractionation would be prevented. Using our results, we discuss the appropriate shock conditions for producing chondrules by the shock-wave heating.

Next, we notice the three-dimensional shapes of chondrules. Most of them are not perfect spheres. It is thought that the deformed shapes of chondrules reflect the deformations when the precursor dust particles melt in the gas flow. Although it has been suggested that the ram pressure of the gas flow and the rotation of the molten droplets are important factors for the deformations, there is no report to consider those two effects simultaneously. We simulate the rapidly rotating molten droplets exposed to the high-velocity gas flow by numerically solving three-dimensional hydrodynamical equations. We find that the molten droplets take various shapes as shown in the observational data of chondrule shapes. The droplet shapes mainly depend on the angular velocities of the rotation. We also analytically derive the three-dimensional shapes of droplets and find that the numerical simulations well match with the analytic solutions. From above analysis, we conclude that the rotation of molten droplets exposed to the gas flow produces a variety in its shapes and the rotation rate is an important factor to determine the droplet shapes. Moreover, we find that the droplet shapes as shown in our analysis seem to be similar to the chondrule data.

In this thesis, we investigate two themes about the shock-wave heating model for chondrule formation: the effect of radiation transfer on the isotopic fractionation, and the relation between the rotation rate and the shapes of molten dust particles exposed to the gas flow. Those themes have not been noticed in the framework of the shock-wave heating model, but closely relate the theoretical studies of this field and the observational studies of meteorites (isotopic fractionation, the three-dimensional shapes of chondrules, and so forth). We believe that our results in this thesis can promote the developments of those scientific fields.

Acknowledgments

I am very grateful to my collaborator, Taishi Nakamoto for fruitful discussions, suggestions, and his continuous encouragement. I thank Akira Iida for the introduction to study shock-wave heating model for chondrule formation. I also greatly appreciate helpful comments and offering the observational data of chondrules by Akira Tsuchiyama. I am grateful to Masayuki Umemura, Naomasa Nakai, Nobuyuki Ishibashi, Sei-ichiro Watanabe, Ryoichi Nishi, Hajime Susa, Shinichi Sirono, Hiroko Nagahara, Shogo Tachibana, Katsuo Tukamoto, Hisayoshi Yurimoto, and Minoru Sekiya for their comments and encouragements. I thank my coworkers for the useful discussions. I owe thanks to the computer system of the Center for Computational Sciences (Univ. of Tsukuba) for the numerical calculations. This work is supported by Research Fellowships of the Japan Society for the Promotion of Science for Young Scientists.

Finally, I would like to offer my sincere and heartfelt thanks to sympathetic parents, Yoshihiro Miura and Sayoko Miura, who understood and supported my research activities.

Contents

Chapter 1

Chondrules and Shock-Wave Heating Model

Chondrules are millimeter-sized, spherical-shaped grains universally contained in chondritic meteorites, which command a majority of meteorites falling onto the Earth. It is believed that the existence of chondrules is a strong evidence of the silicate dust melting processes in the protoplanetary disk. In order to melt the silicate dust particles, they must be heated up to about 1500 K or more. The shock-wave heating model is considered to be one of the most plausible models for chondrule formation. The model has been investigated theoretically by many authors and it has been found that it meets various observational constraints to form chondrules.

In this chapter, we briefly summarize chondrules and the observational constraints to form chondrules. Moreover, we take up some results of the shock-wave heating model and explain the relations with the chondrule formation.

1.1 Chondrules

Chondrules are millimeter-sized, once-molten, spherical-shaped grains mainly composed of silicate material (see Figure 1.1). They are universally contained in chondritic meteorites, which command a majority of meteorites falling onto the Earth. They are considered to have formed from chondrule precursor dust particles about 4.56×10^9 yr ago in the solar nebula (Amelin et al. 2002); they were heated and melted through flash heating events in the solar nebula and cooled again to solidify in a short period of time (e.g., Jones *et al.* 2000 and references therein). So they must have great information on the early history of our solar system. Since it is naturally expected that protoplanetary disks around young stars in star forming regions have similar dust particles and processes, the study of chondrule formation may provide us much information on the planetary system formation. Chondrules have many features: physical properties (sizes, shapes, densities, degree of magnetization, etc.), chemical properties (elemental abundances, degree of oxidation/reduction, etc.), isotopic compositions (oxygen, nitrogen, rare gases, etc.), mineralogical and petrologic features (structures, crystals, degrees of alteration, relicts, etc.), and so forth, each of which should be a clue that helps us to reveal their own formation process and that of the planetary system. To reveal their formation history, many works have been carried out observationally, experimentally, and theoretically.

1.2 Shock-Wave Heating Model

Shock-wave heating model is considered to be one of the most plausible models for chondrule formation (Boss 1996, Jones et al. 2000). It has been studied by many authors (Hood & Horanyi 1991, 1993, Ruzmaikina & Ip 1994, Tanaka *et al.* 1998, Iida *et al.* 2001 (hereafter INSN), Desch & Connolly 2002 (hereafter DC02), Miura *et al.* 2002, Ciesla & Hood 2002 (hereafter CH02), Miura & Nakamoto 2005 (hereafter MN05)). Basic mechanism of the shock-wave heating is rather simple (see Figure 1.2). Let's suppose there is a gas medium containing dust particles with a dynamical equilibrium, i.e. they do not have a relative velocity initially. And let's suppose a shock wave passes the medium. Then, the gas is accelerated by the gas

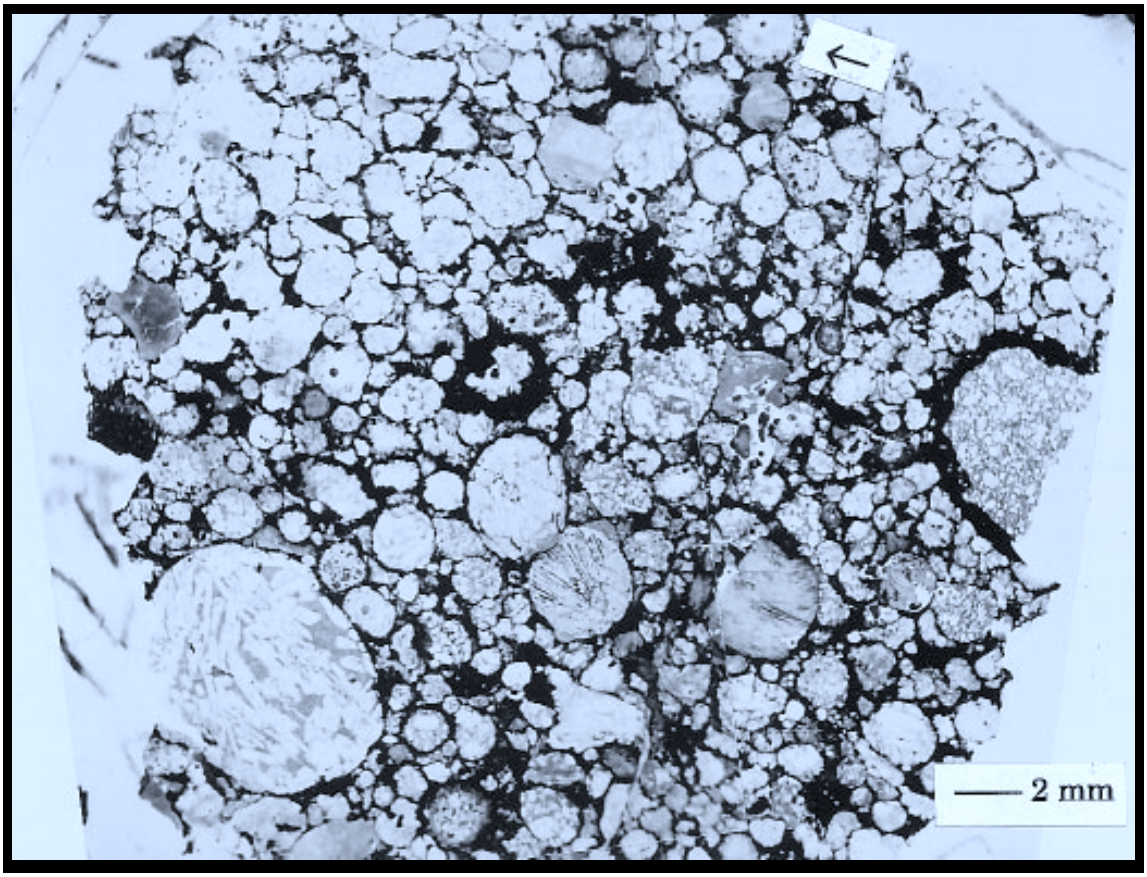

Figure 1.1: A transmitted light image of a thin section of Semarkona (LL3.0; USNM 1805-4), an unequilibrated ordinary chondrite (Connolly & Love 1998). The spherical components in the figure are chondrules.

pressure and obtains some amount of velocity, while dust particles tend to remain the initial position. This causes the relative velocity between the dust particles and the gas. When the relative velocity is present, the frictional force and drag heating work on the dust particles; the intensity of the force and the heating depend mainly on the relative velocity and the gas density. Also, the high temperature gas in the post-shock region, heated by the compressional heating, heats the dust particles by thermal collisions. Moreover, dust particles are heated by radiation emitted from gas molecules and other dust particles. Dust particles are heated by those three processes, and cooled by emission of thermal radiation, the collision with cooler gas, and the latent heat cooling due to the evaporation. If the gas frictional heating is strong enough to heat the silicate dust particles up to the melting temperature and not so strong that the dust particles evaporate completely, they could become chondrules.

1.3 Observational Constraints

In order to form chondrules, the dust heating mechanism has to satisfy some constraints described below. These constraints are derived from observational aspects. In this section, we introduce some observational constraints in this chapter. Jones et al. (2000) summarized those observational constraints in detail. We also describe the results of the shock-wave heating model regarding each constraint.

1.3.1 Peak Temperature

The essential condition for chondrule formation is to heat the silicate dust particles up to the melting temperature. The melting temperature is thought to be in a range of $\sim 1500 - 2200\,\mathrm{K}$ (Jones et al. 2000, Tachibana & Huss 2005). Many authors have been numerically simulated the thermal history of the silicate dust particles in the shock-wave heating event and discussed the condition to melt the silicate dust particles.

Hood & Horanyi (1991) numerically simulated the thermal histories of dust particles taking into account the gas-dust energy and momentum transfer in detail. In

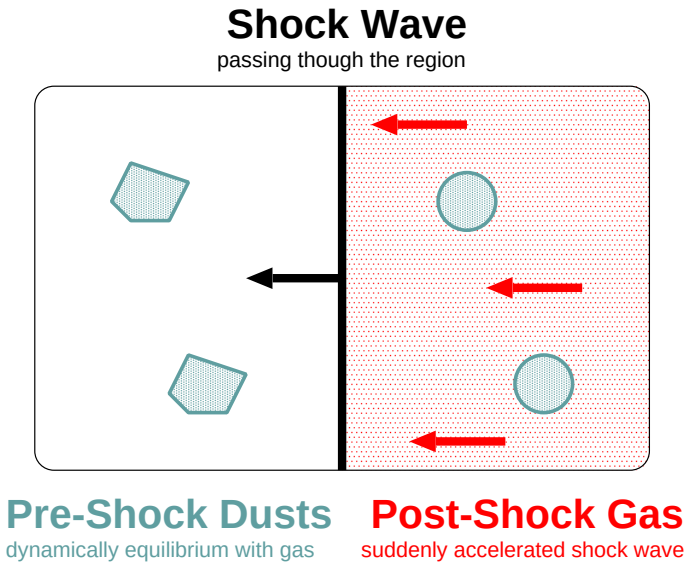

Figure 1.2: Schematic picture of the shock-wave heating model. There is a gas medium containing silicate dust particles with a dynamical equilibrium in the protoplanetary disk. If a shock wave passes though the region, the post-shock gas is accelerated suddenly. On the contrary, the dust particles tend to remain the initial position. This causes the relative velocity between the dust particles and the gas. Therefore, the gas frictional heating takes place on the dust particles.

their model, initial gas number density and temperature are taken to be representative of solar nebula conditions. They assumed the gas-dust relative velocity of up to the Kepler orbit velocity at 3 AU from the central star ($= 15\,\mathrm{km\,s^{-1}}$). They concluded that melting of chondrule precursor dust particles by the gas frictional heating is possible only for relative velocity in excess of the sound speed and only within dust-rich zones where radiative cooling of the dust particles is reduced. On the other hand, Ruzmaikina & Ip (1994) took into account gas cooling and compression in the post-shock region, which was neglected in the model by Hood & Horanyi (1991). They found that shocked gas is cooled efficiently by dipole molecules and small dust particles, and this results in a sharp increase in gas density in the post-shock region. Submillimeter and larger dust particles cross the region of cooling before being decelerated, and are heated by the gas frictional heating more strongly than in an adiabatic shock. They concluded that this effect opens the possibility of melting of millimeter-size dust aggregates (chondrule precursors) in that cooler region, even when the matter is transparent for the thermal radiation of the aggregates. Iida et al. (2001) solved the non-equilibrium chemical reactions of gas species with the hydrodynamics of the gas in order to determine the properties of the post-shock region more precisely. They examined the thermal histories of dust particles for a wide variety of shock conditions and summarized the chondrule-forming conditions on the plot of v_s vs. n_0, where v_s is the shock propagating velocity (shock velocity) and n_0 is the pre-shock gas number density (see Figure 1.3). They also analytically derived the conditions for the shock velocity and the pre-shock gas number density to melt the dust particles. Fig. 1.3 is a very useful plot when considering the appropriate shock conditions for chondrule formation.

1.3.2 Rapid Heating

Tachibana & Huss (2005) found that the degree of isotopic fractionation of sulfur in troilites (FeS) in chondrules from Bishunpur (LL3.1) and Semarkona (LL3.0) is quite small ($< 0.1\%$/amu for all the grains, except one grain that has $0.27 \pm 0.14\%$/amu). The absence of isotopic fractionation in troilites suggests that chondrules have to be heated rapidly ($> 10^4\,\mathrm{K/hr}$) at a temperature range of $1273 - 1473\,\mathrm{K}$, in

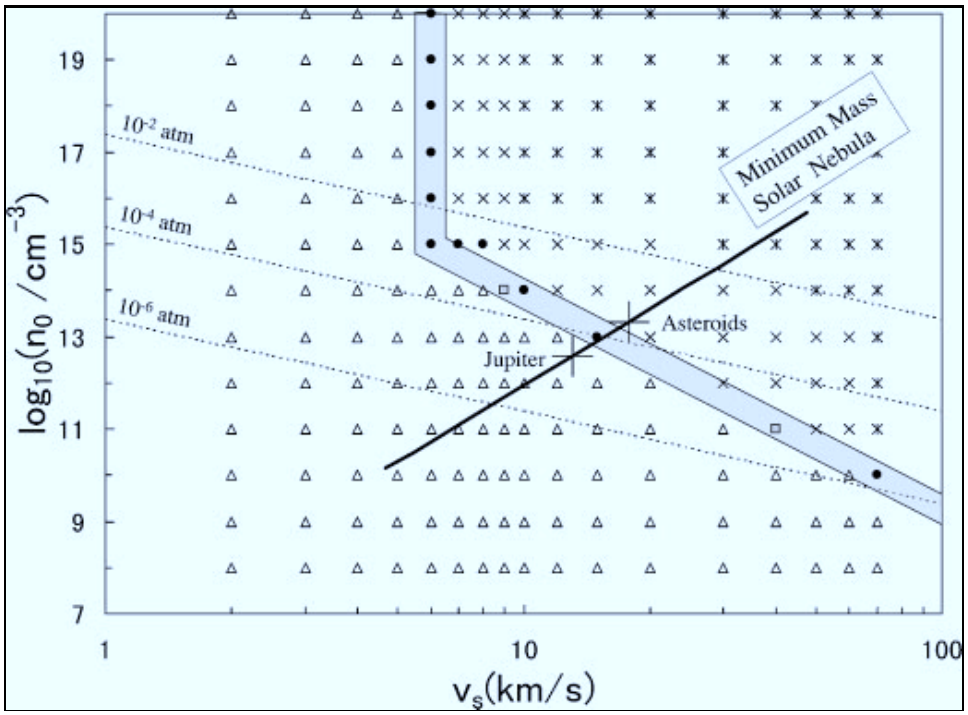

Figure 1.3: The shock conditions for chondrule formation are plotted as a function of the shock velocity v_s and the pre-shock gas number density n_0. The gray colored region represents conditions with which chondrules can be formed (Iida et al. 2001).

which the isotopic fractionation should occur associated with evaporation of troilites (Tachibana & Huss 2005). Below 1273 K, troilites is solid state and it is assumed that no isotopic fractionation occurs when solid troilite evaporates because the time scale of sulfur diffusion in FeS is much larger than that of evaporation (the evaporation Péclet number for troilites at temperatures close to the eutectic point is about 100 for 50 μm-sized grain). On the contrary, above 1473 K, the melting troilite grains would have been surrounded by melted silicate. In this case, evaporation of sulfur would be controlled by diffusion through the surrounding silicate melt. However, since sulfur can hardly dissolve to the chondrule silicate melt, the troilite would not evaporate and a large degree of isotopic fractionation is not expected. Dust aggregates that have never melted before are thought to be fluffy. When such aggregates are heated, the isotopic fractionation of troilites should occur associated the evaporation from inside of fluffy aggregates. If the heating rate is slow, it is impossible to suppress the isotopic fractionation, because the duration of the evaporation becomes long enough to produce certain amount of isotopic fractionation. On the other hand, since once molten dust particles are not fluffy, they do not have to be heated rapidly to prevent from isotopic fractionation because FeS in the dust particle is completely covered by silicate components. It is also the reason why we do not take into account the isotopic fractionation during the cooling phase. Namely, chondrules have to be heated rapidly at least in the first melting heating event.

The isotopic fractionation can be suppressed due to not only the rapid heating but also the presence of back reaction from evaporated sulfur gas if the dust-to-gas mass ratio is large enough, however, in our situation, this effect can be negligible. Tachibana & Huss (2005) also calculated the degree of isotopic fractionation of sulfur under conditions of sufficiently high dust-to-gas mass ratio in a closed system, and concluded that the required dust-to-gas mass ratio to suppress the isotopic fractionation by the back reaction is higher than about ten thousands times the solar value. It means that the dust-to-gas mass ratio should be greater than about 100. It has not been well investigated whether the shock-wave heating (the gas drag heating) works well in such extremely high dust-to-gas mass ratio environment or not, and to answer this problem is beyond the scope of this paper. Thus, we do not

take into account the back reaction in this study.

Tachibana *et al.* (2004) investigated the heating rate of chondrules in the framework of the shock-wave heating model and concluded that the gas drag heating in the post-shock region can heat chondrules rapidly enough to suppress the isotopic fractionation. However, it is known that chondrules are also heated in the pre-shock region due to the radiation emitted by ambient dust particles (DC02, CH02). The effect is well known as the blanket effect, which was not taken into account in the study by Tachibana *et al.* (2004). Results by DC02, in which the dust thermal radiation is taken into consideration as the radiation source, showed that the heating speed due to the radiation is too slow to suppress the isotopic fractionation ($\sim 300\,\mathrm{K/hr}$). CH02 also performed numerical simulation taking the transfer of the dust thermal continuum emission into consideration. In contrast with DC02, results of CH02 showed that the heating rate of chondrules is large enough to suppress the isotopic fractionation even if the pre-shock region is dusty environment (dust-to-gas mass ratio is about 1.5, which is a few hundreds times larger than that of the minimum mass solar nebula).

In previous studies of shock-wave heating model taking into account the radiation transfer (DC02, CH02), only the dust thermal continuum was taken into consideration as the radiation source. However, there is the other radiation source, the line emission of gas molecules. DC02 and CH02 neglected the line cooling because they assumed that the shock region is too optically thick to its own line emission to lose gas thermal energy effectively. On the contrary, Miura & Nakamoto (2005) showed an estimation that the post-shock gas is not so optically thick and the post-shock gas can cool in a few $100 - 1000\,\mathrm{km}$ behind the shock front. Therefore, the line cooling should be taken into account.

1.3.3 Cooling Rate

In order to produce chondrules, it is thought that cooling rates after the flash melting event should be appropriate values. However, the cooling rate constraint has not been well determined. The data of Jones & Lofgren (1993), who compared the textures and zoning profiles of olivine grains tens of micrometers across in natu-

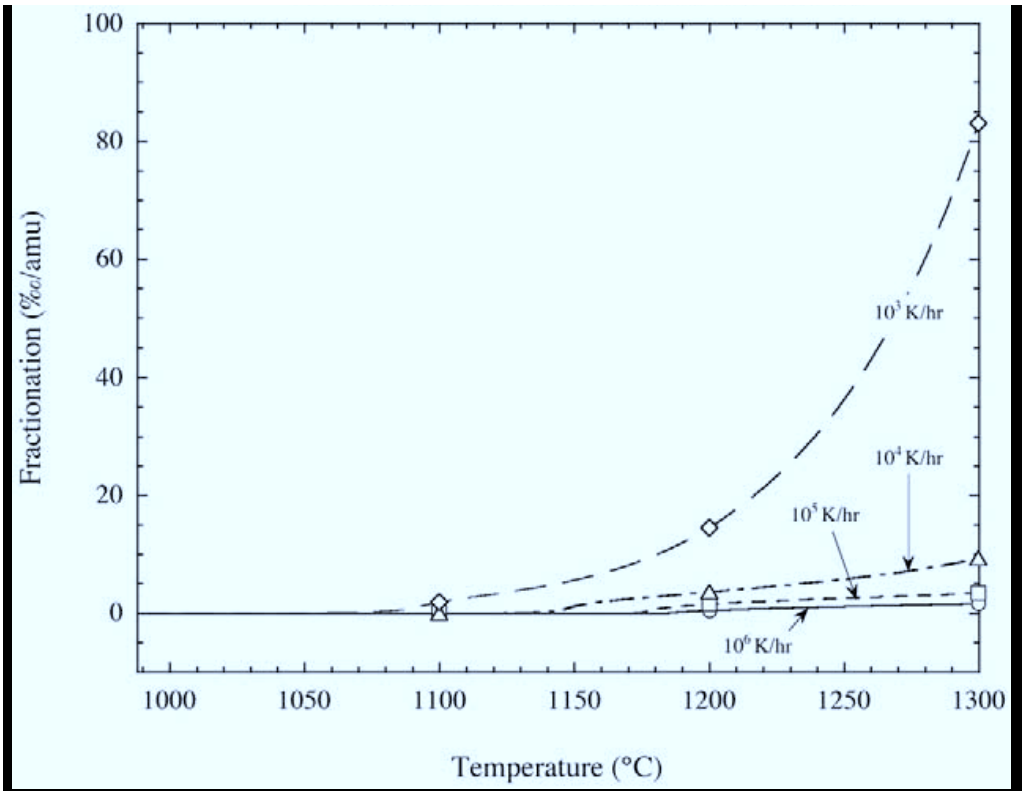

Figure 1.4: The change of the sulfur isotopic fractionation of the bulk condensed phase for a grain with an initial radius of 50 μm heated with various heating rates ($10^3 - 10^6\,\mathrm{K\,hr^{-1}}$). The dust particle is assumed to be heated with each constant heating rate (Tachibana & Huss 2005). The measured values of the isotopic fractionation were smaller than about 0.3%.

ral chondrules and experimental analogs, clearly showed that the range of cooling rates experienced by type IIA chondrules was $5-100\,\mathrm{K/hr}$. For higher cooling rates ($500-1000\,\mathrm{K/hr}$), olivine textures in these experiments were generally more elongate and skeletal than those grown at the slower cooling rates, and moreover, chemical zoning was rather limited. On the contrary, Wasson & Rubin (2003) measured overgrowths on low-FeO relict grains contained within almost type II chondrules and found that the overgrowths are narrow, in the range of $2-12\,\mu\mathrm{m}$. Wasson (2004) inferred the cooling rate of chondrules assuming that the overgrowths represent the maximum amount of material that can reach the crystal/melt interface by diffusion in the melt during the cooling interval. Diffusion length can be estimated as $\delta^2 \sim Dt_{\mathrm{cool}}$, where δ is the diffusion length, D is the diffusion coefficient, and t_{cool} is the cooling time scale. Thus, the results that the amount of the overgrowths was about 30 times smaller than the grain sizes simulated in order to estimate cooling rates (*e.g.,* Jones & Lofgren 1993) indicate that the cooling rates should be about 900 ($= 30^2$) times faster than that suggested by Jones & Lofgren (1993). Additionally, Yurimoto & Wasson (2002) modeled the O-isotopic and FeO/(FeO+MgO) gradients in a type II chondrule from the Yamato-81020 CO3.0 chondrite and inferred an extremely fast cooling rate ($10^5 - 10^6\,\mathrm{K/hr}$) at high temperatures ($\sim 1900\,\mathrm{K}$). Additionally, various constraints for the cooling rates have been proposed by many authors (summarized in DC02). To summarize, though the information of the cooling rates is very important for chondrule formation mechanism, the appropriate values have not been well determined yet. Therefore, we think that it is no problem to compare the simulation results of cooling rate with observational constraints, but we should not restrict the shock wave generation mechanism even if the cooling rate does not meet the observational constraints.

1.3.4 Elevated Gas Pressure

When the dust particles melt in the shock-wave heating event, the ambient gas pressure should be larger than the vapor pressure of the molten dust particles. If not, the bubbles would be generated in the molten droplets (boiling) and the droplets might vaporize away not to form chondrules.

Miura et al. (2002) investigated the high pressure conditions to prevent the boiling in a framework of the shock-wave heating model. They assumed that the material consisting of precursor dust particles is only forsterite (Mg_2SiO_4), which is one of the main components of chondrules, in order to obtain precise thermodynamic constants and calculate the boiling process exactly. They found that if the pre-shock gas number density is smaller than about $10^{13}\,\mathrm{cm}^{-3}$, the static gas pressure in the post-shock region is too small to suppress the boiling in the forsterite melt. However, they also found that if considering the ram pressure acting on the molten silicate dust particles, it is possible to suppress the boiling and could form chondrules. In the post-shock region, there is a relative velocity of a few km s^{-1} or more between the molten droplet and the gas. In that case, the ram pressure acting on the molten droplet dominates the static pressure of the post-shock gas. Miura et al. (2002) concluded that the ram pressure plays an important role to suppress the boiling.

1.3.5 Size Distribution

It is well known that chondrules have typical size distributions. Measured sizes of chondrules in some chondrite groups are listed in Table 1.1. We can see that diameters of most of chondrules are in a range from a few tens of μm to a few mm. It should be noticed that small chondrules whose diameter is smaller than $1\,\mu$m are quite rare. But this size distribution seems strange when we think of the size distribution of interstellar dust particles that must be ancestors of dust particles in the early solar nebula. The maximum size of interstellar dust particles is estimated to be about $1\,\mu$m or less (e.g., Mathis et al. 1977). This suggests that the chondrule precursors are formed though coagulation of small dust particles in the solar nebula. If this is the case, one can easily expect that the size distribution of the precursor particles should be in a range from sub-micron to a few mm or more. However, we do not see abundant small chondrules whose radius is smaller than $1\,\mu$m. Thus, the absence of small chondrules seems to imply the presence of a mechanism that determines the minimum size of chondrules, which were formed from large precursor particles.

Susa & Nakamoto (2002) showed that the characteristic size of chondrules can

Table 1.1: Diameter range of chondrules determined by petrographic analysis of thin sections. BO = barred olivine; RP = radial pyroxene; C = cryptocrystalline; PO = porphyritic olivine; PP = porphyritic pyroxene; POP = porphyritic olivine-pyroxene; GP = granular pyroxene; GOP = granular olivine-pyroxene. Abbreviations in the column of "reference" stand for Rubin & Keil (1984) (RK84), Rubin & Grossman (1987) (RG87), and Rubin (1989) (Rubin89), respectively.

Chondrite group	Chondrule type	No.	Diameter-range (μm)	Median diam. (μm)	Mean diam.	Reference
L3	BO	173	140-5973		1038	RK84
L3	RP + C	201	48-4278		852	RK84
L3	BO	163	90-5080		680	RK84
L3	RP + C	70	73-1780		622	RK84
EH3	RP	86	30-1768		245	RG87
EH3	C	35	49-676		183	RG87
EH3	GP	10	62-158		110	RG87
EH3	POP + PO	27	70-570		252	RG87
EH3	PP	531	42-1350		219	RG87
CO3	POP	1868	24-1790	137	144	Rubin89
CO3	PP	494	31-967	146	146	Rubin89
CO3	PO	203	40-1360	206	196	Rubin89
CO3	BO	37	67-655	250	228	Rubin89
CO3	RP	132	28-790	145	133	Rubin89
CO3	C	96	34-830	119	120	Rubin89
CO3	GOP	4	72-255		119	Rubin89

be explained naturally, in the framework of the shock-wave heating model. The sizes of chondrules are bounded by the balance between the surface tension and the ram pressure on a molten droplet. The acceptable upper bound is $a_{\rm crit} \simeq 1\,{\rm mm}$. Their estimation seems to meet the upper limit of measured chondrule size distributions. On the other hand, Miura & Nakamoto (2005) calculated the thermal history of chondrule precursor dust particles taking into account the dust shrinkage by the evaporation. They found that the small precursor dust particles whose radii are smaller than a critical value, $a_{\rm pre}^{\rm min}$, cannot form chondrules because they evaporate away completely in the post-shock region. The acceptable lower limit of $a_{\rm pre}^{\rm min}$ is about $10\,\mu$m, though it depends on the shock velocity and the pre-shock gas number density. The results seem to well explain the lower boundary of the measured chondrule size distributions.

1.3.6 Shape

Tsuchiyama et al. (2003) studied three-dimensional shapes of chondrules using X-ray microtomography. They measured twenty chondrules with perfect shapes and smooth surfaces, which were selected from forty-seven chondrules separated from the Allende meteorite (CV3). The external shapes were approximated as three-axial ellipsoids with a-, b-, and c-axes (axial radii are A, B, and C ($A \geq B \geq C$), respectively) using the moments of inertia of the chondrules, where the rotation axes with the minimum and maximum moments correspond to the a- and c-axes, respectively. The plot of C/B vs. B/A (Figure 1.5) shows that (1) the shapes are diverse from oblate ($A \sim B > C$), general three-axial ellipsoid ($A > B > C$) to prolate chondrules ($A > B \sim C$), and (2) two groups can be recognized: oblate to prolate chondrules with large C/B and B/A of 0.9 - 1.0 (group-A) and prolate chondrules with relatively small B/A of 0.74-0.78 (group-B).

Sekiya et al. (2003) derived the deformation and the internal flow of the molten chondrule precursor dust particle exposed to the high-velocity rarefied gas flow. It could occur in the shock-wave heating model. Sekiya et al. (2003) analytically solved the hydrodynamical equations of the molten droplet assuming that the non-linear terms of the hydrodynamical equations as well as the surface deformation are sufficiently small so that linearized equations are appropriate. However, their solutions do not explain the origin of chondrule shapes of prolate and general three-axial ellipsoid. On the other hand, Tsuchiyama et al. (2003) proposed that the oblate chondrules were rotating with high speed when the precursor dust particles have been melted. Assuming that the molten droplet re-solidified to form chondrules keeping its shapes, such chondrules should take the oblate shape, where the centrifugal force was balanced with the surface tension of a chondrule melt. However, they also could not naturally explain the prolate-shaped and general three-axial ellipsoid chondrules.

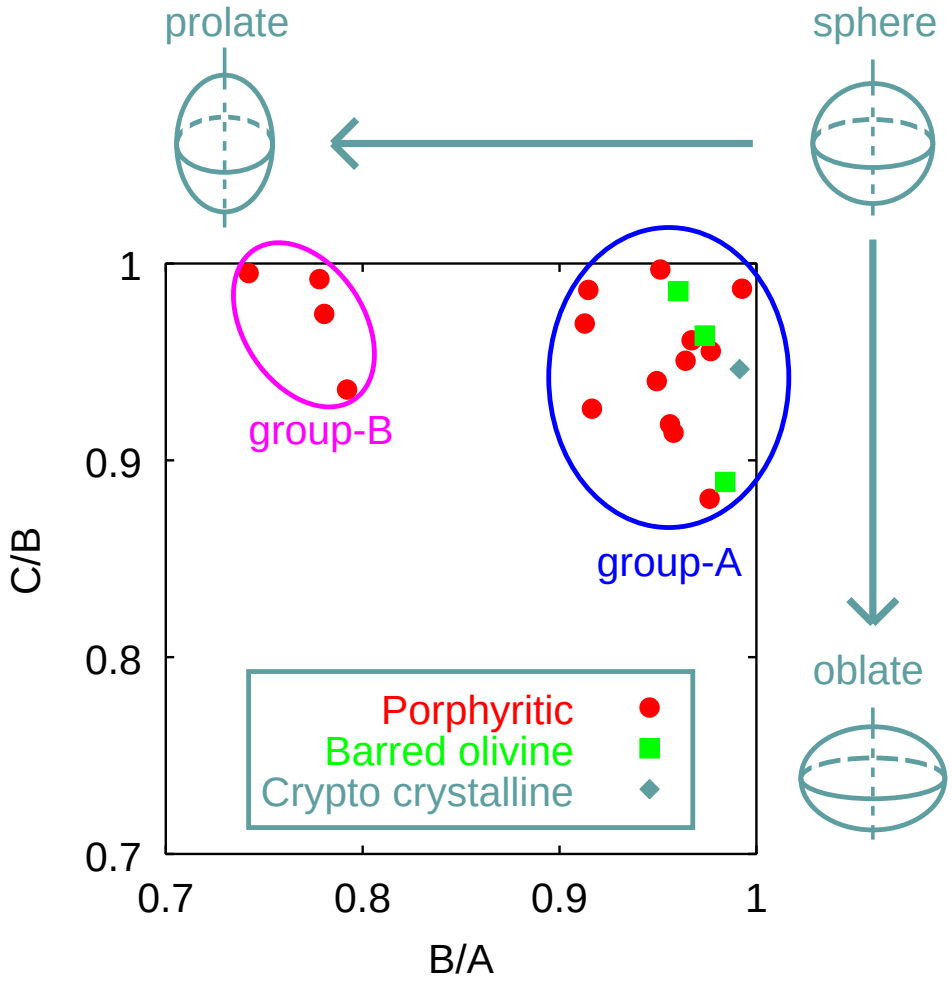

Figure 1.5: Chondrule shapes approximated as three-axial ellipsoids with the axial radii of A, B, and C (A≥B≥C) (Tsuchiyama et al. 2003). Two axial ratios B/A and C/B which both are unity indicate a perfect sphere. The shapes with B/A∼1 and C/B<1 is oblate shapes, and the shapes with B/A<1 and C/B∼1 is prolate shapes. It is found that chondrules can be classified into two groups in the shapes, group-A and -B. Chondrule textural types are also indicated.

1.4 Goals of the Thesis

As shown in the previous section, there are a lot of the observational constraints for chondrule formation. In those constraint, we are interested in the following topics, which have not been well investigated theoretically in the framework of the shock-wave heating model. One is about the dust thermal history, especially in the pre-shock region. The other one is about the hydrodynamics of molten droplet exposed to the high-velocity rarefied gas flow.

1. Recently, Tachibana & Huss (2005) suggested that the rapid heating is required in order to prevent the isotopic fractionation of sulfur in chondrules. Tachibana et al. (2004) confirmed that the gas frictional heating in the post-shock region is rapid enough the prevent the isotopic fractionation. However, the dust particles in the pre-shock region can be heated by the radiation mainly coming from the post-shock region.

    - In the previous studies taking into account the radiation transfer, only the thermal continuum radiation emitted from the dust particles has been considered (DC02, CH02). However, the post-shock gas emits the line emissions due to the radiative transitions of molecules and atoms (Miura & Nakamoto 2005). We should model the line emissions to obtain the thermal histories of dust particles.
    - What the heating rate of chondrules becomes in the pre-shock region, when the radiative heating cannot be neglected? Is it rapid enough to prevent the isotopic fractionation of sulfur in chondrules?
    - What is the physical process to determine the heating rate of the chondrule precursor dust particles?
    - In order to produce chondrules, the cooling rate through the crystallization temperature should be an appropriate value. Are there the appropriate shock conditions to satisfy both constraints; the rapid heating to prevent the isotopic fractionation and the appropriate cooling rate?

2. Tsuchiyama et al. (2003) studied three-dimensional shapes of chondrules and found that there are various shapes; oblate, prolate, and general three-axial ellipsoid. It is thought that the external shapes when the chondrule precursor dust particles melt reflect the final chondrule shapes.

    - The molten droplet is exposed to high-velocity rarefied gas flow in the shock-wave heating model. How do the molten droplets deform? Does the deformation of the droplet meet the measured chondrule shapes? What happens when the gas drag force is so strong that the droplet cannot keep its shape by the surface tension?
    - Tsuchiyama et al. (2003) suggested that the rotation of the droplet play an important role to determine the chondrule shapes. How do the molten droplets deform? Does the deformation of the droplet meet the measured chondrule shapes? What happens when the droplet rotation is so fast that the shape instability occurs?
    - In the shock-wave heating model, the rotation of chondrule precursor dust particles is expected in the gas flow, if its shapes are irregular. Therefore, it is important to investigate the dynamics of rapidly rotating droplet exposed to the gas flow. How do the molten droplets deform? Does the deformation of the droplet meet the measured chondrule shapes?

The former question is the topic about the thermal properties of chondrules. In order to answer the question, we have to carry out the numerical simulations of the hydrodynamics of the gas and the dynamical/thermodynamical evolutions of the precursor dust particles taking into account the radiation transfer in the chondrule-forming region. The latter question is the topic about the dynamical properties of the molten droplet. In order to answer the question, the three-dimensional hydrodynamical simulations for the incompressible fluid are required.

The organization of this thesis is as follows. In Chapter 2, we introduce the basic mechanism of the shock-wave heating. The topics about the thermal evolutions of chondrules are described in Chapters 3-5. In Chapter 3, we state the basic equations and the numerical procedures for calculations. We also show some results of the

simulations in this chapter. In Chapter 4, we discuss the mechanism to determine the heating rate of chondrules and conditions to prevent the isotopic fractionation. In Chapter 5, we consider the relation between the heating rate and the cooling rate, and the appropriate shock mechanism for chondrule formation. The topics about the dynamical properties of the molten droplets are described in Chapters 6-10. In Chapter 6, we review the theoretical studies about the deformation of the molten droplet. In Chapter 7, we describe the numerical scheme of the hydrodynamic simulations. The results of (1) only the gas drag force acting, (2) the droplet rotating without the rotation, and (3) the rotating droplet exposed to the gas flow, are described in Chapter 8, 9, and 10, respectively.

Chapter 2

Basic Properties of Shock-Wave Heating

The basic picture of dust thermal processing has been well investigated by many authors and this shows a good agreement with most of observational constraints to make chondrules. Recently, the shock-wave heating model has been developed by considering complex physics, however, the basic mechanism is rather simple. Therefore, we can estimate the basic properties of the shock-wave heating (e.g., the heating rate, the cooling rate, and the peak temperature of the chondrule precursor dust particles).

In this chapter, we introduce the basic equations for the dynamical/thermodynamical evolutions of the dust particles and derive the basic properties of the dust thermal histories in the shock-wave heating model.

2.1 Rest Frame of Shock Front

We briefly explained the basic mechanism of the shock-wave heating in Section 1.2. Fig. 1.2 showed the schematic picture of the model in the rest frame of the medium in the pre-shock region. However, in order to formalize the model, it is convenient to describe it in the rest frame of the shock front.

Figure 2.1(a) shows the picture in the rest frame of the medium in the pre-shock region, which is the same as Fig. 1.2. In the frame, the gas and the dust particles in the pre-shock region remain stationary. The gas number density in the pre-shock region is denoted as n_0. If shock waves are coming into the region, the dust particles are heated by the gas frictional heating in the post-shock region as described in Section 1.2. We denote the shock propagation speed against the pre-shock medium as $v_{\rm s}$ and call it the shock velocity. The intensity of the gas frictional heating acting on the dust particles in the post-shock region mainly depends on the pre-shock gas number density n_0 and the shock velocity $v_{\rm s}$.

Figure 2.1(b) shows the same process as Fig. 2.1(a) except of in the rest frame of the shock front. In the frame, the gas and the dust particles are approaching to the shock front with the shock velocity $v_{\rm s}$. After passing through the shock front, the gas is decelerated suddenly, while the dust particles tend to keep its initial velocity. This causes the relative velocity between the gas and the dust particles, and the gas frictional heating takes place in the post-shock region. We adopt the rest frame of the shock front for the formalizations in this chapter.

Before we explain the formalizations, we state the notations of the physical variables for the gas. The pre-shock gas number density n_0 and the shock velocity $v_{\rm s}$ mean the variables at far up the stream where the gas flow is not disturbed by the propagation of the shock front. The variables just before the shock front are denoted as n_1 and v_1. Generally speaking, although the values of n_1 and v_1 are different from n_0 and $v_{\rm s}$ respectively if considering the radiation coming from the post-shock region (see Chapter 3), we approximate $n_1 \simeq n_1$ and $v_1 \simeq v_{\rm s}$ in this chapter. The variables just behind the shock front are transcribed as n_2 and v_2. Finally, we use n_3 and v_3 for the variables at far down the stream.

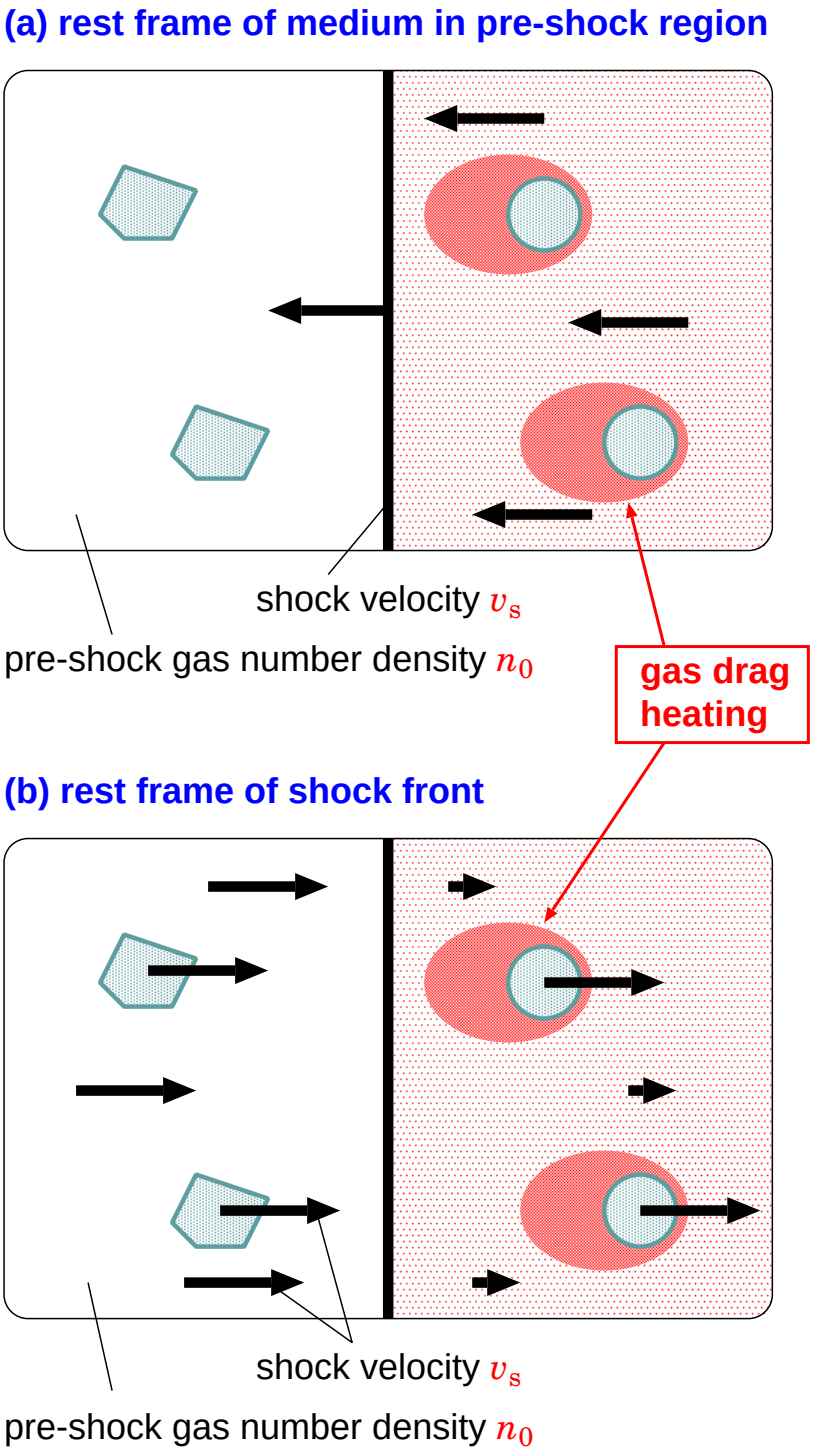

Figure 2.1: Schematic picture of the shock-wave heating. Top panel (a) shows the picture in the rest frame of the medium in pre-shock region, and bottom panel (b) is in the rest frame of the shock front.

2.2 Post-shock Gas

When the gas flow meets the shock front, it is suddenly compressed and decelerated by the pressure of gas in the post-shock region. The jump condition is given by the Rankine-Hugoniot relation,

$$\frac{\rho_2}{\rho_1} = \frac{n_2}{n_1} = \frac{v_1}{v_2} = \frac{(\gamma+1)\mathcal{M}^2}{(\gamma-1)\mathcal{M}^2+2}, \tag{2.1}$$

$$\frac{T_2}{T_1} = \frac{\{2\gamma\mathcal{M}^2-(\gamma-1)\}\{(\gamma-1)\mathcal{M}^2+2\}}{(\gamma+1)^2\mathcal{M}^2}, \tag{2.2}$$

where ρ, v, T, and γ are the density, the velocity against the shock front, the temperature, and the ratio of specific heat of gas, respectively. The gas number density is $n = \rho/\bar{m}$, where $\bar{m}$ is the mean molecular weight, and we assume that $\bar{m}$ is constant. The suffix "1" and "2" stand for immediately before and behind the shock front, respectively. The Mach number in the pre-shock region is expressed as $\mathcal{M} \equiv v_1/\sqrt{\gamma k_{\rm B} T_1/\bar{m}}$, where $\bar{m}$ is the mean molecular weight of the gas and $k_{\rm B}$ is the Boltzmann constant.

As the post-shock gas goes apart from the shock front, it cools due to some cooling mechanisms (e.g., Lyman α emission, dissociation of H_2 molecules, molecular line emission, and so on). However, the post-shock region is approximately isobaric in the case of the strong shock ($\mathcal{M} \gg 1$), which is analytically derived by Susa et al. (1998). In other words, the product of the gas number density and the gas temperature should be approximately constant. Therefore, we obtain

$$n_2 T_2 \simeq n_3 T_3, \tag{2.3}$$

where the suffix "3" means the post-shock region far from the shock front. Taking the strong shock limit and eliminating n_2 and T_3 from Eqs. (2.1)-(2.3), we obtain the post-shock gas number density n_3 and velocity v_3 as

$$\frac{n_3}{n_1} \simeq \frac{2\gamma}{\gamma+1}\frac{\bar{m}}{\gamma k_{\rm B} T_3} v_1^2 \simeq 12.1\left(\frac{v_1}{10\,{\rm km\,s^{-1}}}\right)^2\left(\frac{T_3}{2,000\,{\rm K}}\right)^{-1} \tag{2.4}$$

and

$$\frac{v_3}{v_1} \simeq \frac{n_1}{n_3} \simeq 0.083\left(\frac{v_1}{10\,{\rm km\,s^{-1}}}\right)^{-2}\left(\frac{T_3}{2,000\,{\rm K}}\right), \tag{2.5}$$

respectively.

2.3 Dust Dynamics

The chondrule precursor dust particles exchange the momentum and energy with the ambient gas. In the shock-wave heating model for chondrule formation, the formulations of the momentum/energy transfer rates are done by assuming that the gas flow around the dust particles behaves as the free molecular flow, in which molecules scattered and reemitted from the dust surface do not disturb the free stream velocity distribution. It is because the mean free path of the gas molecules is much greater than the typical size of the dust particles.

2.3.1 Equation of Motion

If there is a relative velocity of dust particles to the gas, dust motion is changed by the gas drag force. The equation of motion is written by

$$\frac{4}{3}\pi a_{\rm d}^3 \rho_{\rm mat} \frac{dv_{\rm d}}{dt} = -\pi a_{\rm d}^2 \frac{C_{\rm D}}{2} \bar{m} n |v_{\rm rel}| v_{\rm rel}, \tag{2.6}$$

where $\rho_{\rm mat}$, $v_{\rm d}$, $C_{\rm D}$, and $v_{\rm rel}$ are the dust particle material density, the velocity of dust particle, the drag coefficient, and the relative velocity of dust particle to the gas, respectively. The expression of drag coefficient is given as (e.g., Probstein 1968, Hood & Horanyi 1991, Iida et al. 2001)

$$C_{\rm D} = \frac{2}{3s_{\rm a}} \left(\frac{\pi T_{\rm d}}{T} \right)^{1/2} + \frac{2s_{\rm a}^2 + 1}{s_{\rm a}^3 \pi^{1/2}} \exp(-s_{\rm a}^2) + \frac{4s_{\rm a}^4 + 4s_{\rm a}^2 - 1}{2s_{\rm a}^4} {\rm erf}(s_{\rm a}), \tag{2.7}$$

where $T_{\rm d}$ is the dust temperature and $s_{\rm a} \equiv |v_{\rm rel}|/\sqrt{2k_{\rm B}T/\bar{m}}$. In the limit of $s_{\rm a} \gg 1$, $C_{\rm D} \to 2$. On the contrary, $C_{\rm D} \to (2/(3s_{\rm a}))(\pi T_{\rm d}/T)^{1/2}$ for $s_{\rm a} \ll 1$.

2.3.2 Equation of Energy

The dust temperature changes due to some heating/cooling mechanisms; energy transfer with the gas, absorption of ambient radiation, radiative energy loss, and latent heat cooling due to the evaporation. The energy equation for the dust particle which governs the dust temperature is written as

$$\frac{4}{3}\pi a_{\rm d}^3 \rho_{\rm mat} C \frac{dT_{\rm d}}{dt} = 4\pi a_{\rm d}^2 (\Gamma_{\rm g-p} + \Gamma_{\rm rad} - \Lambda_{\rm rad} - \Lambda_{\rm evap}), \tag{2.8}$$

where C and $T_{\rm d}$ are the specific heat of dust particles and the dust temperature, respectively. Regarding the heating rate of the energy transfer with gas $\Gamma_{\rm g-p}$, we adopt the same expression of previous studies as (Probstein 1968, Hood & Horanyi 1991)

$$\Gamma_{\rm g-p} = \bar{m} n |v_{\rm rel}| (T_{\rm rec} - T_{\rm d}) C_{\rm H}, \tag{2.9}$$

where $T_{\rm rec}$ and $C_{\rm H}$ are the recovery temperature and the heat transfer function, respectively. They are given as

$$T_{\rm rec} = \frac{T}{\gamma+1}\left[2\gamma + 2(\gamma-1)s_{\rm a}^2 - \frac{\gamma-1}{0.5 + s_{\rm a}^2 + s_{\rm a}\pi^{-1/2}\exp(-s_{\rm a}^2){\rm erf}^{-1}(s_{\rm a})}\right] \tag{2.10}$$

and

$$C_{\rm H} = \frac{\gamma+1}{\gamma-1}\frac{k_{\rm B}}{8\bar{m}s_{\rm a}^2}[\pi^{-1/2}s_{\rm a}\exp(-s_{\rm a}^2) + (0.5+s_{\rm a}^2){\rm erf}(s_{\rm a})], \tag{2.11}$$

respectively. In the limit of $s_{\rm a} \gg 1$, $T_{\rm rec} \to 2[(\gamma-1)/(\gamma+1)]s_{\rm a}^2 T$ and $C_{\rm H} \to [(\gamma+1)/(\gamma-1)]k_{\rm B}/(8\bar{m})$. On the contrary, in the limit of $s_{\rm a} \ll 1$, $T_{\rm rec} \to T$ and $C_{\rm H} \to [2/(\pi^{1/2}s_{\rm a})][(\gamma+1)/(\gamma-1)]k_{\rm B}/(8\bar{m})$. The heating/cooling rates due to the absorption of ambient radiation $\Gamma_{\rm rad}$, the emission of dust thermal continuum radiation $\Lambda_{\rm rad}$, and the latent heat cooling by evaporation $\Lambda_{\rm evap}$ are given as

$$\Gamma_{\rm rad} = \epsilon_{\rm abs}\pi\mathcal{J}, \quad \Lambda_{\rm rad} = \epsilon_{\rm emit}\sigma_{\rm SB}T_{\rm d}^4, \quad \Lambda_{\rm evap} = J_{\rm evap}L_{\rm evap}, \tag{2.12}$$

where $\epsilon_{\rm abs}$ ($\epsilon_{\rm emit}$), $\mathcal{J}$, $\sigma_{\rm SB}$, $J_{\rm evap}$, and $L_{\rm evap}$ are the planck-mean absorption (emission) coefficient, the mean intensity of ambient radiation, the Stefan-Boltzmann constant, the evaporation rate of dust component per unit area, and the latent heat of dust component, respectively. If the dust temperature increases as high as the boiling temperature, the boiling takes place in the molten droplet. After reaching at the boiling point, the dust temperature does not change because the input energy is consumed for the phase transition from liquid to gas. Assuming bubbles generated in molten dust particle go away to outside quickly, the boiling leads to shrinkage of the dust particle (Miura *et al.* 2002).

2.3.3 Evolution of Dust Radius

The particle radius decreases due to the evaporation from the dust surface. The evolution of the particle radius due to evaporation is given by (Miura *et al.* 2002)

$$-\frac{da_{\rm d}}{dt} = \frac{J_{\rm evap}}{\rho_{\rm mat}}. \tag{2.13}$$

We use the evaporation rate of forsterite given by Tsuchiyama *et al.* (1998).

Finally, we should mention the fragmentation of molten dust particle due to the ram pressure. In the post-shock region, the ram pressure acts on the surface of molten dust particles. Susa & Nakamoto (2002) estimated the maximum radius of molten dust particles above which the ram pressure dominates the surface tension and the molten dust particle should be fragmented. In our study, if the dust radius is larger than the maximum radius during its melting phase, we assume that the dust particle is divided into two molten droplets which have the same volume.

2.4 Dust Thermal History

In this section, we show the thermal history of precursor dust particle in the post-shock region in the case without the radiation heating and the effect of the evaporation. After passing through the shock front, the dust particle is heated due to the gas frictional heating. We call it "heating phase." As the dust temperature increases, the cooling processes due to the thermal radiation and the interaction with the ambient gas become equal to the gas frictional heating. At the time when the energy balance on the dust particle is established, the heating phase ceases and the dust particle takes "peak temperature." After that, as the relative velocity between the gas and the dust particles is deduced by the gas drag force, the heating rate by the gas friction decreases. Therefore, the dust particles cool gradually. We call the pahse as "cooling phase."

2.4.1 Heating Phase

After passing through the shock front, the gas frictional heating takes place on precursor dust particle. Simultaneously, the gas drag force also works on the dust

particle and it tends to decrease the relative velocity between the post-shock gas and the dust particle. In the shock-wave heating model, the dust temperature increases faster than that the relative velocity decreases. Therefore, the gas frictional heating can heat the dust particle effectively.

Above discussions are easily confirmed by comparing two time scales; the stopping time scale, $t_{\rm stop}$, and the heating time scale, $t_{\rm heat}$. The stopping time scale means the time taken for dumping the initial dust velocity due to the gas frictional force. Using Eq. (2.6) and taking the limit of $s_{\rm a} \gg 1$, we obtain

$$t_{\rm stop} \simeq \frac{4a_{\rm d}\rho_{\rm mat}}{3\bar{m}n_3 v_{\rm rel}}, \tag{2.14}$$

where we use n_3 as the post-shock gas number density. On the other hand, the heating time scale means the time taken for heating the dust particle up to the melting point. Using Eq. (2.8) and taking the limit of $s_{\rm a} \gg 1$, we obtain

$$t_{\rm heat} \simeq \frac{8a_{\rm d}\rho_{\rm mat}CT_{\rm melt}}{3\bar{m}n_3 v_{\rm rel}^3}, \tag{2.15}$$

where $T_{\rm melt}$ is the melting temperature of the dust particle. The ratio of these two time scales is $t_{\rm heat}/t_{\rm stop} \simeq 0.06\,(v_{\rm rel}/10\,{\rm km\,s^{-1}})^{-2}$, assuming $C = 1.4\times10^7\,{\rm erg\,g^{-1}\,K^{-1}}$ and $T_{\rm melt} = 2,000\,{\rm K}$. Considering that the shock velocity must be larger than about $6\,{\rm km\,s^{-1}}$ or more to melt silicate dust particle (see Fig. 1.3), it is found that the heating time scale is much shorter than the stopping time scale. In other words, the dust particle keeps its initial velocity in the pre-shock region when it is heated up to the melting point due to the gas frictional heating. On the contrary, the gas velocity decreases to one-tenth or less of in the pre-shock region. Therefore, the relative velocity of the dust particle to the gas is almost the same as the initial velocity in the pre-shock region, so we can approximate $v_{\rm rel} \simeq v_1$.

We can also estimate the heating rate of the dust particle by the frictional heating. The heating rate $R_{\rm heat}$ is given by $dT_{\rm d}/dt$, so we obtain

$$R_{\rm heat} \sim \frac{3\bar{m}n_3 v_{\rm s}^3}{8a_{\rm d}\rho_{\rm mat}C} \simeq \frac{3\bar{m}^2 n_0 v_{\rm s}^5}{4(\gamma+1)a_{\rm d}\rho_{\rm mat}Ck_{\rm B}T_3}, \tag{2.16}$$

where we substitute n_3 in Eq. (2.4), and take $n_1 = n_0$ and $v_1 = v_{\rm s}$.

2.4.2 Peak Temperature

For chondrule formation, the frictional heating must be strong enough to heat precursor dust particle up to the melting temperature of silicate components. The peak temperature of dust particle can be estimated by considering the energy balance, namely, just take $dT_{\rm d}/dt = 0$ in Eq. (2.8). Here, we neglect $\Gamma_{\rm rad}$ because the term is smaller than $\Gamma_{\rm g-p}$ where the dust particle takes the peak temperature. We also neglect $\Lambda_{\rm evap}$ because it is not so important to determine the melting criterion for shock parameters (Miura et al. 2002). Therefore, the energy balance which gives the peak dust temperature is written as

$$\Gamma_{\rm g-p} - \Lambda_{\rm rad} = 0. \tag{2.17}$$

Taking the limit of $s_{\rm a} \gg 1$ and rewriting each term explicitly, we obtain

$$\frac{1}{8}\bar{m}n_3|v_{\rm rel}|^3 - \frac{1}{8}\frac{\gamma+1}{\gamma-1}n_3|v_{\rm rel}|k_{\rm B}T_{\rm peak} - \epsilon_{\rm emit}\sigma_{\rm SB}T_{\rm peak}^4 = 0. \tag{2.18}$$

In order to rewrite the above equation with the initial shock parameters, $v_{\rm s}$ and n_0, substituting Eqs. (2.4) and (2.5) to the above equation, we obtain the final form of the energy balance equation;

$$\frac{\bar{m}^2 n_0 v_{\rm s}^5}{4(\gamma+1)k_{\rm B}T_3} - \frac{\bar{m}n_0 v_{\rm s}^3 T_{\rm peak}}{4(\gamma-1)T_3} - \epsilon_{\rm emit}\sigma_{\rm SB}T_{\rm peak}^4 = 0. \tag{2.19}$$

It is easily found that the second term in Eq. (2.19) dominants the third term in the high density limit because the second term is proportional to n_0 and the third term is independent to n_0. The critical density $n_{0,\rm crit}$ above which the second term dominants the third term is given by equating the second and the third terms. We obtain

$$n_{0,\rm crit} = \frac{4(\gamma-1)\epsilon_{\rm emit}\sigma_{\rm SB}T_3T_{\rm peak}^3}{\bar{m}v_{\rm s}^3}. \tag{2.20}$$

If $n_0 \gg n_{0,\rm crit}$, the peak temperature is given by equating the first and the second terms. We obtain

$$T_{\rm peak} = \frac{\gamma-1}{\gamma+1}\frac{\bar{m}}{k_{\rm B}}v_{\rm s}^2 \quad \text{for } n_0 \gg n_{0,\rm crit}. \tag{2.21}$$

On the contrary, if $n_0 \ll n_{0,\rm crit}$, the peak temperature is given by equating the first and the third terms. We obtain

$$T_{\rm peak} = \left(\frac{\bar{m}^2 n_0 v_{\rm s}^5}{4(\gamma+1)\epsilon_{\rm emit}\sigma_{\rm SB} k_{\rm B} T_3} \right)^{1/4} \quad \text{for } n_0 \ll n_{0,\rm crit}. \tag{2.22}$$

In Figure 2.2, we plot $T_{\rm peak}$ as functions of $v_{\rm s}$ and n_0. The black lines indicate contours of $T_{\rm peak} = 1100\,{\rm K}$, $1300\,{\rm K}$, $\cdots$, and $2900\,{\rm K}$, respectively. We assume $\bar{m} = 4 \times 10^{-24}\,{\rm g}$ and $\epsilon_{\rm emit} = 1$. In the high density region above $n_{0,\rm crit}$, $T_{\rm peak}$ seems not to depend on n_0. In this case, the energy balance is given by equating the first and second term in Eq. (2.18). Since both terms are proportional to n_0, $T_{\rm peak}$ does not depend on n_0. On the contrary, in the low density region below $n_{0,\rm crit}$, the required shock velocity to form chondrules increases as the pre-shock gas number density decreases. In such low density environment, since the energy balance is given by equating the first and third terms in Eq. (2.18), we have to increase $v_{\rm s}$ in order to gain the same heating intensity. It is easily found that the shock velocity is proportional to the pre-shock density as $n_0^{-1/5}$ along the constant $T_{\rm peak}$ lines.

2.4.3 Cooling Phase

After the dust particle has the peak temperature, it begins to cool as the relative velocity between the gas and the dust particles are deduced. If ignoring the gas frictional heating, the molten dust particle cools very rapidly. Using Eq. (2.8), we can estimate the radiative cooling rate as

$$\frac{dT_{\rm d}}{dt} \simeq \frac{3\epsilon_{\rm emit}\sigma_{\rm SB} T_{\rm d}^4}{a_{\rm d}\rho_{\rm mat} C} \simeq 2 \times 10^6 \left(\frac{a_{\rm d}}{1\,{\rm mm}} \right)^{-1} {\rm K\,hr^{-1}}, \tag{2.23}$$

where we take $\epsilon_{\rm emit} = 1$, $T_{\rm d} = 2000\,{\rm K}$, $\rho_{\rm mat} = 3\,{\rm g\,cm^{-3}}$, and $C = 1.4 \times 10^7\,{\rm erg\,g^{-1}\,K^{-1}}$. However, the dust particles cannot cool so rapidly because the relative velocity between the gas and the dust particles remains n the cooling phase and the gas frictional heating takes place. Therefore, in the cooling phase, the gas frictional heating is balanced with the radiative cooling, and the dust particles cool as the relative velocity decreases. Since the cooling rate $R_{\rm cool}$ is given by $T_{\rm melt}/t_{\rm stop}$ (see Eq. 2.14), we obtain

$$R_{\rm cool} \simeq \frac{3\bar{m} n_3 v_{\rm rel} T_{\rm melt}}{4 a_{\rm d}\rho_{\rm mat}} \simeq \frac{3\bar{m}^2 n_0 v_{\rm s}^3 T_{\rm melt}}{2(\gamma+1) a_{\rm d}\rho_{\rm mat} k_{\rm B} T_3}. \tag{2.24}$$

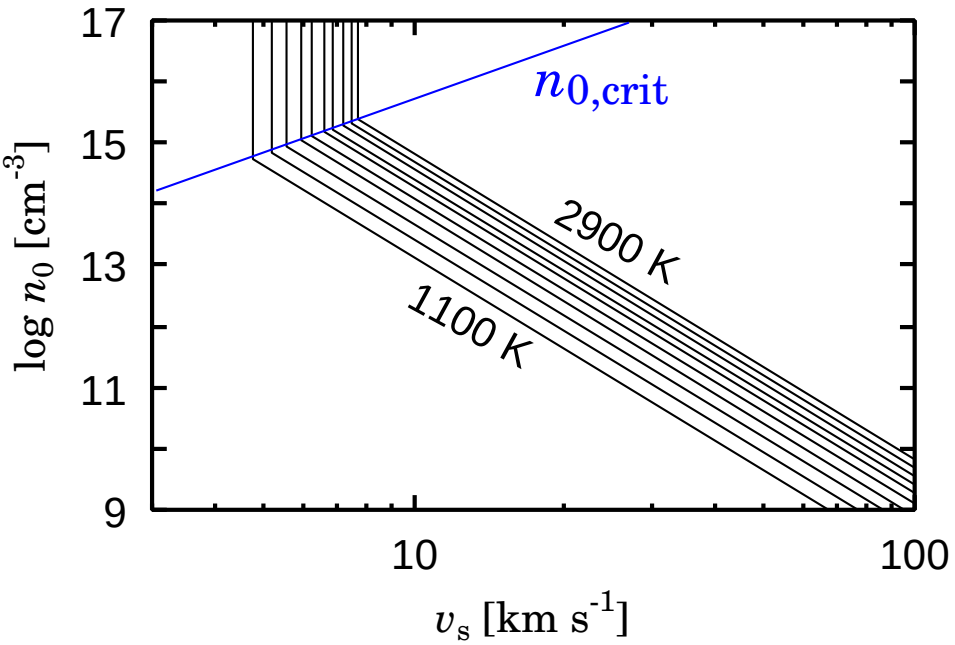

Figure 2.2: Peak temperature of precursor dust particle as functions of the shock velocity v_s and the pre-shock gas number density n_0. We plot contours of the peak temperature from 1100 K to 2900 K with interval of 200 K.

2.4.4 Predicted Dust Thermal Histories

We obtained the heating rate and the cooling rate of the chondrule precursor dust particles as functions of the pre-shock gas number density n_0, the shock velocity v_s, and the dust radius a_d (see Eqs. 2.16 and 2.24). We also obtain the shock conditions which are appropriate to heat the precursor dust particles up to the melting temperature (see Eqs. 2.21 and 2.22, and Fig. 2.2). Based on those estimations, we can predict the dust thermal histories in the shock-wave heating if considering only the gas frictional heating and the radiative cooling (neglecting the ambient radiation field as the heating source for the dust particles).

From Fig. 2.2, it is found that we have to select the appropriate pair of the pre-shock gas number density n_0 and the shock velocity v_s in order to heat the precursor dust particles up to about the melting temperature. If n_0 or/and v_s are smaller than the required value, the gas frictional heating would not be strong enough to melt the silicate dust particles. On the contrary, if n_0 or/and v_s are much larger than the appropriate values, the dust particles would evaporate away not to form chondrules. In Table 2.1, some pairs of n_0 and v_s are listed. We estimate the peak temperature T_{peak}, the heating rate R_{heat}, and the cooling rate R_{cool} using the pairs of n_0 and v_s. We find that the heating rate becomes about $10^6\,\mathrm{K\,hr^{-1}}$ for any set of n_0 and v_s in Table 2.1. The reason why the heating rate does not depend on the shock conditions can be easily understood from Eqs. (2.16) and (2.22), because both of the heating rate R_{heat} and the peak temperature T_{peak} are proportional to $\propto n_0 v_s^5$. Of course, since the (n_0, v_s)-dependence of T_{peak} changes if $n_0 \gg n_{0,crit}$, the hating rate would be larger values for the high-density shock waves. On the contrary, it is also found that the cooling rate R_{cool} takes the values about from $10^3 - 10^5\,\mathrm{K\,hr^{-1}}$ depending on the shock conditions. It is because the (n_0, v_s)-dependence of T_{peak} and R_{cool} are deferent (see Eqs. 2.22 and 2.24). The predicted dust thermal histories are briefly summarized in Figure 2.3.

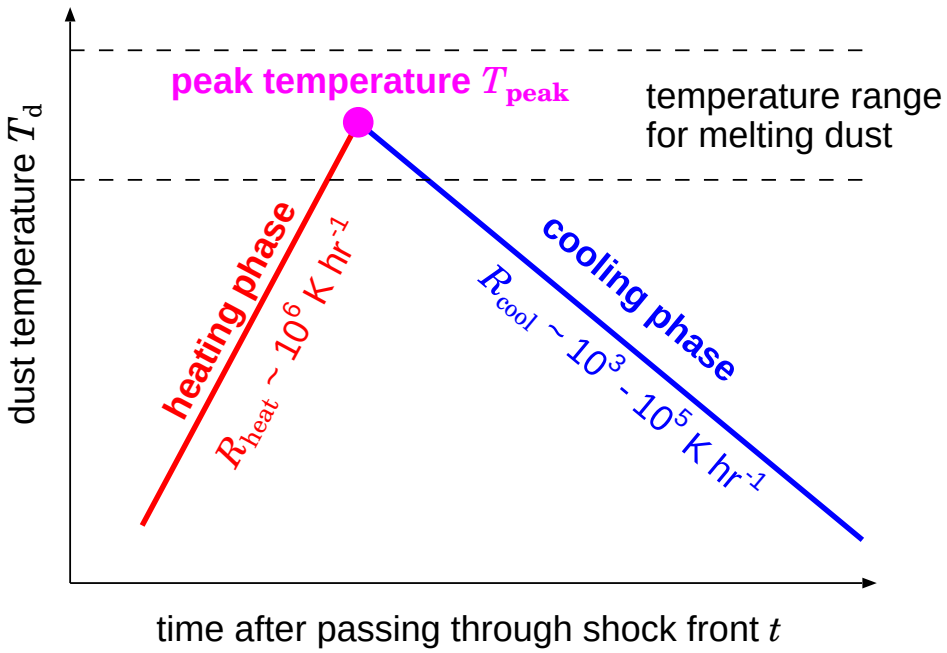

Figure 2.3: Schematic picture of the dust thermal histories in the post-shock region when the gas frictional heating dominates the heating by the radiation.

Table 2.1: Thermal history of precursor dust particle for chondrule-forming shock conditions. The dust radius is assumed to be $a_{\rm d} = 1\,{\rm mm}$. The heating rate and the cooling rate are inversely proportional to $a_{\rm d}$.

n_0 [cm^{-3}]	$v_{\rm s}$ [km s^{-1}]	$T_{\rm peak}$ [K]	$R_{\rm heat}$ [K hr^{-1}]	$R_{\rm cool}$ [K hr^{-1}]
10^{15}	6	1739	1.2×10^6	1.9×10^5
10^{14}	10	1807	1.6×10^6	8.7×10^4
10^{13}	16	1828	1.6×10^6	3.6×10^4
10^{12}	25	1796	1.5×10^6	1.4×10^4
10^{11}	40	1817	1.6×10^6	5.6×10^3

2.5 Ram Pressure

We can roughly estimate the ram pressure acting on the molten silicate dust particles in the post-shock region. The ram pressure, $p_{\rm fm}$, is given as $p_{\rm fm} = \bar{m} n_3 v_{\rm rel}^2$, where $\bar{m}$ is the mean molecular weight of the gas, n_3 is the gas number density in the post-shock region, and $v_{\rm rel}$ is the relative velocity between the post-shock gas and the dust particle. Substitute n_3 of Eq. (2.4), $v_{\rm rel} = v_{\rm s}$ and $n_1 = n_0$, we obtain

$$p_{\rm fm} \simeq 4.8 \times 10^3 \left(\frac{n_0}{10^{14}\,{\rm cm}^{-3}}\right)\left(\frac{v_{\rm s}}{10\,{\rm km\,s}^{-1}}\right)^4\left(\frac{T_3}{2000\,{\rm K}}\right)^{-1} {\rm dyne\,cm}^{-2}, \qquad (2.25)$$

where we take $\bar{m} = 4 \times 10^{-24}\,{\rm g}$. Considering that the heating rate due to the gas frictional heating $\Gamma_{\rm g-p}$ is $\propto n_0 v_{\rm s}^5$ (see the first term of the left hand side in Eq. 2.19), it is found that $p_{\rm fm}$ and $\Gamma_{\rm g-p}$ depend on n_0 and $v_{\rm s}$ differently. Therefore, the ram pressure acting on the dust particle should be different if the chondrule-forming shock parameters change. Figure 2.4 shows the ram pressure $p_{\rm fm}$ and the chondrule-forming shock condition on the $v_{\rm s} - n_0$ diagram. It is found that the higher the pre-shock gas density is, the higher the ram pressure on the red region becomes. However, the dependence is very weak if $n_0 \lesssim 10^{15}\,{\rm cm}^{-3}$ because the slopes of the blue lines and the red region is similar. In real situation, the ram pressure is slightly different from the simple estimation in Fig. 2.4 because the gas temperature where the dust particles melt might not be 2000 K or the mean molecular weight $\bar{m}$ might not be $4 \times 10^{-24}\,{\rm g}$ as a result of the dissociation of gas molecules. Here, we estimate the ram pressure as $p_{\rm fm} \simeq 4000\,{\rm dyne\,cm}^{-2}$ for high-density shock waves ($n_0 \simeq 10^{14}\,{\rm cm}^{-3}$) and $p_{\rm fm} \simeq 1000\,{\rm dyne\,cm}^{-2}$ for low-density shock waves ($n_0 \simeq 10^{11}\,{\rm cm}^{-3}$).

2.6 Conclusions

We explained the basic properties of the shock-wave heating model. The basic equations for the dynamical/thermodynamical evolution of the chondrule precursor dust particles are introduced. Approximating those equations, we analytically derived the thermal histories of the chondrule precursor dust particles (the heating rate, the

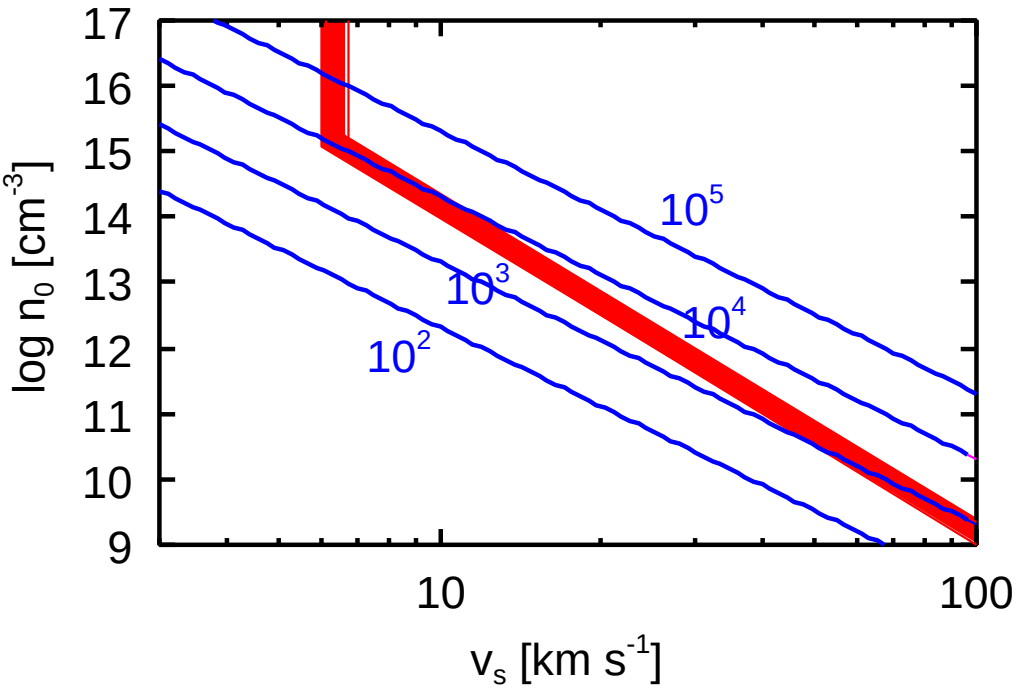

Figure 2.4: The ram pressure acting on the dust particles in the post-shock region (blue lines). The numbers in the panel indicate the values of ram pressure in the unit of dyne cm^{-2}. The red region is the chondrule-forming shock condition, in which the dust particles are heated up to between 1800 K and 2200 K.

cooling rate, and the peak temperature) when the gas frictional heating dominates the heating by the radiation, and the dynamical effect of the gas drag force acting on the dust particles (the ram pressure of the gas flow). We obtained the following conclusions:

1. The peak temperatures of the dust particles are mainly determined from the pre-shock gas number density n_0 and the shock velocity v_s. In order to obtain the appropriate peak temperature for chondrule formation, we have to select the appropriate set of n_0 and v_s (see Figure 2.2).

2. The expected heating rate when the dust particles are heated by the gas frictional heating is about $10^6\,\mathrm{K\,hr^{-1}}$ when the appropriate sets of n_0 and v_s for melting the silicate dust particles are adopted. The values of the heating rate do not strongly depend on the shock conditions because both of the heating rate and the peak temperature are proportional to $\propto n_0 v_s^5$.

3. The expected cooling rate when the dust particles cool as the relative velocity between the gas and the dust particles are deduced is in a range of about $10^3 - 10^5\,\mathrm{K\,hr^{-1}}$. The values depend on the set of n_0 and v_s.

4. The expected ram pressure of the gas flow acting on the dust particles in the post-shock region is about $4000\,\mathrm{dyne\,cm^{-2}}$ for $n_0 \sim 10^{14}\,\mathrm{cm^{-3}}$ and about $1000\,\mathrm{dyne\,cm^{-2}}$ for $n_0 \simeq 10^{11}\,\mathrm{cm^{-3}}$.

Part I

Thermal History of Precursor Dust Particles

Chapter 3

Basic Equations and Numerical Procedures

In order to calculate the thermal history of the dust particles, not only we have to solve the hydrodynamics of the gas flow passing though the shock front, but also the radiation transfer process is also an important factor. The existence of the strong radiation field contributes to heat the dust particles. The main sources of the radiation energy is the shocked gas and the dust particles heated by the gas frictional heating in the post-shock region. Namely, the thermal histories of the gas and the dust particles are correlating with the radiation field. In other words, while the thermal histories of the gas and the dust particles affect the radiation field, the radiation field affects the thermal history of the dust particles. Therefore, they must be solved consistently.

In this chapter, we explain basic equations of the radiative hydrodynamic processes and the numerical procedures to solve it. We also show some examples of the numerical simulations before discussing the thermal history of the dust particles in detail.

3.1 Radiative Shock-Wave Heating Model

When the thermal histories of the chondrule precursor dust particles are considered, the effects of the radiation field should be taken into account. The main sources of the radiation energy are the line emission of the gas molecules/atoms and the thermal continuum radiation of the dust particles heated by the gas frictional heating in the post-shock region (see Figure 3.1). Those radiations not only heat the dust particles in the post-shock region, but also penetrate into the pre-shock region and heat the dust particles there. Then The heated dust particles emit the thermal radiation and the other dust particles absorb the thermal radiation. Therefore, the dust particles are heated more and more. In this paper, we call above process "the blanket effect." In order to calculate the mean intensity of the radiation field, we have to solve the radiation transfer equation consistently with the gas/dust thermal properties in the chondrule-forming region.

In this paper, we consider the steady, one-dimensional, plane-parallel structures as shown in Fig. 3.1, in which all of the physical variables depend on only the spatial coordinate x.

3.2 Gas Dynamics

The heating and cooling processes violate the adiabatic condition of the gas. Then, 1-dimensional, steady flow is governed by the conservation equations of mass/momentum and the energy equation as follows:

$$\rho_0 v_{\rm s} = \rho v, \tag{3.1}$$

$$\rho_0 v_{\rm s}^2 + p_0 = \rho v^2 + p, \tag{3.2}$$

$$\frac{de}{dt} = \frac{e+p}{\rho}\frac{d\rho}{dt} - \Lambda, \tag{3.3}$$

where $v_{\rm s}$ is the shock velocity, ρ, v, p, and e are the density, velocity, pressure of the gas and the gas internal energy per unit volume, respectively. The suffix "0" stands for values at the upstream boundary of the calculation ($x = -x_{\rm m}$). The net cooling

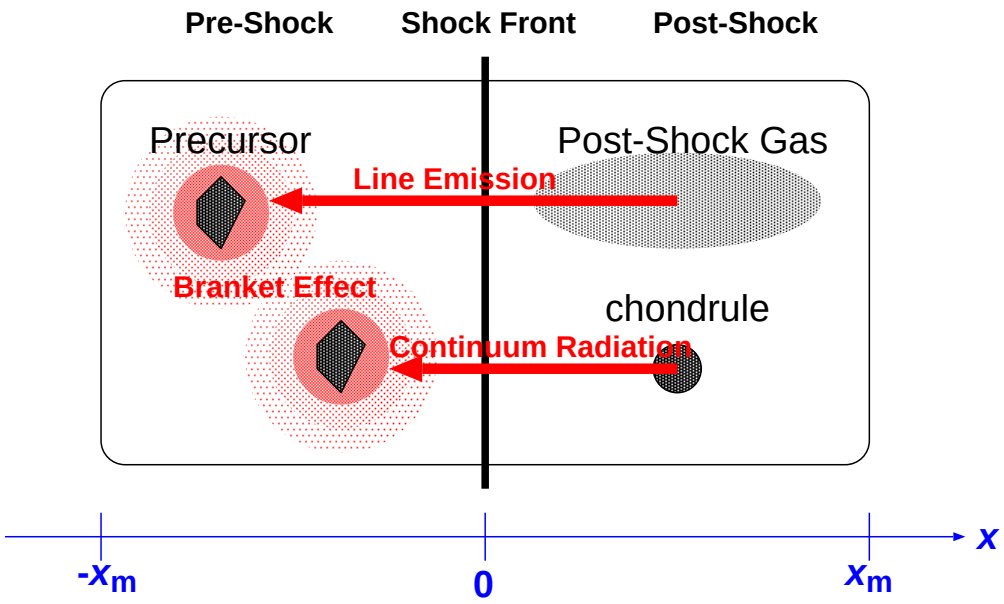

Figure 3.1: Schematic picture of the shock-wave heating model taking into account the radiation transfer of the line emission of the gas and the thermal continuum radiation of the dust particles. The spatial coordinate x is taken to be perpendicular to the shock front. The shock front is assumed to locate at $x = 0$.

rate Λ contains the atomic/molecular cooling processes, chemical heating/cooling processes, and energy transfer between the gas and dust particles, and is given by

$$\Lambda = \Lambda_{\mathrm{Ly}\alpha} + \Lambda_{\mathrm{H_2O(V)}} + \Lambda_{\mathrm{CO(V)}} + \Lambda_{\mathrm{H_2O(R)}} + \Lambda_{\mathrm{CO(R)}} + \Lambda_{\mathrm{dust}} + \Lambda_{\mathrm{H_2diss}} - \Gamma_{\mathrm{H_2form}}, \quad (3.4)$$

where Lyα, H_2O(V), CO(V), H_2O(R), and CO(R) stand for the cooling processes due to the line emission of Lyman α, H_2O vibration, CO vibration, H_2O rotation, and CO rotation, respectively. The energy transfer rate from gas to dust particles is Λ_{dust}. The cooling (heating) processes associated with the H_2 dissociation (formation) is $\Lambda_{\mathrm{H_2diss}}$ ($\Gamma_{\mathrm{H_2form}}$). We consider the effect that the line emissions are absorbed by the molecules or atoms in the chondrule-forming region , and the net cooling rate by the line emission is deduced. The method that we adopt to consider the line absorption is similar to the "on-the-spot approximation" method used in many astrophysical calculations, e.g., calculations for ionization of H II regions (Osterbrock 1988). In this approximation, photons that would be absorbed by gas atoms/molecules apart from the emission place ("spot") are considered that they are absorbed by gas atoms/molecules at the emission place ("on-the-spot"). The Detailed procedures are described in Section 3.2.1.

The system of rate equations which governs nonequilibrium chemical reactions among gas species is written as

$$\frac{dy_i}{dt} = n_{\mathrm{H_0}} \sum_{j=1}^{28} \sum_{k=1}^{28} k_{jk} y_j y_k + n_{\mathrm{H_0}}^2 \sum_{l=1}^{28} \sum_{m=1}^{28} \sum_{n=1}^{28} k_{lmn} y_l y_m y_n, \quad (3.5)$$

where $n_{\mathrm{H_0}}$ is the total number density of hydrogen nuclei, y_i is the relative abundance of species i to $n_{\mathrm{H_0}}$, k_{jk} and k_{lmn} are the reaction rate coefficients, respectively. The first and second terms in Eq.(3.5) describe the two-body and three-body interactions in the gas phase, respectively. We include 156 reactions among 28 gas species (see Appendix B). The interaction of particles with radiation is not included. Included processes in Eq.(3.5) and adopted rate coefficients are listed in Iida et al. (2001)[1]. The time derivatives in Eq.(3.3) and (3.5) are Lagrangian derivatives. We

[1]Iida et al. (2001) included 176 reactions among 35 gas species. In this study, we neglect D- and Si-inclusive species because they do not contribute to the gas cooling processes as coolant species.

numerically integrate Eqs.(3.1)-(3.3) and (3.5) using a finite difference algorithm described in Shapiro & Kang (1987).

When the gas flow meets the shock front, it is suddenly compressed and decelerated by the pressure of gas in the post-shock region. The jump condition is given by the Rankine-Hugoniot relation (Eqs. 2.1 and 2.2).

In Eqs. (3.1) and (3.2), we neglect the mass loading by evaporation of dust materials and the momentum exchange with dust particles. This assumption is valid because we consider low dust-to-gas mass ratio (≤ 0.1, see Section 3.4). However, we take into account the energy exchange with dust particles in Eq. (3.3) because the dust cooling for the gas can work well even in the low dust-to-gas mass ratio environment.

3.2.1 Net Cooling Rate

We consider line photons emitted at a certain point $x_{\rm emit}$ in the post-shock region ($0 < x_{\rm emit} < x_{\rm m}$, see Fig. 3.1). We assume that the photons which achieve at $x = x_{\rm m}$ without being absorbed can remove the gas thermal energy to outside. Similarly, it is assumed that the gas molecules in the pre-shock region do not absorb the line photons emitted in the post-shock region because of the doppler shift; the relative velocity between the pre- and post-shock gases is larger than the velocity dispersion of gas molecules. According to Neufeld & Kaufman (1993), the net cooling rate for each molecule depends on the temperature, the density, and an optical depth parameter $\tilde{N}$(M) (see Appendix A.1). Neufeld & Kaufman considered a static plane-parallel slab of thickness d, in which physical parameters (density and temperature) are constant spatially, however, in our model, those physical parameters are functions of the spatial coordinate x. Therefore, we estimate the optical depth parameter by integrating n(M)/Δv. We define the optical depth parameter of the upstream (downstream) side of the emitting point, $\tilde{N}^{up}$ ($\tilde{N}^{down}$), as

$$\tilde{N}^{up}(\mathrm{M}) = 2\int_0^{x_{\rm emit}} \frac{n(\mathrm{M})}{\Delta v} dx, \quad \tilde{N}^{down}(\mathrm{M}) = 2\int_{x_{\rm emit}}^{x_{\rm m}} \frac{n(\mathrm{M})}{\Delta v} dx. \tag{3.6}$$

The factor 2 in front of integral of each equation is needed to consider that the emitting point is placed at the center of slab. We obtain the rate coefficient for each

direction, L^{up} and L^{down}, by substituting $\tilde{N}^{up}$ and $\tilde{N}^{down}$ into Eq. (A.4). Finally, we obtain the cooling rate for each direction as

$$\Lambda^{up} = \frac{L^{up}}{2} n(\mathrm{H_2}) n(\mathrm{M}), \quad \Lambda^{down} = \frac{L^{down}}{2} n(\mathrm{H_2}) n(\mathrm{M}). \tag{3.7}$$

The total cooling rate is given as $\Lambda = \Lambda^{up} + \Lambda^{down}$.

3.3 Radiation Transfer

In the shock-wave heating model, the main heating process to heat the dust particles is the gas frictional heating in the post-shock region. However, the radiation field in the chondrule-forming region also affects the dust thermal histories. The radiation is mainly emitted in the post-shock region, where the shock-heated gas and the dust particles heated by the gas frictional heating are located. The radiation penetrates into the pre-shock region and heats the dust particles there. In order to know the intensity of the radiation field and estimate the effects in the dust thermal histories, we have to solve the radiation transfer equation.

3.3.1 Radiative Transfer Equation

One of the purposes of this study is to develop the numerical code of shock-wave heating model taking into account the dust thermal continuum emission and the line emission of gas molecules. However, to solve the transfer of the line mission with no approximation needs a large amount of computational time. So, we approximate the line transfer problem as follows.

Assuming the isotopic scattering, the radiation transfer equation taking into account absorption and scattering by the gas molecules and dust particles is given as (e.g., Rybicki & Lightman 1979)

$$\frac{d\mathcal{I}_\nu}{dx} = -(\alpha_{\nu,\mathrm{g}} + \alpha_{\nu,\mathrm{d}} + \sigma_{\nu,\mathrm{g}} + \sigma_{\nu,\mathrm{d}})\mathcal{I}_\nu + j_{\nu,\mathrm{d}} + j_{\nu,\mathrm{g}} + (\sigma_{\nu,\mathrm{g}} + \sigma_{\nu,\mathrm{d}})\mathcal{J}_\nu, \tag{3.8}$$

where α_ν, σ_ν, and j_ν are the absorption coefficient, the scattering coefficient, and the emission coefficient, respectively. The suffixes "g" and "d" mean the gas and

dust particles, respectively. The specific intensity is $\mathcal{I}_\nu$ and the mean intensity is $\mathcal{J}_\nu$ ($\equiv (4\pi)^{-1}\int \mathcal{I}_\nu d\Omega$). The first term of the right hand side means the extinction by absorption and scattering, the second and third terms are the source term due to the dust thermal continuum emission and the line emission, and firth term is the source term due to the scattering. We assume that terms of the absorption and the scattering of the line emission term. We denote the net emission coefficient taking into account the absorption/scattering of the line emission by the gas molecules/atoms as $j'_{\nu,\mathrm{g}}$. Using the notation, the radiation transfer equation can be rewritten as

$$\frac{d\mathcal{I}_\nu}{dx} = -(\alpha_{\nu,\mathrm{d}} + \sigma_{\nu,\mathrm{d}})\mathcal{I}_\nu + j_{\nu,\mathrm{d}} + j'_{\nu,\mathrm{g}} + \sigma_{\nu,\mathrm{d}}\mathcal{J}_\nu. \tag{3.9}$$

Integrating Eq. (3.9) by ν, we obtain

$$\frac{d\mathcal{I}}{dx} = -(\tilde{\alpha} + \tilde{\sigma})\mathcal{I} + j_{\mathrm{d}} + j'_{\mathrm{g}} + \bar{\sigma}\mathcal{J}, \tag{3.10}$$

where $\tilde{\alpha} \equiv \int \alpha_{\nu,\mathrm{d}}\mathcal{I}_\nu d\nu / \int \mathcal{I}_\nu d\nu$, $\tilde{\sigma} \equiv \int \sigma_{\nu,\mathrm{d}}\mathcal{I}_\nu d\nu / \int \mathcal{I}_\nu d\nu$, and $\bar{\sigma} \equiv \int \sigma_{\nu,\mathrm{d}}\mathcal{J}_\nu d\nu / \int \mathcal{J}_\nu d\nu$ are the frequency-averaged absorption/scattering coefficients. Here, we replace these frequency-avaraged absorption/scattering coefficients to the planck mean values. We think that it is appropriate approximation because the line center frequency is similar to the peak frequency of the dust thermal continuum emission. Finally, we can rewrite Eq.(3.10) into more simple form

$$\frac{d\mathcal{I}}{dx} = -(\alpha_{\mathrm{p}} + \sigma_{\mathrm{p}})(\mathcal{I} + \mathcal{S}), \tag{3.11}$$

where

$$\mathcal{S} \equiv \frac{j_{\mathrm{d}} + j'_{\mathrm{g}} + \sigma_{\mathrm{p}}\mathcal{J}}{\alpha_{\mathrm{p}} + \sigma_{\mathrm{p}}}. \tag{3.12}$$

3.3.2 Mean Intensity and Net Flux

We are considering the steady, one-dimensional, plane-parallel structure for the chondrule-forming region. The radiation transfer equation along the ray inclining with the angle θ against the spatial coordinate x is written as (see Eq. 3.11)

$$\mu\frac{d\mathcal{I}}{dx} = -(\alpha_{\mathrm{p}} + \sigma_{\mathrm{p}})(\mathcal{I} + \mathcal{S}), \tag{3.13}$$

where μ is equal to $\cos\theta$, $\alpha_{\rm p}$ ($\sigma_{\rm p}$) is the planck mean absorption (scattering) coefficients of dust particles, and $\mathcal{S}$ is the frequency-integrated source function. The absorption/scattering coefficients are given by integrating the absorption/scattering cross sections with dust radius as

$$\begin{pmatrix}\alpha_{\rm p}\\ \sigma_{\rm p}\end{pmatrix} = \int n_{\rm d}\pi a_{\rm d}^2 \begin{pmatrix}\epsilon_{\rm abs}\\ \epsilon_{\rm scat}\end{pmatrix} da_{\rm d}, \tag{3.14}$$

where $n_{\rm d}$ is the number density of dust particles per unit radius and $\epsilon_{\rm scat}$ is the planck-mean scattering efficiency. The source function includes three terms; dust thermal continuum emission, the line emission of gas molecules, and the isotropic scattering (see Eq. 3.12). If the scattering is taken into consideration, the radiation intensity $\mathcal{I}$, which is the solution of the radiation transfer equation, is included in the source function. Therefore, we calculate the radiation transfer equation iteratively until the solution converges at a certain value. The numerical procedures are summarized in Section 3.5.

The source term of the dust thermal continuum emission $j_{\rm d}$ is given as the total contribution of all dust sizes;

$$j_{\rm d} = \int n_{\rm d} a_{\rm d}^2 \epsilon_{\rm emit} \sigma_{\rm SB} T_{\rm d}^4 da_{\rm d}. \tag{3.15}$$

DC02 assumed that sub-micron sized dust particles are dynamically well coupled to the gas and are always in thermal equilibrium with the gas and the radiation field, however, we solve the dust thermal histories of various sized dust particles ($a_{\rm d} = 0.01\,\mu{\rm m} - 1\,{\rm cm}$) without the assumption of the thermal equilibrium.

The source term of the line emission $j'_{\rm g}$ is given as the summation of all cooling mechanisms due to the line emissions. The line emission would be absorbed or scattered by the gas molecules in traveling from the emitting point to a certain point at which we want to know the radiation intensity. As a result, the values of $j'_{\rm g}$ is deducing as the distance among two points are separated more and more. We described how to estimate the net source term of the line emissions $j'_{\rm g}$ in Section 3.3.3.

Here, we define the optical depth as

$$\tau(x) = \int_{-x_{\rm m}}^{x} (\alpha_{\rm p} + \sigma_{\rm p}) dx. \tag{3.16}$$

Given the incident radiation fields and the source function at all optical depths $\mathcal{S}$, the mean intensity of radiation $\mathcal{J}$ can be found:

$$\mathcal{J}(\tau) = \frac{\mathcal{I}_{\rm pre}}{2} E_2(\tau) + \frac{1}{2}\int_0^{\tau_{\rm m}} \mathcal{S}(\tau') E_1(|\tau - \tau'|) d\tau' + \frac{\mathcal{I}_{\rm post}}{2} E_2(\tau_{\rm m} - \tau), \tag{3.17}$$

where E_n is the exponential integrals; $E_n(x) \equiv \int_1^\infty y^{-n} e^{-xy} dy$, $\mathcal{I}_{\rm pre}$ and $\mathcal{I}_{\rm post}$ are given as the boundary conditions of radiation intensity at $x = -x_{\rm m}$ and $x = x_{\rm m}$, respectively. We set $\mathcal{I}_{\rm pre} = \mathcal{I}_{\rm post} = 1.46 \times 10^5\,{\rm erg\,cm^{-2}\,ster^{-1}\,s^{-1}}$, which corresponds to the black body radiation with temperature of 300 K. Notice that we calculate the value of $j_{\rm g}$ for any set of τ and τ' based on Neufeld & Kaufman (1993). We can also solve for the net flux of radiation energy $\mathcal{F}$:

$$\begin{aligned} \mathcal{F}(\tau) &= 2\pi \mathcal{I}_{\rm pre} E_3(\tau) + 2\pi \int_0^{\tau} \mathcal{S}(\tau') E_2(\tau - \tau') d\tau' \\ &- 2\pi \int_{\tau}^{\tau_{\rm m}} \mathcal{S}(\tau') E_2(\tau' - \tau) d\tau' - 2\pi \mathcal{I}_{\rm post} E_3(\tau_{\rm m} - \tau). \end{aligned} \tag{3.18}$$

3.3.3 Source Function of Line Emission

The line emission would be absorbed or scattered by the gas molecules in traveling from the emitting point ($x_{\rm emit}$) to a certain point ($x_{\rm cert}$), where $x_{\rm cert}$ is the point at which we want to know the mean intensity of the radiation field. We take into account these effects in the form of $j_{\rm g}$ by reducing its value. According to Neufeld & Kaufman (1993), the extinction for the line emission depends on the parameter $\tilde{N}({\rm M})$ (see appendix A.1). When we estimate the extinction of $j_{\rm g}$, we calculate $\tilde{N}({\rm M})$ as

$$\tilde{N}({\rm M}) = \left| 2 \int_{x_{\rm emit}}^{x_{\rm cert}} \frac{n({\rm M})}{\Delta v} H(x', x_{\rm emit}) dx' \right|, \tag{3.19}$$

where

$$H(x_1, x_2) = \begin{cases} 1 & (x_1 x_2 \geq 0) \\ 0 & (x_1 x_2 < 0) \end{cases}. \tag{3.20}$$

The function $H(x_1, x_2)$ indicates the Doppler shift for the line emission. Namely, the line photons emitted in the post- (pre-) shock region are not absorbed/scattered by the pre- (post-) shock gas molecules because of the large difference in the gas balk velocity between these two regions. Here, notice that the shock front is located

Table 3.1: Dust models we adopted in this study are listed. The charactor "P" in the dust model means power-law size distribution and "L" means lognormal one. The number "10", "03", and "01" stand for the dust-to-gas mass ratio $C_{\rm d} = 0.10$, 0.03, and 0.01, respectively.

dust model	size dist.	$C_{\rm d}$
P10	power-law	0.10
P03	power-law	0.03
P01	power-law	0.01
L10	lognormal	0.10
L03	lognormal	0.03
L01	lognormal	0.01

at $x = 0$. If once we obtain the value of $\tilde{N}$(M) for any two points separated each other, we can estimate the extinction of $j_{\rm g}$ by the gas molecules using the tables of Neufeld & Kaufman (1993). When integrating the radiative transfer equation along the ray of the photons, we use the extinct source function for $j_{\rm g}$.

3.4 Dust Model

The radiation field could be significantly affected by the blanket effect due to dust particles. Thus, the optical properties of the flow, which are mainly determined by the dust-to-gas mass ratio and the initial size distribution of precursor dust particles, should be paid attention in our study. We assume two size distribution models; power-law distribution and lognormal one. In the power-law one, the dust number density per unit radius is given as $n_{\rm d}(a_{\rm d}) \propto a_{\rm d}^{-m}$, in which we assume $m = 3.5$ in this study. The lognormal one is similar to the size distribution of chondrules in ordinary chondrites (Fig. 3.2). We assume that the size range of dust particles is from 0.01μm to 1 cm. We divide it into 31 bins and calculate time evolution of those particles simultaneously with gas dynamics. We change the dust-to-gas mass ratio in the pre-shock region as 0.01, 0.03, and 0.1. Totally, we have six cases as the dust particle model. The dust models are summarized in Table 3.1.

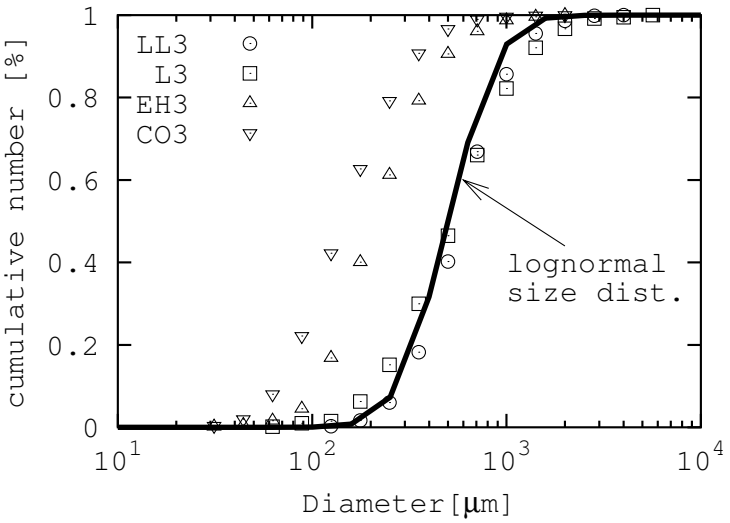

Figure 3.2: Initial dust size distribution model we adopted in this study is plotted in case of lognormal one. The vertical axis is normalized cumulative number of chondrules whose radii are smaller than that of horizontal axis. The thick solid curve is the lognormal size distribution that we adopt in this study. Measured chondrule size distributions are also displayed for comparison; each symbol means results of LL3 chondrites by Nelson & Rubin (2002) (LL3), L3 chondrites by Rubin & Keil (1984) (L3), EH3 chondrites by Rubin & Grossman (1987) (EH3), and CO3 chondrites by Rubin (1989) (CO3), respectively.

3.5 Numerical Procedures

3.5.1 Shock-Wave Heating Part

For the numerical procedure to solve the hydrodynamical equations for the gas taking into account the non-equilibrium chemical reactions, we adopt the finite difference algorithm described in Shapiro & Kang (1987). Eq. (3.3) can be rewritten as a temperature equation, using the relations $e = y_t n_{\rm H_0} k_{\rm B} T/(\gamma-1)$, $p = y_t n_{\rm H_0} k_{\rm B} T$, $\mu = \sum y_i m_i / y_t$, and $\rho = n_{\rm H_0} \sum y_i m_i$, where $y_t/(\gamma-1) = \sum y_i/(\gamma_i - 1)$, $y_t = \sum y_i$, $y_i = n_i/n_{\rm H_0}$, and $n_{\rm H_0}$ = the total number density of hydrogen nuclei. The result is given by

$$\frac{dT}{T} = (\gamma-1)\Big[\frac{(-\Lambda)dt}{p} + \frac{dy_t}{y_t} + \frac{dn_{\rm H_0}}{n_{\rm H_0}} - d\Big(\frac{1}{\gamma-1}\Big)\Big] + \gamma\frac{d\mu}{\mu}. \tag{3.21}$$

From Eqs. (3.1) and (3.2) and the equation of state, $p = \rho k_{\rm B} T/\mu$, the relative compression $x = \rho/\rho_2$ is given by

$$\frac{k_{\rm B}T}{\mu}x^2 - Av_2^2 x + v_2^2 = 0. \tag{3.22}$$

If $A \geq 2$ or $\rho_1 v_{\rm s}^2 \geq 3p_1$, this yields

$$x = \frac{Av_{\rm s}^2 + (A^2 v_{\rm s}^4 - 4k_{\rm B}Tv_{\rm s}^2/\mu)^{1/2}}{2k_{\rm B}T/\mu}, \tag{3.23}$$

while if $A \leq 2$ or $\rho_1 v_{\rm s}^2 \leq 3p_1$, this yields

$$x = \frac{Av_{\rm s}^2 - (A^2 v_{\rm s}^4 - 4k_{\rm B}Tv_{\rm s}^2/\mu)^{1/2}}{2k_{\rm B}T/\mu}, \tag{3.24}$$

where

$$A = 1 + \frac{p_2}{\rho_2 v_2^2}. \tag{3.25}$$

The detailed procedure is described in Appendix A of Shapiro & Kang (1987).

3.5.2 Radiation Transfer Part

The radiation transfer equation is solved after the results of above hydrodynamical calculations are obtained. The hydrodynamical calculations give us the source terms of the radiation field; the line emission from gas molecules/atoms and the thermal continuum radiation from the dust particles. Using the source function, we can solve Eqs. (3.17) and (3.18) by the finite difference algorithm. The source function contains the mean intensity $\mathcal{J}$ in it because we consider the scattering term. Therefore, we need to iterate the calculations until the solutions converge enough. In this paper, we carry out the iteration as follows:

1. We solve the radiation transfer equation without the scattering term. The solutions are the initial values for the iteration.

2. Substituting the mean intensity obtained in the previous iteration into the source function, we solve the equation taking into account the scattering.

3. We iterate the procedure 2 until the mean intensity converges within 0.1%.

3.5.3 Combination of Two Parts

In the shock-wave heating part, the thermal histories of the precursor dust particles depend on the mean intensity of the radiation field. At the same time, the dust thermal histories affect the radiation field. Therefore, we need to iterate the shock-wave heating part and the radiation transfer part until the solution converges enough (Figure 3.3). In this paper, we iterate these two parts until the mean intensity $\mathcal{J}$ converges within 1%.

3.6 Initial Conditions and Physical Parameters

3.6.1 Gas

Appropriate shock conditions for chondrule formation, in which the precursor dust particles are heated enough to melt and do not vaporize completely, is numerically and analytically derived by Iida et al. (2001) as a function of the pre-shock gas

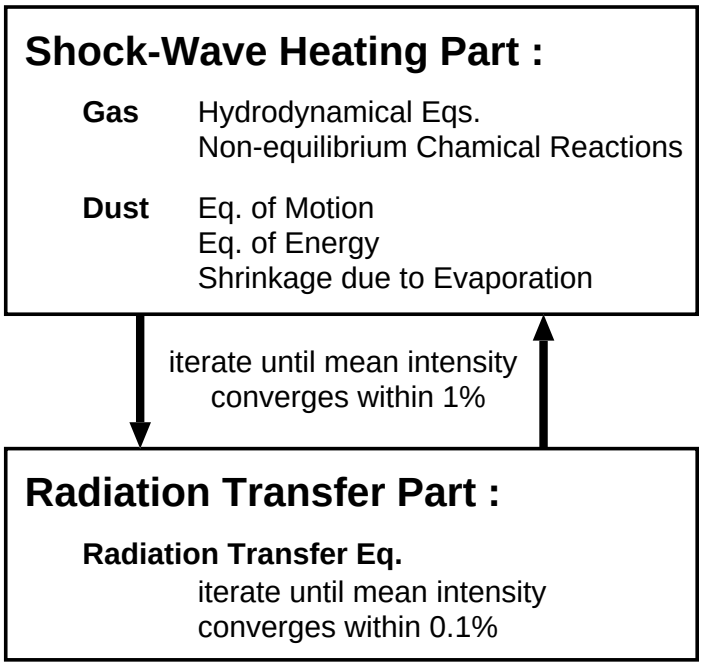

Figure 3.3: Schematic picture of the numerical procedure to simulate the shock-wave heating taking into account the radiation transfer.

Table 3.2: Notation of the shock condition. The pre-shock gas number density is n_0 and the shock velocity is v_s.

notation	n_0 [cm^{-3}]	v_s [km s^{-1}]
n14v08	10^{14}	8
n14v10	10^{14}	10
n14v13	10^{14}	13
n13v16	10^{13}	16
n13v20	10^{13}	20
n13v25	10^{13}	25
n12v30	10^{12}	30
n12v35	10^{12}	35
n12v40	10^{12}	40
n11v50	10^{11}	50
n11v55	10^{11}	55
n11v60	10^{11}	60

number density n_0 and the shock velocity v_s (see Fig. 1.3). Based on their results, we select some set of the n_0 and v_s for the initial conditions: v_s = 8, 10, 13 km s^{-1} for $n_0 = 10^{14}\,\mathrm{cm}^{-3}$, v_s = 16, 20, 25 km s^{-1} for $n_0 = 10^{13}\,\mathrm{cm}^{-3}$, v_s = 30, 35, 40 km s^{-1} for $n_0 = 10^{12}\,\mathrm{cm}^{-3}$, and v_s = 50, 55, 60 km s^{-1} for $n_0 = 10^{11}\,\mathrm{cm}^{-3}$. We abbreviate the shock condition of $n_0 = 10^{14}\,\mathrm{cm}^{-3}$ and $v_s = 10\,\mathrm{km\,s}^{-1}$ as "n14v10", and so forth (see Table 3.2). The initial gas temperature is assumed to be 300 K. The initial gas-phase elemental abundance (ratio by number to hydrogen nuclei) is taken from Finocchi et al. (1997) for the solar nebula: $y_\mathrm{H} = 10^{-5}$, $y_\mathrm{He} = 9.75 \times 10^{-2}$, $y_\mathrm{CO} = 1.065 \times 10^{-4}$, and $y_{\mathrm{H_2O}} = 5.978 \times 10^{-4}$. Other hydrogen nuclei are assumed to exist as hydrogen molecules. Other species = 0. Moreover, the heavy elements like Si are assumed to be in the dust particles and do not exist in the gas phase.

3.6.2 Dust Particles

The The precursor dust particles are assumed to be composed of only forsterite with the mass density ρmat $= 3.22\,\mathrm{g\,cm}^{-3}$ (Saxene et al. 1993). The specific heat

$C = 1.42 \times 10^7\,\mathrm{erg\,g^{-1}\,K^{-1}}$, the latent heat of evaporation $L_{\rm evap} = 1.12 \times 10^{11}\,\mathrm{erg\,g^{-1}}$, and the latent heat of boiling $L_{\rm boil} = 1.64 \times 10^{11}\,\mathrm{erg\,g^{-1}}$ (NIST WebBook).[2] For the values of absorption/emission/scattering coefficients ($\epsilon_{\rm abs}/\epsilon_{\rm emit}/\epsilon_{\rm scat}$), we use the optical properties of astronomical silicate (Miyake & Nakagawa 1993).

3.7 Test Calculations

3.7.1 Gas thermal Profiles in Post-Shock Region

We show the numerical results of the gas thermal profiles in the post-shock region for some cases. Figure 3.4 shows the results for the case that the pre-shock gas number density $n_0 = 10^{14}\,\mathrm{cm^{-3}}$, the shock velocity $v_{\rm s} = 10\,\mathrm{km\,s^{-1}}$, and the dust model L01. The horizontal axis is the distance from the shock front. The gas temperature $T_{\rm g}$ is displayed by the thick solid curve. The heating/cooling rates of the various chemical reactions and the line emissions are also displayed; Lyman α emission (Lyα), H_2 formation (H_2form) and dissociation (H_2diss), H_2O vibrational/rotational emission (H_2O(V/R)), CO vibrational/rotational emission (CO(V/R)), and the energy transfer with the dust particles (dust), respectively. In this case, the gas temperature just behind the shock front is 4409 K. The post-shock gas cools due to the dissociation of hydrogen molecules. At a few tens km behind the shock front, the heating process by the H_2 formation dominates the cooling process by the H_2 dissociation. Then the heating due to the formation of hydrogen molecule balances with the cooling due to the dissociation, so the temperature plateau is formed at $T_{\rm g} \simeq 2000\,\mathrm{K}$, on which the gas temperature does not change significantly. In this phase, we find that the line cooling plays an important role; the line cooling due to the H_2O vibrational emission can remove the H_2 formation energy effectively. Thus, the abundance of hydrogen molecule increases gradually during the gas temperature is on the plateau. If no line cooling exists, the cooling mechanism which can remove the formation energy is only the dust cooling. However, its cooling rate is too low to cool the gas effectively. The formation energy released until all hydrogen nuclei become hydrogen molecules

[2]NIST WebBook. A gateway to the data collections of the National Institute of Standards and Technology. Available at http://webbook.nist.gov.

is estimated as $E = y_{\rm H_2} n_{\rm H_0} E_{\rm form} \sim 10^3\,{\rm erg\,cm^{-3}}$, where $y_{\rm H_2} \sim 0.1$, $n_{\rm H_0} \sim 10^{15}\,{\rm cm^{-3}}$, and $E_{\rm form} = 7.17 \times 10^{-12}\,{\rm erg}$ is the formation energy per molecule, and the cooling rate by dust particles is about $\Lambda_{\rm dust} \simeq 10^{-2}\,{\rm erg\,cm^{-3}\,s^{-1}}$ (see Fig. 3.4), so it takes about $10^5\,{\rm s}$ to remove the formation energy. Since the gas velocity is about $1\,{\rm km\,s^{-1}}$ in the post-shock region, the gas would run away from the calculation region before their energy is removed completely. Therefore, the line emission is important for the gas cooling. Moreover, this result indicates that the line emission is an important radiation source.

Figure 3.5 shows the results for the different shock condition; $n_0 = 10^{11}\,{\rm cm^{-3}}$ and $v_{\rm s} = 55\,{\rm km\,s^{-1}}$. In this case, the gas temperature just behind the shock front is $1.2 \times 10^5\,{\rm K}$. The thermal energy is rapidly radiated away by the Lyman α emission and the gas temperature decreases down to a few thousands K. The almost the all hydrogen molecules are dissociated before the gas cools. Although the H_2 formation takes place after the gas cools, the formation rate is too small to convert all atoms to molecules before the gas flow reaches at the left boundary of the calculation region ($x = 10^5\,{\rm km}$). In this study, we focus the thermal histories of the dust particles and the dust heating processes would have terminated at $x \leq 10^5\,{\rm km}$, so we do not need to extend the calculation region more.

3.7.2 Radiation Field

We think that it is helpful for readers to show the structure of radiation field in the chondrule-forming region. Because of the blanket effect, the radiation intensity strongly depends on the optical depth, which is specified by the size distribution and the dust-to-gas mass ratio $C_{\rm d}$. Fig. 3.6 shows the mean intensity $\mathcal{J}$ (top) and the radiation flux $\mathcal{F}$ (bottom) as a function of the distance from the shock front. The shock condition is n14v10 and the dust models are L10 ($C_{\rm d} = 0.10$), L03 ($C_{\rm d} = 0.03$), and L01 ($C_{\rm d} = 0.01$). We find that the more the pre-shock region becomes optically thick, the more strongly the radiation intensity is amplified by the blanket effect. This result is naturally expected. The mean intensity immediately in front of the shock front is $\mathcal{J} = 8.46$ for L10, 3.87 for L03, and 2.45 for L01 in unit of $10^7\,{\rm erg\,cm^{-2}\,ster^{-1}\,s^{-1}}$, respectively. The temperature of dust particles

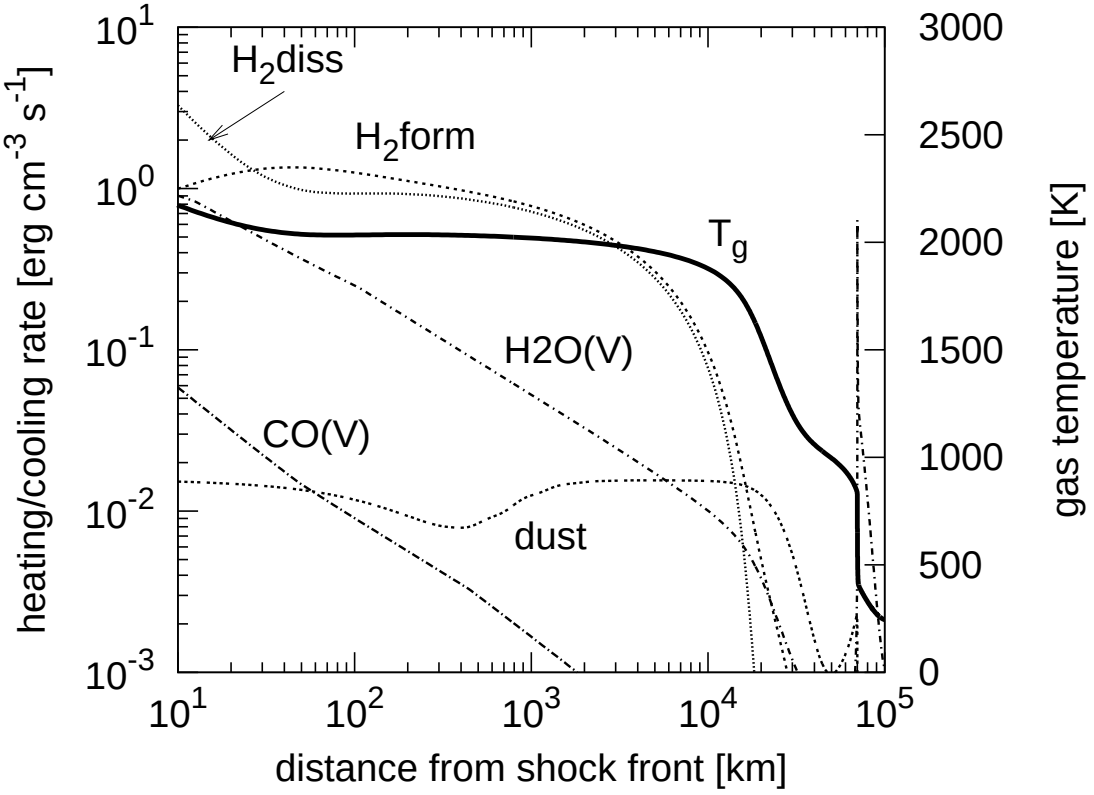

Figure 3.4: The gas thermal profile in the post-shok region. The horizontal axis is the distance from the shock front x. The thick solid curve is the gas temperature $T_{\rm g}$. The heating/cooling rates of the various chemical reactions and the line emissions are also displayed; Lyman α emission (Lyα), H_2 formation (H_2form) and dissociation (H_2diss), H_2O vibrational/rotational emission (H_2O(V/R)), CO vibrational/rotational emission (CO(V/R)), and the energy transfer with the dust particles (dust), respectively. The shock conditions are the gas number density of the pre-shock region $n_0 = 10^{14}\,{\rm cm}^{-3}$ and the shock velocity $v_{\rm s} = 10\,{\rm km\,s}^{-1}$.

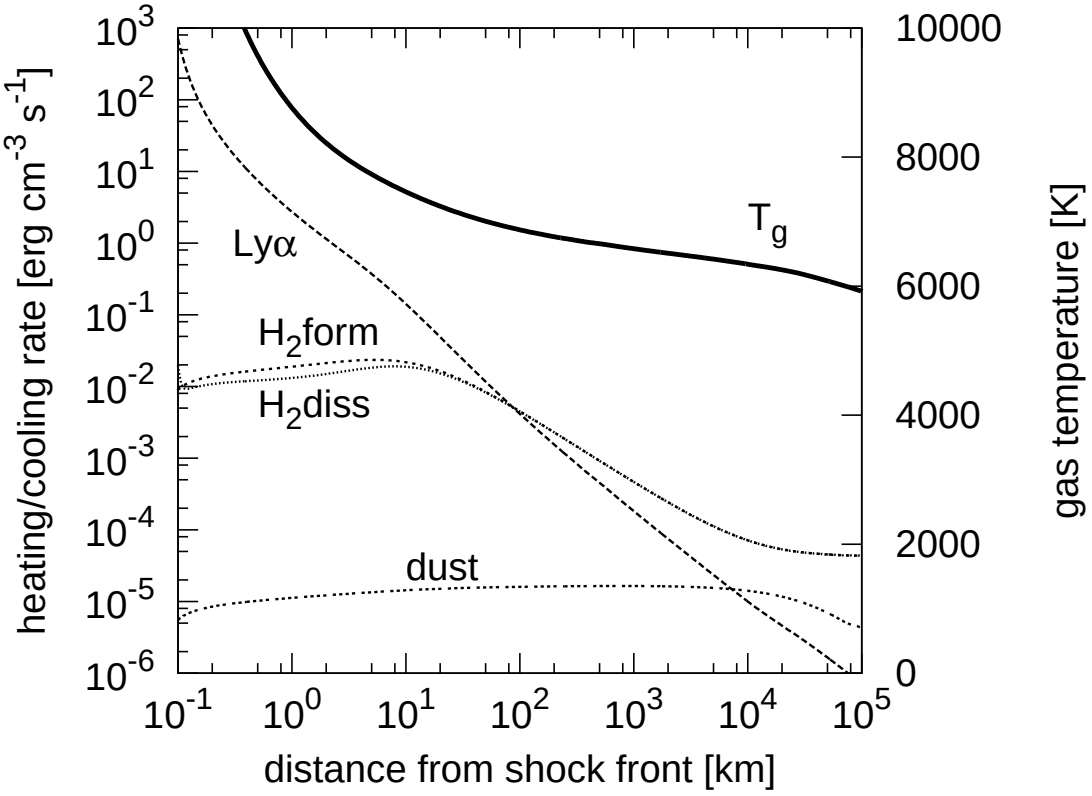

Figure 3.5: Same as Fig. 3.4 except for $n_0 = 10^{11}\,\mathrm{cm}^{-3}$ and $v_\mathrm{s} = 55\,\mathrm{km\,s}^{-1}$.

which are in the thermal equilibrium with the radiation field is given as $T_{\rm rad} = (\pi \mathcal{J}/\sigma_{\rm SB})^{1/4}$. Hereafter, we call it the radiation temperature. For each case, the radiation temperature is $T_{\rm rad} = 1471\,{\rm K}$ for L10, $1210\,{\rm K}$ for L03, and $1079\,{\rm K}$ for L01, respectively. Therefore, in the case of L10, the dust temperature in the pre-shock region exceeds $1273\,{\rm K}$, which is the melting point of FeS, and the isotopic fractionation begins to take place. Since the heating rate due to the blanket effect is lower than $10^3\,{\rm K/hr}$ (DC02), the isotopic fractionation will be observed if chondrules have been formed in such dusty shock waves. On the contrary, in cases of L03 and L01, the radiation temperature does not exceed $1273\,{\rm K}$ in the pre-shock region, so the isotopic fractionation begins to take place after passing though the shock front. Behind the shock front, the gas drag heats dust particles very rapidly ($> 10^5\,{\rm K/hr}$, Tachibana *et al.* 2004) up to $1573\,{\rm K}$, above which the isotopic fractionation cannot occur because the silicate melt surrounds FeS melt and suppresses its evaporation.

The radiation flux is also an important information to understand our study. In the bottom panel of Fig. 3.6, it is found that the radiation flux is almost constant in the pre-shock region. In the case of L10, the pre-shock region is optically thick ($\tau_{\rm pre} = 2.44$), where $\tau_{\rm pre}$ is defined as the optical depth of the pre-shock region;

$$\tau_{\rm pre} = \int_{-x_{\rm m}}^{0} (\alpha_{\rm p} + \sigma_{\rm p}) dx. \tag{3.26}$$

The reason why the radiation flux is almost constant in spite of the optically thick environment is the re-emission of dust thermal continuum emission. Since the dust temperature near the shock front is higher than far from the shock front, the re-emitted dust thermal continuum emission produces net radiation flux toward upstream. This effect can be understood with the radiative diffusion approximation (Rybicki & Lightman 1979).

3.7.3 Gas Thermal Profiles in Pre-Shock Region

We show the thermal profiles of the gas in the pre-shock region. As a result that the dust particles in the pre-shock region are heated by the radiation, the gas is also heated by the energy transfer with the dust particles. Therefore, it is expected that the gas temperature in the pre-shock region depends on the dust model. The thermal

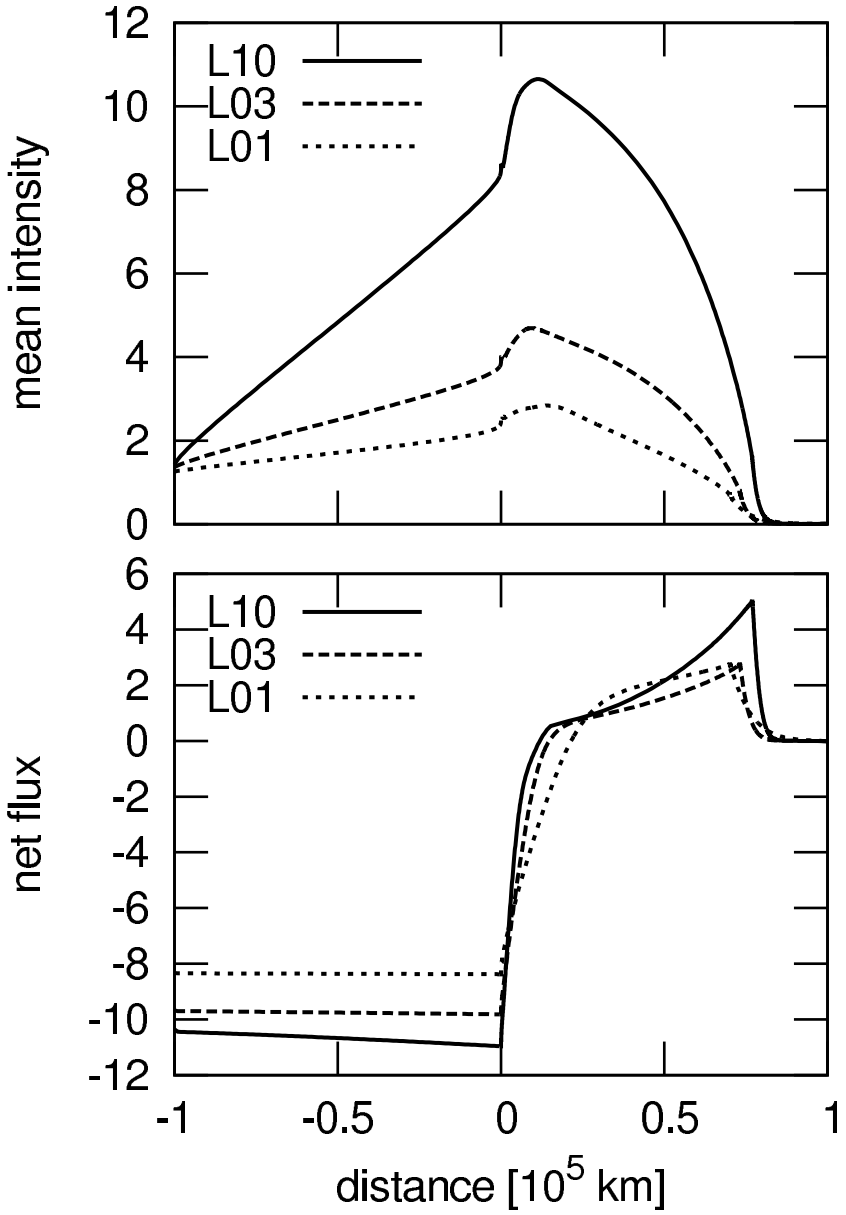

Figure 3.6: Radiation fields in the chondrule-forming region for various dust model are plotted as a function of distance from the shock front. Shock condition is assumed to be $n_0 = 10^{14}\,\mathrm{cm}^{-3}$ and $v_\mathrm{s} = 10\,\mathrm{km\,s}^{-1}$. Top panel is the mean intensity in unit of $10^7\,\mathrm{erg\,cm}^{-2}\,\mathrm{ster}^{-1}\,\mathrm{s}^{-1}$ and the bottom panel is the net flux in unit of $10^7\,\mathrm{erg\,cm}^{-2}\,\mathrm{s}^{-1}$. The negative flux means the net radiation flux going toward upstream.

profiles of the gas in the pre-shock region for various dust models are displayed in Figure 3.7. The shock condition is $n_0 = 10^{14}\,\mathrm{cm}^{-3}$ and $v_\mathrm{s} = 10\,\mathrm{km\,s}^{-1}$. We also show the radiation temperature defined as $T_\mathrm{rad} = (\pi\mathcal{J}/\sigma_\mathrm{SB})^{1/4}$. The dust temperatures tend to approach toward T_rad when there is no energy exchanges except for the radiative processes. Roughly speaking, we can consider T_rad as the dust temperature in the pre-shock region.

It is found that the larger the dust-to-gas mass ratio is, the higher the the pre-shock gas temperature becomes. it is naturally understood because the more dusty environment causes the more effective energy transfer from the dust particles to the gas. It is also found that the power-low dust size distribution results higher gas temperature than that of the log-normal size distribution when the dust-to-gas mass ratio is the same value. In the case that the dust-to-gas mass ratio is fixed, the smaller mean dust size means the larger total area facing to the ambient gas. Since the mean dust radius of the power-low size distribution is smaller than that of the log-normal size distribution, the gas temperature is higher for the power-low size distribution.

3.8 Conclusions

We developed the numerical simulation code of the shock-wave heating model for chondrule formation, taking into account the radiation transfer of the line emissions of the gas molecules/atoms and the thermal continuum radiation of the dust particles. We introduced the basic equations of the radiative shock-wave heating model and explained the numerical method to solve them. We also showed some results of the gas thermal profiles and the radiation field. We obtained following conclusions:

1. The line emissions of the gas molecules/atoms are thought to be an important cooling mechanism for the gas to remove the formation energy of the hydrogen molecules effectively.

2. The mean intensity of the radiation field strongly depends on the optical depth of the pre-shock region τ_pre. There is a case that the radiation temperature T_rad exceeds 1273 K at the pre-shock region. Therefore, the dust particles would

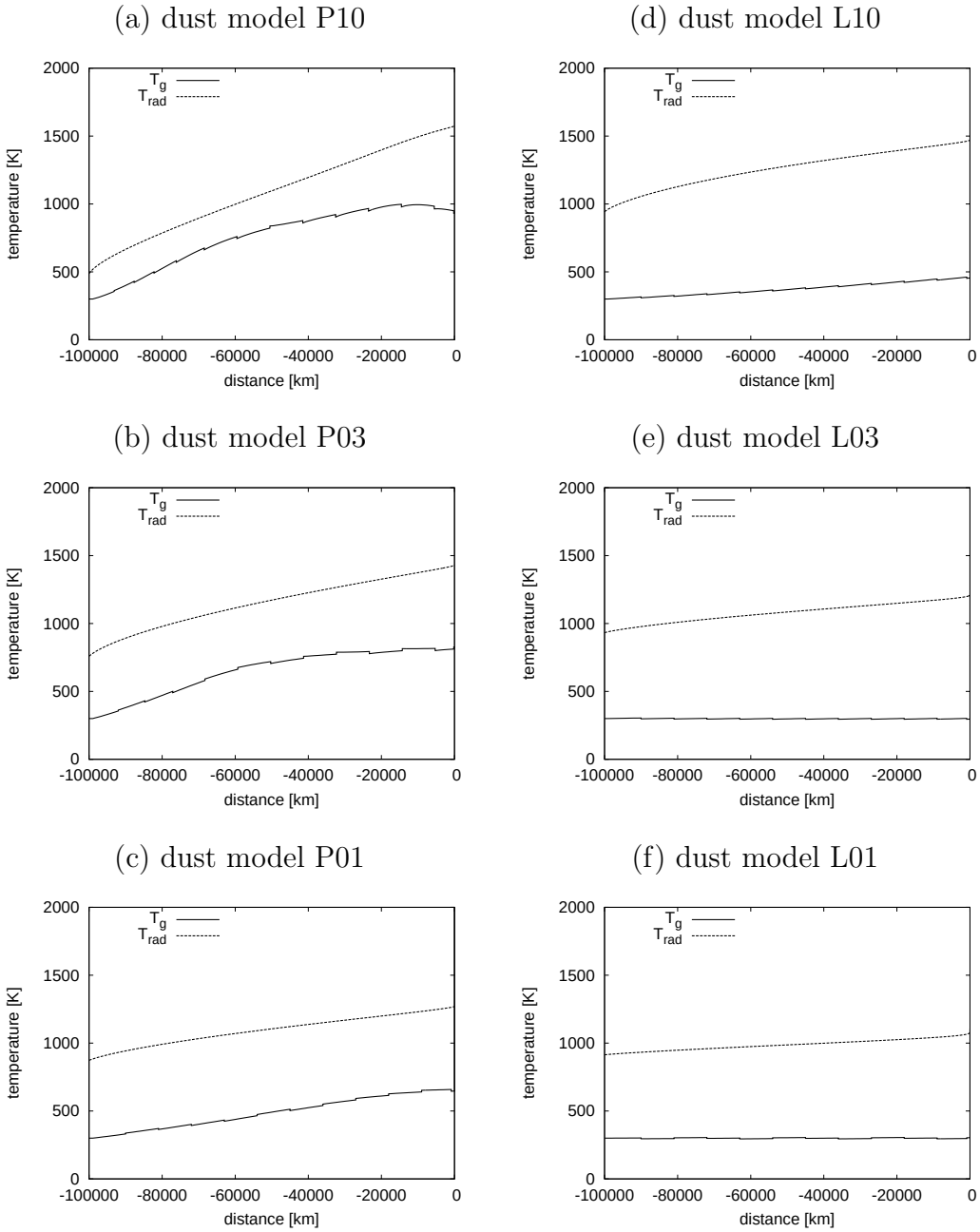

Figure 3.7: The gas temperatures in the pre-shock region for various dust models are plotted as a function of the distance from the shock front. The shock condition is $n_0 = 10^{14}\,\mathrm{cm}^{-3}$ and $v_\mathrm{s} = 10\,\mathrm{km\,s}^{-1}$.

be heated up to 1273 K or more in the pre-shock region and the isotopic fractionation would take place.

3. The pre-shock gas temperature depends on the dust models. The larger the dust-to-gas mass ratio is, the higher the pre-shock gas temperature becomes. Moreover, the power-low dust size distribution leads the higher pre-shock gas temperature than that of the log-normal size distribution.

Chapter 4

Blanket Effect

It is known that the degree of isotopic fractionation of sulfur in troilites in chondrules from some chondritic meteorites is quite small. Tachibana & Huss (2005) measured the isotopic fractionation and suggested that chondrules have to be heated rapidly ($> 10^4\,\mathrm{K\,hr^{-1}}$) at a temperature range of $1273 - 1473\,\mathrm{K}$, in which the isotopic fractionation should occur associated with evaporation of troilites. In the shock-wave heating model, the gas frictional heating can heat the silicate dust particles rapidly enough to prevent the isotopic fractionation in the post-shock region. However, the radiation mainly coming from the post-shock region heats the dust particles in the pre-shock region. The condition to prevent the isotopic fractionation has not been well investigated in cases taking into account the radiation transfer effects.

In this chapter, we focus the thermal history of the dust particles in the pre-shock region and discuss the condition to prevent the isotopic fractionation.

4.1 Dust Thermal Histories

In the pre-shock region, since the gas and the dust particles move together toward the shock front, there is no relative velocity between them. Therefore, the gas frictional heating does not take place on the dust particles in the pre-shock region. The main heating source in the region is the radiative heating. On the other hand, after passing through the shock front, the dust particles are rapidly heated by the gas frictional heating.

Figure 4.1 shows dust thermal histories in the pre- and post-shock regions. Calculation conditions are the same as that of Fig. 3.6; the shock condition is assumed to be $n_0 = 10^{14}\,\mathrm{cm}^{-3}$ and $v_\mathrm{s} = 10\,\mathrm{km\,s}^{-1}$, and dust models are L10, L03, and L01. The initial dust radius is 251 μm. The horizontal axis indicates the distance from the shock front. Notice that the horizontal scales are different between the left and right panel. The left panel is the pre-shock region and the right panel is the post-shock region. The dust temperature T_d is the solid curve and the radiation temperature T_rad, which is defined as $T_\mathrm{rad} = (\pi\mathcal{J}/\sigma_\mathrm{SB})^{1/4}$, is the thick dashed curve. A horizontal dotted line indicates 1273 K, above which the isotopic fractionation takes place until the dust temperature exceeds 1473 K. We found that in the pre-shock region, the dust temperatures are almost the same as the radiation temperature. In cases of L03 and L01, dust temperatures do not exceed 1273 K in the pre-shock region, so the isotopic fractionation does not take place in this region. On the contrary, in the case of L10, since the dust temperature exceeds 1273 K, the isotopic fractionation should take place. After passing through the shock front, dust particles are rapidly heated by the gas drag heating. It is found that in the post-shock region, the dust temperatures are different from the radiation temperature. In the cases of L03 and L01, the isotopic fractionation takes place in the post-shock region.

Here, we compare our results with that of DC02 and CH02, which took into account the radiation transfer of dust thermal continuum emission, but not the gas line emission (line cooling). The canonical case of DC02 had following parameters; the initial gas density is $10^{-9}\,\mathrm{g\,cm}^{-3}$, the shock velocity is $7\,\mathrm{km\,s}^{-1}$, and the dust-to-gas mass ratio is 0.005. Despite the low dust-to-gas mass ratio, the pre-shock dust temperature reaches about 1700 K at the shock front (see Fig. 4 of DC02).

We guess that it is because of their treatment of the sub-μm sized dust particles in the source function (Eq. 5 of DC02). They used the gas temperature in the source term of sub-μm sized dust particles. However, dust temperature is not perfectly the same as the gas temperature due to the ambient radiation field and the radiative cooling of dust particle themselves. For example, in the case of Fig. 3.4, the post-shock gas temperature is 2019 K at $x = 10^3$ km, where the μm-sized dust particles are in thermal equilibrium with the gas and the radiation field because there is no relative velocity between the gas and μm-sized dust particles. The μm-sized dust temperature at this point is 1269 K according to our results. The radiation source term is proportional to the forth power of the temperature. Thus, DC02 overestimated the source term of sub-μm sized dust particles about by one order of magnitude. On the contrary, we think that the model of CH02 underestimated the radiation intensity in the pre-shock region because they did not take into account the line emission of the gas. As we showed in Sect. 3.7.1, some amount of the line emission emitted in the post-shock region can penetrate into the pre-shock region. Considering the line emission, the radiation intensity in the pre-shock region should be larger than the model without this effect.

4.2 Heating Rate

We calculate the thermal histories of dust particles for various shock conditions and dust models and obtain the dust temperature when the dust particle reaches at the shock front $T_{\rm sf}$, the peak dust temperature as a result of the gas frictional heating in the post-shock region $T_{\rm peak}$, the heating rate $R_{\rm haet}$ in a temperature range of $1273 - 1473$ K, in which the isotopic fractionation occurs, the cooling rate $R_{\rm cool}$ thought the crystallization temperature $1550 - 1400$ K, and the final dust radius $a_{\rm fin}$. Our results are summarized in Tables 4.1-4.3. In this section, we notice the heating rates in order to consider the isotopic fractionation. We discuss the cooling rates in the later section (section 5.1).

The heating rate, $R_{\rm heat}$, is defined as

$$R_{\rm heat} \equiv \frac{1473\,{\rm K} - 1273\,{\rm K}}{\Delta t}, \tag{4.1}$$

(a) dust model L10 (log-normal size distribution, $C_{\rm d} = 0.10$)

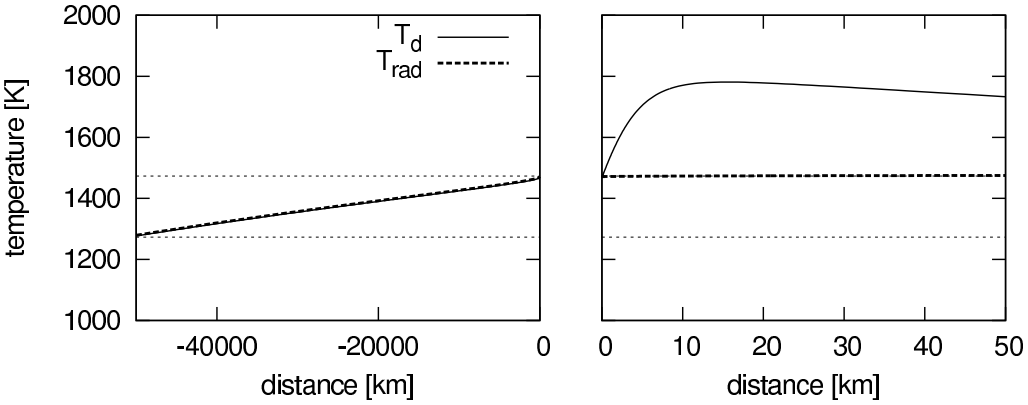

(b) dust model L03 (log-normal size distribution, $C_{\rm d} = 0.03$)

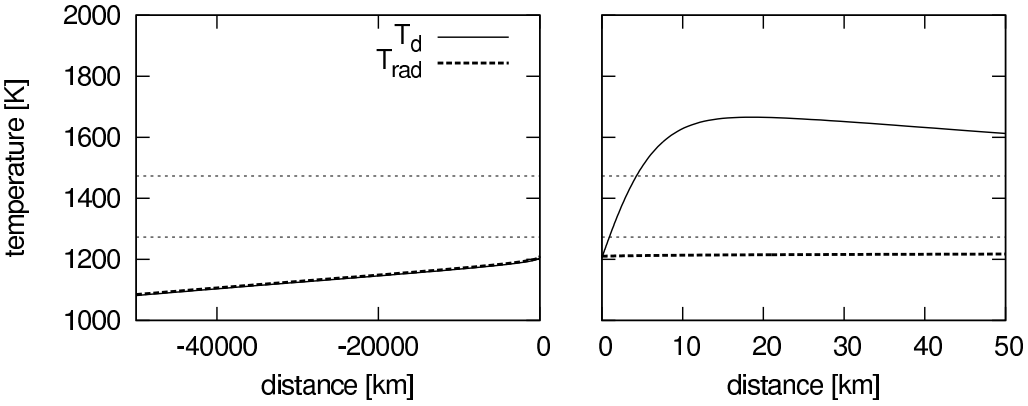

(c) dust model L01 (log-normal size distribution, $C_{\rm d} = 0.01$)

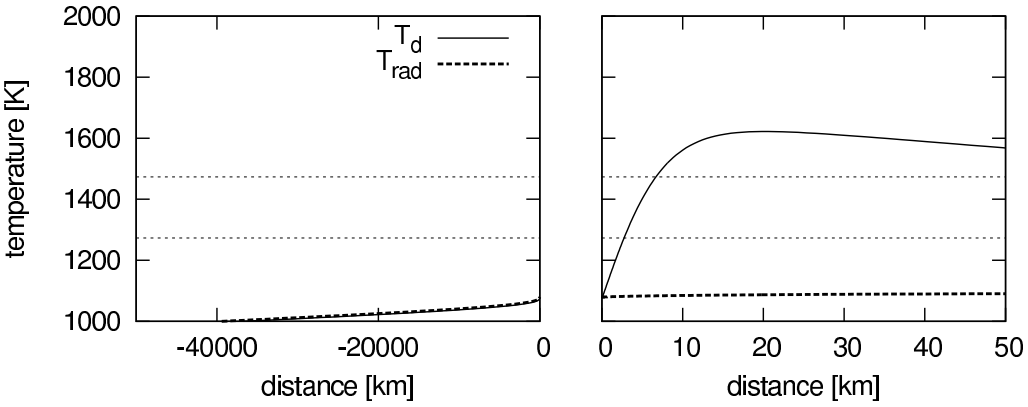

Figure 4.1: Dust thermal histories in the pre- and post-shock regions for various dust models are plotted as a function of distance from the shock front. This figures show the results of $a_{\rm d} = 251\,\mu$m. Shock condition is assumed to be the case of $n_0 = 10^{14}\,{\rm cm}^{-3}$ and $v_{\rm s} = 10\,{\rm km\,s}^{-1}$. The radiation temperatures $T_{\rm rad}$ are also displayed as thick dashed curves.

where Δt is the duration in which dust temperature increases from 1273 K to 1473 K in the heating phase. Here, let's return to Fig. 4.1 and calculate the heating rate of the dust particles. According to Table 4.2, the heating rate is $141\,\mathrm{K\,hr^{-1}}$ for L10, $2.14 \times 10^6\,\mathrm{K\,hr^{-1}}$ for L03, and $1.80 \times 10^6\,\mathrm{K\,hr^{-1}}$ for L01, respectively. Therefore, in the case of L10, the dust particles are heated up to 1273 K or more in the pre-shock region by the radiative heating and the heating rate is too slow, so the isotopic fractionation would occur. On the contrary, in the cases of L03 and L01, the dust temperature increases up to 1273 K in the pre-shock region by the gas frictional heating and the heating rate is too fast, so the isotopic fractionation would be suppressed. Above results are also shown in other calculation conditions. Namely, if $T_{\rm sf} > 1273\,\mathrm{K}$, the heating rate is too slow ($R_{\rm heat} \lesssim 10^3\,\mathrm{K\,hr^{-1}}$) to suppress the isotopic fractionation. On the contrary, if $T_{\rm sf} < 1273\,\mathrm{K}$, the heating rate is so large ($R_{\rm heat} \sim 10^6\,\mathrm{K\,hr^{-1}}$) that the isotopic fractionation would not take place. To summarize, the heating rate of the dust particles strongly depends on the dust temperature at the shock front $T_{\rm sf}$. In order to suppress the isotopic fractionation, $T_{\rm sf} < 1273\,\mathrm{K}$ is required.

4.3 Radiative Diffusion

In order to suppress the isotopic fractionation, the heating rate of the dust particles in a temperature range of $1273-1473\,\mathrm{K}$ should be larger than $10^4\,\mathrm{K\,hr^{-1}}$ (Tachibana & Huss 2005). In the previous section, we found that if the dust temperature when the dust particle reaches at the shock front $T_{\rm sf}$ is lower than 1273 K, the isotopic fractionation would not occur. In this section, we consider how to determine $T_{\rm sf}$.

In the bottom panel of Fig. 3.6, it is found that the radiation flux is almost constant in the pre-shock region. In the case of L10, the pre-shock region is optically thick ($\tau_{\rm pre} = 2.45$). In this case, it is expected that the radiation flux emitted from the post-shock region decreases by a factor of about $e^{-2.44} \sim 0.087$ until it reaches at the pre-shock boundary ($x = -x_{\rm m}$). The reason why the radiation flux is almost constant in spite of the optically thick environment is the re-emission of dust thermal continuum emission. The dust temperature near the shock front is higher than

Table 4.1: Calculation results of dust thermal histories with the initial radius $a_0 = 100\,\mu$m are summarized; the optical depth of the pre-shock region $\tau_{\rm pre}$, the dust temperature at the shock front $T_{\rm sf}$, the peak dust temperature $T_{\rm peak}$, the heating rate $R_{\rm heat}$, the cooling rate $R_{\rm cool}$, and the final dust radius $a_{\rm fin}$. The notation of "n14v10" indicates the pre-shock gas number density $n_0 = 10^{14}\,{\rm cm}^{-3}$ and the shock velocity $v_{\rm s} = 10\,{\rm km\,s}^{-1}$ and so forth.

shock	dust	$\tau_{\rm pre}$	$T_{\rm sf}$ [K]	$T_{\rm peak}$ [K]	$R_{\rm heat}$ [K/hr]	$R_{\rm cool}$ [K/hr]	$a_{\rm fin}$ [μm]
n14v08	P10	15.1	—	1551	—	—	81
	P03	4.64	—	1448	—	—	98
	P01	1.46	—	1334	—	—	100
	L10	2.45	—	1397	—	—	100
	L03	0.73	—	1304	—	—	100
	L01	0.25	—	1270	—	—	100
n14v10	P10	15.0	—	—	—	—	0
	P03	4.81	1427	1735	232	12.9	76
	P01	1.57	1268	1663	5.11(6)	5.69(4)	97
	L10	2.44	—	—	—	—	0
	L03	0.73	1208	1652	5.00(6)	8.17(4)	99
	L01	0.24	1076	1607	4.15(6)	1.21(5)	100
n14v13	P10	13.7	—	—	—	—	0
	P03	4.25	—	—	—	—	0
	P01	1.62	1364	2089	409	7.9	50
	L10	2.44	—	—	—	—	0
	L03	0.73	—	—	—	—	0
	L01	0.24	1292	2085	2.87(3)	2.53(4)	73
n13v16	P10	1.52	1150	1584	2.99(6)	3.70(4)	98
	P03	0.43	—	1526	—	—	100
	P01	0.14	—	1510	—	—	100
	L10	0.25	—	1525	—	—	100
	L03	0.074	—	1512	—	—	100
	L01	0.025	—	1507	—	—	100
n13v20	P10	1.60	1284	1884	3.99(3)	1.65(4)	85
	P03	0.46	1113	1845	9.66(6)	4.21(4)	98
	P01	0.15	1006	1824	9.23(6)	5.33(4)	100
	L10	0.24	1087	1841	9.60(6)	4.65(4)	99
	L03	0.073	975	1820	9.15(6)	5.67(4)	100
	L01	0.025	908	1811	8.84(6)	6.14(4)	100
n13v25	P10	1.67	1428	1938	407	4.7	16
	P03	0.48	1239	1878	1.10(7)	8.72(3)	88
	P01	0.16	1134	1850	1.02(7)	1.69(4)	98
	L10	0.24	1269	1888	1.13(7)	4.1	58
	L03	0.073	1135	1852	1.02(7)	1.69(4)	99
	L01	0.024	1022	1829	9.44(6)	2.30(4)	100

Table 4.1: Continue.

shock	dust	$\tau_{\rm pre}$	$T_{\rm sf}$ [K]	$T_{\rm peak}$ [K]	$R_{\rm heat}$ [K/hr]	$R_{\rm cool}$ [K/hr]	$a_{\rm fin}$ [μm]
n12v30	P10	0.13	—	1358	—	—	100
	P03	0.040	—	1352	—	—	100
	P01	0.013	—	1348	—	—	100
	L10	0.025	—	1350	—	—	100
	L03	0.0074	—	1341	—	—	100
	L01	0.0025	—	1343	—	—	100
n12v35	P10	0.14	1044	1659	4.08(6)	1.28(4)	100
	P03	0.042	1033	1655	4.02(6)	1.43(4)	100
	P01	0.014	1029	1653	4.00(6)	1.46(4)	100
	L10	0.025	1038	1658	4.04(6)	1.36(4)	100
	L03	0.0074	1001	1648	3.91(6)	1.43(4)	100
	L01	0.0025	1007	1648	3.93(6)	1.42(4)	100
n12v40	P10	0.15	1210	1962	1.17(7)	1.82(4)	100
	P03	0.044	1202	1958	1.17(7)	1.69(4)	100
	P01	0.015	1201	1957	1.17(7)	1.64(4)	100
	L10	0.024	1211	1961	1.17(7)	1.48(4)	100
	L03	0.0073	1202	1958	1.17(7)	1.42(4)	100
	L01	0.0024	1189	1953	1.17(7)	1.45(4)	100
n11v50	P10	0.013	—	1444	—	—	100
	P03	0.0038	—	1443	—	—	100
	P01	0.0013	—	1441	—	—	100
	L10	0.0025	—	1441	—	—	100
	L03	0.00074	—	1442	—	—	100
	L01	0.00025	—	1444	—	—	100
n11v55	P10	0.013	867	1624	3.44(6)	4.52(3)	100
	P03	0.0040	876	1622	3.46(6)	6.47(3)	100
	P01	0.0013	869	1620	3.44(6)	6.87(3)	100
	L10	0.0025	866	1621	3.44(6)	6.39(3)	100
	L03	0.00074	873	1621	3.45(6)	6.64(3)	100
	L01	0.00025	890	1623	3.48(6)	6.61(3)	100
n11v60	P10	0.013	934	1808	7.49(6)	6.98(3)	100
	P03	0.0041	946	1806	7.49(6)	7.52(3)	100
	P01	0.0014	940	1803	7.47(6)	7.77(3)	100
	L10	0.0025	957	1807	7.52(6)	7.14(3)	100
	L03	0.00074	945	1804	7.49(6)	7.34(3)	100
	L01	0.00025	962	1806	7.51(6)	7.28(3)	100

Table 4.2: Same as Table 4.1 except for the initial dust radius $a_0 = 251\,\mu$m.

shock	dust	$\tau_{\rm pre}$	$T_{\rm sf}$ [K]	$T_{\rm peak}$ [K]	$R_{\rm heat}$ [K/hr]	$R_{\rm cool}$ [K/hr]	$a_{\rm fin}$ [μm]
n14v08	P10	15.1	—	1558	—	—	232
	P03	4.64	—	1457	—	—	249
	P01	1.46	—	1346	—	—	251
	L10	2.45	—	1408	—	—	251
	L03	0.73	—	1317	—	—	251
	L01	0.25	—	1284	—	—	251
n14v10	P10	15.0	1573	1826	354	10.7	118
	P03	4.81	1427	1746	232	12.9	227
	P01	1.57	1268	1676	2.17(6)	2.14(4)	248
	L10	2.44	1469	1781	141	7.5	144
	L03	0.73	1207	1666	2.14(6)	3.22(4)	250
	L01	0.24	1076	1622	1.80(6)	4.84(4)	251
n14v13	P10	13.7	—	—	—	—	0
	P03	4.78	1520	2137	248	9.5	37
	P01	1.62	1364	2096	410	7.9	200
	L10	2.44	—	—	—	—	0
	L03	0.73	1444	2132	151	8.0	74
	L01	0.24	1292	2092	2.89(3)	9.44(3)	223
n13v16	P10	1.52	1150	1599	1.33(6)	1.32(4)	249
	P03	0.43	—	1540	—	—	251
	P01	0.14	—	1525	—	—	251
	L10	0.25	—	1540	—	—	251
	L03	0.074	—	1527	—	—	251
	L01	0.025	—	1521	—	—	251
n13v20	P10	1.60	1283	1894	4.01(3)	11.0	236
	P03	0.46	1113	1854	4.07(6)	1.58(4)	249
	P01	0.15	1006	1833	3.89(6)	2.07(4)	251
	L10	0.24	1087	1851	4.04(6)	1.84(4)	251
	L03	0.073	975	1830	3.85(6)	2.24(4)	251
	L01	0.025	908	1820	3.76(6)	2.42(4)	251
n13v25	P10	1.67	1427	1971	407	4.8	167
	P03	0.48	1238	1905	4.41(6)	3.66(3)	239
	P01	0.16	1133	1878	4.07(6)	6.98(3)	249
	L10	0.24	1268	1913	4.54(6)	4.2	209
	L03	0.073	1134	1878	4.09(6)	7.23(3)	250
	L01	0.024	1021	1856	3.82(6)	9.75(3)	251

Table 4.2: Continue.

shock	dust	$\tau_{\rm pre}$	$T_{\rm sf}$ [K]	$T_{\rm peak}$ [K]	$R_{\rm heat}$ [K/hr]	$R_{\rm cool}$ [K/hr]	$a_{\rm fin}$ [μm]
n12v30	P10	0.13	—	1378	—	—	251
	P03	0.040	—	1368	—	—	251
	P01	0.013	—	1363	—	—	251
	L10	0.025	—	1366	—	—	251
	L03	0.0074	—	1357	—	—	251
	L01	0.0025	—	1358	—	—	251
n12v35	P10	0.14	1022	1676	1.81(6)	1.00(4)	251
	P03	0.042	1010	1670	1.79(6)	5.51(3)	251
	P01	0.014	1006	1666	1.78(6)	5.78(3)	251
	L10	0.025	1014	1674	1.80(6)	5.49(3)	251
	L03	0.0074	973	1662	1.74(6)	5.80(3)	251
	L01	0.0025	980	1662	1.75(6)	5.77(3)	251
n12v40	P10	0.15	1178	1980	5.08(6)	1.21(4)	251
	P03	0.044	1169	1974	5.06(6)	7.50(3)	251
	P01	0.015	1168	1972	5.05(6)	6.90(3)	251
	L10	0.024	1178	1980	5.07(6)	6.67(3)	251
	L03	0.0073	1168	1973	5.05(6)	6.02(3)	251
	L01	0.0024	1153	1967	5.02(6)	6.03(3)	251
n11v50	P10	0.013	—	1520	—	—	251
	P03	0.0038	—	1453	—	—	251
	P01	0.0013	—	1451	—	—	251
	L10	0.0025	—	1452	—	—	251
	L03	0.00074	—	1453	—	—	251
	L01	0.00025	—	1455	—	—	251
n11v55	P10	0.013	847	1725	1.51(6)	7.17(3)	251
	P03	0.0040	857	1634	1.51(6)	2.14(3)	251
	P01	0.0013	849	1631	1.50(6)	2.64(3)	251
	L10	0.0025	845	1633	1.50(6)	2.38(3)	251
	L03	0.00074	853	1633	1.50(6)	2.62(3)	251
	L01	0.00025	870	1634	1.52(6)	2.66(3)	251
n11v60	P10	0.013	912	1884	3.22(6)	1.16(4)	250
	P03	0.0041	924	1818	3.22(6)	2.74(3)	251
	P01	0.0014	917	1815	3.21(6)	3.07(3)	251
	L10	0.0025	935	1820	3.25(6)	2.83(3)	251
	L03	0.00074	922	1816	3.22(6)	2.96(3)	251
	L01	0.00025	940	1818	3.23(6)	2.93(3)	251

Table 4.3: Same as Table 4.1 except for the initial dust radius $a_0 = 398\,\mu$m.

shock	dust	$\tau_{\rm pre}$	$T_{\rm sf}$ [K]	$T_{\rm peak}$ [K]	$R_{\rm heat}$ [K/hr]	$R_{\rm cool}$ [K/hr]	$a_{\rm fin}$ [μm]
n14v08	P10	15.1	—	1562	—	—	379
	P03	4.64	—	1461	—	—	396
	P01	1.46	—	1351	—	—	398
	L10	2.45	—	1413	—	—	398
	L03	0.73	—	1323	—	—	398
	L01	0.25	—	1290	—	—	398
n14v10	P10	15.0	1573	1829	354	10.7	265
	P03	4.81	1427	1750	232	13.0	374
	P01	1.57	1268	1681	1.41(6)	1.31(4)	395
	L10	2.44	1469	1786	141	7.5	291
	L03	0.73	1207	1671	1.39(6)	2.03(4)	397
	L01	0.24	1075	1627	1.18(6)	3.04(4)	398
n14v13	P10	13.7	—	—	—	—	0
	P03	4.78	1520	2138	248	9.5	182
	P01	1.62	1364	2098	410	7.9	345
	L10	2.44	—	—	—	—	0
	L03	0.73	1444	2134	151	8.0	220
	L01	0.24	1291	2093	2.90(3)	6.22(3)	369
n13v16	P10	1.52	1149	1603	8.80(5)	7.61(3)	396
	P03	0.43	—	1544	—	—	398
	P01	0.14	—	1528	—	—	398
	L10	0.25	—	1543	—	—	398
	L03	0.074	—	1530	—	—	398
	L01	0.025	—	1525	—	—	398
n13v20	P10	1.60	1283	1897	4.02(3)	11.5	383
	P03	0.46	1112	1856	2.62(6)	9.37(3)	396
	P01	0.15	1006	1834	2.50(6)	1.28(4)	398
	L10	0.24	1087	1853	2.61(6)	1.16(4)	397
	L03	0.073	975	1832	2.48(6)	1.41(4)	398
	L01	0.025	908	1822	2.42(6)	1.53(4)	398
n13v25	P10	1.67	1427	1987	408	4.8	314
	P03	0.48	1238	1921	2.79(6)	2.58(3)	386
	P01	0.16	1133	1894	2.58(6)	4.49(3)	396
	L10	0.24	1268	1928	2.87(6)	4.2	356
	L03	0.073	1133	1894	2.59(6)	4.76(3)	397
	L01	0.024	1019	1872	2.42(6)	6.36(3)	398

Table 4.3: Continue.

shock	dust	$\tau_{\rm pre}$	$T_{\rm sf}$ [K]	$T_{\rm peak}$ [K]	$R_{\rm heat}$ [K/hr]	$R_{\rm cool}$ [K/hr]	$a_{\rm fin}$ [μm]
n12v30	P10	0.13	—	1450	—	—	398
	P03	0.040	—	1374	—	—	398
	P01	0.013	—	1368	—	—	398
	L10	0.025	—	1372	—	—	398
	L03	0.0074	—	1363	—	—	398
	L01	0.0025	—	1364	—	—	398
n12v35	P10	0.14	1015	1736	1.19(6)	5.76(3)	398
	P03	0.042	1003	1676	1.18(6)	3.36(3)	398
	P01	0.014	998	1670	1.17(6)	3.60(3)	398
	L10	0.025	1007	1680	1.19(6)	3.52(3)	398
	L03	0.0074	960	1667	1.15(6)	3.71(3)	398
	L01	0.0025	967	1666	1.15(6)	3.68(3)	398
n12v40	P10	0.15	1161	2015	3.30(6)	9.12(3)	396
	P03	0.044	1151	1979	3.29(6)	5.57(3)	398
	P01	0.015	1150	1975	3.29(6)	4.53(3)	398
	L10	0.024	1160	1987	3.30(6)	4.66(3)	398
	L03	0.0073	1150	1978	3.28(6)	3.99(3)	398
	L01	0.0024	1134	1971	3.27(6)	3.94(3)	398
n11v50	P10	0.013	772	1653	1.11(4)	6.23(3)	398
	P03	0.0038	—	1457	—	—	398
	P01	0.0013	—	1454	—	—	398
	L10	0.0025	—	1456	—	—	398
	L03	0.00074	—	1457	—	—	398
	L01	0.00025	—	1458	—	—	398
n11v55	P10	0.013	838	1887	9.95(5)	1.18(4)	392
	P03	0.0040	848	1637	9.93(5)	1.07(3)	398
	P01	0.0013	840	1634	9.85(5)	1.60(3)	398
	L10	0.0025	836	1637	9.85(5)	1.42(3)	398
	L03	0.00074	844	1637	9.91(5)	1.65(3)	398
	L01	0.00025	862	1638	9.97(5)	1.68(3)	398
n11v60	P10	0.013	902	2054	2.09(6)	1.44(4)	375
	P03	0.0041	915	1822	2.08(6)	2.76(3)	398
	P01	0.0014	908	1819	2.08(6)	1.90(3)	398
	L10	0.0025	926	1825	2.10(6)	2.03(3)	398
	L03	0.00074	913	1821	2.09(6)	1.90(3)	398
	L01	0.00025	931	1822	2.09(6)	1.87(3)	398

that far from the shock front, so the re-emitted dust thermal continuum emission produces net radiation flux toward upstream. In the optically thick environment, the equation of radiative diffusion (Rosseland approximation) gives the relation between the radiative flux and the temperature gradient as (Rybicki & Lightman 1979)

$$\mathcal{F} = -\frac{4\sigma_{\rm SB}}{3}\frac{\partial T_{\rm d}^4}{\partial \tau}, \tag{4.2}$$

where $d\tau = \kappa_{\rm R} dx$ and $\kappa_{\rm R}$ is the Rosseland mean absorption coefficient. In this discussion, we assume $\kappa_{\rm R} = \kappa$, for simplicity. Assuming $\mathcal{F}$ to be constant and integrating Eq. (4.2) from $x = -x_{\rm m}$ to $x = 0$, we obtain the dust temperature at the shock front $T_{\rm sf}$ as

$$T_{\rm sf}^4 = T_0^4 + \frac{3}{4\sigma_{\rm SB}}|\mathcal{F}|\tau_{\rm pre}, \tag{4.3}$$

where T_0 is the dust temperature at $x = -x_{\rm m}$ and estimated by assuming the thermal equilibrium with the radiation field as $T_0 = (\pi\mathcal{J}/\sigma_{\rm SB})^{1/4}$. At $x = -x_{\rm m}$, the radiation intensity comes only from the calculation region ($x > -x_{\rm m}$). Since the radiation intensity coming from outer region ($x < -x_{\rm m}$) is weaker than that from the chondrule-forming region, we neglect its effect. Assuming the isotropic intensity in an angle range of $\pi/2 < \theta < \pi$, the mean intensity is given as $\mathcal{J} = \mathcal{I}/2 = |\mathcal{F}|/(2\pi)$. Next, the radiation flux $\mathcal{F}$ can be estimated by a following consideration. The origin of the radiative energy is the gas kinetic energy entering into the shock front. The gas kinetic energy flux is approximately estimated as $\frac{1}{2}\rho_0 v_{\rm s}^3$. Some fraction of the gas energy flux returns toward upstream as a form of radiation flux. Assuming the fraction is f, we obtain $|\mathcal{F}| = \frac{f}{2}\rho_0 v_{\rm s}^3$. Finally, we can estimate the dust temperature immediately in front of the shock front as

$$T_{\rm sf} = \left(\frac{2 + 3\tau_{\rm pre}}{4\sigma_{\rm SB}}\frac{f}{2}\rho_0 v_{\rm s}^3\right)^{1/4}. \tag{4.4}$$

In Fig. 4.2, we compare the dust temperature at the shock front estimated by Eq. (4.4) with the calculated results. The horizontal axis is the optical depth $\tau_{\rm pre}$. The shock condition is $n_0 = 10^{14}\,{\rm cm}^{-3}$ and $v_{\rm s} = 10\,{\rm km\,s}^{-1}$. The circle symbols indicate the simulation results for the power-low dust size distribution and the triangle symbols are for the log-normal size distribution. The solid curves are the results of Eq.

(4.4), in which $\rho_0 = 2.35 \times 10^{-10}\,\mathrm{g\,cm^{-3}}$ and $v_\mathrm{s} = 10\,\mathrm{km\,s^{-1}}$ are substituted. We draw three curves which correspond to $f = 0.3$, 0.5, and 1.0, respectively. The calculation results seem to well match with the estimated curves if the difference of f among each dust models is taken into account. It is found that the corresponding values of f for the power-low size distribution cases (filled circles) are systematically smaller than that of the log-normal cases. It is thought to be because the post-shock region is optically thinner for the power-low size distribution than that of the log-normal one. The power-low size distribution has some amount of the micron-sized dust particles and those small particles would evaporate away in the post-shock region as a result of the shock-wave heating. On the contrary, the amount of such small dust particles in the log-normal size distribution is negligibly small. The chondrule-sized dust particles, which are major components, survive in the post-shock region and contribute the optical depth. As a result, the post-shock region in the case of the power-low cases becomes optically thinner than that of the log-normal one. The optically thin post-shock region makes the radiation leaks toward downstream more effectively.

We would like to mention the effect of the radiation intensity coming from outer region ($x < -x_\mathrm{m}$), which is neglected in above estimation. In an optically thick environment, the radiation intensity is proportional to T_d^4. We assume the radiation intensity coming from outer region corresponds to the black body radiation of 300 K. If the typical dust temperature in chondrule-forming region is 1200 K, the ratio of the radiation intensity coming from outer region to that in the chondrule-forming region becomes only about 0.004. Therefore, our assumption that the radiation intensity coming from outer region is negligible is valid. Even if the temperature in outer region is 500 K, its contribution is only about 0.03 in radiation intensity. To summarize, the dust temperature immediately in front of the shock front T_sf does not depend on the temperature in outer environment significantly.

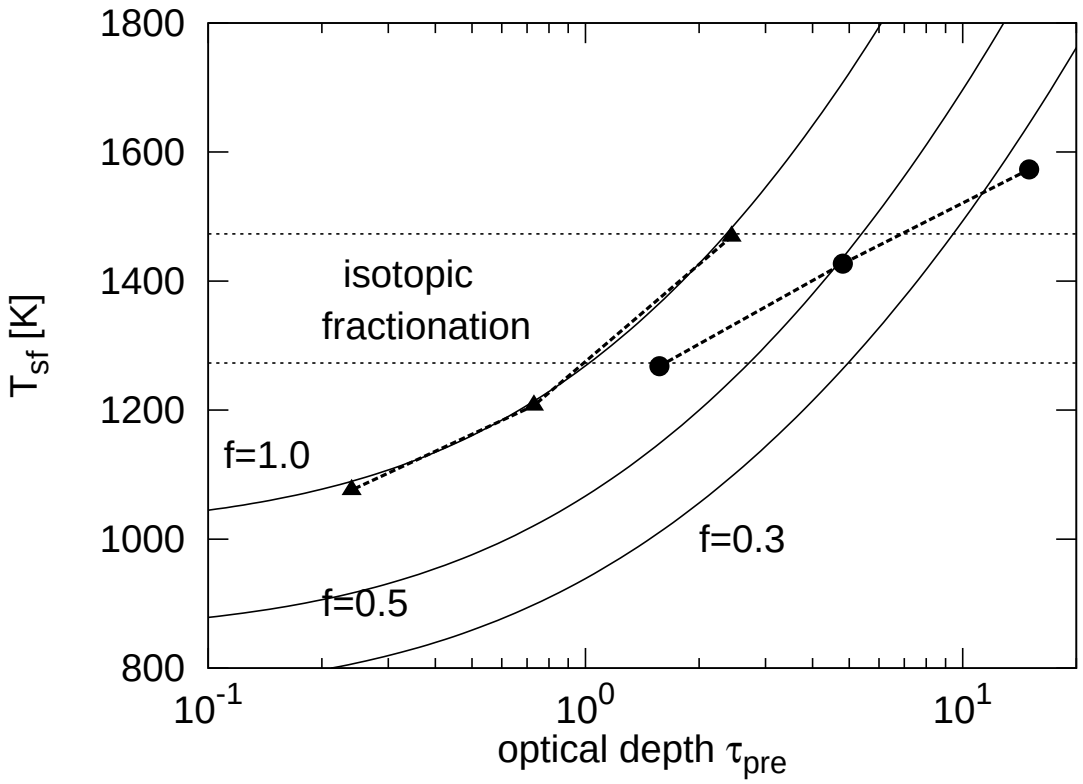

Figure 4.2: Comparison of the dust temperatures at the shock front $T_{\rm sf}$ estimated by using the radiative diffusion approximation (solid curve) with numerically calculated results: the filled circles are for the power-low size distribution and the filled triangles are for the log-normal one. The parameter f is the fraction of the net radiation flux returning from the shock front to the gas energy flux entering into the shock front.

4.4 Critical Optical Depth

In order to suppress the isotopic fractionation, it seems that the pre-shock dust temperature, $T_{\rm sf}$ in Eq. (4.4), should be lower than 1273 K. The requirement gives the upper limit of the optical depth of the pre-shock region above which the isotopic fractionation should occur. Rewriting Eq. (4.4), the condition in which the isotopic fractionation is suppressed is given as

$$\tau_{\rm pre} < \tau_{\rm cr} \equiv \frac{\dfrac{4\sigma_{\rm SB}(1273\,{\rm K})^4}{\frac{f}{2}\rho_0 v_{\rm s}^3} - 2}{3}. \tag{4.5}$$

We plot the upper limit of the optical depth $\tau_{\rm cr}$ for each shock condition as a function of f in Fig. 4.3. In all shock conditions, large amount of radiation flux returning from the shock front requires the smaller optical depth to suppress the isotopic fractionation. Moreover, the shock condition n11v55 allows the larger optical depth than that of the shock condition n14v10 because the radiation flux is smaller than that of the shock condition n14v10. If the optical depth of the pre-shock region is lower than the upper limit in Fig. 4.3, the pre-shock dust temperature does not exceed 1273 K and the isotopic fractionation would be suppressed in the pre-shock region. In this case, in the post-shock region, since the silicate component of dust particles melts quickly due to the gas drag heating, the evaporation of FeS is suppressed and the isotopic fractionation does not take place.

4.5 Conclusions

We investigated the conditions for the rapid heating constraint to prevent the isotopic fractionation. We considered the steady, one-dimensional, plane-paralled shock waves characterized by the pre-shock gas number density n_0 and the shock velocity $v_{\rm s}$, and various dust models: the size distribution (power-low or log-normal) and the dust-to-gas mass ratio. We found that the conditions to prevent the isotopic fractionation can be summarized by the value of the optical depth of the pre-shock region $\tau_{\rm pre}$. The detailed conclusions are as follows:

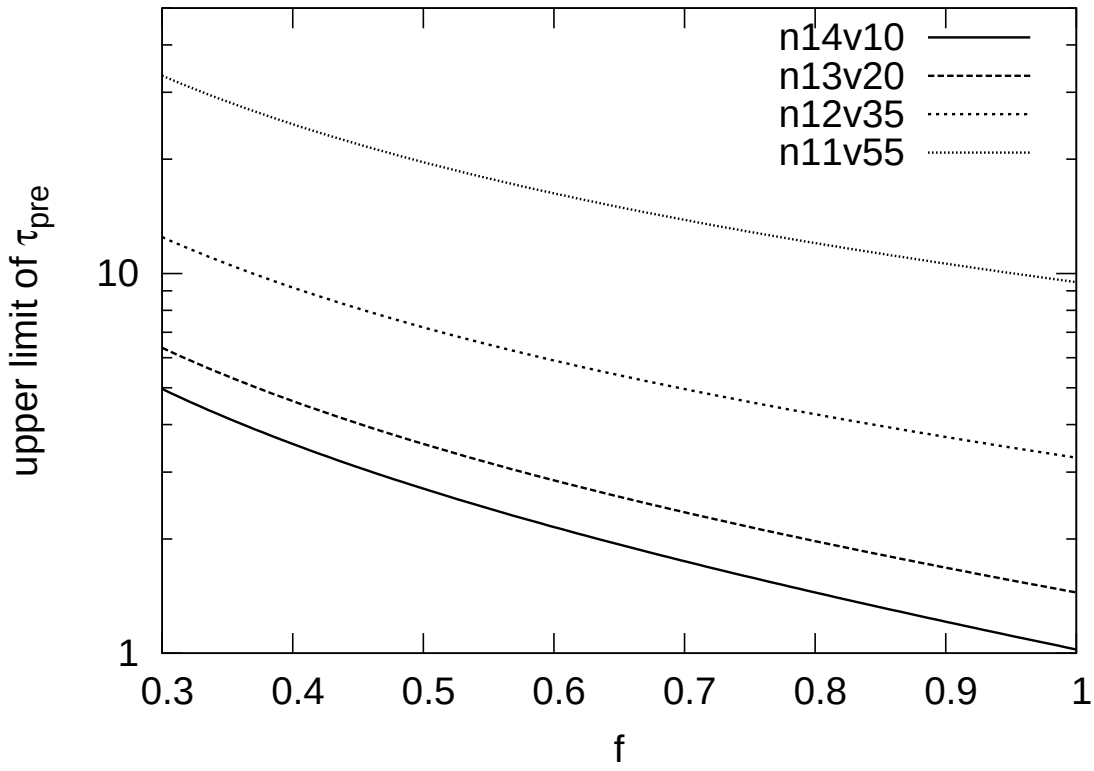

Figure 4.3: Upper limit of the optical depth of the pre-shock region above which the isotopic fractionation should occur is plotted as a function of f, which is the fraction of the net radiation flux returning from the shock front to the gas energy flux entering into the shock front. Each curve indicates the result for different shock condition.

1. The optically thicker environment in the pre-shock region results the higher dust temperatures in the pre-shock region. If the dust temperature at the shock front exceeds 1273 K, the heating rate of the dust particles in a temperature range of $1273 - 1473\,\mathrm{K}$ is too slow to prevent the isotopic fractionation. On the contrary, the dust temperature at the shock front is lower than 1273 K, the dust particle is heated by the gas frictional heating so rapidly in the temperature range that the isotopic fractionation is prevented. Therefore, the condition to prevent the isotopic fractionation is that the dust temperature at the shock front is lower than 1273 K.

2. We analytically derived the dust temperature at the shock front using the theory of the radiative diffusion. The analytic solution explains the results of the numerical simulations well.

3. Comparing the analytic solution and the numerical results, we also found that the net flux of the radiation returning toward upstream depends on the dust model. In cases of the power-low dust size distribution, the returning radiation flux is smaller than cases of the log-normal size distribution. The reason is thought to be the evaporation of micron-sized dust particles in the post-shock region.

4. We obtained the upper limit of the optical depth of the pre-shock region $\tau_{\rm cr}$ above which the isotopic fractionation would take place. It depends on the shock condition, for example, $\tau_{\rm cr} \simeq 1$ for the high-density shock waves like $n_0 = 10^{14}\,\mathrm{cm^{-3}}$ and $v_{\rm s} = 10\,\mathrm{km\,s^{-1}}$, or $\tau_{\rm cr} \simeq 10$ for the low-density shock waves like $n_0 = 10^{11}\,\mathrm{cm^{-3}}$ and $v_{\rm s} = 55\,\mathrm{km\,s^{-1}}$.

Chapter 5

Appropriate Shock Condition

The conditions for the rapid heating constraint to prevent the isotopic fractionation were investigated in the previous chapter. Additionally, in order to form chondrules, the cooling rate at a crystallization temperature should be an appropriate range. Therefore, we have to consider both constraints simultaneously.

In this chapter, we discuss the appropriate shock conditions in which the rapid heating constraint and the appropriate cooling rate constraint are satisfied.

5.1 Heating Rate vs. Cooling Rate

In order to discuss the chondrule formation, the cooling rate in the phase that the precursor dust particle re-solidifies after the melting phase is a important information. We numerical calculate the thermal histories of the dust particles in the shock-wave heating. We estimate the cooling rate as

$$R_{\rm cool} \equiv \frac{1550\,{\rm K} - 1400\,{\rm K}}{\Delta t}, \tag{5.1}$$

where Δt is the duration in which dust temperature decreases from 1550 K to 1400 K in the cooling phase. The results for various shock conditions and the dust models are summarized in Table 4.2.

Figures 5.1 - 5.3 show the plot of the heating rate vs. the cooling rate. Symbols indicate the simulation results and the difference of the symbols means the different gas number density in the pre-shock region; $n_0 = 10^{14}\,{\rm cm}^{-3}$ (circle), $10^{13}\,{\rm cm}^{-3}$ (square), $10^{12}\,{\rm cm}^{-3}$ (triangle), and $10^{11}\,{\rm cm}^{-3}$ (inverse triangle), respectively. The vertical dashed line indicates the lower limit of the heating rate below which the isotopic fractionation would take place. We draw the horizontal lines at $R_{\rm cool} = 5\,{\rm K\,hr}^{-1}$ and $100\,{\rm K\,hr}^{-1}$ between which the textures and zoning profiles of olivine grains tens of micrometers across in natural chondrules are well explained (Jones & Lofgren 1993). We also draw the horizontal line at more higher cooling rate ($R_{\rm cool} \gtrsim 5000\,{\rm K\,hr}^{-1}$) suggested from the measurement of the overgrowth on low-FeO relict grains contained within almost type II chondrules (Wasson 2004).

It is found that the numerical results are roughly classified into two cases; the first is the slow heating ($R_{\rm heat} = 10^2 - 10^3\,{\rm K\,hr}^{-1}$) and slow cooling ($R_{\rm cool} = 5 - 20\,{\rm K\,hr}^{-1}$), and the second is the rapid heating ($R_{\rm heat} \sim 10^6\,{\rm K\,hr}^{-1}$) and rapid cooling ($R_{\rm cool} = 10^3 - 10^5\,{\rm K\,hr}^{-1}$). The former case appears when the gas number density in the pre-shock region is relatively high ($n_0 \gtrsim 10^{13}\,{\rm cm}^{-3}$) and the optical depth is larger than about unity. On the contrary, if the pre-shock gas number density is low ($n_0 \lesssim 10^{12}\,{\rm cm}^{-3}$) or the optical depth is lower than about unity, the thermal histories of the dust particles become the later case. Namely, the heating rate and the cooling rate become extremely small only when the radiation field is strong enough. The reason can be easily understood as follow. If the mean intensity of the radiation field

is strong enough to heat the dust particle up to 1273 K or more in the pre-shock region, the heating rate is determined at the pre-shock region and it becomes small (see chapter 4). Moreover, when the radiation field is strong in the pre-shock region, the mean intensity of the radiation field is also strong in the post-shock region (see Fig. 3.6). The strong radiation field keeps the dust particle at high temperature for a long time, so the cooling rate becomes small.

The rapid heating/cooling case satisfies the rapid heating constraint for suppressing the isotopic fractionation. The cooling rate meets the measurement of the overgrowths on low-FeO relict grains contained within almost type II chondrules (Wasson 2004). On the contrary, in the slow heating/cooling case, the isotopic fractionation must take place. However, the cooling rate well matches with the estimation suggested by comparing the textures and zoning profiles of olivine grains tens of micrometers across in natural chondrules and experimental analogs (Jones & Lofgren 1993).

5.2 Appropriate Shock Mechanism

In order to form chondrules, the shock wave generation mechanism should satisfy at least the rapid heating constraint. We discuss which shock wave generation mechanism is appropriate for chondrule formation in view of the rapid heating constraint.

Recently, Boss & Durisen (2005) showed that the marginally gravitational instability in the nebula can drive inward spiral shock fronts at asteroidal orbits, sufficient to account for melting of dust particles. Shock waves generated by this mechanism are similar to the shock condition A. They did not examine if the rapid heating is satisfied or not. If the spatial scale of shock waves is $10^5\,\mathrm{km\,s^{-1}}$, which is the same as the calculation region we assumed in this study, a shock wave with the dust-to-gas mass ratio less than about 0.03 satisfies the rapid heating condition. However, if the spatial scale is $10^6\,\mathrm{km\,s^{-1}}$, which is ten times larger than that of our assumption, it is impossible to suppress the isotopic fractionation even if the dust-to-gas mass ratio is 0.01, which is a standard value of the minimum mass solar nebula model. For a case that all dust particles have the same radius, we can

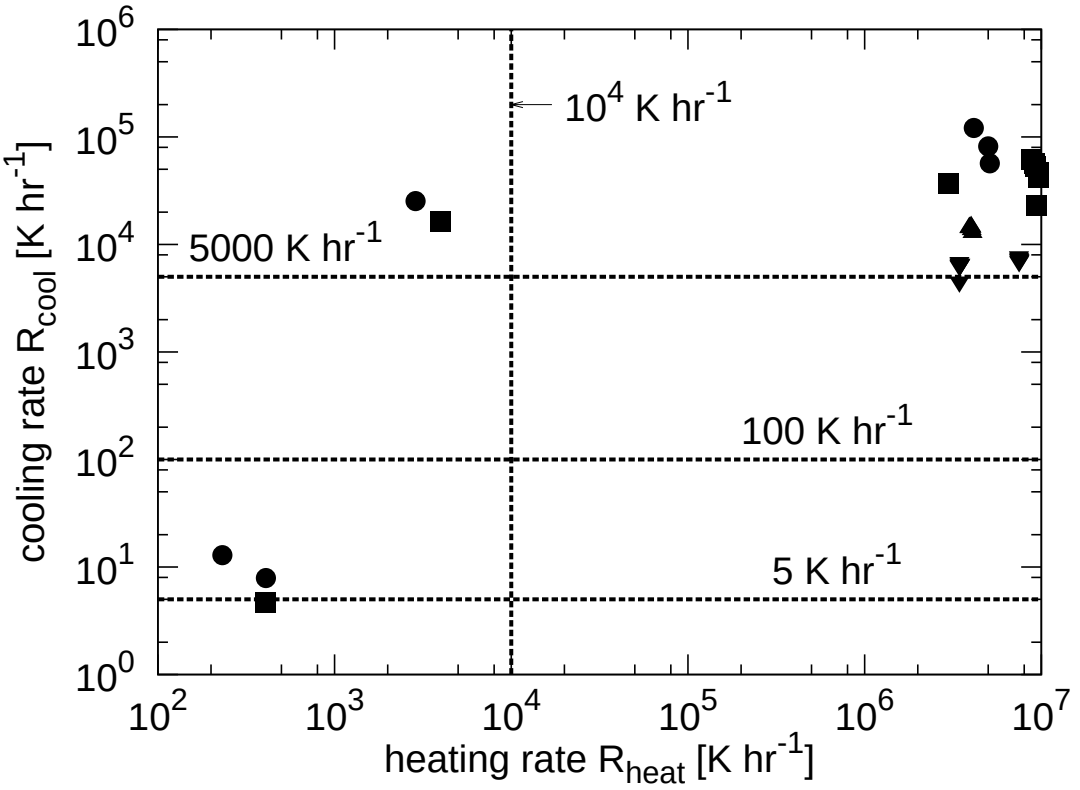

Figure 5.1: Heating rates and cooling rates of chondrules for the initial dust radius $a_0 = 100\,\mu$m. Each symbol means different gas number density of the pre-shock region; $n_0 = 10^{14}\,\mathrm{cm}^{-3}$ (circle), $10^{13}\,\mathrm{cm}^{-3}$ (square), $10^{12}\,\mathrm{cm}^{-3}$ (triangle), and $10^{11}\,\mathrm{cm}^{-3}$ (inverse triangle), respectively.

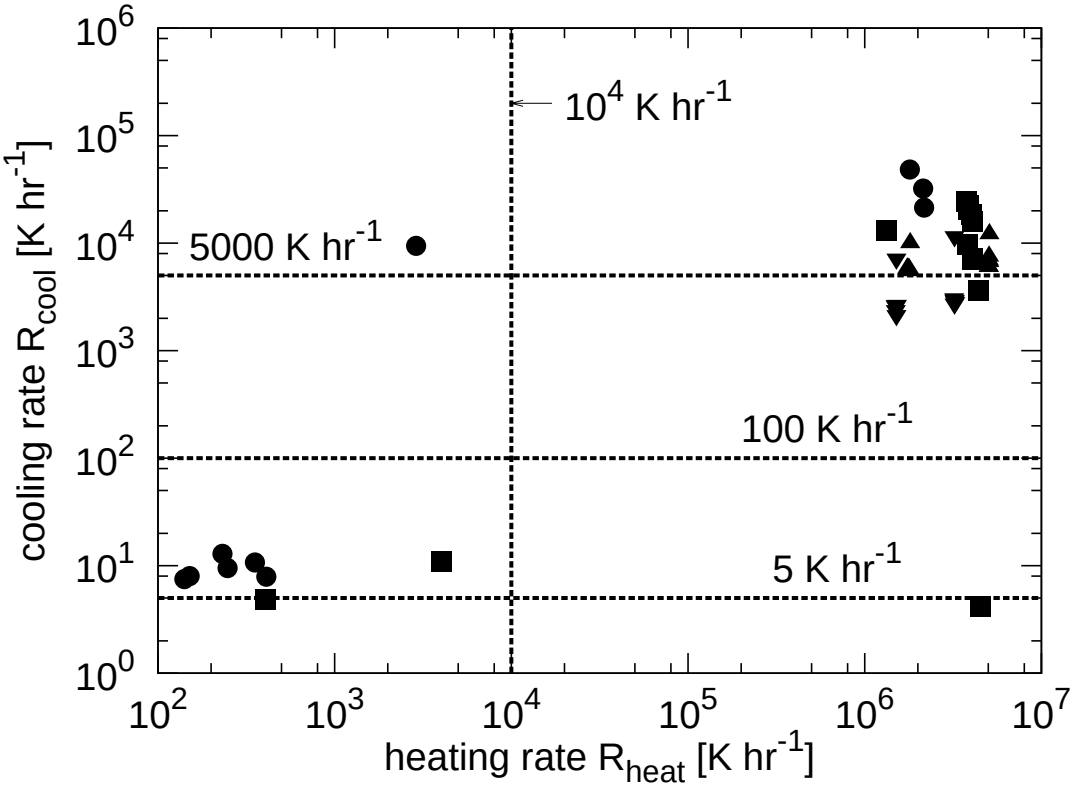

Figure 5.2: Same as Fig. 5.1 except for $a_0 = 251\,\mu$m.

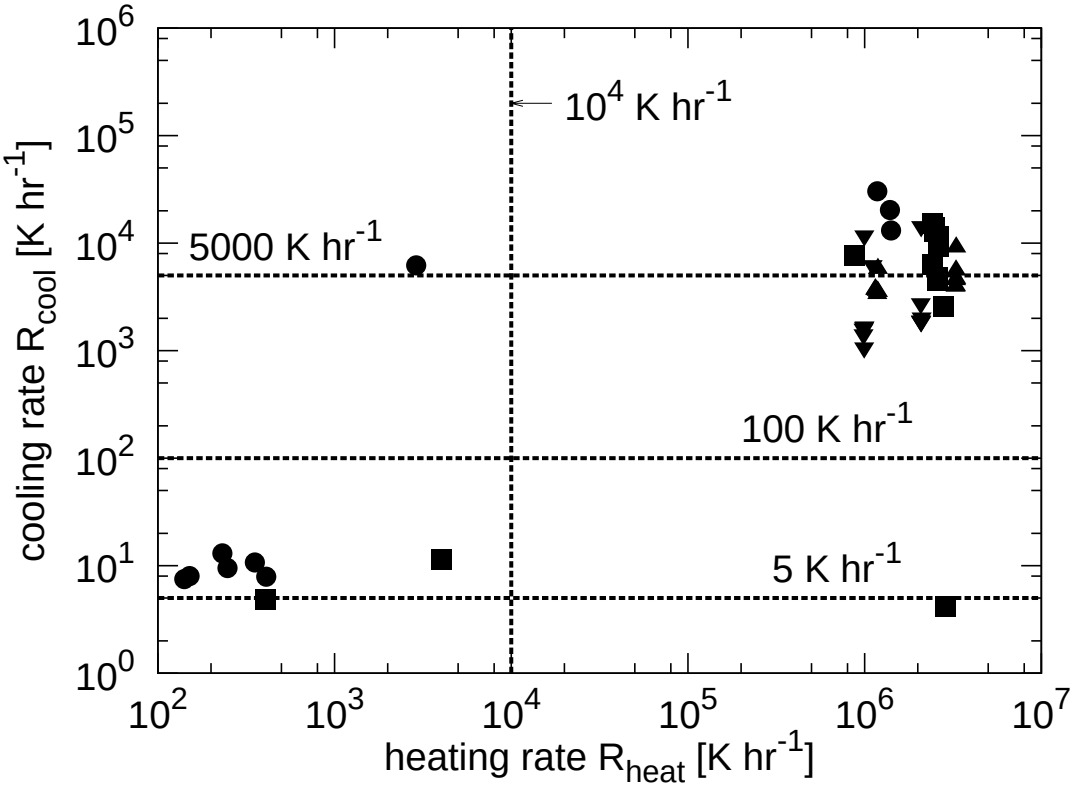

Figure 5.3: Same as Fig. 5.1 except for $a_0 = 398\,\mu$m.

easily derive the same conclusion as follows. The optical depth of the pre-shock region is calculated as $\tau_{\rm pre} \sim (\alpha_{\rm p} + \sigma_{\rm p})x_{\rm m}$, where $\alpha_{\rm p} + \sigma_{\rm p} = \pi a_{\rm d}^2(\epsilon_{\rm abs} + \epsilon_{\rm scat})n_{\rm d}$. Here, we assume that the dust particles have the same radius of 500 μm. Assuming $\rho_0 = 4 \times 10^{-10}\,{\rm g\,cm^{-3}}$ and the dust-to-gas mass ratio $C_{\rm d} = 0.01$, the number density of dust particles is $n_{\rm d} \sim 2 \times 10^{-9}\,{\rm cm^{-3}}$. For the astronomical silicate with radius of 500 μm, $\epsilon_{\rm abs} + \epsilon_{\rm scat} \sim 2$. Therefore, substituting $x_{\rm m} = 10^6\,{\rm km}$, we finally obtain $\tau_{\rm pre} \sim 3$ and it exceeds the upper limit of the optical depth in Fig. 4.3.

On the contrary, Nakamoto *et al.* (2005) proposed a new shock wave generation mechanism: shock waves in the upper region of the solar nebula induced by X-ray flares associated with the young Sun. X-ray flares, common among T Tauri stars (Feigelson *et al.* 2002), emit plasma gas, which cools to be a strong neutral gas wind. Hayashi *et al.* (1996) suggested that the magnetocentrifugal acceleration (Blandford & Payne 1982) also plays an important role to produce the wind. Because of the enormous amount of energy released by the X-ray flares and the magnetocentrifugal acceleration, the flares should have some effects on the dynamics and energetics of a protoplanetary disk around the star. Nakamoto *et al.* (2005) carried out 2-D MHD numerical simulations of X-ray flares around a central star and expanding magnetic bubles/winds with a disk. They showed that shock waves which are sufficient to melt precursor dust particles can be generated in the upper region of the nebula inside about the asteroid belt. In that case, since shock waves are generated in the upper solar nebula where the gas density is low, the region is naturally expected to be optically thin. The estimated shock condition is similar to the shock condition of $n_0 = 10^{11}\,{\rm cm^{-3}}$ and $v_{\rm s} = 55\,{\rm km\,s^{-1}}$ in this model. We also estimate the optical depth for this model. Assuming the same parameters as above estimation except of $\rho_0 = 4 \times 10^{-13}\,{\rm g\,cm^{-3}}$, the optical depth is lower than unity even if $x_{\rm m}$ is assumed to be 1 AU. Therefore, this case seems to satisfy the rapid heating constraint.

5.3 Conclusions

In chapter 4, we obtained the dust thermal histories for various shock conditions and the dust models. In this chapter, we discussed the appropriate shock mechanism

to satisfy the two constraints for the chondrule formation; the rapid heating and the appropriate cooling rate. The required heating rate is larger than $10^4\,\mathrm{K\,hr^{-1}}$ in a temperature range of $1273 - 1473\,\mathrm{K}$ in order to suppress the isotopic fractionation. Regarding to the appropriate cooling rate, we refereed the following two observational suggestions; the comparison between the textures and zoning profiles of olivine grains tens of micrometers across in natural chondrules and experimental analogs, and the other one is the measurement of the overgrowths on low-FeO relict grains contained within almost type II chondrules. In the former case, the suggested cooling rate is $5 - 100\,\mathrm{K\,hr^{-1}}$. In the latter case, the suggested cooling rate is about 900 times larger than that of the former case ($\sim 5000 - 10^5\,\mathrm{K\,hr^{-1}}$). We found the following conclusions;

1. The numerical results on the plot of the heating rate vs. the cooling rate seems to be classified into two case; one is the slow heating ($R_{\mathrm{heat}} = 10^2 - 10^3\,\mathrm{K\,hr^{-1}}$) and slow cooling ($R_{\mathrm{cool}} = 5 - 20\,\mathrm{K\,hr^{-1}}$), and the other one is the rapid heating ($R_{\mathrm{heat}} \sim 10^6\,\mathrm{K\,hr^{-1}}$) and the rapid cooling ($R_{\mathrm{cool}} = 10^3 - 10^5\,\mathrm{K\,hr^{-1}}$). The former case satisfies the rapid heating constraint for suppressing the isotopic fractionation and the cooling rate meets the measurement of the overgrowths on low-FeO relict grains contained within almost type II chondrules. On the contrary, in the latter case, the isotopic fractionation must take place, but the cooling rate well matches with the comparison between the textures and zoning profiles of olivine grains tens of micrometers across in natural chondrules and experimental analogs.

2. It is suggested that the marginally gravitational instability in the protoplanetary nebula can drive inward spiral shock fronts at asteroid orbits, sufficient to account for melting of dust particles. In this case, since the optical depth of the chondrule-forming region tends to be larger than about unity, the dust thermal histories would be the slow heating/cooling case. Therefore, the isotopic fractionation should occur if a certain mechanism to suppress the isotopic fractionation does not exist.

3. It is suggested that shock waves in the upper region of the solar nebula induced

by X-ray flares associated with the young Sun can contribute the dust thermal processing. If the gas frictional heating is strong enough to melt the silicate dust particles and the chondrule-sized dust particles exist at the upper region of the nebula, the chondrule formation can occur. In this case, it is expected that the optical depth at the region is much lower than unity, so the isotopic fractionation would not take place. As a result, the dust thermal histories would be the rapid heating/cooling case.

Part II

Hydrodynamics of Molten Droplets

Chapter 6

Chondrule Shapes

The data of chondrule shapes is a strong clue for elucidating the chondrule formation mechanism. Recently, the three-dimensional data has been measured using X-ray microtomography. It is considered that the rotation of the chondrules when they melted in their formation process plays an important role in chondrule shapes. On the other hand, the gas drag force in the shock-wave heating is strong enough to deform the molten silicate dust particles as expected from the chondrule data. Therefore, the both effects (rotation and gas drag force) should be investigated simultaneously in the framework of the shock-wave heating.

In this chapter, we briefly summarize the observational data of three-dimensioinal chondrule shapes and some theoretical researches about the deformation of the molten droplet in the framework of the shock-wave heating model.

6.1 Three-Dimensional Data

Tsuchiyama et al. (2003) studied three-dimensional shapes of chondrules using X-ray microtomography. They measured twenty chondrules with perfect shapes and smooth surfaces, which were selected from forty-seven chondrules separated from the Allende meteorite (CV3). The external shapes were approximated as three-axial ellipsoids with a-, b-, and c-axes (axial radii are A, B, and C (A≥B≥C), respectively) using the moments of inertia of the chondrules, where the rotation axes with the minimum and maximum moments correspond to the a- and c-axes, respectively. The plot of C/B vs. B/A (Figure 1.5) shows that (1) the shapes are diverse from oblate (A∼B>C), general three-axial ellipsoid (A>B>C) to prolate chondrules (A>B∼C), and (2) two groups can be recognized: oblate to prolate chondrules with large C/B and B/A of 0.9 - 1.0 (group-A) and prolate chondrules with relatively small B/A of 0.74-0.78 (group-B).

Tsuchiyama et al. (2003) proposed that the oblate chondrules were rotating with high speed when the precursor dust particles have been melted. Assuming that the molten droplet re-solidified to form chondrules keeping its shapes, such chondrules should take the oblate shape, where the centrifugal force was balanced with the surface tension of a chondrule melt. The equilibrium shape of rotating droplet depends on the non-dimensional parameter (Chandrasekhar 1965)

$$\Sigma = \frac{\rho_{\rm mat}\Omega^2 a^3}{8\gamma}, \tag{6.1}$$

where Ω is the angular velocity of rotation, a is the equatorial radius of the droplet, $\rho_{\rm mat}$ is its density, and γ is the surface tension coefficient. The required angular velocity in order to obtain the oblate shape as shown in group-A is about 300 to 2000 s^{-1}, which corresponds to the rotation rate of about 50 to 350 rps (rotation per second). Tsuchiyama et al. commented that the shock-wave heating model may be favorable to produce such rapid rotation (Susa & Nakamoto 2002).

On the contrary, they considered that the prolate chondrules shown in group-B have been also formed from rapidly rotating droplets. In these cases, the stable axis for the rotation was the minor axis (c-axis). The group-B chondrules can be

explained by spitted droplets as a result of the shape instability, which occurs when Σ exceeds a critical value of 0.8440 (the critical value is 0.4587 if some dissipative mechanism is present) (Chandrasekhar 1965). Tsuchiyama et al. also discussed the general three-axial ellipsoids and prolate chondrules in group-A might be formed by some modifications during solidification and/or precession during rotation. However, the idea has not been investigated quantitatively.

The size-dependence of the chondrule shapes are also important informations. We show the size dependence of chondrule shapes in Figure 6.1. Fig. 6.1 is the same as Fig. 1.5 except for the symbols whose radii are proportional to the sizes measured chondrules (the chondrule radius is defined as $(ABC)^{1/3}$ in this paper). Although the number of the data might not be enough to discuss statistically, we can find some tendencies about the size-dependence of the chondrule shapes. First, in group-A, larger chondrules seem to have larger magnitude of the deformation than smaller ones. Moreover, the tendency seems not to depend on whether the chondrule shapes are oblate or prolate. This might indicate that the origin of the prolate chondrules in group-A was not different from that for the oblate chondrules. If so, the chondrule formation mechanism should naturally produce the oblate, prolate, and general three-axial ellipsoids. On the contrary, three chondrules in group-B have relatively large radii of about $500\,\mu$m or more. One of them is very small, which radius is about $200\,\mu$m. However, the data is so few that we cannot find any tendency about the size-dependence.

6.2 Equilibrium Shapes of Rotating Droplets

Chandrasekhar (1965) derived the equilibrium shapes of rotating droplets and discussed the stabilities analytically. According to him, the equilibrium shape depends on the value of the non-dimensional parameter Σ (see Eq. 6.1). A sequence of equilibrium shapes is illustrated in Figure 6.2. This figure shows the sections of the equilibrium droplets in xz-plane, where z-axis is the rotation axis. Both axes are normalized by the equatorial radius a. The values of Σ, a, and Ω for each curves labeled as "0", "1", *cdots*, and "8" are listed in Table 6.1. When $\Sigma = 0$ (labeled as

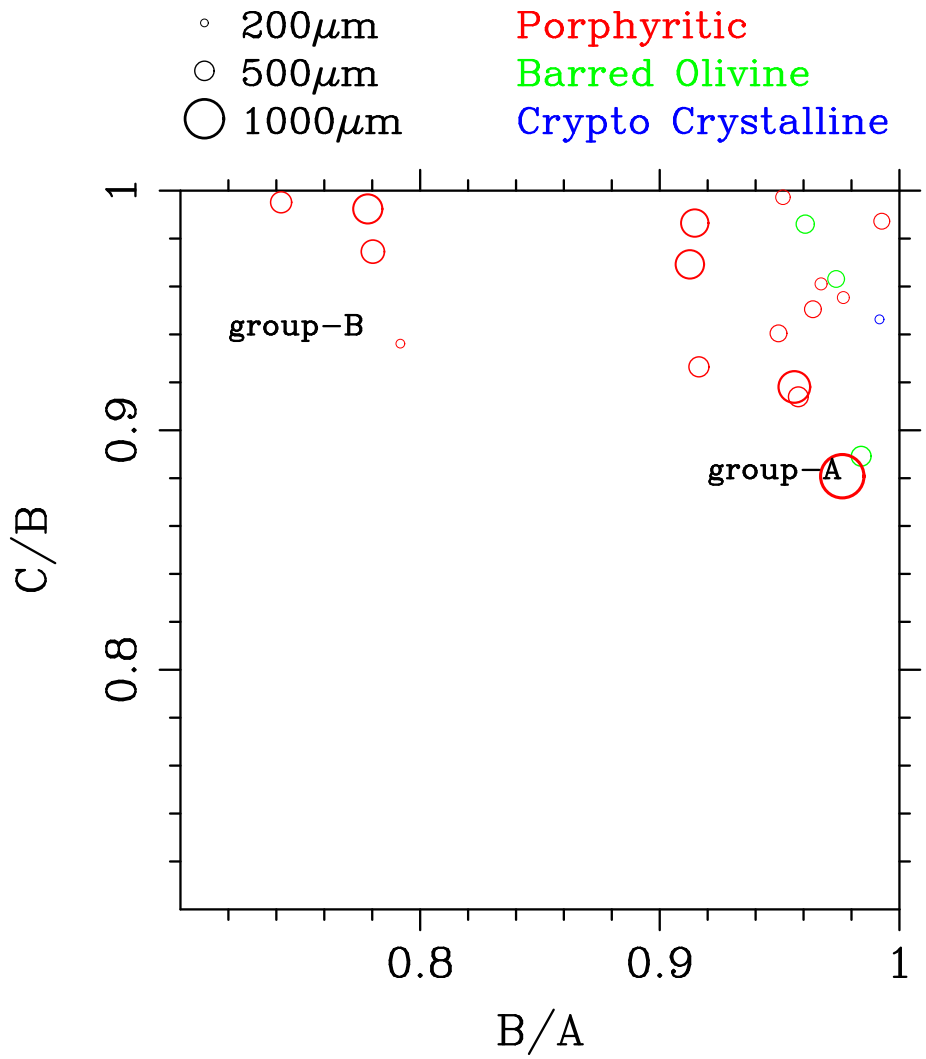

Figure 6.1: Size dependences of the chondrule shapes in the C/B-B/A diagram (Tsuchiyama, priv. comm.). Radii of the symbols are proportional to the measured chondrule radii. The colors of symbols indicate the textural types of chondrules, porphyritic (red), barred olivine (green), and crypto crystalline (blue), respectively.

"0"), the figure becomes a perfect sphere. It is found that the shape deforms significantly as Σ increases. Chandrasekhar also found that the shapes with Σ larger than 0.4587 are unstable if some dissipative mechanism is present. In Figure 6.2, these unstable shapes are drawn by dashed curves.

Figure 6.3 shows the axial ratio C/B of the equilibrium figures for rotating droplets as a function of Σ. The dashed curve indicates the unstable solution. In Fig. 6.2, since the equatorial radius a corresponds to A and B, C/B is the same the values of z/a at which each curve crosses with the z-axis. The group-A chondrules in Fig. 1.5 have the values of C/B about 0.9 or more. Therefore, it is found that the value of Σ should be about 0.1 in order to deform the droplet to the oblate shape with C/B=0.9 (see Fig. 6.3). Assuming the equatorial radius of the droplet $a = 500\,\mu$m, the surface tension $\gamma = 400\,\mathrm{dyne\,cm^{-1}}$, and the density $\rho_{\mathrm{mat}} = 3\,\mathrm{g\,cm^{-3}}$, we obtain the angular velocity $\Omega = 926\,\mathrm{s^{-1}}$ for producing the oblate chondrules in group-A, which corresponds to the rotation rate of 147 rps. In this case, when the angular velocity exceeds about 2000 $\mathrm{s^{-1}}$ (315 rps in rotation rate), Σ is larger than the critical value of 0.4587 and the equilibrium shapes become unstable. If the bar-mode perturbation grows, the droplet would take the prolate shapes before it separates into two small pieces. If the droplets could re-solidify before the fragmentation occurs, it can be prolate chondrules in group-B (see Fig. 1.5).

6.3 Deformation due to Gas Drag Force

A distinguishing characteristic of the shock-wave heating model is the gas drag force acting on the dust surface. It causes the internal flow and the deformation of the molten droplet. Sekiya et al. (2003) analytically derived the deformation and the internal flow of the droplet assuming that the non-linear terms of the hydrodynamical equations as well as the surface deformation are sufficiently small so that linearized equations are appropriate. They expressed the radius of the deformed droplet as $r_s = r_0 + r_1$, where r_0 is the unperturbed radius of the spherical droplet and r_1 is the perturbation from the sphere ($r_1 \ll r_0$). According to their analytic solutions, the magnitude of the deformation defined as r_1/r_0 is proportional to the value of

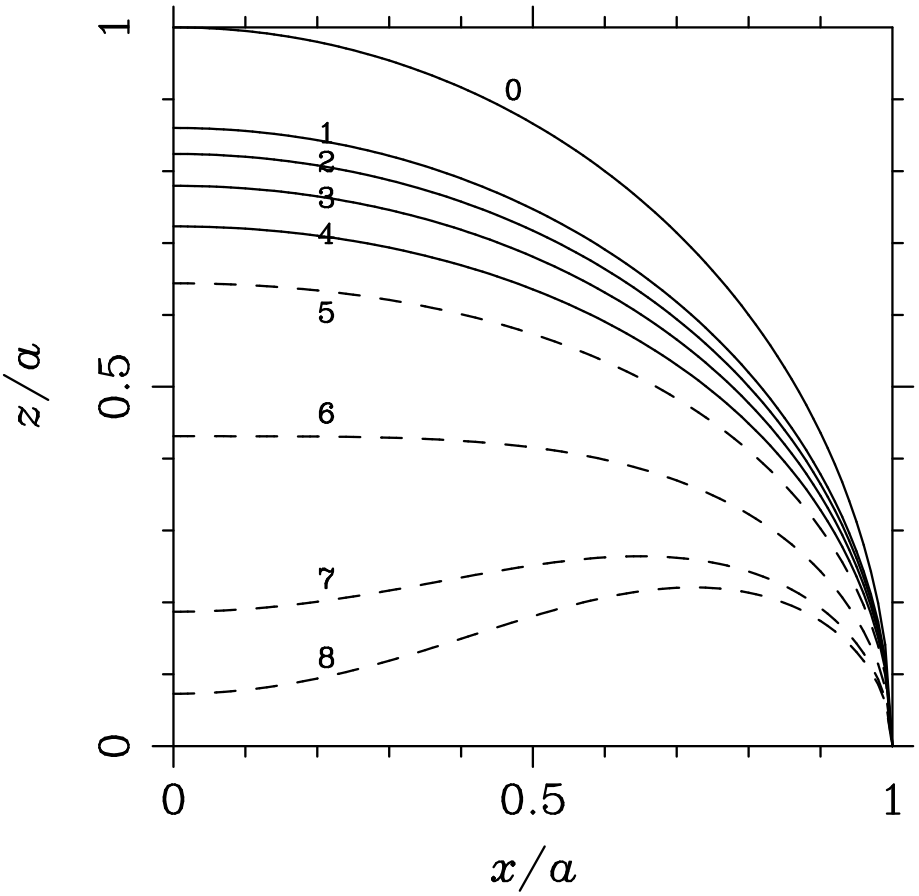

Figure 6.2: The equilibrium shapes of a rotating droplets for various values of the parameter Σ (values of Σ for labeled curves are shown in Table 6.1).

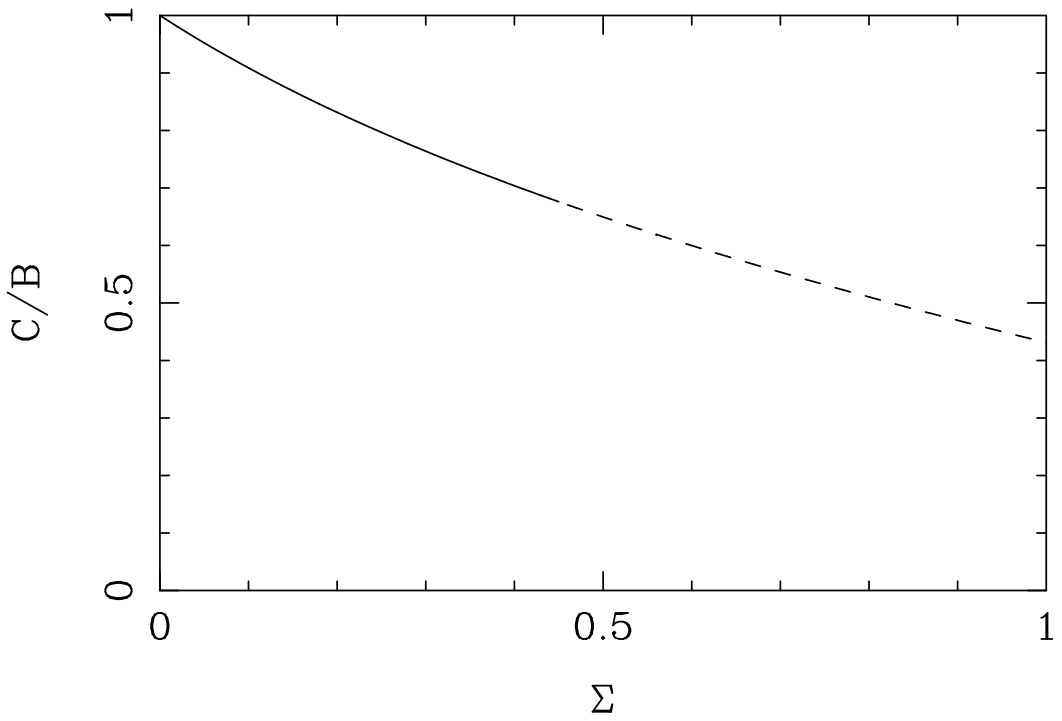

Figure 6.3: The axial ratio C/B of the equilibrium shape of rotating droplet as a function of the non-dimensional parameter Σ (see Eq. 6.1).

Table 6.1: Physical parameters of equilibrium shapes of rotating droplets for various values of Σ. a is the equatorial radius of the equilibrium shapes in order to be the same volume with a sphere whose radius is r_0 (here, we set $r_0 = 500\,\mu$m). Ω is the angular velocity of the equilibrium shape.

label	Σ	a [μm]	Ω [s^{-1}]
0	0.00000	500	0
1	0.16118	525	1090
2	0.21048	532	1221
3	0.27562	541	1363
4	0.36675	553	1521
5	0.51079	571	1710
6	1.0000	630	2066
7	1.7260	724	2201
8	2.0959	786	2146

$W_e = p_{\rm fm} r_0/\gamma$, where W_e is called as the Weber number and it is a non-dimensional parameter indicating the ratio of the ram pressure of the gas flow to the surface tension of the droplet. Figure 6.4 shows the shape of the droplet surface for various value of the Weber number, 0.0 (unperturbed), 0.5, and 1.0. The figures are the projections into the xy-plane, and both axes are normalized by the unperturbed radius r_0. The gas flow comes from the left side of the panel. The asymmetrical structures of the front and back of the droplet are found from these figures. The reason why the deformation due to the gas flow was not discussed as the origin of the deformed chondrules in Tsuchiyama et al. (2003) might be the asymmetrical structures.

Sekiya et al. (2003) also discussed the limitation of their analytic solutions for applying the chondrule formation. Their solutions can be applied if the non-linear terms of the hydrodynamical equations is negligibly small and the magnitude of the deformation is much smaller than unity. According to their discussions, the former condition corresponds to the Reynolds number $R_e = 0.11\rho_{\rm mat} p_{\rm fm} r_0^2/\mu^2$ is much smaller than unity. The latter one corresponds to the Weber number $W_e =$

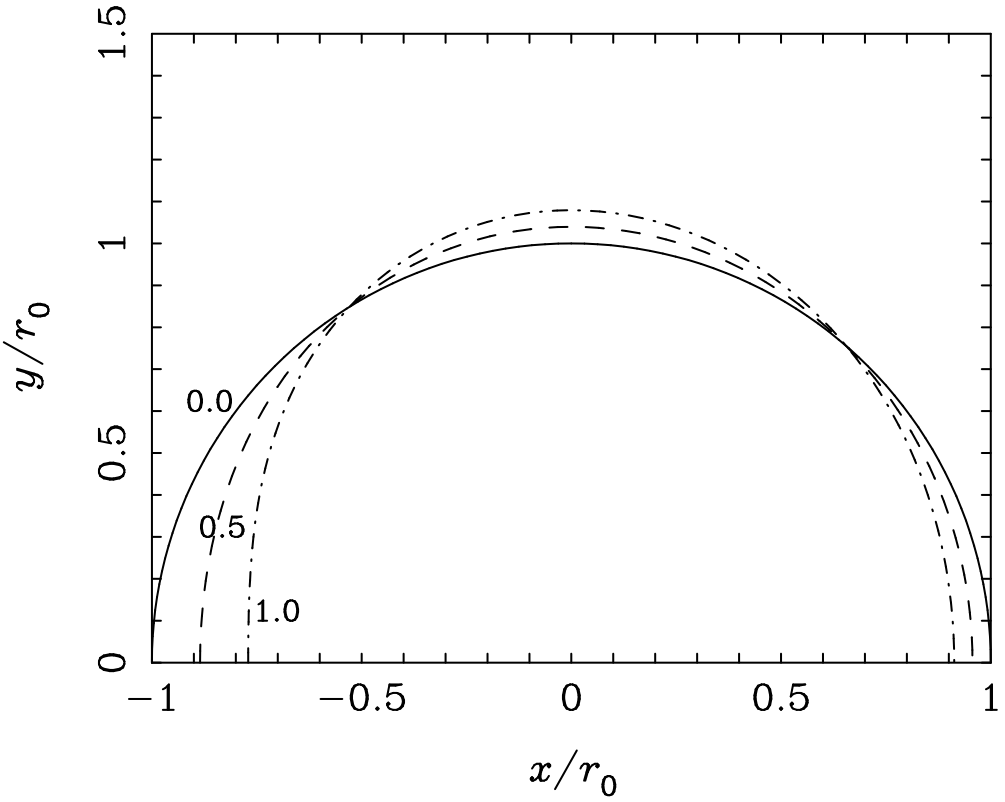

Figure 6.4: The shapes of the droplet exposed to the gas flow for various conditions (Sekiya et al. 2003). Both axes are normalized by the radius of the unperturbed spherical droplet r_0. The gas flow comes from the left side of this panel. The numbers in the panel indicate the values of Weber number, which is defined as $W_e = p_{\rm fm} r_0/\gamma$, where $p_{\rm fm}$ is the ram pressure of the gas flow and γ is the surface tension.

$p_{\rm fm} r_0/\gamma$ is much smaller than 5.

In order to confirm the validity of the analytic solutions by Sekiya et al. (2003), we can estimate the Weber number W_e acting on the molten silicate dust particles in the post-shock region. The ram pressure, $p_{\rm fm}$, is given by Eq. (2.25). Here, we estimate the ram pressure as $p_{\rm fm} \simeq 4000\,{\rm dyne\,cm^{-2}}$ for high-density shock waves ($n_1 \simeq 10^{14}\,{\rm cm^{-3}}$) and $p_{\rm fm} \simeq 1000\,{\rm dyne\,cm^{-2}}$ for low-density shock waves ($n_1 \simeq 10^{11}\,{\rm cm^{-3}}$). Assuming the unperturbed droplet radius $r_0 = 500\,\mu{\rm m}$ and the surface tension $\gamma = 400\,{\rm dyne\,cm^{-2}}$, the typical value of the Weber number for high-density

shock waves becomes about 0.5, and it is expected that the droplet slightly deforms due to the gas drag force. If there are much larger dust particles in the chondrule-forming region and it melts, we obtain the large Weber number (e.g., $W_e = 5$ for $r_0 = 5000\,\mu$m) and the droplet would deform significantly. The analytic solutions derived by Sekiya et al. (2003) cannot be applied for cases of such large Weber number. On the contrary, for low-density shock waves, the magnitude of the deformation is expected to be smaller than that of the high-density shock waves because of the small ram pressure. For the droplet with radius of 500 μm, we obtain $W_e \simeq 0.13$ and it is too small to deform the droplet significantly. Even for the droplet with radius of 5000 μm, the Weber number is $W_e \simeq 1.3$ at most. In this study, we especially pay attention to the deformation of molten droplets in the high-density shock waves in which the droplets are expected to deform more significantly than that of the low-density shock waves.

6.4 Rotating Droplets exposed to Gas Flow

In previous subsections, we know that the deformations due to the rotation and the gas drag force play important roles for the shapes of chondrules. However, these two effects have been investigated separately. In the shock-wave heating model, the situation that the rapidly rotating droplets are exposed to the high-velocity gas flow can be considered. Therefore, we have to take into account these two effects simultaneously.

Figure 6.5 briefly explains the origin of the rotation of precursor dust particles in the shock-wave heating model. Before the dust particles melt in the post-shock region, it is thought that the precursor dust particles are not perfect spheres and have many bumps on its surface. The asymmetrical structures would cause the net torque in the gas flow and the precursor dust particles should begin to rotate. Since the stopping time scale of the rotation due to the frictional with the ambient gas is much longer than the cooling time scale, the rotation continues during the precursor dust particles melt by the gas frictional heating. We can estimate the angular momentum that the precursor dust particles will gain. The angular momentum obtained during

the time duration Δt can be estimated as

$$I\Omega \sim f\pi r_0^2 p_{\rm fm} r_0 \Delta t, \tag{6.2}$$

where I is the inertial moment of the particle and r_0 is the particle radius (we assume that the radius of the precursor dust particle is almost the same as that of the molten droplet). The non-dimensional parameter f stands for the degree of anti-symmetry of the precursor particle, in other words, $f\pi r_0^2$ is the effective area which can contribute to generate the net torque on the precursor particle. We call the non-dimensional parameter f as an asymmetric parameter. Regarding to Δt, we assume that the angular momentum which is gained during 1/2 rotation is the upper limit for the precursor particle to obtain. Because after 1/2 rotation, the effective area which contributes to generate the net torque is moving to the opposite side. It causes deceleration of rotation of the precursor particle. The time duration is given as

$$\Delta t \sim \frac{\pi}{\Omega}. \tag{6.3}$$

Using eqs. (6.2) and (6.3), the upper value of angular velocity which the precursor particle obtains is estimated as

$$\begin{aligned} \Omega &\sim \left(\frac{15}{8}\frac{f\pi p_{\rm fm}}{r_0^2 \rho_{\rm mat}}\right)^{1/2} \\ &= 280\left(\frac{f}{0.1}\right)^{1/2}\left(\frac{p_{\rm fm}}{4000\,{\rm dyne\,cm^{-2}}}\right)^{1/2}\left(\frac{r_0}{1\,{\rm mm}}\right)^{-1}{\rm s^{-1}}, \end{aligned} \tag{6.4}$$

where $\rho_{\rm mat}$ is the density of the precursor particle and we set $\rho_{\rm mat} = 3\,{\rm g\,cm^{-3}}$. The inertial moment of the particle is assumed to be the same as the sphere with uniform density, $I = (8/15)\pi r_0^5 \rho_{\rm mat}$. Notice that the rotation axis is perpendicular to the direction of the rarefied gas flow.

In order to confirm the validity of Eq. (6.4), we consider the rotation of irregular-shaped precursor dust particle in the gas flow by numerically solving the equation of motion about the rotation (see Appendix C). The time evolution of the angular velocity depends on the dust shapes and the initial directions against the gas flow. However, roughly speaking, Eq. (6.4) can be used for estimating the angular velocity

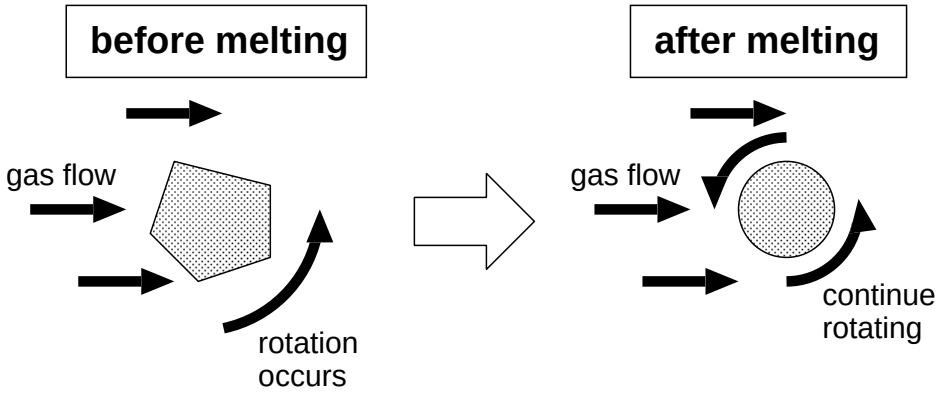

Figure 6.5: Rotating droplets in the shock-wave heating model. In the post-shock region, the precursor dust particles are not thought to be a perfect sphere. The asymmetrical shapes would induce the rotation in the gas flow (left figure). After melting, the rotation would continue until the droplet cools to re-solidify because the stopping time scale of the rotation due to the friction with the ambient gas is longer than the cooling time scale of the molten droplets. Notice that the rotation axis is perpendicular to the direction of the gas flow.

that the precursor dust particle obtains.

In the shock-wave hating model, the situation that the molten droplets are rapidly rotating in the high-velocity gas flow can be considered. The analysis by Sekiya et al. (2003) did not take into account the effects of rotation, so their analytic solutions are axis-symmetrical. However, the situation in Fig. 6.5 would produce the three-dimensional structures in the droplet shape, which are no longer the axis-symmetrical because the rotational axis is perpendicular to the direction of the gas flow. Moreover, although Sekiya et al. (2003) solved the hydrodynamical equations assuming the steady states, it is not clear that some steady state can be established in the situations. Therefore, we need to perform the non-linear, time-dependent, three-dimensional hydrodynamic simulations in order to analyze the hydrodynamics of rapidly rotating droplet exposed to the gas flow.

6.5 Conclusions

1. The three-dimensional shapes of chondrules have been observed. It is found that most of chondrules seem not to be a perfect sphere and take various shapes like as oblate, prolate, and general three-axial ellipsoid.

2. The deformation when the precursor dust particles melt in the gas flow may reflect the deformed chondrule shapes.

3. The rotation of the molten droplet plays an important role to deform the droplet. However, a equilibrium shape of rotating droplet is oblate. It is difficult to produce other shapes (prolate and general three-axial ellipsoid) only by the effect of the rotation.

4. The gas drag force acting on the molten droplet also plays an important role to deform the droplet. However, the deformed shape becomes oblate.

5. In the shock-wave heating model, the molten droplet may rotate rapidly being exposed to the gas flow. It is interesting to investigate the deformation of the rapidly rotating droplet exposed to the gas flow, however, there is no manuscript about those researches in the framework of the shock-wave heating. In order to analyze the hydrodynamics of the droplets, we need to perform the non-linear, time-dependent, three-dimensional hydrodynamic simulations.

Chapter 7

Hydrodynamic Simulations for Molten Droplets

In order to consider the deformation of the molten droplet in the shock-wave heating model, the rotation of the molten droplet and the gas drag force should be taken into account consistently. The analysis of the hydrodynamics for rapidly rotating droplet exposed to the gas flow would be very complex, so the numerical simulation is required.

In this chapter, we model the rapidly rotating droplet exposed to the high-velocity rarefied gas flow and develop the three-dimensional hydrodynamic simulation code.

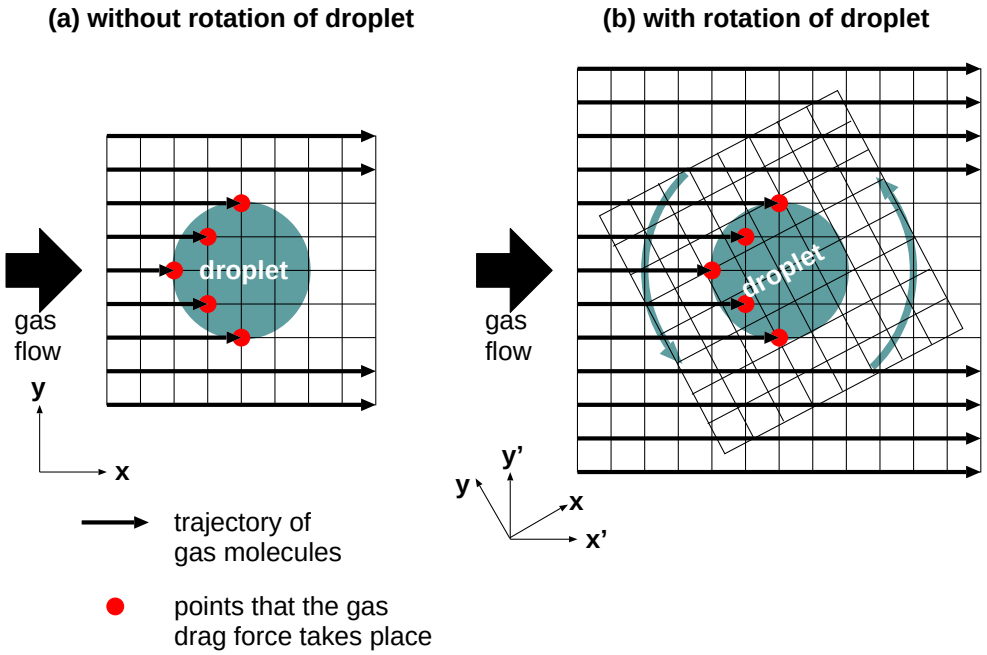

Figure 7.1: Sketch of the coordinate system we adopted in this study. If the dust particle does not rotate initially, the coordinate system is corresponds to the accelerated frame (x', y', z') which is moving with the mass center of the droplet (a). If the droplet is rotating, we adopt the coordinate system (x, y, z) which is rotating with the angular velocity $\mathbf{\Omega} = (0, 0, \Omega)$, where Ω_0 is the initial angular velocity of the droplet.

7.1 Hydrodynamical Equations

7.1.1 Coordinate System

We place the molten droplet and the ambient nebula gas in the Cartesian coordinate system (x, y, z), which is rotating with the angular velocity $\mathbf{\Omega} = (0, 0, \Omega)$ against the non-rotating, but accelerated frame (x', y', z') which is moving with the mass center of the droplet (Figure 7.1). We assume the initially solid-rotating droplet with the angular velocity $\mathbf{\Omega}$. The gas flow comes from the negative direction of x'-axis. Therefore, in the rotation coordinate, the direction of the gas flow changes with time.

7.1.2 Fluid Dynamics

The droplet behaves as an incompressible fluid since sound velocity is very large. On the other hand, the ambient gas does not follow the fluid equations because the mean free path of the gas molecules is much greater than the typical size of the droplet. The condition corresponds to a free molecular flow in which molecules scattered and reemitted from the droplet surface do not disturb the free stream velocity distribution. Therefore, in our model, it is assumed that the ambient gas does not flow against the droplet, and the gas drag force is explicitly in the hydrodynamic equations. The fluid equations are written in a form

$$\frac{\partial \boldsymbol{f}}{\partial t} + (\boldsymbol{u} \cdot \boldsymbol{\nabla})\boldsymbol{f} = \boldsymbol{G} + \boldsymbol{G}', \tag{7.1}$$

by using

$$\boldsymbol{f} = (\rho, \boldsymbol{u}, p), \tag{7.2}$$

$$\boldsymbol{G} = (\rho \boldsymbol{\nabla} \cdot \boldsymbol{u},\ (-\boldsymbol{\nabla} p + \mu \Delta \boldsymbol{u} + \boldsymbol{F}_{\rm s} + \boldsymbol{F}_{\rm g})/\rho,\ -\rho c_{\rm s}^2 \boldsymbol{\nabla} \cdot \boldsymbol{u}), \tag{7.3}$$

$$\boldsymbol{G}' = \left(0,\ \boldsymbol{g} + \frac{1}{2}\boldsymbol{\nabla}|\boldsymbol{\Omega} \times \boldsymbol{r}|^2 + 2\boldsymbol{u} \times \boldsymbol{\Omega},\ 0\right), \tag{7.4}$$

where ρ is the density, $\boldsymbol{u}$ is the velocity, p is the pressure, μ is the coefficient of viscosity, and $c_{\rm s}$ is the sound velocity. The external force due to the surface tension and the gas drag are $\boldsymbol{F}_{\rm s}$ and $\boldsymbol{F}_{\rm g}$, respectively. The gas drag force causes the deceleration of the center of mass of the droplet. In our coordinate system co-moving with the center of mass, the apparent gravitational acceleration $\boldsymbol{g}$ should appear in the equation of motion (Sekiya et al. 2003). The term of $\boldsymbol{\Omega} \times \boldsymbol{r}$ in Eq. (7.4) stands for the centrifugal force and the term of $\boldsymbol{u} \times \boldsymbol{\Omega}$ is the Coriolis force.

The surface tension $\boldsymbol{F}_{\rm s}$ is given as

$$\boldsymbol{F}_{\rm s} = -\gamma \kappa \delta(\boldsymbol{x} - \boldsymbol{x}_i)\boldsymbol{n}_i, \tag{7.5}$$

where γ is the fluid surface tension coefficient, κ is the local surface curvature, $\boldsymbol{x}_i$ is the position of the liquid-gas interface, and $\boldsymbol{n}_i$ is the unit normal vector of the interface. The delta function $\delta(\boldsymbol{x} - \boldsymbol{x}_0)$ means that the surface tension works at the interface only. We adopt the numerical model of the surface tension by Brackbill et al. (1992).

The gas drag force $\boldsymbol{F}_{\rm g}$ is given by an explicit form as

$$\boldsymbol{F}_{\rm g} = \begin{cases} -p_{\rm fm}\delta(\boldsymbol{x}-\boldsymbol{x}_i)(\boldsymbol{n}_i\cdot\boldsymbol{n}_g)\boldsymbol{n}_g & \text{for} \quad \boldsymbol{n}_i\cdot\boldsymbol{n}_g \le 0 \\ 0 & \text{for} \quad \boldsymbol{n}_i\cdot\boldsymbol{n}_g > 0 \end{cases} \tag{7.6}$$

where $p_{\rm fm}$ is the ram pressure of the rarefied gas flow and $\boldsymbol{n}_{\rm g}$ is the unit vector pointing the direction in which the gas flows. Notice that $\boldsymbol{n}_g$ is a function of the time because the coordinate system is rotating.

7.2 Numerical Scheme

As shown in Eq. (7.1), the fluid equations can be separated into two terms; the advection term and the non-advection term. Using the time splitting technique, we can solve these equations in order that the first is the advection phase as

$$\frac{\partial \boldsymbol{f}}{\partial t} + (\boldsymbol{u}\cdot\boldsymbol{\nabla})\boldsymbol{f} = 0, \tag{7.7}$$

and the second is the non-advection phase as

$$\frac{\partial \boldsymbol{f}}{\partial t} = \boldsymbol{G} + \boldsymbol{G'}. \tag{7.8}$$

After these two phases are completed, we obtain the solutions at the next time step.

The constrained interpolation profile (CIP) method is one of the powerful tools for solving the advection equation (e.g., Yabe et al. 2001). When the velocity is constant at any points, the solution of Eq. (7.7) gives a simple translational motion of a wave with velocity $\boldsymbol{u}$. However, to solve the advection equation Eq. (7.7) is not so easy. To show that, we solve the one-dimensional advection equation by various numerical methods. Figure 7.2 shows the results of the test calculations. The horizontal axis is the spatial coordinate x and the vertical axis is the value of f. We set the initial profile of f as the solid line, the velocity $u = 1.0$, the interval of the computational grid $\Delta x = 1.0$, and the time interval $\Delta t = 0.2$. This conditions are corresponds to the CFL number $\nu \equiv u\Delta x/\Delta t = 0.2$. The filled circles indicate the numerical results after 300 time steps and the dashed line is the exact solution of the advection equation. It is found that the Rational CIP (R-CIP) scheme gives a good

solution which does not show a oscillational profile (panel d). The R-CIP-CSL2 (conservative semi-Lagrangian), which is one of the exactly conservative schemes based on the CIP concept (e.g., Nakamura et al. 2001), provide the similar solution with the R-CIP scheme (panel e). Additionally, using the anti-diffusion technique described in section 7.2.3, we can obtain less diffusive solution that any other schemes (panel f). As shown in Fig. 7.2, the CIP method can be suitable for our analysis, so we adopt this method in this study.

We can solve the non-advection phase using the finite difference method as $\boldsymbol{f}^{**} = \boldsymbol{f}^{*} + (\boldsymbol{G} + \boldsymbol{G'})\Delta t$, where suffixes * and ** indicate the values before and after the non-advection phase, respectively. However, the analysis of the incompressible fluids is not so simple because of its large sound velocity. General methods for the compressible fluids solve the hydrodynamical equations in order of the equation of motion and the continuity equation at the first, and the equation of state at the second. On the contrary, since the incompressible fluids have very large sound velocity $c_{\rm s}$, the slight change in the density ρ results the significant change in the pressure p. In order to avoid the tiny time interval Δt which is determined by the CFL condition of the sound speed, the term related to the pressure should be solved implicitly. This method is called as the pressure-based algorithm (e.g., Yabe & Wang 1991, Yabe et al. 2001).

7.2.1 Original CIP Method

We briefly explain the strategy of the CIP method by using a one-dimensional advection equation,

$$\frac{\partial f}{\partial t} + u\frac{\partial f}{\partial x} = 0, \tag{7.9}$$

which gives a simple translational motion of a wave f with velocity u toward x direction when u is constant. We assume u is constant below for simplicity. Let's consider that the values of f at any grid points are given at a time step n. The exact solution at the next time step $n+1$ is given by $f^{n+1}(x_i) = f^{n}(x_i - u\Delta t)$, where Δt is the duration from the time step n to $n+1$. However, since the point of $x_i - u\Delta t$ is not necessarily on the grid points on which the physical values are given, we have to postulate the value of f between the grid points by some method. In the CIP

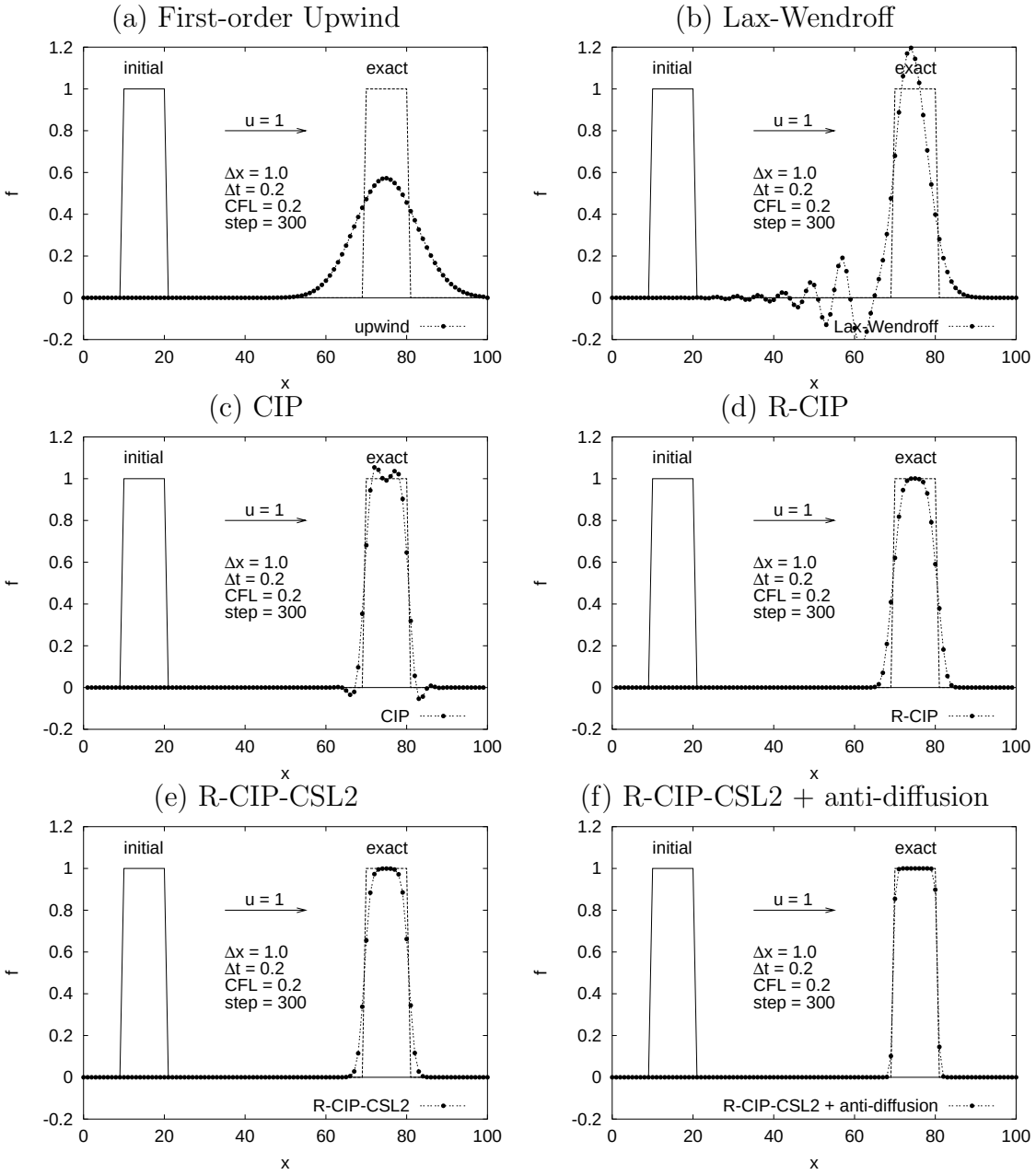

Figure 7.2: Numerical solutions of the advection equation for a rectangle wave with various schemes: (a) first-order upwind scheme, (b) Lax-Wendroff scheme, (c) CIP method, (d) Rational CIP method, (e) Rational CIP-CSL2, and (f) Rational CIP-CSL2 with an anti-diffusion technique, respectively. The solid curve is the initial profile and the dashed curve is the exact solution of the advection equation.

method, we use $g \equiv \partial f/\partial x$ in order to construct the profile of f between the grid points. The profile between the grid points $i-1$ and i is given

$$F_i(x) = A(x-x_i)^3 + B(x-x_i)^2 + g_i(x-x_i) + f_i, \tag{7.10}$$

where

$$\begin{aligned} A &= \frac{g_i + g_{i-1}}{\Delta x^2} - \frac{2(f_i - f_{i-1})}{\Delta x^3}, \\ B &= \frac{3(f_{i-1} - f_i)}{\Delta x^2} + \frac{2g_i + g_{i-1}}{\Delta x}. \end{aligned} \tag{7.11}$$

The profile function $F_i(x)$ satisfies the following conditions;

$$F_i(x_i) = f_i^n, \quad F_i(x_{i-1}) = f_{i-1}^n, \quad \left.\frac{\partial F_i}{\partial x}\right|_{x_i} = g_i^n, \quad \text{and} \quad \left.\frac{\partial F_i}{\partial x}\right|_{x_{i-1}} = g_{i-1}^n. \tag{7.12}$$

Using the profile function $F_i(x)$, we obtain $f_i^{n+1} = F_i(x_i - u\Delta t)$.

The characteristic of the CIP method is to treat $g \equiv \partial f/\partial x$ as an independent variable in the system. Namely, g is not determined from the value of f and it evolves independently. If we differentiate Eq. (7.9) with spatial variable x, we get

$$\frac{\partial g}{\partial t} + u\frac{\partial g}{\partial x} = -g\frac{\partial u}{\partial x}. \tag{7.13}$$

We can trace the time evolution of g by using Eq. (7.13) as well as for f by using Eq. (7.9). The value of g after the advection phase is given as

$$g_i^{**} = \left.\frac{\partial F_i}{\partial x}\right|_{x_i - u\Delta t}. \tag{7.14}$$

After the advection phase is calculated, the result of the advection phase is advanced to the value of the next time step g^{n+1} in the non-advection phase. The non-advection phase can be solved by the finite difference method as

$$g_i^{n+1} = g_i^{**} - g_i^{**}\frac{\partial u}{\partial x}\Delta t, \tag{7.15}$$

where the spatial derivative of the velocity $\partial u/\partial x$ is approximated by the simple centered finite difference.

We can obtain the expressions of these coefficients including the cases of $u < 0$, and the extension to the R-CIP scheme in Yabe et al. (2001). For the extension to the multi-dimensions, we can use a directional splitting technique to perform sequential one-dimensional advection in each direction (e.g., Nakamura & Yabe 1999).

7.2.2 Conservative Semi-Lagrangian Scheme (CIP-CSL2)

Recently, the new conservative semi-Lagrangian schemes based on the concept of the CIP scheme have been developed. These schemes are called CIP-CSL (conservative semi-Lagrangian). There are some version of the CIP-CSL, CIP-CSL2 (Nakamura et al. 2001), CIP-CSL4 (e.g., Yabe et al. 2001), and CIP-CSL3 (e.g., Xiao & Yabe 2001). In this study, we use the CIP-CSL2 scheme because it is the simplest scheme in the CIP-CSL schemes. We briefly explain the CIP-CSL2 scheme below.

The CIP-CSL2 scheme solves the one-dimensinal conservative equation

$$\frac{\partial f}{\partial t} + \frac{\partial (uf)}{\partial x} = 0, \tag{7.16}$$

where u is a variable now. Using the new value defined as $D \equiv \int f dx$, it is found that the following equation corresponds to Eq. (7.16);

$$\frac{\partial D}{\partial t} + u\frac{\partial D}{\partial x} = 0. \tag{7.17}$$

Namely, the problem to solve the one-dimensional conservative equation comes down to a one-dimensional advection equation for $D \equiv \int f dx$. This procedure is exactly the same as that in Eq. (7.9), simply replacing f by D, together with Eq. (7.13), in which g is replaced by f. Thus the CIP procedure can be used for a pair of D and f instead of f and g.

The CIP scheme given in the previous subsection uses the value f and its first-order spatial derivative g at the computational grid points as constraints for constructing a profile inside the grid cell. The CIP-CSL2 scheme requires a new constraint of the value integrated over neighboring two grid points,

$$\sigma^n_{i-1/2} = \int_{x_{i-1}}^{x_i} f(x')dx', \tag{7.18}$$

where n indicates the time. The integrated value means the mass included between the grid points $i-1$ and i. The CIP-CSL2 scheme adopts a following profile function

$$\begin{aligned} D_i(x) &\equiv \int_{x_{i-1}}^{x} f(x')dx' \\ &= A(x-x_{i-1})^3 + B(x-x_{i-1})^2 + f_{i-1}(x-x_{i-1}), \end{aligned} \tag{7.19}$$

where

$$\begin{aligned} A &= \frac{f_{i-1}^n + f_i^n}{\Delta x^2} - \frac{2\sigma_{i-1/2}^n}{\Delta x^3}, \\ B &= -\frac{2f_{i-1}^n + f_i^n}{\Delta x} + \frac{3\sigma_{i-1/2}^n}{\Delta x^2}. \end{aligned} \tag{7.20}$$

The profile function $D_i(x)$ satisfies the following conditions;

$$D_i(x_i) = \sigma_{i-1/2}^n, \quad D_i(x_{i-1}) = 0, \quad \left.\frac{\partial D_i}{\partial x}\right|_{x_i} = f_i^n, \quad \text{and} \quad \left.\frac{\partial D_i}{\partial x}\right|_{x_{i-1}} = f_{i-1}^n. \tag{7.21}$$

The value of $\sigma_{i-1/2}$ at the next time step $n+1$ is given by considering the mass conservation. Integrating Eq. (7.16) by the spatial coordinate x among the grid points $i-1$ and i, we obtain

$$\frac{\partial \sigma_{i-1/2}}{\partial t} = (fu)_{i-1} - (fu)_i. \tag{7.22}$$

Moreover, using the finite difference method, we obtain

$$\sigma_{i-1/2}^{n+1} = \sigma_{i-1/2}^n + (fu\Delta t)_{i-1} - (fu\Delta t)_i, \tag{7.23}$$

where $(fu\Delta t)_i$ indicates the mass flux during the time duration Δt which moves from the cell $[i-1,\, i]$ to $[i,\, i+1]$. In the case of $u > 0$, the mass flux $fu\Delta t$ can be calculated by

$$(fu\Delta t)_i = \sigma_{i-1/2}^n - D_i(x_i - u_i\Delta t), \tag{7.24}$$

in which we assume that the velocity u_i remains constant during the time interval $t^{n+1} - t^n = \Delta t$.

The time evolution of f is given as well as the original CIP scheme, in which the g is evolved by Eq. (7.13). The value of f_i after calculating the advection

term is given as $\partial D_i/\partial x|_{x_i - u_i \Delta t}$. After the advection phase is calculated, the result of the advection phase is advanced to the value of the next time step f^{n+1} in the non-advection phase. The non-advection phase can be solved by the finite difference method as well as g in Eq. (7.13).

We can extent the CIP-CSL2 scheme to the oscillation preventing scheme by using a rational interpolation function (R-CIP-CSL2) as well as the original CIP scheme. Moreover, for the multi-dimensions, we can use a directional splitting technique to perform sequential one-dimensional advection in each direction as well as the original CIP method. The formulations for the oscillation preventing scheme and the multi-dimension can be shown in Nakamura et al. (2001).

7.2.3 Anti-Diffusion

As shown in Figure 7.2(e), the R-CIP-CSL2 scheme provides the excellent solution of the one-dimensional conservative equation. However, we would like to reduce the numerical diffusion in order to keep the shape interface between the molten droplet and the ambient gas. For the purpose, we introduce the anti-diffusion technique to the R-CIP-CSL2 scheme. The anti-diffusion technique introduced here is a kind of the mass re-distribution method.

Figure 7.3 briefly shows the basic idea of the anti-diffusion technique used in this study. Let's assume that the initial profile of σ has the shape discontinuity (a). In this panel, $\sigma_{\max 0}$ indicates the maximum value of the initial profile of σ. For example, $\sigma_{\max 0} = \Delta x$ when the maximum value of initial f is unity. If the numerical diffusion takes place, the discontinuity is losing its shapeliness (b). In order to recover the initial shape discontinuity, we re-distribute σ from the cell with small σ to with large one (c). Finally, the profile recovers the shape discontinuity (d). Notice that we need some limiter in order to avoid the over re-distribution (e).

In order to re-distribute σ appropriately, we have to decide the mass flux J_i in Fig. 7.3(c) appropriately. In this study, we choose to set J_i as

$$J_i = \alpha_i \times \mathrm{minmod}(S_{i-1}, S_i, S_{i+1}), \tag{7.25}$$

where the minimum modulus function is defined as

$$\mathrm{minmod}(a,b,c) = \begin{cases} \mathrm{sign}(a) \times \min(|a|,|b|,|c|), & \text{if } a,\ b, \text{ and } c \text{ have same sign,} \\ 0, & \text{otherwise,} \end{cases} \tag{7.26}$$

and

$$\mathrm{sign}(a) = \begin{cases} 1, & \text{if } a \geq 0, \\ -1, & \text{if } a < 0. \end{cases} \tag{7.27}$$

The function S_i indicates the difference of σ between the neighbor cells and is given as

$$S_i = \sigma_{i+1/2} - \sigma_{i-1/2}. \tag{7.28}$$

When the coefficient α_i is negative, Eq. (7.25) gives the mass flux from large-σ to small-σ. It is the concept of the normal diffusion. On the contrary, the positive α_i gives the mass flux from small-σ to large-σ. It is the concept of the anti-diffusion. In this study, we set the value of α_i as

$$\alpha_i = \begin{cases} -0.1, & \text{if } \sigma_{i-1/2} < 0 \text{ or } \sigma_{i-1/2} > \sigma_{\max 0} \text{ or } \sigma_{i+1/2} < 0 \text{ or } \sigma_{i+1/2} > \sigma_{\max 0}, \\ 0.1, & \text{otherwise.} \end{cases} \tag{7.29}$$

After the R-CIP-CSL2 procedure has finished, we take the anti-diffusion procedure and obtain

$$\sigma^{n+1}_{i+1/2} = \sigma^{n}_{i+1/2} + J_i - J_{i-1}. \tag{7.30}$$

It can be easily confirmed that the anti-diffusion procedure does not violate the mass conservation.

7.2.4 Pressure-Based Algorithm

The non-advection phases of the equation of motion and the equation of state are written as (see Eq. 7.1)

$$\frac{\partial \boldsymbol{u}}{\partial t} = -\frac{\boldsymbol{\nabla} p}{\rho} + \frac{\boldsymbol{Q}}{\rho}, \tag{7.31}$$

$$\frac{\partial p}{\partial t} = -\rho c_{\mathrm{s}}^2 \boldsymbol{\nabla} \cdot \boldsymbol{u}, \tag{7.32}$$

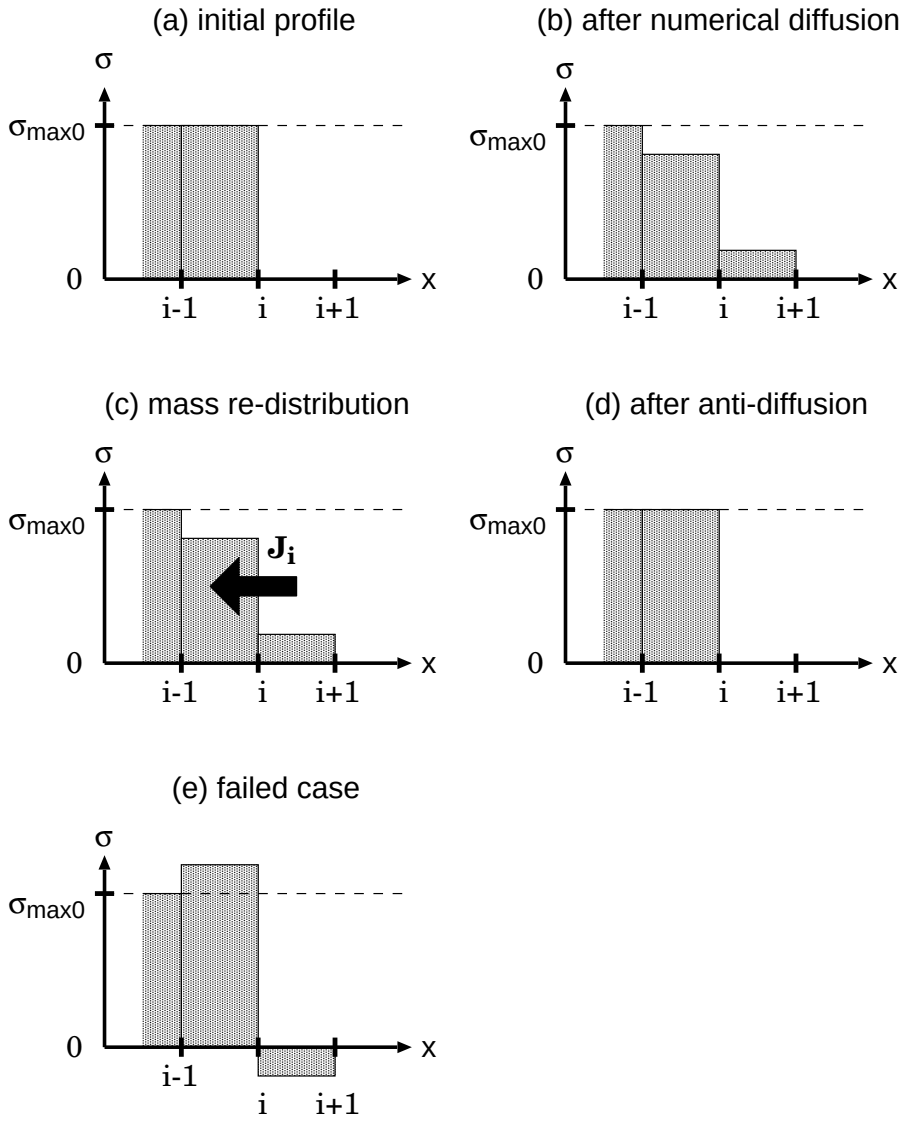

Figure 7.3: Sketch of the anti-diffusion technique.

where $\boldsymbol{Q}$ is the summation of the surface tension and the gas drag force (the viscosity term is neglected here). Using the finite difference method, we obtain

$$\frac{\boldsymbol{u}^* - \boldsymbol{u}^n}{\Delta t} = -\frac{\boldsymbol{\nabla} p^*}{\rho^n} + \frac{\boldsymbol{Q}}{\rho^n}, \tag{7.33}$$

$$\frac{p^* - p^n}{\Delta t} = -\rho^n c_{\mathrm{s}}^2 \boldsymbol{\nabla} \cdot \boldsymbol{u}^*, \tag{7.34}$$

where n and * indicate the times before and after calculating the non-advection phase, respectively. Since the sound speed can be very large in the incompressible fluid, the term related to the pressure should be solved implicitly. In order to obtain the implicit equations for p^*, we take the divergence of Eq. (7.33) and substitute $\boldsymbol{\nabla} \cdot \boldsymbol{u}^*$ into Eq. (7.34). Then we obtain an equation

$$\boldsymbol{\nabla} \cdot \left(\frac{\boldsymbol{\nabla} p^*}{\rho^n} \right) = \frac{p^* - p^n}{\rho^n c_{\mathrm{s}}^2 \Delta t^2} + \frac{\boldsymbol{\nabla} \cdot \boldsymbol{u}^n}{\Delta t} + \boldsymbol{\nabla} \cdot \left(\frac{\boldsymbol{Q}}{\rho^n} \right). \tag{7.35}$$

Using the finite difference method, Eq. (7.35) is written as

$$\begin{aligned}
&\frac{(p^*_{i+1,j,k} - p^*_{i,j,k})/\rho^n_{i+1/2,j,k} - (p^*_{i,j,k} - p^*_{i-1,j,k})/\rho^n_{i-1/2,j,k}}{\Delta x^2} \\
&+ \frac{(p^*_{i,j+1,k} - p^*_{i,j,k})/\rho^n_{i,j+1/2,k} - (p^*_{i,j,k} - p^*_{i,j-1,k})/\rho^n_{i,j-1/2,k}}{\Delta y^2} \\
&+ \frac{(p^*_{i,j,k+1} - p^*_{i,j,k})/\rho^n_{i,j,k+1/2} - (p^*_{i,j,k} - p^*_{i,j,k-1})/\rho^n_{i,j,k-1/2}}{\Delta z^2} \\
&= \frac{p^*_{i,j,k} - p^*_{i,j,k}}{\rho^n_{i,j,k} c_{\mathrm{s}}^2 \Delta t^2} + \frac{(\boldsymbol{\nabla} \cdot \boldsymbol{u}^n)_{i,j,k}}{\Delta t} + \boldsymbol{\nabla} \cdot \left(\frac{\boldsymbol{Q}}{\rho^n} \right)_{i,j,k},
\end{aligned} \tag{7.36}$$

where the densities on the grid edge as $\rho_{i+1/2,j,k}$ are given by taking the average of two grid-centered values as $\rho_{i+1/2,j,k} = (\rho_{i,j,k} + \rho_{i+1,j,k})/2$. The divergence of the velocity and the external force are given by the simple centered finite difference. The problem to solve Eq. (7.36) resolves itself into to solve a set of linear algebraic equations in which the coefficients become an asymmetric sparse matrix. In three-dimensional calculations, the dimension of the coefficient matrix becomes very large, so the most of computational time would consume to solve Eq. (7.36). In order to achieve a high computing performance, we adopt an incomplete LU preconditioned

conjugate gradient squared method to solve Eq. (7.36). After p^* is solved, we can calculate $\boldsymbol{u}^*$ by solving the equation of motion (Eq. 7.33).

Notice that we have to evolve the spatially differenced value g. The equation for evolving g can be obtained as follows. Differencing the non-advection term $f_i^* = f_i^n + H_i\Delta t$, we obtain $g_i^* = g_i^n + \partial_x H_i \Delta t$. On the contrary, using the finite difference method, we get another expression as $(f_{i+1}^* - f_{i-1}^*)/(2\Delta x) = (f_{i+1}^n - f_{i-1}^n)/(2\Delta x) + \partial_x H_i \Delta t$. Eliminating $\partial_x H_i$ from these two equations, we finally obtain

$$g_i^* = g_i^n + \frac{f_{i+1}^* - f_{i-1}^*}{2\Delta x} - \frac{f_{i+1}^n - f_{i-1}^n}{2\Delta t}. \tag{7.37}$$

7.2.5 Color Function

Treatment of the interface that lies between materials of different properties remains a formidable challenge to the computation of multiphase fluid dynamics (Yabe et al. 2001). Generally, Eulerian methods use color function to distinguish among regions containing different materials. Consider the molten droplet material occupying a certain area Z in the computational domain. We identify it with the color function $\phi_{i,j,k}$ according to the following definition:

$$\phi_{i,j,k} = \begin{cases} 1, & (i,j,k) \in \mathrm{Z}, \\ 0, & \text{otherwise.} \end{cases} \tag{7.38}$$

The time evolution of ϕ is solved by the CIP-CSL2 scheme (Section 7.2.2) substituting ϕ into f, so the integrated value of ϕ are conserved accurately. Although the value of ϕ can be larger than unity or smaller than zero if the velocity field has some divergence ($\boldsymbol{\nabla} \cdot \boldsymbol{u} < 0$ or $\boldsymbol{\nabla} \cdot \boldsymbol{u} > 0$), it is possible to suppress the overshoot or undershoot by a combination with the anti-diffusion method (Section 7.2.3). Using the color function, the density of the grid point (i,j,k) is given by

$$\rho_{i,j,k} = \phi_{i,j,k}\rho_l + (1 - \phi_{i,j,k})\rho_g, \tag{7.39}$$

where ρ_l and ρ_g are the density of the molten droplet material and the ambient gas, respectively.

7.2.6 Surface Tension

The surface tension is the normal force per unit interfacial area. Brackbill et al. (1992) introduced a method to treat the surface tension as a volume force by replacing the discontinuous interface to the transition region which has some width. According to them, the surface tension is expressed as

$$\boldsymbol{F}_{\mathrm{s}} = \gamma\kappa\boldsymbol{\nabla}\phi/[\phi], \tag{7.40}$$

where γ is the surface tension coefficient, κ is the local surface curvature, ϕ is the color function, and $[\phi]$ is the jump in color (in our definition, $[\phi] = 1$). The curvature is given by

$$\kappa = -(\boldsymbol{\nabla}\cdot\hat{\boldsymbol{n}}), \tag{7.41}$$

where

$$\hat{\boldsymbol{n}} = \boldsymbol{\nabla}\phi/|\boldsymbol{\nabla}\phi|. \tag{7.42}$$

Using the finite difference method for Eq. (7.41), the curvature κ is calculated by

$$\kappa_{i,j,k} = -\Big(\frac{\hat{n}_{xi+1/2,j,k} - \hat{n}_{xi-1/2,j,k}}{\Delta x} + \frac{\hat{n}_{yi,j+1/2,k} - \hat{n}_{yi,j-1/2,k}}{\Delta y} + \frac{\hat{n}_{zi,j,k+1/2} - \hat{n}_{zi,j,k-1/2}}{\Delta z}\Big). \tag{7.43}$$

Finally, calculating $\boldsymbol{\nabla}\phi$ at each grid point and substituting it into Eqs. (7.40) and (7.43), we obtain the surface tension $\boldsymbol{F}_{\mathrm{s}}$.

7.2.7 Gas Drag Force

The ambient gas flow does not follow the fluid equations because the mean free path of the gas molecules is much greater than the typical size of the droplet. The condition corresponds to a free molecular flow in which molecules scattered and reemitted from the droplet surface do not disturb the free stream velocity distribution. Therefore, in our model, it is assumed that the ambient gas does not flow against the droplet, and the gas drag force is explicitly given by Eq. (7.6). In this subsection, we explain the numerical model for the gas drag force.

Figure 7.1 briefly shows the numerical model for the gas drag force. Since the gas flow behaves the free molecular flow, the stream of the gas molecules which does not

collide to the molten droplet is not disturbed. The gas molecular flow terminates when it collides with the droplet surface. Since a decrease of the momentum of the gas molecular flow per unit length corresponds to the gas drag force acting on the droplet per unit volume, we obtain

$$F_{\rm gas} = -\frac{\partial}{\partial x'}(\rho v^2), \tag{7.44}$$

where $F_{\rm gas}$ is the x'-component of the gas drag force, ρ is the gas density, and v is the velocity of the gas molecular flow against the droplet. Using the finite difference method, we obtain

$$F_{{\rm gas},i} = \frac{(\rho v^2)_{i-1} - (\rho v^2)_i}{\Delta x'}. \tag{7.45}$$

The momentum flux ρv^2 takes the initial value of $p_{\rm fm} = (\rho v^2)_0$ at the upper stream. The value at the lower stream point is determined by the explicit formula

$$(\rho v^2)_i = (\rho v^2)_{i-1} - (\rho v^2)_0 \times \max[0, (\phi_i - \phi_{i-1})], \tag{7.46}$$

where ϕ is the color function, $\phi = 1$ ($\phi = 0$) indicates that the grid point is in the molten droplet (the ambient region). When ϕ increases with x', namely, when the gas molecular flow collides at the droplet surface, ρv^2 decreases with x' and vanishes at the point where ϕ becomes unity (notice that ϕ is 0 at the upper stream point). On the contrary, when ϕ decreases, namely, when the droplet surface does not face to the gas molecular flow, ρv^2 does not change with x' and the gas drag force does not work at the point. We calculate the spatial distribution of ρv^2 at every points in the coordinate (x', y', z'). Then, the gas drag force can be obtained by using Eq. (7.45).

Even if the droplet is rotating, we can get the gas drag force with almost the same procedure (see Fig. 7.1b). First, we re-distribute ϕ in the coordinate (x, y, z) to (x', y', z'). Second, we obtain the gas drag force $F_{\rm gas}$ in the coordinate (x', y', z'). Finally, we just re-distribute $F_{\rm gas}$ to the coordinate (x, y, z).

7.2.8 Smoothing

We can obtain the numerical results keeping the shape interface between the droplet and the ambient region. However, the smooth interface is suitable for calculating

the smooth surface tension. We take a smoothing filter only at the time to calculate the surface tension and the gas drag force. The value of the color function ϕ after the smoothing is given as

$$\begin{aligned}
\bar{\phi} &= \frac{1}{2}\rho_{i,j,k} + \frac{1}{2}\frac{1}{1+6C_1+12C_2+8C_3} \\
&\times [\phi_{i,j,k} + C_1(\phi_{i-1,j,k} + \phi_{i+1,j,k} + \phi_{i,j-1,k} + \phi_{i,j+1,k} + \phi_{i,j,k-1} \\
&+ \phi_{i,j,k+1}) + C_2(\phi_{i-1,j-1,k} + \phi_{i-1,j+1,k} + \phi_{i+1,j-1,k} + \phi_{i+1,j+1,k} + \phi_{i-1,j,k-1} \\
&+ \phi_{i-1,j,k+1} + \phi_{i+1,j,k-1} + \phi_{i+1,j,k+1} + \phi_{i,j-1,k-1} + \phi_{i,j-1,k+1} + \phi_{i,j+1,k-1} \\
&+ \phi_{i,j+1,k+1}) + C_3(\phi_{i-1,j-1,k-1} + \phi_{i-1,j-1,k+1} + \phi_{i-1,j+1,k-1} + \phi_{i-1,j+1,k+1} \\
&+ \phi_{i+1,j-1,k-1} + \phi_{i+1,j-1,k+1} + \phi_{i+1,j+1,k-1} + \phi_{i+1,j+1,k+1})] \qquad (7.47)
\end{aligned}$$

where

$$C_1 = 1/(6 + 12/\sqrt{2} + 8/\sqrt{3}), \quad C_2 = C_1/\sqrt{2}, \quad C_3 = C_1/\sqrt{3}. \qquad (7.48)$$

We iterate the smoothing five times. Then we obtain the smooth transition region of about twice grid interval width. We use the smooth profile of ϕ only when calculating the surface tension and the gas drag force, and the original profile with the shape interface is not changed.

7.2.9 Procedures

Figure 7.4 briefly shows the procedures of numerical simulations. Let's assume that the variables at the time step n are given (p^n, $\boldsymbol{u}^n$, σ^n, ϕ^n, and ρ^n). First, we solve the non-advection phase of p and $\boldsymbol{u}$ using the pressure-based algorithm and the equation of motion. Then, we solve the advection phase of p and $\boldsymbol{u}$ by the R-CIP method, and σ and ϕ by the R-CIP-CSL2 scheme. Finally, we convert ϕ^{n+1} to ρ^{n+1} as $\rho^{n+1} = \phi^{n+1}\rho_l + (1-\phi^{n+1})\rho_g$, where ρ_l and ρ_g are the density of the material composing the chondrules and the ambient gas, respectively. Additionally, we adopt the staggered grid for digitizing the physical variables in the hydrodynamic equations (see Figure 7.5). The scalar variables are defined at the cell-center and the velocity $\boldsymbol{u} = (u, v, w)$ is defined on the cell-edge. The external force like the surface tension and the gas drag force are defined at the cell-center.

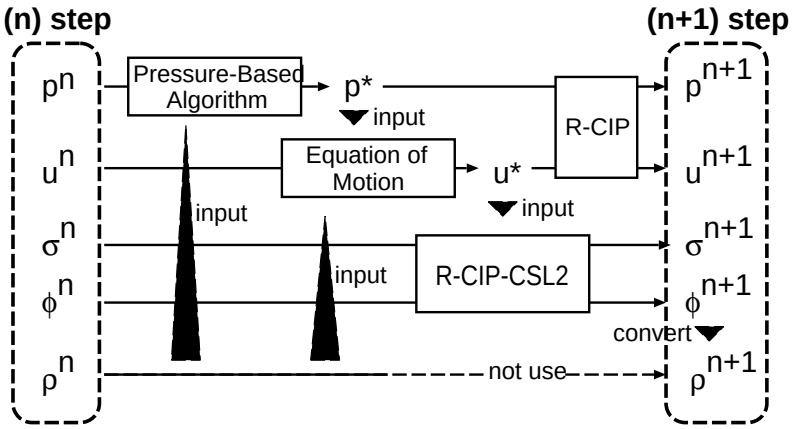

Figure 7.4: The procedures to obtain the variables at the next time step $n+1$ from the previous time step n.

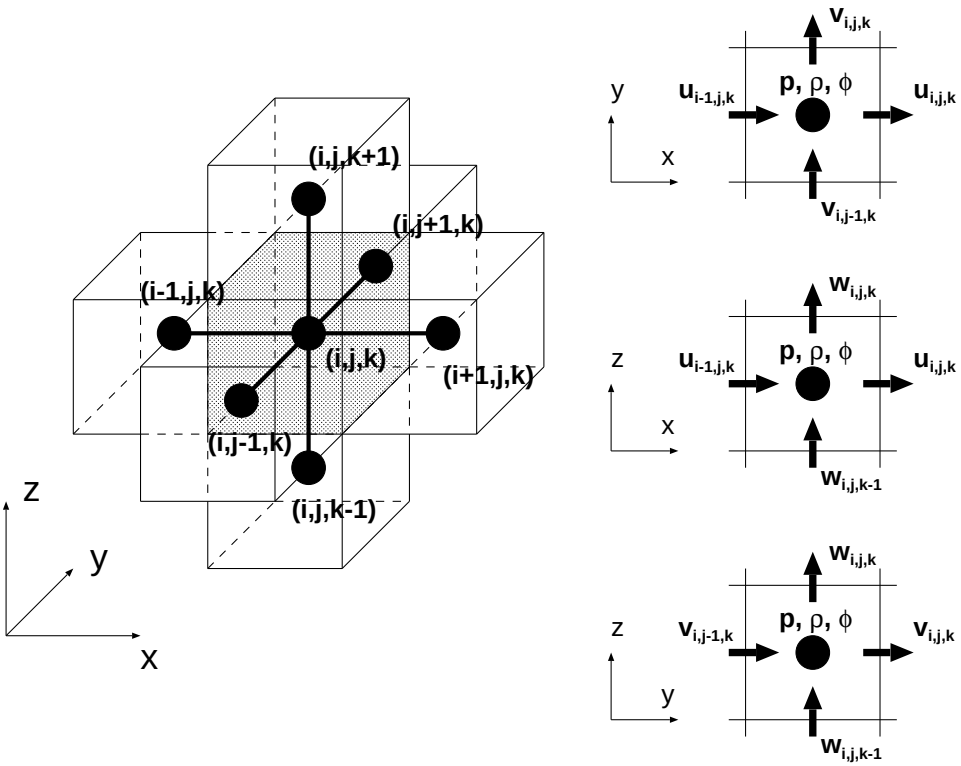

Figure 7.5: The staggered grid adopted in this study. The scalar variables are defined at the cell-center and the velocity $\boldsymbol{u} = (u, v, w)$ is defined on the cell-edge. The external force like the surface tension and the gas drag force are defined at the cell-center.

Chapter 8

Deformation due to Gas Drag Force

We show our calculation results of the non-rotating molten droplet exposed to the high-speed rarefied gas flow. Sekiya et al. (2003) analytically solved the hydrodynamical equations of molten droplets assuming that the non-linear terms of the hydrodynamical equations as well as the surface deformation are sufficiently small so that linearized equations are appropriate. On the contrary, the hydrodynamics when the droplet deforms significantly would play an important role in the shock-wave heating model, e.g., the fragmentation of the droplet and the maximum size of chondrules are limited (Susa & Nakamoto 2002).

In this chapter, we numerically simulate the molten droplet exposed to the high-velocity gas flow when the droplet does not rotate.

8.1 Input Parameters and Initial Settings

We investigate various cases about the droplet radius. Other input parameters are listed in Table 8.1.

Table 8.1: Input physical parameters for simulations of molten droplet exposed to the gas flow.

parameters	sign	value	reference
Ram Pressure	$p_{\rm fm}$	4000 dyne cm^{-2}	high-density shock (Fig. 2.4)
		1000 dyne cm^{-2}	low-density shock (Fig. 2.4)
Surface Tension	γ	400 dyne cm^{-1}	Murase & McBirney (1973)
Viscosity	μ	1.3 poises	Uesugi et al. (2003)
Density of Droplet	ρ_l	3 g cm^{-3}	typical silicate value
Density of Ambient	ρ_g	10^{-6} g cm^{-3}	ambient region (nebula gas)

Figure 8.1 is the example of the snapshot of the calculation results in the section of xy-plane. The horizontal and vertical axes are the x- and y-axes normalized by the unperturbed droplet radius r_0. The gas flow comes from the left side of the figure. The color contour indicates the hydrostatic pressure p in the unit of dyne cm^{-2} and the arrows are the velocity field. The red curves indicate the contour of the color function ϕ after smoothing. Thick solid curve indicates the value of $\phi = 0.5$, which means the interface between the droplet and the ambient region, and the dashed and the dotted-dashed curves are the values of $\phi = 0.1$ and 0.9, which are drawn in order to show the effective width of the transition region between the molten droplet and the ambient region.

The value of the color function $\phi_{i,j,k}$ is 1 for the molten droplet and 0 for the ambient region. Initially, we set $\phi_{i,j,k} = 1$ for $r < r_0 - \Delta r/2$ and $\phi_{i,j,k} = 0$ for $r > r_0 + \Delta r/2$, where r is the distance from the origin of the coordinate system and Δr indicates the width of the transition region between the droplet and the ambient region and we set $\Delta r = 2.5\Delta x$. The profile of ϕ in the transition region is assumed

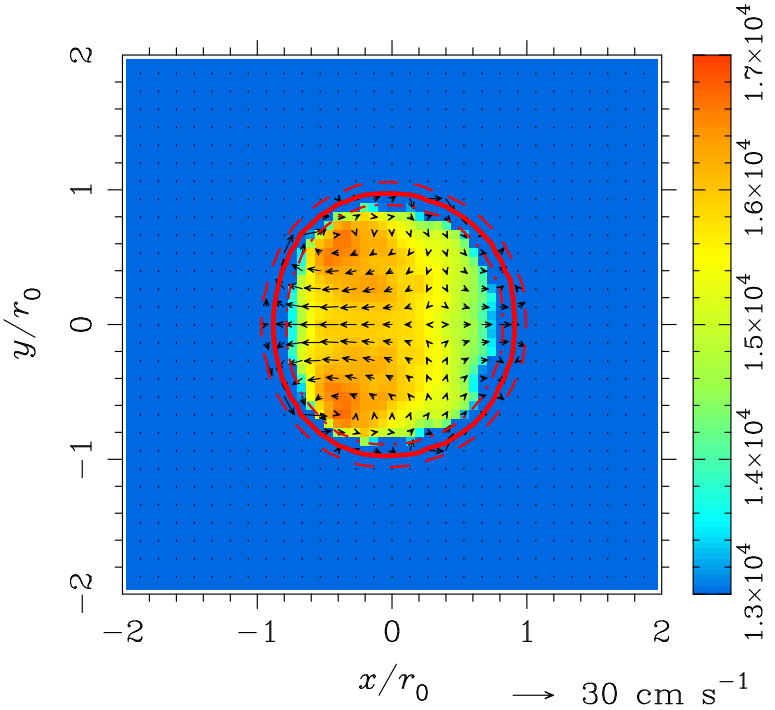

Figure 8.1: The snap shot of the simulation result of the molten droplet exposed to the gas flow. The figure is the section of xy-plane and the both axes are normalized by the unperturbed droplet radius r_0. The gas flow comes from the left side. The color contour indicates the hydrostatic pressure p in the unit of dyne cm^{-2}. The red curves are the contour of the color function ϕ of 0.1 (dashed curve), 0.5 (thick solid curve), and 0.9 (dashed dotted curve), respectively. The arrows express the velocity field.

to be

$$\phi_{i,j,k} = \frac{1}{2}\Big(1 - \sin\Big[\frac{r - r_0}{\Delta r}\pi\Big]\Big), \quad \text{for } r_0 - \Delta r/2 \leq r \leq r_0 + \Delta r/2. \tag{8.1}$$

The hydrostatic pressure inside the droplet is higher than that of the ambient region due to the surface tension. In the case of a sphere, the pressure jump between the transition region is given as $\Delta p = 2\gamma/r_0$. So, we set the initial hydrostatic pressure to be $p = \phi\Delta p$. The initial velocity field $\boldsymbol{u}_{i,j,k}$ is set to be all zero. The density ρ can be determined by $\rho = \phi\rho_l + (1 - \phi)\rho_g$, where ρ_l is the density of the material composed to the droplet and ρ_g is the density of the ambient region. In the CIP-CSL2 scheme, we need to prepare the initial values of the integrated color functions between the grid points; $\sigma_x = \int \phi dx$, $\sigma_y = \int \phi dy$, $\sigma_z = \int \phi dz$, $\sigma_{xy} = \int\int \phi dxdy$, $\sigma_{yz} = \int\int \phi dydz$, $\sigma_{zx} = \int\int \phi dzdx$, and $\sigma_{xyz} = \int\int\int \phi dxdydz$. We can determine these values from $\phi_{i,j,k}$ by the finite difference method. The computational grid points are set to be $60 \times 60 \times 60$.

8.2 Vibrational Motion

Figure 8.2 shows the time evolution of molten droplet exposed to the gas flow. The unperturbed droplet radius r_0 is set as $500\,\mu$m. In this case, since the ram pressure is not so strong comparing the surface tension, the droplet does not undergo the fragmentation. A panel (a) shows the initial condition for the calculation. The gas flow is coming from the left side to the right side. The panel (b) shows the results after 1.0 msec. The left side of the droplet is directly facing the gas flow, so the hydrostatic pressure at the left side becomes higher than that of the opposite side. The fluid elements at the surface layer are blown to the downstream, but the inner velocity is facing upstream because the apparent gravitational acceleration takes place. The droplet continues to deform more and more, and after 2.1 msec, the magnitude of the deformation is maximum. After that, the droplet begins to recover its shape to the sphere due to the surface tension. The panel (e) shows the shape on a way to the recover, and the recover motion is all but almost over at the panel (f). The droplet would repeat the deformation by the gas drag force and the

recovery motion by the surface tension until the vibrational motion is dumped due to the viscosity.

8.3 Deformation at Steady State

As shown in Figure 8.2, the droplet exposed to the gas flow shows the vibrational motion; deformation by the gas drag force and recovery motion by the surface tension. It is expected that the vibrational motion ceases by the viscous dissipation and finally settles to a steady state. In order to show that, we plot the time evolution of the axial ratio C/B, where C and B are the minor axis and middle-length axis in the three-axial ellipsoid, respectively. In the case of Fig. 8.2, C and B correspond to the x- and y-axes of the droplet.

Figure 8.3 shows the time evolution of the axial ratios C/B for various radii of the droplet. The horizontal axis is the time after the gas drag force begins to act on the droplet. The solid curves are the computational results and the dashed curves indicate the time-averaged values calculated as

$$(\mathrm{C/B})_{\mathrm{ave}} \equiv \frac{\int (\mathrm{C/B}) t dt}{\int t dt}, \tag{8.2}$$

and the interval of the integration about t is from 0 to the final time step of the calculation. Although some time evolutions shown in Fig. 8.3 indicate that the vibrational motions do not terminate at the end of each simulation, the time-averaged values seem to show the axial ratio C/B at the final steady states. Then, we compared these time-averaged axial ratios with the analytical solutions derived by Sekiya et al. (2003), which describes the steady state of the droplet exposed to the gas flow.

Figure 8.4 shows the comparisons of the time-averaged axial ratio (filled circles) with the analytic solutions (solid curve). The horizontal axis is the initial droplet radius r_0 and the vertical axis is the axial ratio C/B. We calculate the droplet axes of the analytic solutions as $\mathrm{C} = (r_s(0) + r_s(\pi))/2$ and $\mathrm{B} = r_s(\pi/2)$, respectively, where $r_s(\theta)$ is the radius of the droplet as a function of the angle between the stream line of the gas flow θ ($\theta = 0$ is the direction facing upstream). The dashed curve is a simple extrapolation of the analytic solutions. If $r_0 \gtrsim 358\,\mu$m, the analytic

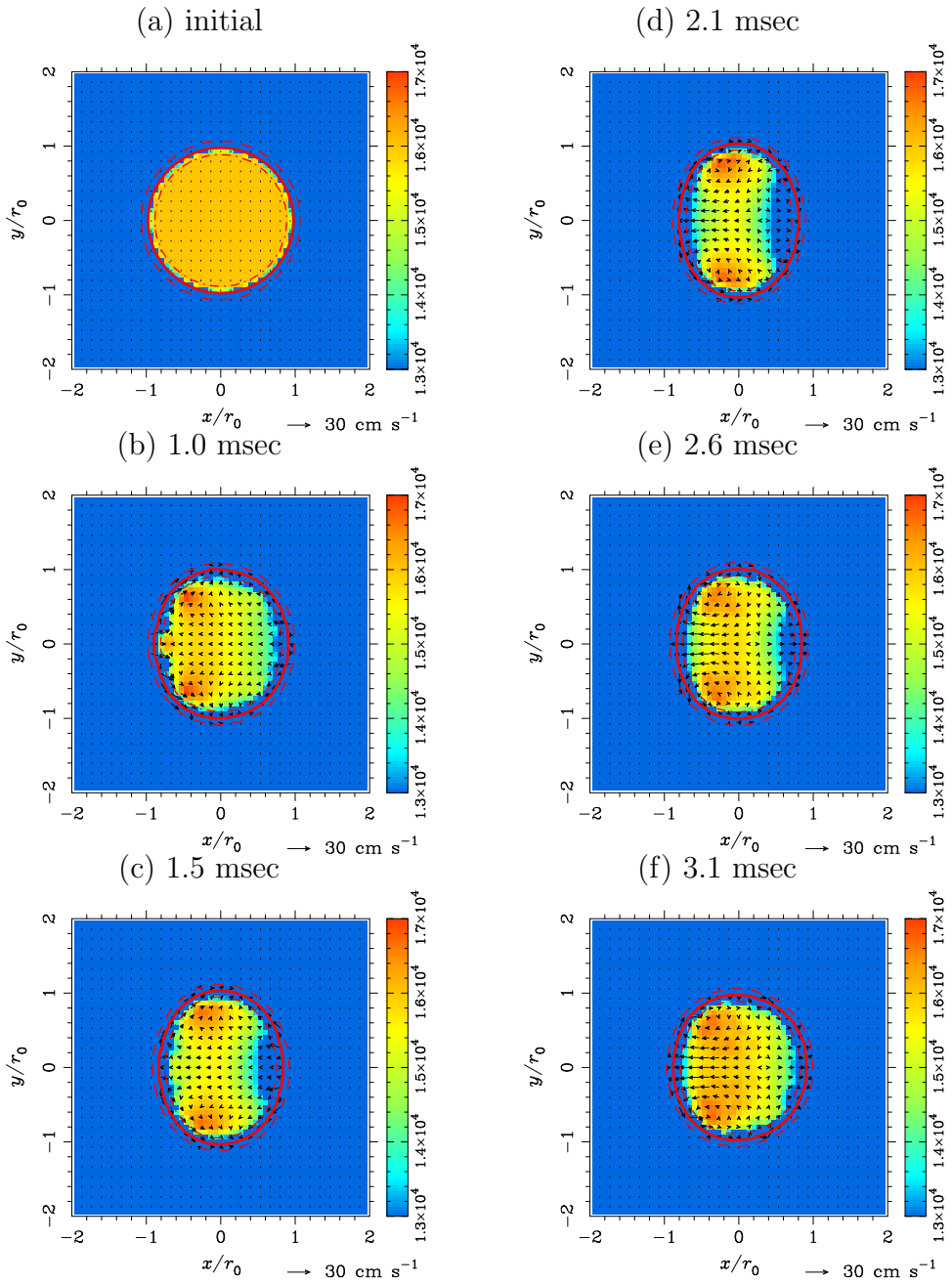

Figure 8.2: Time evolution of molten droplet exposed to the gas flow. The initial droplet radius is $r_0 = 500\,\mu$m (it corresponds to the Weber number $W_e = 0.5$).

solutions of Sekiya et al. (2003) cannot be applied because the Reynolds number R_e exceeds unity (see section 6.3). It is found that the time-averaged values of C/B seem to show a good agreements not only at the radius range in which the analytic solutions can be applied but also out of the range ($r_0 \lesssim 1000\,\mu$m). If the radius exceeds about $1000\,\mu$m, the effects of the non-linear terms of the hydrodynamical equations appear in the simulation results. The result of $r_0 = 2000\,\mu$m (panel e), in which the vibrational motion almost terminates and the droplet shape settles to the steady state, shows the slightly different value of C/B comparing with the extrapolation of the analytic solutions. The result of $r_0 = 5000\,\mu$m is apart from the extrapolation of the analytic solutions. As shown in the panel (f), the droplet once deforms significantly around $t \simeq 50\,$msec, then the surface tension recovers its shape to the initial shape. Although this behavior is also shown in other panels, the case of the panel (f) does not undergo the vibrational motion around the time-averaged value of C/B. After the first recovery motion, the droplet shape does not deform again. At the end of this calculation, the droplet settles around C/B $\simeq 0.9$ with a slightly large scatter. In the next subsection, we show the hydrodynamics of the droplet with $r_0 = 5000\,\mu$m.

8.4 Cavitation

We show the hydrodynamics of largely deformed droplet in this subsection. In Fig. 8.4, we found that the axial ratio C/B of the droplet of $r_0 = 5000\,\mu$m is apart from the extrapolation of the analytic solution by Sekiya et al. (2003). Sekiya et al. (2003) assumed that the non-linear terms of the hydrodynamical equations as well as the surface deformation are sufficiently small. Therefore, it is thought that the difference origins the non-linear terms ignored in the analytic solutions.

Figure 8.5 shows the time evolution of the droplet for $r_0 = 5000\,\mu$m. It is found that the droplet deforms significantly around $t = 50\,$msec (panel b). The large amount of the fluid spreads out to the perpendicular direction of the gas flow ($y-$ and $z-$directions). Although the center of the flatten droplet becomes very thin, it does not fragment directly. The fluid blown out at once returns to the back of the

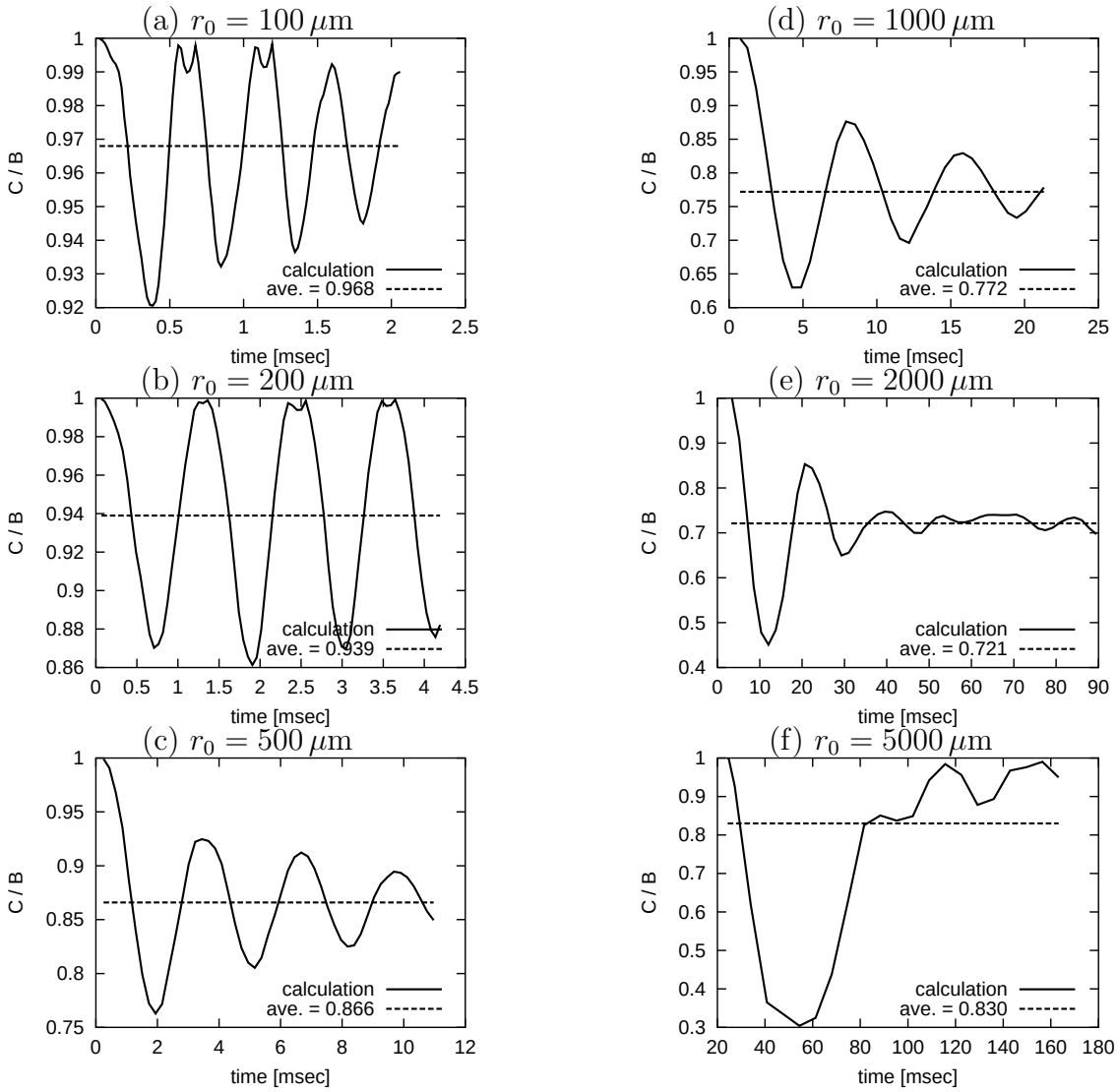

Figure 8.3: Time evolution of the axial ratio C/B for various radii. The horizontal axis is the time since the gas drag force begins to act on the droplet. The solid curves are the computational results and the dashed curves indicate the time-averaged values.

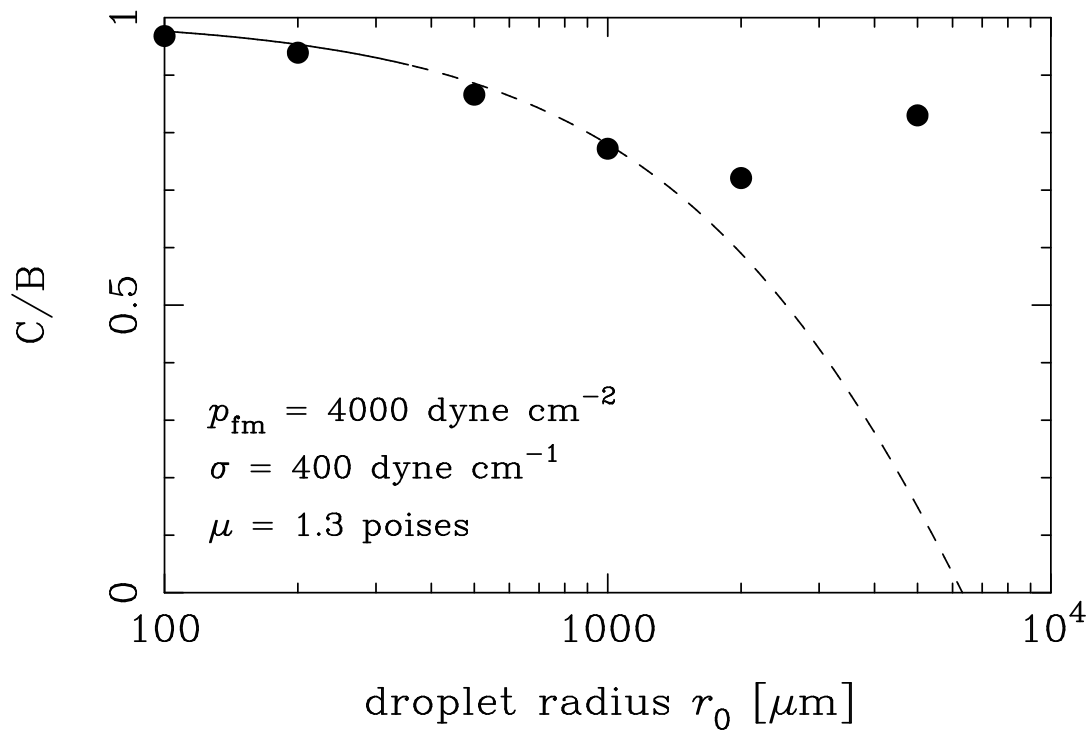

Figure 8.4: Time-averaged values of axial ratios C/B as a function of the unperturbed droplet radius r_0 (filled circles). The analytic solutions derived by Sekiya et al. (2003) are also displayed (solid curve). The dashed curve indicates a simple extrapolation of the analytic solutions.

droplet and gathers at the center (panel c). The center of the droplet at which the fluid elements gather becomes high pressure and the pressure gradient force pushes the fluid elements toward the downstream. As a result, the back of the droplet pops out (panel d). The bump gradually disappears with time, and finally, the droplet settles to almost the steady state with the internal flow largely circulating all around the droplet (panels e and f). In the phase, the hydrostatic pressure is high at the part which is directly facing the gas flow and extremely low around the center of eddies of the circulating internal fluid motion. The final pressure distribution is different qualitatively with the analytic solutions by Sekiya et al. (2003), in which the pressure at the left side of the droplet is relatively lower than that around $\theta \sim \pi/2$.

Here, we would like to point the behavior of the low-pressure region at the center of the eddies. Generally, the boiling (or vaporization) would take place in any liquids if the vapor pressure of the liquid exceeds its hydrostatic pressure inside. The vapor pressure of forsterite, which is one of the main components of chondrules, is only about 1 dyne cm^{-2} at $T_\mathrm{d} = 1850\,\mathrm{K}$ (Miura et al. 2002). Additionally, considering other volatile elements in the molt, the vapor pressure should be larger than that of pure forsterite. However, the hydrostatic pressure at the center of eddies is almost zero. Therefore, the boiling might occur at the center of eddies. The curling motion of the fluid just manages to be maintained by the pressure gradient around the low-pressure region. If the bubbles are generated at the center of eddies and it expands rapidly, the fluid elements around the eddies might scatter to all directions. If it occurs, the droplet would be destroyed and chondrules with the same mass with the precursor dust particles would not be formed.

Miura et al. (2002) discussed that the gas drag force produces the high-pressure environment in the molten droplet, and the effect is strong enough to suppress the boiling in it when the gas frictional heating is strong enough to melt the silicate dust particles. Although they did not take into account the hydrodynamics of the molten droplet. The cavitating fragmentation might be a new mechanism to explain the maximum size of chondrules like as the other mechanisms; the fragmentation due to the gas flow directly (Susa & Nakamoto 2002) or the stripping of the liquid

surface in the gas flow (Kato et al. 2005). To simulate the behavior of the bubbles generated in the liquids should be the challenging task, but we think that such kind of simulations is very important because of the existence of holes in some chondrules (e.g., Kondo et al. 1997). It should be taken into consideration in the future work.

8.5 Fragmentation

In the previous subsection, we discuss that the cavitation might cause the fragmentation of the droplet. Considering larger droplet, it would be destroyed directly by the gas drag force regardless the cavitation.

Figure 8.6 shows the time evolution of the droplet in the case of $r_0 = 2\,\mathrm{cm}$. In this simulation, we take a larger computational domain ($-3 < x/r_0 < 3$ and $-4 < y/r_0$ $(z/r_0) < 4$) than previous simulations in order to calculate the break-up phenomenon in wider region. The computational grid points are $60 \times 80 \times 80$. The panel (a) shows the initial state. After starting the simulation (panels b and c), the droplet deforms significantly as well as Fig. 8.5(b). The different point from Fig. 8.5 is that the fluid elements blown out due to the gas flow do not return to the back of the droplet. The stripped fluid elements begin to be distorted (panels d and e), and finally, the droplet break up into some small fragments (panel f).

We also show the three-dimensional views of above results in Figure 8.7. The panel (a) shows the droplet just before the fragmentations. The gas flow comes from the left side of the view along the x-axis. It is seen that the droplet deforms significantly. The panel (b) is after the fragmentations. We can see that the droplet breaks up to some small fragments. The reason why the fragmentations are not axis-symmetric is thought to be due to the dimension splitting technique for multi-dimensions in the Cartesian coordinate system. Therefore, we would not quantitatively discuss the sizes and number of the fragments. In order to do that, we might need higher spatial resolutions.

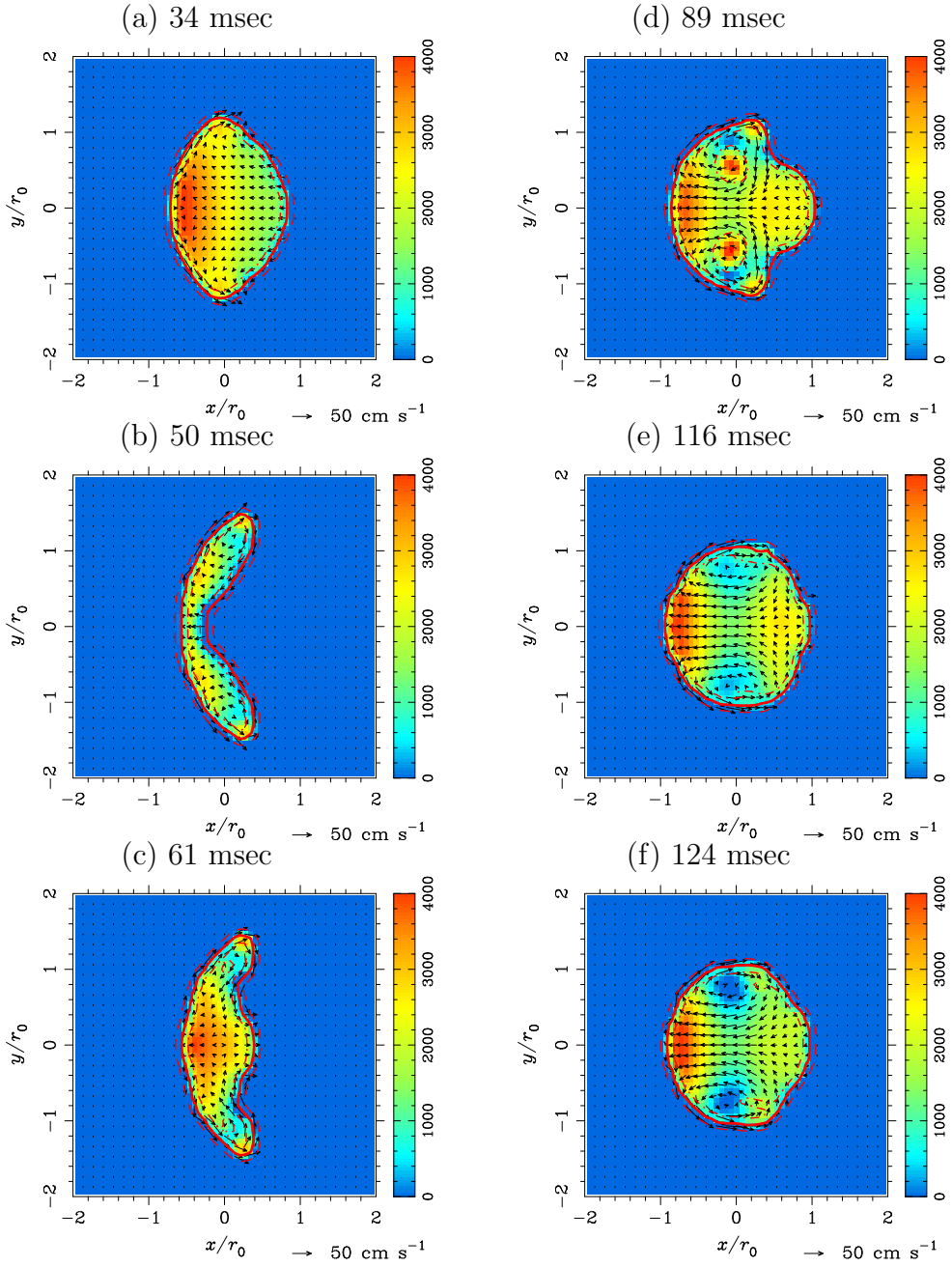

Figure 8.5: Same as Fig. 8.2 except for $r_0 = 5000\,\mu$m ($W_e = 5$).

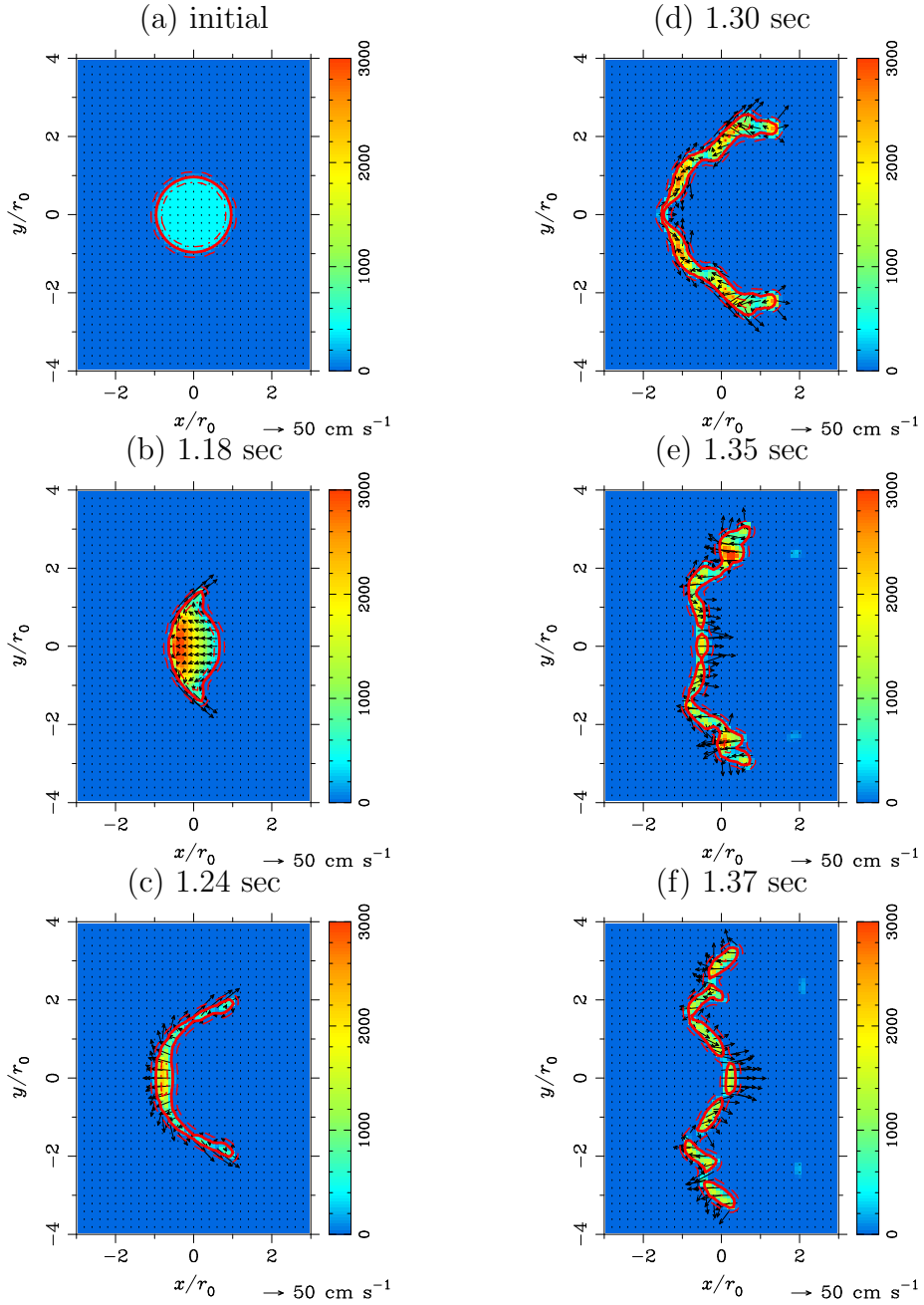

Figure 8.6: Same as Fig. 8.2 except for $r_0 = 2\,\mathrm{cm}$ ($W_e = 20$).

(a) 1.22 sec (b) 1.30 sec

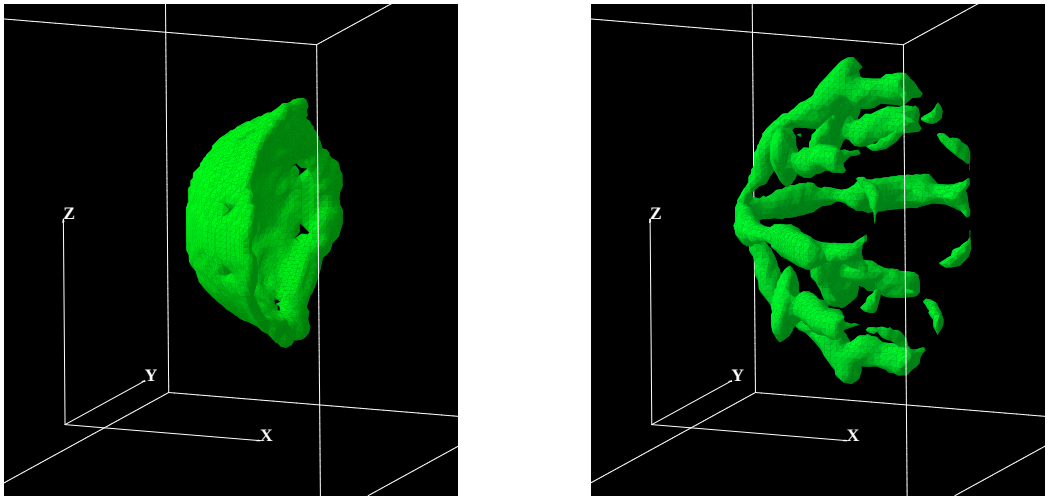

Figure 8.7: Three-dimensional views of the fragmentation of molten droplet.

8.6 Low-Density Shock Waves

We show the simulation results for the high-density shock waves, in which the ram pressure of the gas flow $p_{\rm fm} = 4000\,{\rm dyne\,cm^{-2}}$. The value of $p_{\rm fm}$ is determined by assuming that the gas number density of the pre-shock region is 10^{14} cm^{-3}, which corresponds to the mid-plane of the minimum mass solar nebula model at the distance to the central star $R \sim 1 - 3\,{\rm AU}$ (Hayashi et al. 1985). However, the shock waves which are generated at upper region of the protoplanetary disks have been also investigated; e.g., accretion of a clumpy cloud onto the protoplanetary disk (Tanaka et al. 1998) and the X-ray flare induced shock waves (Nakamoto et al. 2005). The ram pressure for such low-density shock waves can be estimated as $p_{\rm fm} \sim 1000\,{\rm dyne\,cm^{-2}}$ as shown in Fig. 2.4.

Figure 8.8 is the same as Fig. 8.4 except that we also draw the analytic solutions in the case of $p_{\rm fm} = 1000\,{\rm dyne\,cm^{-2}}$ (labeled as "low-density shock"). The meaning of the solid and dashed curves are the same as Fig. 8.4. The magnitude of the deformation is proportional to the Weber number ($W_e = p_{\rm fm} r_0/\gamma$), and the value of C/B for $r_0 = 500\,\mu$m is about 0.89 for the high-density shock waves and 0.97 for

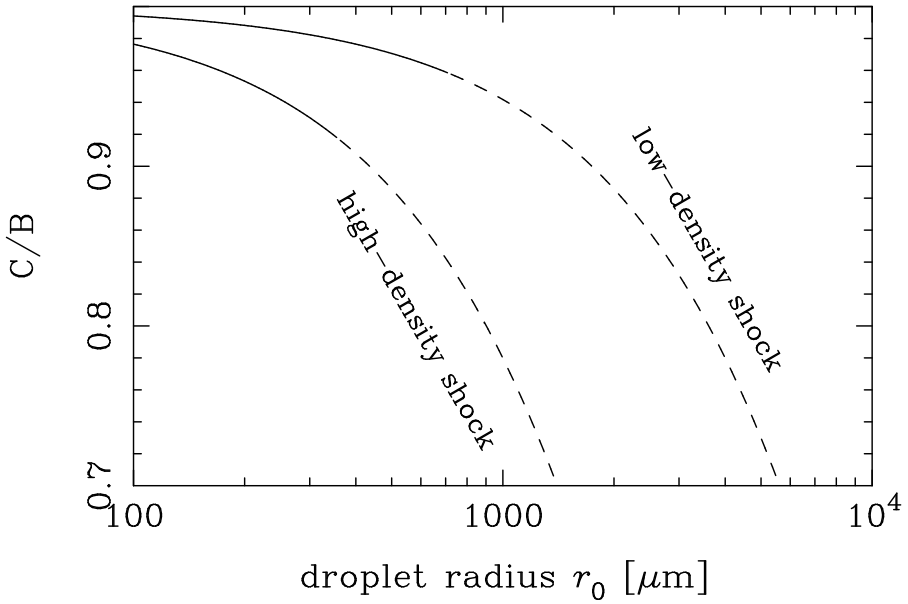

Figure 8.8: Same as Fig. 8.4 except that we also draw the analytic solutions in the case of $p_{\rm fm} = 1000\,{\rm dyne\,cm^{-2}}$ (labeled as "low-density shock").

the low-density shock waves. On the other hand, the group-A chondrules are in a range of $0.9 \lesssim {\rm C/B} \lesssim 1.0$. Therefore, the low-density shock waves might not be able to explain the deformation of the group-A chondrules if we assume the surface tension $\gamma = 400\,{\rm dyne\,cm^{-1}}$. In fact, the value of the surface tension of common igneous rock changes in a range of about $250 - 450\,{\rm dyne\,cm^{-1}}$ depending on the temperature and compositions. In order to discuss more quantitatively, the relation between the chondrule shapes and the physical properties of them should be considered.

8.7 Conclusions

We performed the hydrodynamical simulations of the molten silicate dust particles exposed to the high-velocity rarefied gas flow. The ram pressure of the gas flow was set to be $p_{\rm fm} = 4000\,{\rm dyne\,cm^{-2}}$ assuming the high-density shock waves (the pre-shock gas number density $n_0 \simeq 10^{14}\,{\rm cm^{-3}}$). The coefficient of viscosity of the droplet was set to be $\mu = 1.3$ poises assuming the well-molten droplets composed by silicates.

The value of the surface tension was assumed to be $\gamma = 400\,\mathrm{dyne\,cm^{-1}}$, which is the typical value for silicate melts. We calculated for various sized of droplets, the unperturbed radius is $200\,\mu\mathrm{m} - 2\,\mathrm{cm}$. We obtained following conclusions:

1. The droplet shape shows the vibrational motion before settling into the steady state; the deformation by the gas drag force and the recovery motion by the surface tension. It continues until the viscosity in the droplet dissipates the motion. When it settles into the steady state, the magnitude of the deformation well matches with the analytic solutions of Sekiya et al. (2003) for cases of $r_0 \lesssim 358\,\mu\mathrm{m}$, in which the analytic solutions can be applied. Moreover, we found that the good agreement between our simulations and the analytic solutions was also seen in the cases of $r_0 \lesssim 1000\,\mu\mathrm{m}$, in spite that the analytic solution cannot be applied because the Reynolds number R_e is greater than unity.

2. The non-linear terms of the hydrodynamical equations play an important role for $r_0 \gtrsim 5000\,\mu\mathrm{m}$ (Weber number $W_e \gtrsim 5$). In this case, the center of the circulating internal flow in droplets becomes extremely low pressure as the cavitation (foaming, bubble generation) might occur in the molten droplet.

3. The droplet is destroyed directly by the gas drag force if the radius is larger than 2 cm (Weber number $W_e \gtrsim 20$). In this case, the surface layer of the droplet is stripped away and it might produce a lot of smaller pieces of droplets. However, in order to discuss the physical properties of the small fragments (number, size distribution, velocity dispersion, and so forth) more quantitatively, higher spacial resolutions of simulations might be required.

Chapter 9

Shape Instability by Rapid Rotation

In this chapter, we consider the hydrodynamics of the rapidly rotating droplet when the gas drag force is absent. Such kind of simulations is motivated by the existence of prolate chondrules classified into the group-B (see Fig. 1.5). Tsuchiyama et al. (2003) suggested that the group-B chondrules might have been produced as a result of the shape instability of rapidly rotating droplets. In fact, Chandrasekhar (1965) found that the equilibrium shape of a rotating droplet is unstable if the non-dimensional parameter Σ exceeds a critical value (see section 6.2). However, it has not been investigated whether the droplet shape undergoing the shape instability really deforms to be a prolate, and whether the shape well matches with the group-B chondrules. In order to show the droplet shape undergoing the shape instability, we perform the simulations of rapidly rotating droplets.

9.1 Initial Settings

The initial settings for simulations are almost the same as the section 8 except for the initial droplet shape, the angular velocity of the coordinate system, and the computational grid points. We set the initial droplet shape is the equilibrium shape of a rotating droplet analytically derived by Chandrasekhar (1965). Then, in the section 8, the angular velocity of the coordinate system Ω is zero because we did not consider the rotation of droplets. Therefore, the Coriolis force and the centrifugal force did not appear in the hydrodynamical equations. In this section, since we assume the initially solid-rotating droplets with the angular velocity Ω, we consider the rotating coordinate system. The values of the input parameters are listed in Table 6.1. Finally, we set the computational grid points as $80 \times 80 \times 40$ because the rotation axis is the z-axis, so the wider computational region in the x- and y-directions are required than that of the z-direction.

9.2 Shape Instability

Figure 9.1 shows the time evolution of the rotating droplet in the section of xy-plane. The rotation axis is z-axis. The input parameters of label 5 in Table 6.1 are adopted. In this case, since the non-dimensional parameter Σ exceeds a critical value of 0.4587, the situation should be unstable and cause the shape instability. Panel (a) shows the initial state in which the droplet shape is given as the equilibrium shape of a rotating droplet. The velocity field is the counterclockwise solid rotation. After 0.8 msec (panel b), the hydrostatic pressure at the center of the droplet decreases due to the centrifugal force which works to make the droplet shape expanding toward the x- and y-directions. After 4.9 msec (panel c), it is found that the bar mode perturbation is growing and the droplet shape becomes like a prolate shape. The droplet elongates more and more with time (panel d). After 10.5 msec (panel e), the center of the droplet begins to be pinched. Finally, the droplet is separated away at the pinched point and fragments into two smaller droplets (panel f). After that, the two fragments are departing each other.

Figure 9.2 shows the case of $\Sigma = 1.7260$, in which the droplet rotates more rapidly

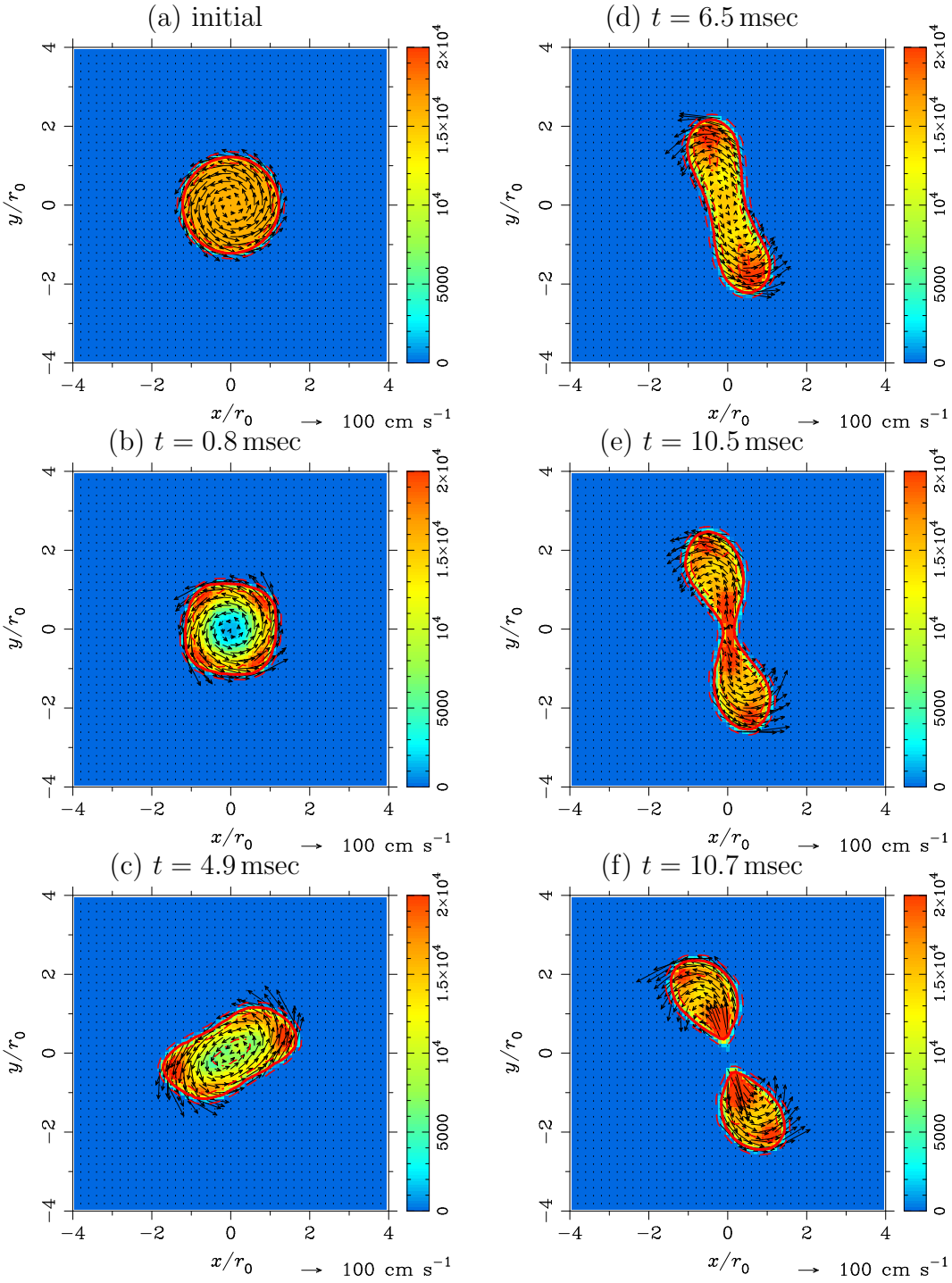

Figure 9.1: Time evolution of rotating droplet. The non-dimensional parameter $\Sigma = 1$ and it is unstable condition. The all data is edited to plot in the non-rotating coordinate system (x', y', z').

than Fig. 9.1. In this case, the droplet finally fragments into four pieces. The panel (a) shows the initial state. After $t = 0.7\,\mathrm{msec}$ (panel b), we can see a hole at the center of the droplet and a small residual piece is located at the center. The most fraction of the droplet is taken into the form of a torus shape. After $t = 1.2\,\mathrm{msec}$ (panel c), the torus is spreading outward and the small fragment located at the center is rotating separately. After $t = 1.9\,\mathrm{msec}$ (panel d), the torus begins to tear into four small pieces and finally separates away (panel e). After that, these pieces would go away to the each directions (panel f).

9.3 Comparison with Chondrules

In order to confirm the scenario that the group-B chondrules might have been formed as a result of the shape instability, we compare the droplet shapes of our simulation results with that of measured chondrules. Figure 9.3 shows the time sequences of shapes of rotating droplets on the B/A-C/B diagram. Solid curves indicate the simulation results for various values of Σ, $\Sigma = 0.51079$ (label 5), 1.0 (label 6), 1.7260 (label 7), and 2.0959 (label 8), respectively. Every cases we selected here are unstable when there are some dissipative mechanisms in the droplets. The origins of these time sequences are located on the axis of $\mathrm{B/A} = 1$ because the equilibrium shape of rotating droplet is oblate (Chandrasekhar 1965) and the initial values of C/B are about 0.65 (label 5), 0.45 (label 6), 0.30 (label 7), and 0.20 (label 8), respectively. We also display the data of chondrules measured by Tsuchiyama et al. (2003) by color filled circles (see Fig. 6.1). Besides that the droplets do not settle into the shape like as the group-B chondrules, they even do not pass through the region where the group-B chondrules are plotted. Therefore, we conclude that it is hard to form the group-B chondrules as a result of the shape instability.

The very short time scale of the shape instability is thought to be one of the disadvantages to explain the group-B chondrules. Even though the time sequence of the shape instability crosses the shapes of group-B chondrules, the droplet would be separated into two fragments before it re-solidifies to form chondrules, because the time scale of the shape instability is about a few tens milli-seconds at most and

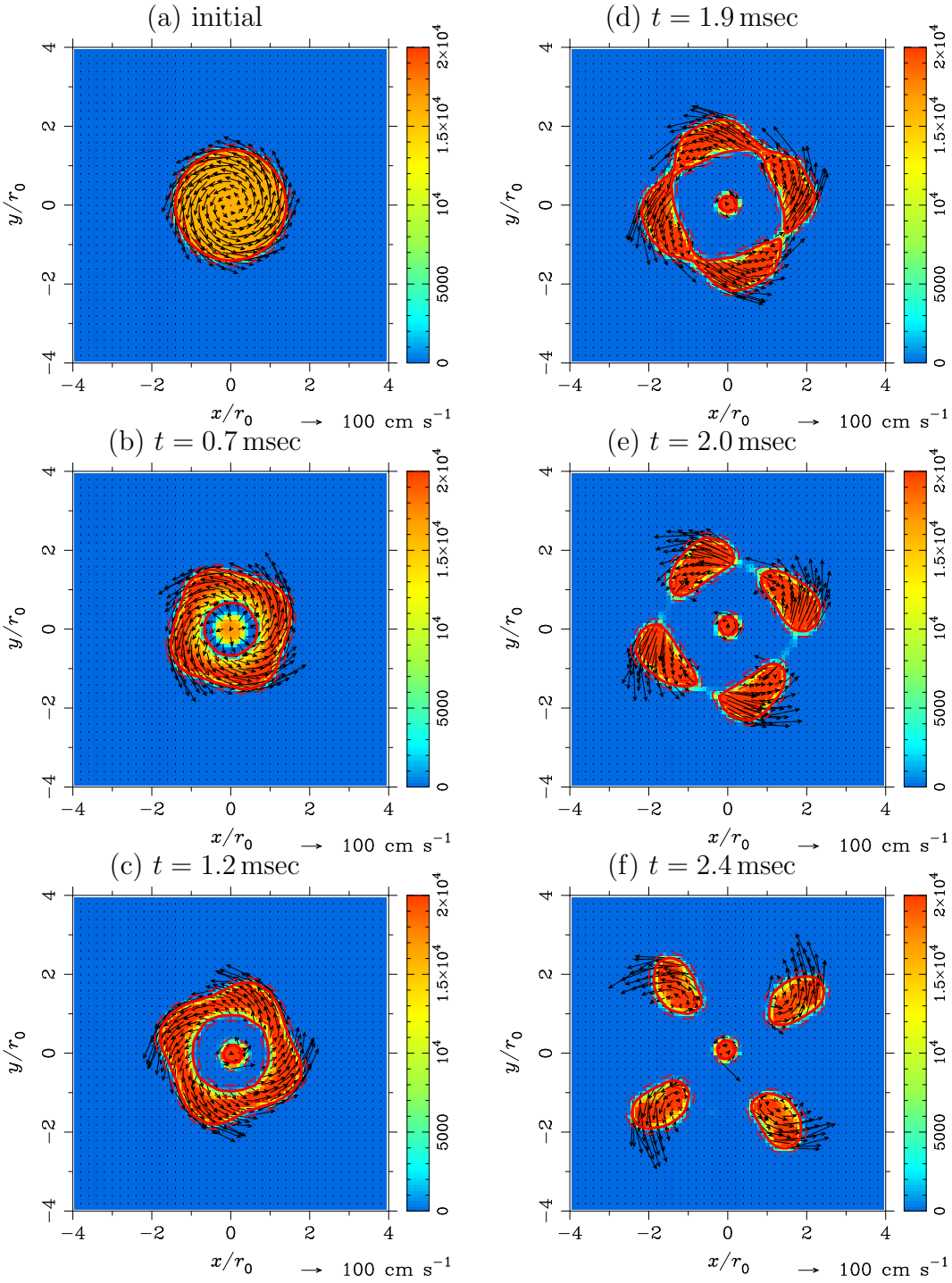

Figure 9.2: Same as Fig. 9.1 except for $\Sigma = 1.7260$.

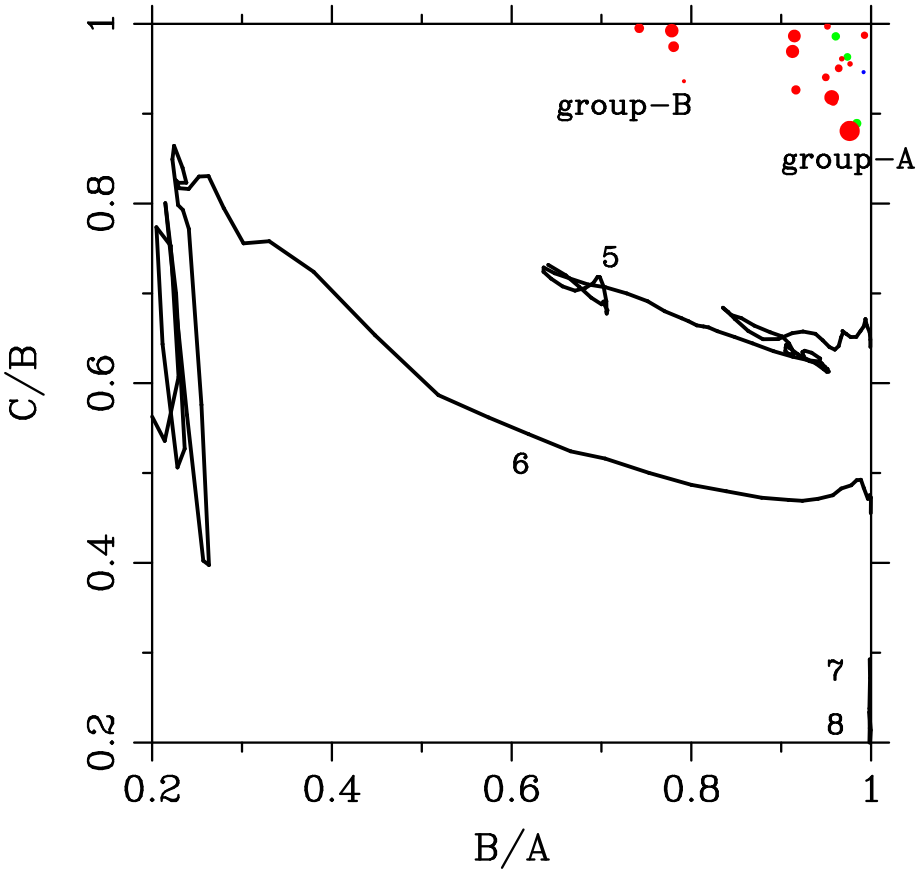

Figure 9.3: Time sequences of shapes of rotating droplets on the B/A-C/B diagram. The input parameters for each labeled curves and the same as in Table 6.1.

it is much shorter than the cooling time scale of the dust particles in the shock-wave heating model ($\sim 1-10\,\mathrm{sec}$). However, considering more viscous fluids as the molten droplets, the time scale of the shape instability will becomes longer and it might be possible to re-solidify before the droplet breaks up. Such viscous situation can be considered just before the droplets resolidified. In fact, significantly deformed shapes have been found in some cosmic spherules that melts when it becomes a meteoritic dust particles passing though the terrestrial atmosphere. Figure 9.4 shows the three-dimensional view of a dumbbell-shaped cosmic spherule (Tsuchiyama, priv. comm.). The shape seems to be similar to our simulation results (see Fig. 9.1b). Such irregular shape might have been formed as a result of the shape instability of rapidly rotating droplet in the cooling phase.

9.4 Conclusions

We performed the hydrodynamical simulations of rapidly rotating molten silicate dust particles when the gas drag force is absent. The coefficient of viscosity of the droplet was set to be $\mu = 1.3$ poises assuming the well-molten droplets composed by silicates. The value of the surface tension was assumed to be $\gamma = 400\,\mathrm{dyne\,cm^{-1}}$, which is the typical value for silicate melts. The initial shape of the droplet is assumed to be the equilibrium shape of rotating droplet with radius of $500\,\mu$m. We calculated for various values of the non-dimensional parameter Σ defined as $\Sigma \equiv \rho_{\mathrm{mat}}\Omega^2 a^3/(8\gamma)$, where ρ_{mat} is the density of droplet, Ω is the angular velocity, and a is the equatorial radius. We obtained following conclusions;

1. The shape instability took place when Σ exceeded a critical value 0.4587. The droplet which is initially oblate deforms to be a general three-axial ellipsoid as the unstable perturbation grows, and finally, it separates into two smaller fragments within a few tens milli-seconds. However, the time evolution of the droplet shape during the deformation does not cross the shapes of the group-B chondrules.

2. If the angular velocity is higher ($\Sigma \gtrsim 1.7260$), the droplet separated into four small fragments.

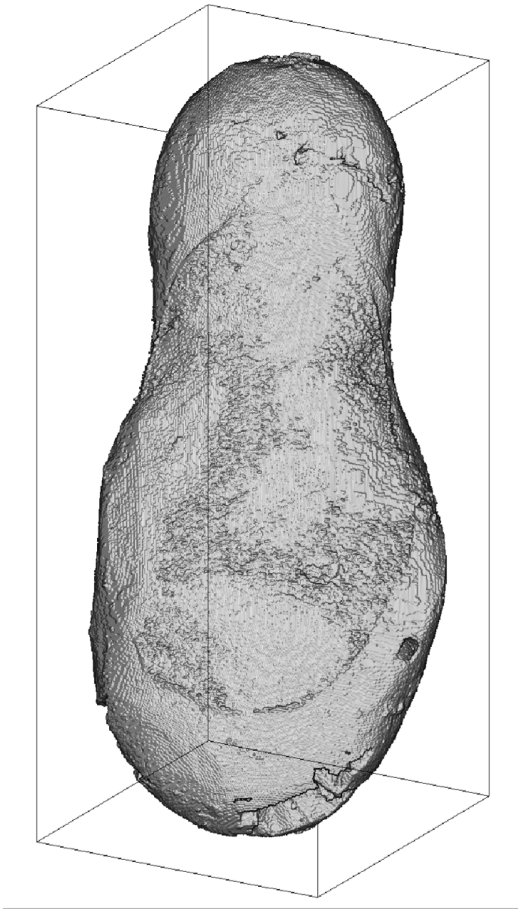

Figure 9.4: The three-dimensional view of a dumbbell-shaped cosmic spherule (Tsuchiyama, priv. comm.).

3. The time scale of the shape instability is much shorter than the cooling time scale of dust particles in the shock-wave heating model. However, if considering the more viscous fluid as the molten silicate particles (e.g., lower temperature than that we assumed in this study), the shape instability would take longer time until the droplet separates away. For example, the dumbbell-shaped cosmic spherule might have been formed as a result of the shape instability when passing though the terrestrial atmosphere.

Chapter 10

Rotating Droplet exposed to Gas Flow

In this section, we consider the rotating molten silicate dust particles exposed to the gas flow. In the shock-wave heating model, the situation that the molten droplet is rotating around the rotation axis which is perpendicular to the gas flow can be considered (see Chapter 6). In this case, the hydrodynamics of the droplets should be more complex than the cases that the rotation axis is parallel to the gas flow, in which the hydrodynamics becomes an axis-symmetrical as long as the shape instability does not take place (see Chapter 9). The difficulty of the three-dimensional hydrodynamical simulations for incompressible fluids might be one of the obstacles to investigate the droplet shape in such complex situations. Our numerical code for hydrodynamical simulations is applicable for the situations. We perform the hydrodynamical simulations of rotating droplet in the high-velocity gas flow.

10.1 Initial Settings

The initial settings for numerical simulations are almost the same as the section 9 except for the ram pressure and the initial droplet shape. We set the ram pressure as $p_{\rm fm} = 4000\,{\rm dyne\,cm^{-2}}$ assuming the high-density shock waves (see Table 8.1). The initial droplet shape assumed to be a perfect sphere which radius r_0. The initial angular velocity of the droplet Ω is given by Eq. (6.4). We calculate for various values of the initial droplet radius r_0 and the asymmetric parameter f. The input parameters are listed in Table 10.1.

Table 10.1: Input parameters of rotating droplets exposed to the gas flow.

r_0 [μm]	f	Ω [s^{-1}]	rotation rate [rps]	Σ	W_e
200	0.1	1401	223	0.015	0.2
200	0.2	1982	315	0.029	0.2
200	0.3	2427	386	0.044	0.2
200	0.4	1401	446	0.059	0.2
200	0.5	1401	499	0.074	0.2
500	0.1	560	89	0.037	0.5
500	0.2	793	126	0.074	0.5
500	0.3	971	155	0.110	0.5
500	0.4	1121	178	0.147	0.5
500	0.5	1253	199	0.184	0.5
1000	0.1	280	45	0.074	1.0
1000	0.2	396	63	0.147	1.0
1000	0.3	485	77	0.221	1.0
1000	0.4	560	89	0.294	1.0
1000	0.5	627	100	0.369	1.0

10.2 Prolate-Shaped Droplet

Figure 10.1 shows the time evolution for the case of $r_0 = 500\,\mu$m and $f = 0.3$. The left panels are the section of the xy-plane and the rights are of the xz-plane. The

top panels are the initial state (panels a1 and a2). The droplet initially rotates counterclockwise about the z-axis. The velocity field is a solid rotation. The middle panels are the snap shots at $t = 1.3\,\mathrm{msec}$ (panels b1 and b2). If not considering rotation, the droplet would simply elongate toward the y- and z-directions due to the gas drag force. However, since the droplet is rotating about the z-axis, the droplet does not elongate along the $z-$axis because the centrifugal force tends to elongate the droplet toward the x- and y-directions (panel b2). Moreover, the major axis of the droplet slightly inclines against the y-axis because of the effect of the rotation (panel b1). The inclined major axis indicates that the deformation and the internal flow of the droplet does not settle into a steady state. In fact, it is found that the major axis becomes parallel to the y-axis with time (panel c1). Notice that the final shape of the droplet seems to have the one major axis (y-axis) and other shorter two axes (x- and y-axes) which are almost the same length. This indicates the prolate shape. In order to confirm that, we show the time evolutions of axial ratios B/C and B/A in Figure 10.2. The horizontal axis is the time and the vertical one is the axial ratios. Before $t \simeq 2\,\mathrm{msec}$, the droplet shape seems not to settle into the steady state because the axial ratios are still evolving. After $t \simeq 2\,\mathrm{msec}$, the axial ratios are settling around about the values of B/C $\simeq 0.96$ and B/A $\simeq 0.88$. In this phase, it is easily confirmed that the droplet shape is kind of prolate. To summarize, we can naturally produce the prolate-shaped droplet by considering the both effects of the rotation and the gas drag force (panel c1 and c2).

10.3 Axial Ratios for Various Conditions

Figure 10.3 shows the time evolutions of the axial ratios C/B and B/A for various cases about the initial droplet radius r_0 of $200\,\mu$m (left), $500\,\mu$m (center), $1000\,\mu$m (right), and the asymmetric parameter f from 0.1 (top) to 0.5 (bottom). One filled circle in each panel corresponds to the result at a certain time and these circles are plotted at even intervals in time. The darker symbols indicate the later stages of the time evolutions. Therefore, if dark symbols concentrate at a certain point on the B/A-C/B diagram, it indicates that the droplets stay with the shapes for

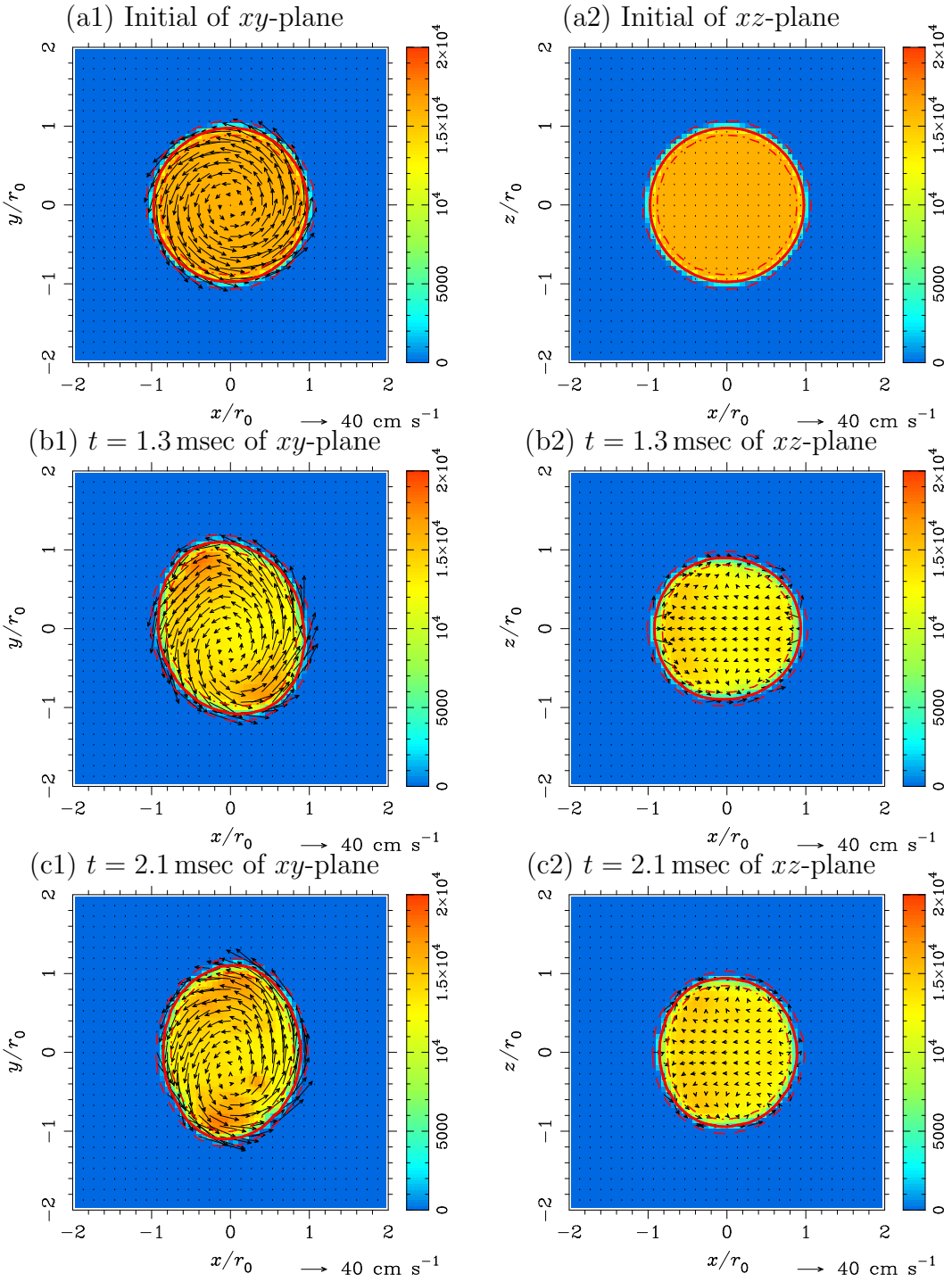

Figure 10.1: The time evolution of rotating droplet exposed to the gas flow for the case of the initial droplet radius $r_0 = 500\,\mu$m and the asymmetric parameter $f = 0.3$. The left panels are the section of the xy-plane and the right ones are of the xz-plane. The top panels are the initial states, middles are $t = 1.3$ msec, and bottoms are $t = 2.1$ msec.

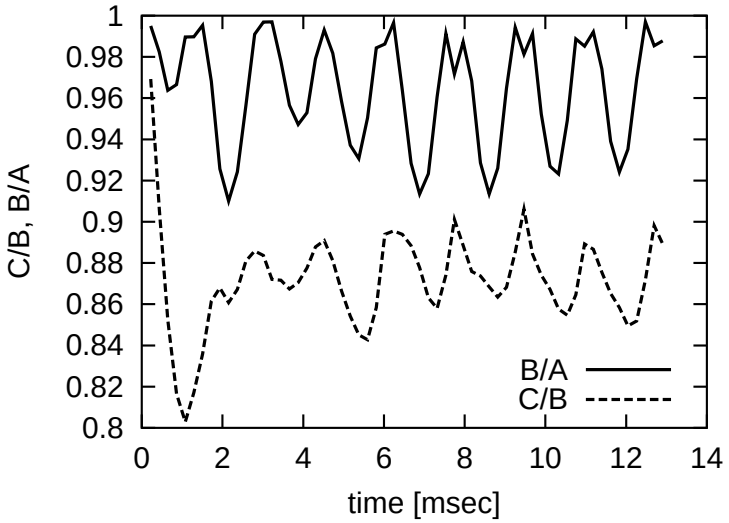

Figure 10.2: The time evolutions of axial ratios C/B and B/A in the case of Fig. 10.1.

a long time. Let's see the results for $r_0 = 500\,\mu$m (center panels). The case of $f = 0.3$ corresponds to the case of Fig. 10.2. When $f = 0.1$, the droplet shape settles around C/B $\simeq 0.90$ and B/A $\simeq 0.98$, so it is a kind of oblate shape. In this case, the rotation is not so rapid that the deformation due to the centrifugal force is much smaller than that due to the gas drag force. As the value of f increases, the droplet shape gradually approaches toward the prolate shape, and it becomes almost a prolate at $f = 0.4$. If $f = 0.5$, the droplet keeps to be a prolate shape but the value of B/A becomes smaller.

In the cases of $r_0 = 200\,\mu$m, the trend of the droplet shape with increasing f are almost the same as the cases of $r_0 = 500\,\mu$m except for the magnitude of the deformation. The droplet shape is kind of oblate for $f = 0.1$ and kind of prolate for $f = 0.4$. However, when $f = 0.1$ (the shape is a kind of oblate), the value of C/B is about 0.96 for $r_0 = 200\,\mu$m and 0.90 for $r_0 = 500\,\mu$m. On the other hand, when $f = 0.4$ (the shape is a kind of prolate), the value of B/A is about 0.95 for $r_0 = 200\,\mu$m and 0.84 for $r_0 = 500\,\mu$m. In addition, the behavior for $f = 0.5$ is slightly different from the case of $r_0 = 500\,\mu$m. In the case of $r_0 = 200\,\mu$m, the

shape seems not to settle into a steady state by presuming from the relatively large dispersion of the dark symbols.

In contrast, the cases of $r_0 = 1000\,\mu$m are very similar to the cases of $r_0 = 500\,\mu$m from $f = 0.1$ to $f = 0.5$ except for the magnitude of the deformation (notice that the scales of both axes become twice of that of $r = 500\,\mu$m). The droplet shape is almost a oblate when $f = 0.1$, and it becomes a prolate when $f = 0.4$. When $f = 0.5$, the droplet elongates more than that of when $f = 0.4$. In this case, the non-dimensional parameter Σ is about 0.37, so the shape is expected not to undergo the shape instability. If the value of f exceeds about 0.62, Σ becomes larger than the critical value of 0.4587 and the shape instability might take place on the droplet.

10.4 Analytic Sequence

In this subsection, we analytically derive the three-dimensional shapes of rotating droplet exposed to the gas flow. We obtained numerical results of hydrodynamical simulations for various input parameters about r_0 and f, and found the trend that the droplet shapes become prolate as the value of f increases. We thought that there should be a physical reason for the trend of the droplet shapes about f.

First of all, let's see the deformation of the droplet for two cases; the case that only the gas drag force acts on the droplet and the case that only the rotation affects the droplet shape. Figure 10.4 shows the droplet shapes in the sections of the xy-plane (left) and the xz-plane (right). Top two figures show the droplet shape when only the gas drag force is acting on the droplet, which becomes oblate with the minor axis being parallel to x-axis because the gas flow comes from the left side of the panel. Middle two figures shows the case of the rotating droplet without the gas flow and it becomes oblate with the minor axis being parallel to z-axis because the droplet rotates about the z-axis. Based on these top and middle panels, we assume that the shape of rotating droplets exposed to the gas flow can be expressed by the simple superposition of the deformations for each directions of top and middle panels. Bottom two figures are the shape of the rotating droplet exposed to the gas flow. In this case, the droplet shape seems to be a prolate of which the major axis

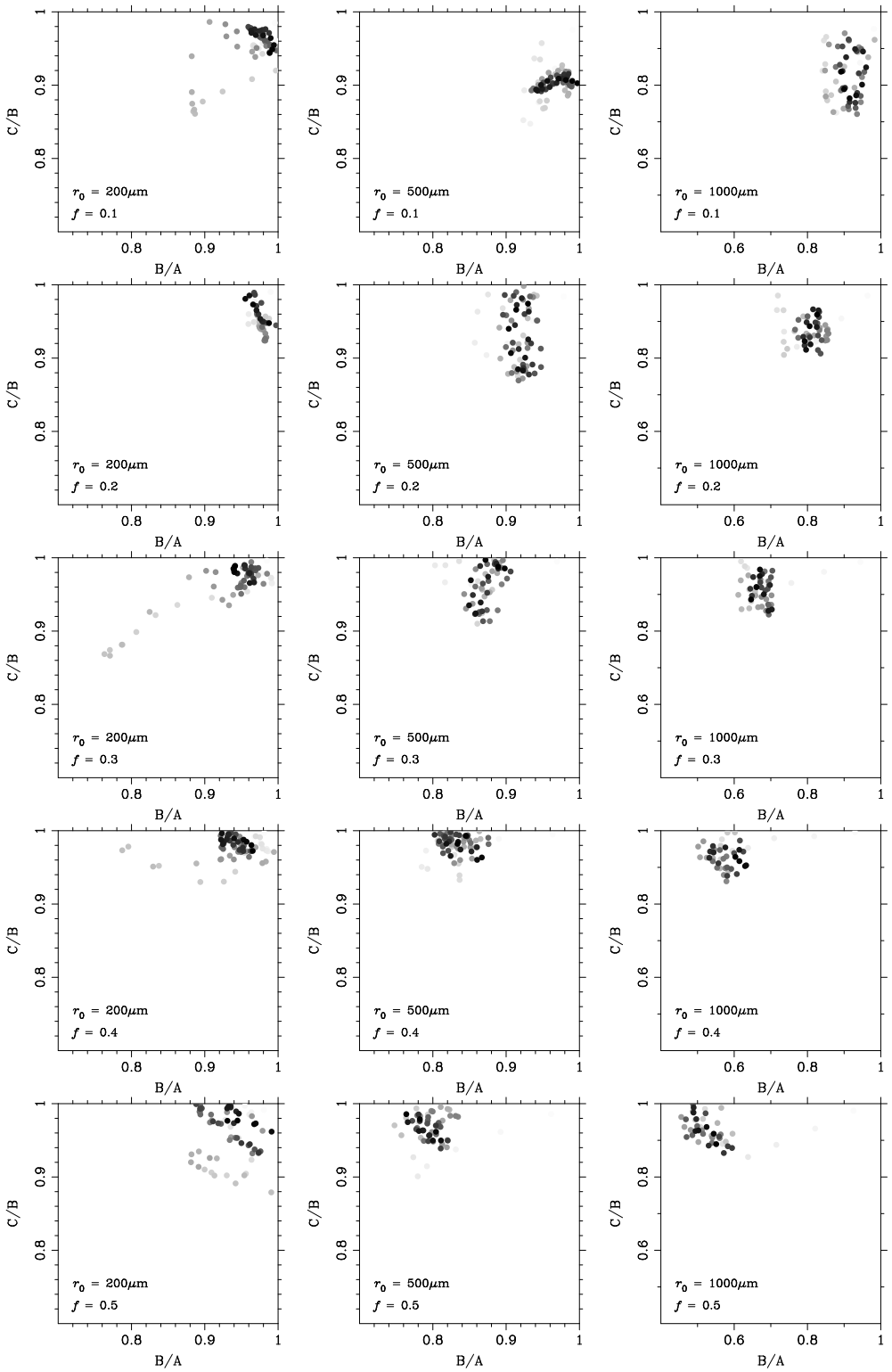

Figure 10.3: Time evolutions of shapes of rotating droplets exposed to the gas flow on the B/A-C/B diagram. The left, middle, and right panels are the cases of $r_0 = 200\,\mu$m, $500\,\mu$m, and $1000\,\mu$m, respectively. The asymmetric parameter f is considered from 0.1 (top) to 0.5 (bottom).

is the y-axis.

We discuss the magnitude of the deformation more quantitatively using the analytic formulations of Sekiya et al. (2003) and Chandrasekhar (1965). Sekiya et al. (2003) analytically derived the magnitude of the deformation when only the gas drag force is acting on the droplet. According to their formulations, the radius of the droplet can be written as

$$r_{s,g}(\phi) = r_0 + r_{1,g}(\phi), \tag{10.1}$$

where ϕ is the angle to the direction of the gas flow, so $\phi = 0$ indicates the direction of upstream and $\phi = \pi/2$ indicates the direction perpendicular to the gas flow. We can find the formalism of $r_{1,g}$ in their articles. On the other hand, Chandrasekhar (1965) analytical derived the radius of the equilibrium shapes of rotating droplet. It can be written as

$$r_{s,r}(\theta) = r_0 + r_{1,r}(\theta), \tag{10.2}$$

where θ is the angle to the rotation axis (z-axis in Fig. 10.4). Although we cannot find the expression corresponding to $r_{1,r}$ directly in his article, it is not so difficult to derive it using his formulations. We assume that the radius of rotating droplet exposed to the gas flow can be expressed by a simple superposition of above two expressions as

$$r_s(\theta, \phi) = r_0 + r_{1,g}(\phi) + r_{1,r}(\theta). \tag{10.3}$$

Figure 10.5 shows the radius of the droplet for each direction (x-, y-, and z-axis) as a function of the asymmetric parameter f. The radius for each direction is given as $[r_s(\pi/2, 0) + r_s(\pi/2, \pi)]/2$ for x-axis, $r_s(\pi/2, \pi/2)$ for y-axis, and $r_s(0, \pi/2)$ for z-axis, respectively. We set $r_0 = 500\,\mu$m. The larger value of f indicates that the droplet rotates more rapidly under the same ram pressure. When $f = 0$, which means no rotation, y- and z-axes are the same and the x-axis is shorter than them. Therefore, the shape is oblate. It is naturally expected from the analytic solutions by Sekiya et al. (2003). If the droplet begins to rotate, the x- and y-axes get longer by the centrifugal force. In contrast, the droplet shrinks in the z-direction, so the droplet shape is a general three-axial ellipsoid. In this case, the minor axis is the x-axis. It is found that the x-axis becomes the same length with the z-axis at a

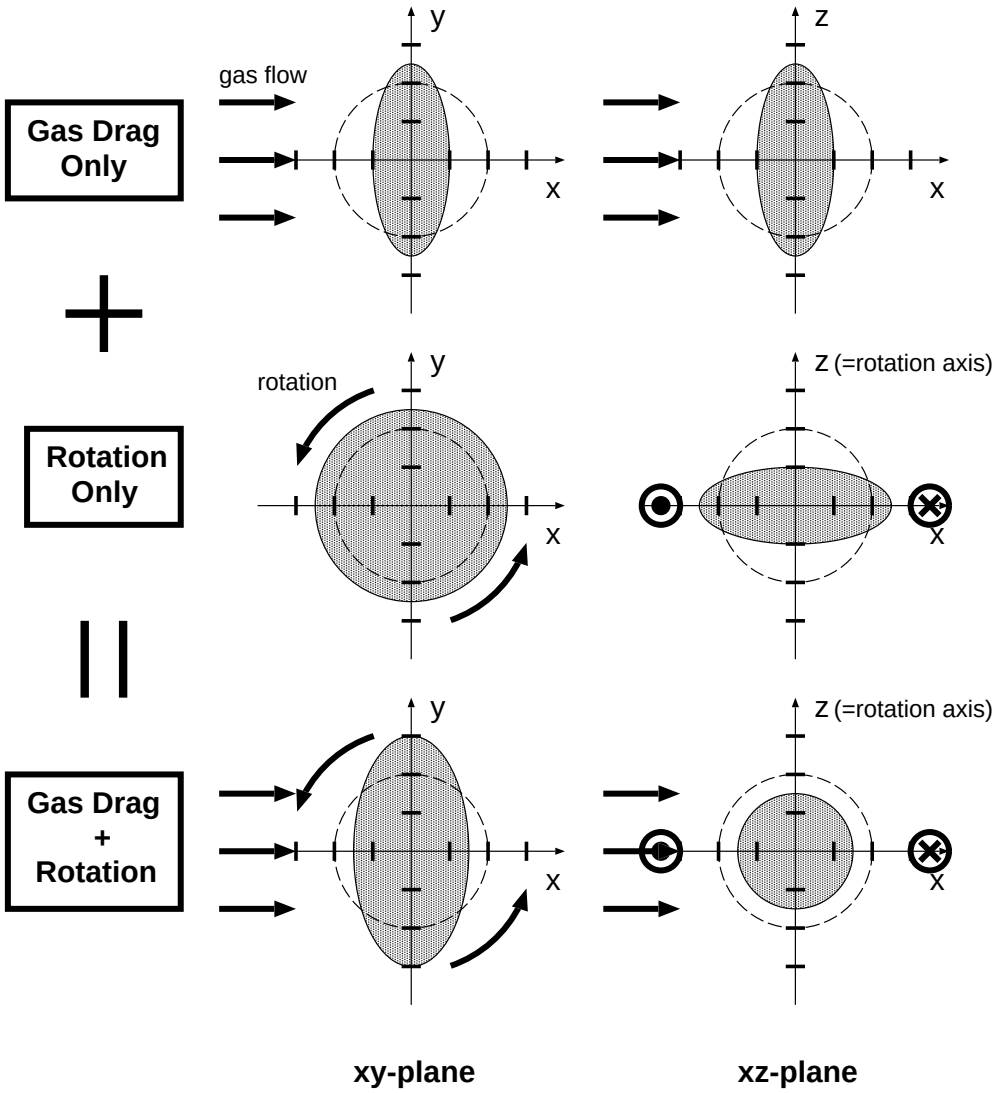

Figure 10.4: Sketches of the shapes of molten droplets under the effects of only the gas drag force (top), only the rotation (middle), and both of two effects (bottom), respectively. The left and right panels are the sections of the xy-plane and the xz-plane.

Table 10.2: The values of f where the droplet shapes become prolate. The corresponding values of the angular velocity, Ω, and the rotation rate are also listed.

r_0 [μm]	$f_{\rm prolate}$	Ω [s^{-1}]	rotation rate [rps]
200	0.333	2557	407
500	0.348	1046	166
700	0.358	758	121
1000	0.373	541	86
2000	0.417	286	46

certain value of f. The critical value, $f_{\rm prolate}$, is listed in Table 10.2 for various cases of r_0. At that point, the droplet shape is prolate. When $f > f_{\rm prolate}$, the x-axis is getting longer but the z-axis is getting shorter, so the shape becomes a general three-axial ellipsoid again. In this case, the minor axis is the z-axis. To summarize, as the rotation rate of the droplet increases under the same ram pressure, it is expected that the droplet shape changes from oblate, three-axial ellipsoid, prolate, and three-axial ellipsoid again.

Figure 10.6 shows the analytic sequences of the droplet shapes on the B/A-C/B diagram when the value of f varies continuously. The unperturbed droplet radius is $r_0 = 200\,\mu$m, $500\,\mu$m, and $1000\,\mu$m. The value of f changes from 0.0 to 1.0. The numbers along the analytic sequences in the panel show the values of f at the corresponding points. The droplet shapes are oblate (B/A = 1) for $f = 0$ in any cases. As f increases, the shapes vary to prolate (C/B = 1) via the general three-axial ellipsoid (B/A $<$ 1 and C/B $<$ 1). When $f = f_{\rm prolate}$ (see table 10.2), the droplet shapes become prolate. It is found that the values of $f_{\rm prolate}$ slightly depend on the droplet radius r_0. When $f > f_{\rm prolate}$, the droplet shapes become the general three-axial ellipsoid again.

The dashed curve on the analytic sequence of $r_0 = 1000\,\mu$m indicates that the non-dimensional parameter Σ exceeds the critical value of 0.4587 for the shape instability. Therefore, the droplet shape might unstable in that case.

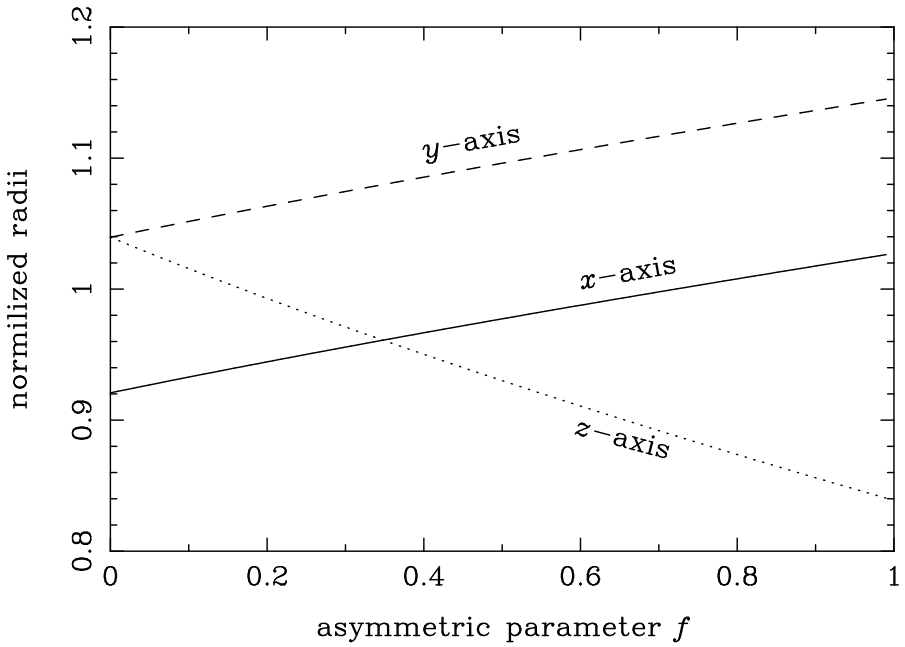

Figure 10.5: The radii for each direction of the rotating droplet exposed to the gas flow as a function of the asymmetric parameter f. As f increases, the rotation rate of the droplet becomes faster under the same ram pressure.

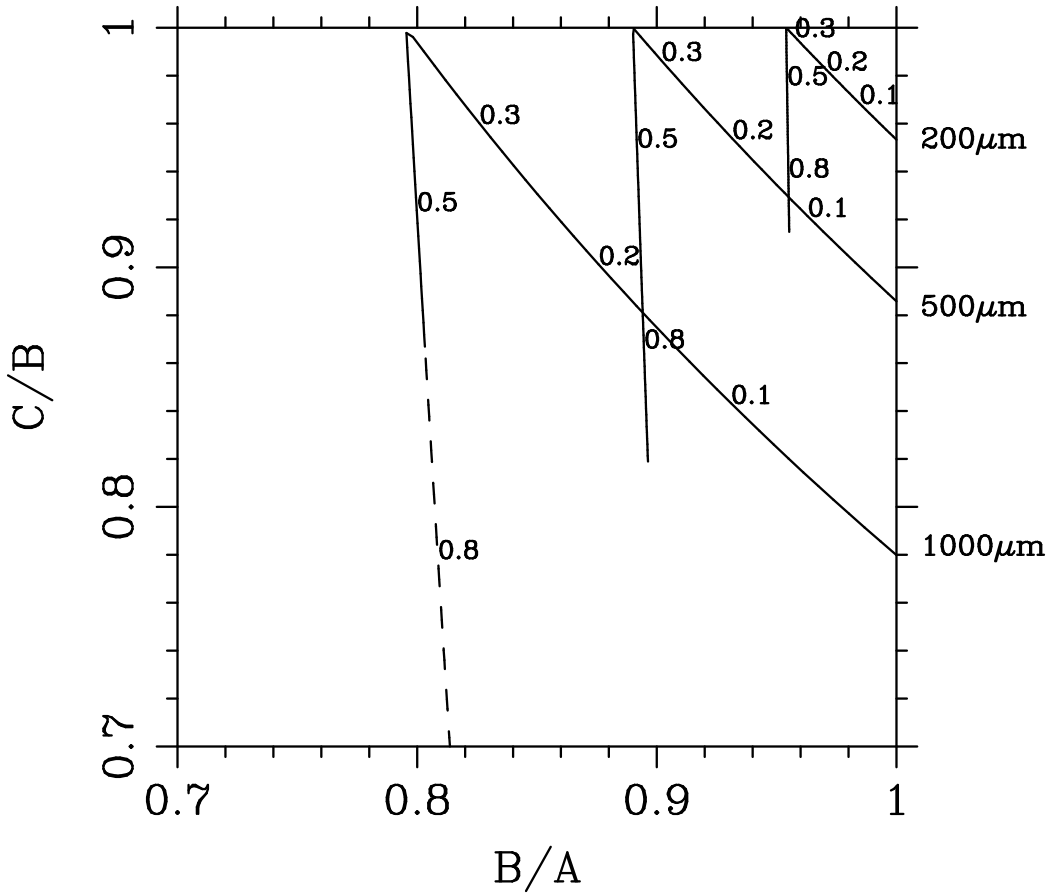

Figure 10.6: The analytic sequences of the droplet shapes when the value of f changes continuously. The unperturbed droplet radius is $r_0 = 200\,\mu$m, $500\,\mu$m, and $1000\,\mu$m. The value of f changes from 0 to 1. The numbers along the analytic sequences in the panel show the values of f at the corresponding points.

10.5 Simulations vs. Analytic Sequences

Figures 10.7-10.9 show the comparisons of our simulation results with the analytic sequences on the B/A-C/B diagram. Fig. 10.7 is for $r_0 = 200\,\mu$m. The values of f on the analytic sequence are displayed on each solid curve. We show the analytic sequences for $0 < f < f_{\rm prolate}$ because the deformation by the rotation dominates that by the gas drag force when $f > f_{\rm prolate}$ and the assumption of the simple superposition of both two effects is thought to be invalid. Filled circles are the simulation results of the time evolutions of the droplet shapes for various values of f, 0.1 (red), 0.3 (green), and 0.5 (blue). The deeper colors indicate the later stage of the evolutions, so if the deeper colored circles concentrate at a certain points on the diagram, it implies that the droplet settles into the steady state. It is found that although the simulation results seem to be slightly scattered on the diagram, the trend that the droplet shapes become prolate as f increases can be obtained. The red circles ($f = 0.1$) distribute around $f = 0.1$ on the analytic sequence, and the blue circles ($f = 0.3$) also distribute around $f = 0.3$ on the analytic sequence. If f increases up to 0.5, the simulation results are more scattered, however, the droplet shape is prolate rather than oblate.

Fig. 10.8 is the same as Fig. 10.7 except for $r_0 = 500\,\mu$m. The distinguishable characteristic is that the simulation results are less scattered on the diagram comparing with the cases of $r_0 = 200\,\mu$m. The red circles ($f = 0.1$) concentrate around $f = 0.1$ on the analytic sequence and the green circles ($f = 0.3$) distribute around $f = 0.3$ as the same. When $f = 0.5\,(> f_{\rm prolate})$, the droplet becomes more deformed prolate shape comparing with the analytic sequence when $f = f_{\rm prolate}$. The value of B/A for $f = 0.5$ is about 0.8, on the other hand, the analytic sequence shows that the value of B/A is about 0.89 when $f = f_{\rm prolate}\,(= 0.348)$. The simulation results indicate that droplet shapes become more deformed prolate rather than the shape returns to kind of oblate as shown in Fig. 10.6 when the deformation by the rotation dominates that by the gas drag force.

Fig. 10.9 is the same as Fig. 10.7 except for $r_0 = 1000\,\mu$m. When $f = 0.1$, the simulation results show a good agreement with the analytic sequence. However, the green circles ($f = 0.3$) seem not to match well with the analytic sequence. It

is thought to be due to the effects of the non-linear terms in the hydrodynamical equations because the Reynolds number R_e estimated by $R_e = 0.11\rho_{\rm mat}r_0^2/\mu^2$ (see section 6.3) exceeds unity in the cases of $r_0 = 1000\,\mu$m, regardless the values of f. Namely, the deformation by the rotation changes the internal flow of the droplet and the non-linear terms cannot be neglected because they depend on the pattern of the internal flow. Therefore, the assumption that the deformation of the rotating droplet exposed to the gas flow can be expressed by the simple superposition of two independent effects is not a good approximation. Therefore, the reason why the simulation results are apart from the analytic sequence is thought to be that the non-linear effects between the deformation by the rotation and the internal flow of the droplet. As a result of the non-linear effects, the droplets become more deformed prolate shapes than that expected from the analytic sequences.

10.6 Origin of Shapes of Group-A Chondrules

In the subsection, we discuss the origin of group-A chondrules measured and classified by Tsuchiyama et al. (2003) (see Figs. 1.5 and 6.1). The group-A chondrules are oblate to prolate chondrules with axial ratios of $0.9 \lesssim {\rm B/A} \lesssim 1$ and $0.9 \lesssim {\rm C/B} \lesssim 1$. Figure 10.10 shows the analytic sequences for various initial droplet radii r_0 and the chondrule data (Tsuchiyama et al. 2003). It is found that the shapes of the group-A chondrules are very similar to the analytic sequences for $0 < f < f_{\rm prolate}$. The small chondrules seem to distribute along the analytic sequence for $r_0 = 200\,\mu$m and the large chondrules seem to distribute along the sequence for $r_0 = 500\,\mu$m. Although the chondrule radii in data seem to slightly deviate from that of the analytic sequences. We can consider the different value of the ram pressure in order to explain the deviation between them because the magnitude of the deformation is almost proportional to $W_e = p_{\rm fm}r_0/\gamma$ (see subsection 6.3). Therefore, even if considering the low-density shock waves, we can obtain the same trend for the droplet shapes except for the magnitude of the deformation. The ram pressure of the gas flow is estimated as about one-fourth of that of the high-density shock waves, so the magnitude of the deformation would be about one-fourth of Fig. 10.10 if the value of

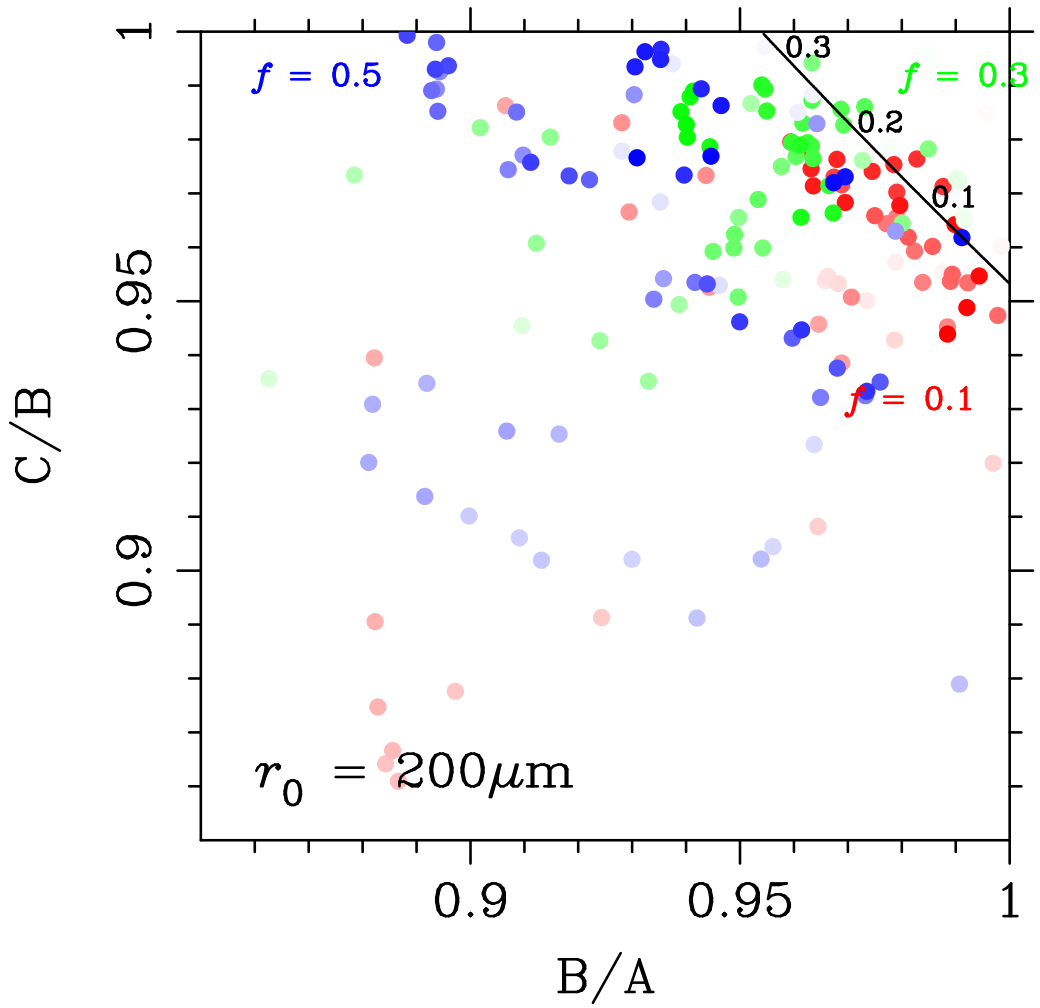

Figure 10.7: Comparison of the simulation results with the analytic sequence. The initial droplet radius, r_0, is assumed to be 200 μm.

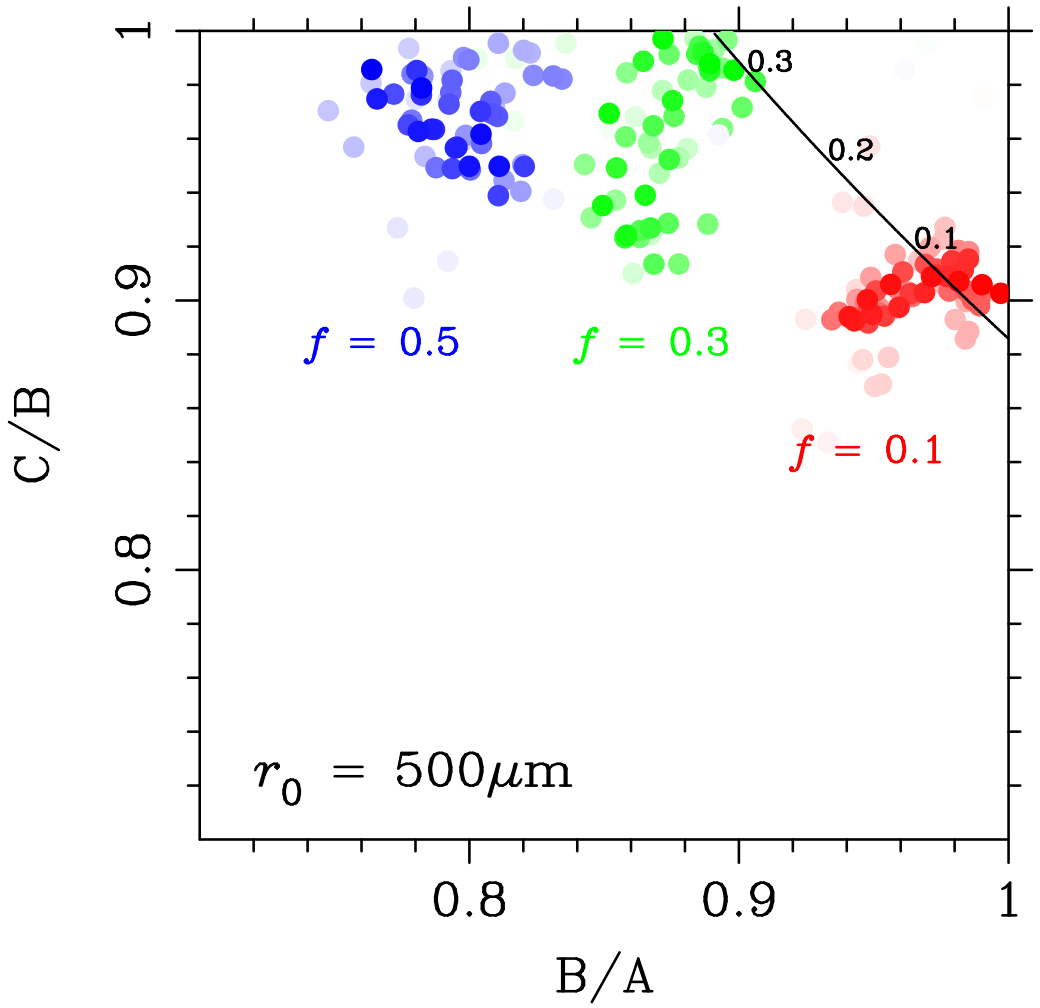

Figure 10.8: Same as Fig. 10.7 except for $r_0 = 500\,\mu$m.

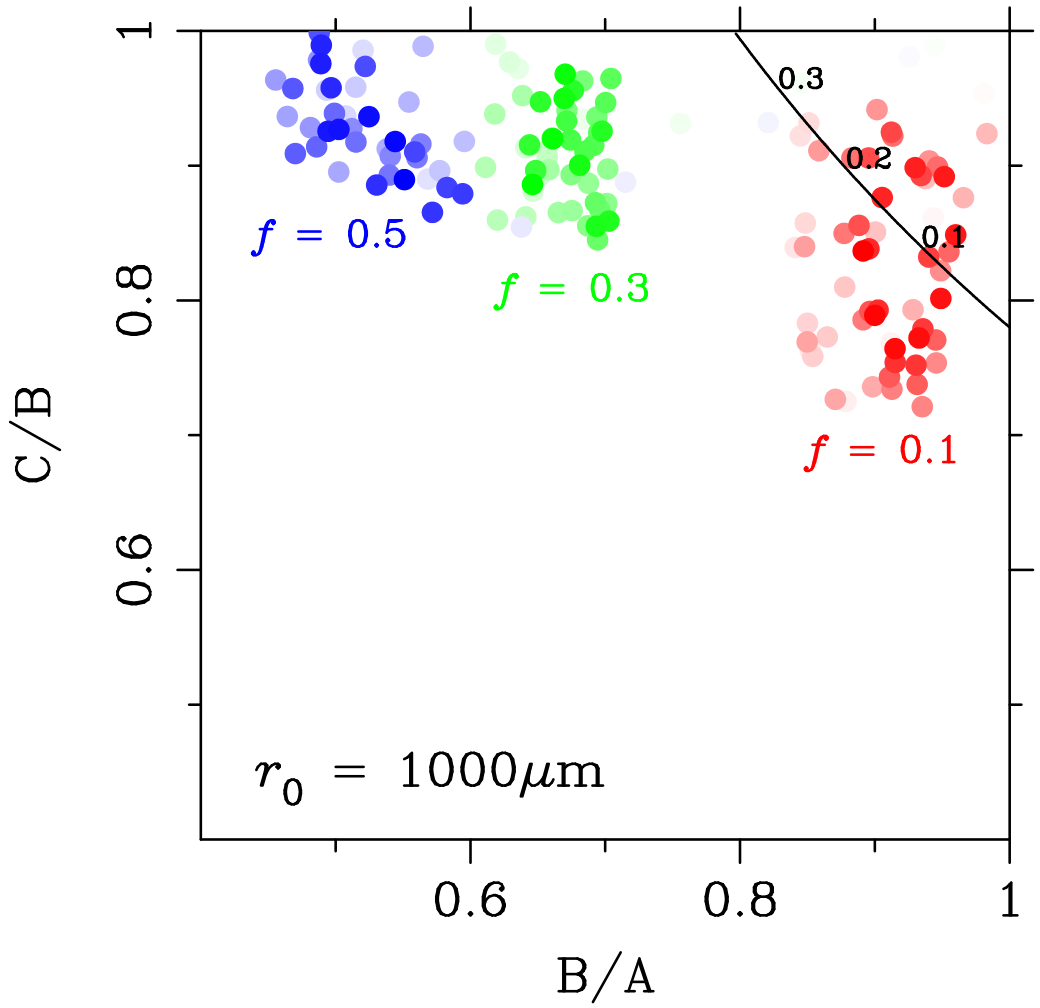

Figure 10.9: Same as Fig. 10.7 except for $r_0 = 1000\,\mu$m.

the surface tension does not change. To summarize, we can explain the trend of chondrule shapes in the group-A by considering the droplet rotating about the axis which is perpendicular to the gas flow. At that time, the angular velocity of the droplets should be smaller as the deformation by the rotation does not dominate that by the gas drag force.

The notable characteristic of above mechanism is that the values of $f_{\rm prolate}$ at which the droplet shapes become prolate (C/B = 1) do not strongly depend on the droplet radius. If $f_{\rm prolate}$ depends on the droplet radius strongly, the fraction of oblate/prolate shapes in the total chondrules would depend on the chondrule radius. The week correlation between r_0 and $f_{\rm prolate}$ predicts that the fraction of oblate/prolate chondrules would not change with r_0 as long as the asymmetric parameter f does not depend on the precursor size before melting. On the other hand, the chondrule data seem to distribute evenly from prolate to oblate regardless of its radii. The good agreement on the fraction of oblate/prolate shapes between the analytic sequences and the chondrule data can be the strong evidence that chondrules have been formed in the high-velocity gas flow from the rotating droplets.

10.7 Origin of Shapes of Group-B Chondrules

In this subsection, we discuss the origin of group-B chondrules (see Figs. 1.5 and 6.1). The group-B chondrules are prolate chondrules with relatively large magnitude of the deformation than the group-A chondrules. It can be thought that the shapes of such more deformed prolate chondrules seem to match with our simulation results with large values of the asymmetric parameter f ($> f_{\rm prolate}$). Figure 10.11 shows the simulation result of the case of $r_0 = 500\,\mu$m and $f = 0.5$ (black filled circles). The simulation result and the chondrule data of the group-B show a good agreement on the B/A-C/B diagram. In Fig. 10.10, it is found that the analytic sequence of $r_0 = 1000\,\mu$m can also explain the group-B chondrules when $f \simeq 0.3$. However, in this case, the simulation results are apart from the analytic solution because of the non-linear effects (see subsection 10.5), and the numerical simulations do not match with the group-B chondrules. Therefore, the origin of the group-B chondrules is

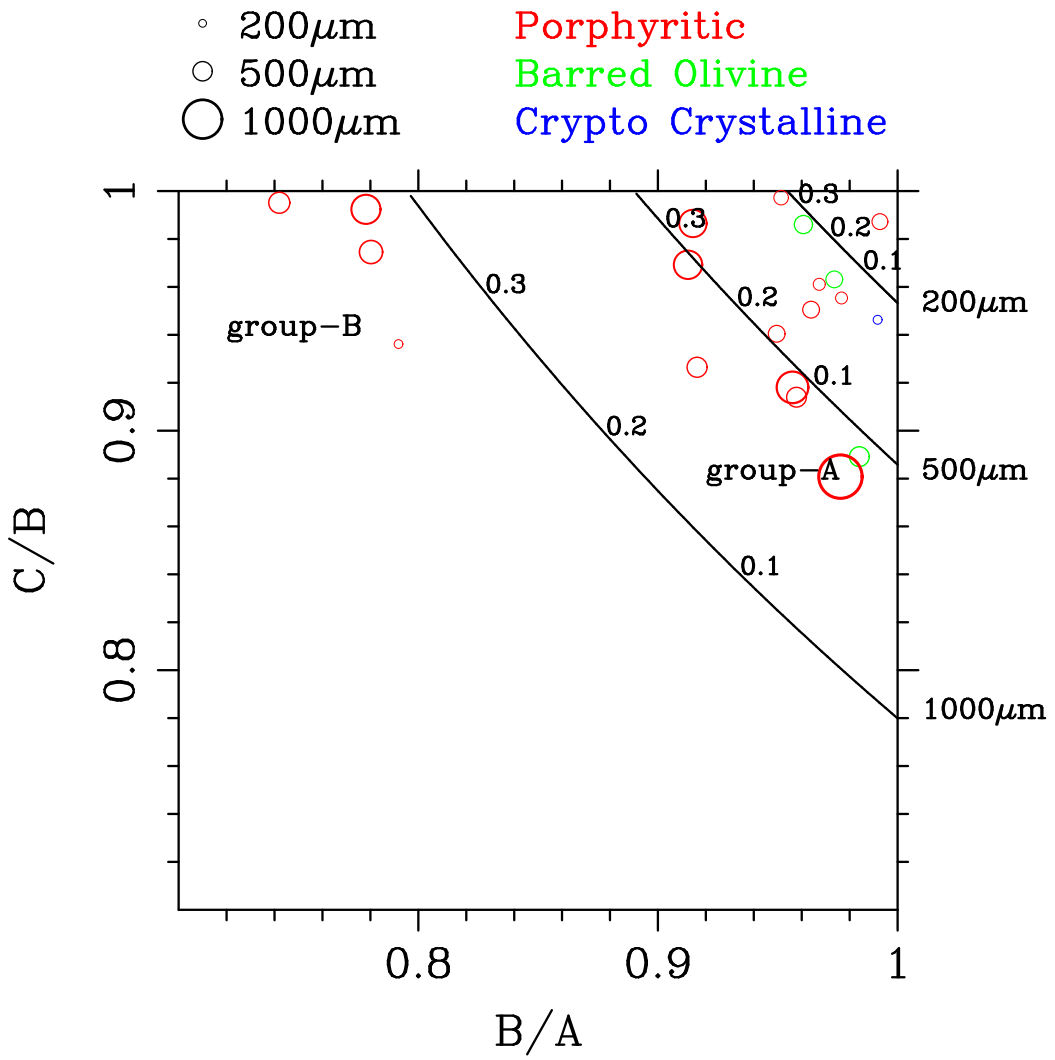

Figure 10.10: The origin of the group-A chondrules. The solid curves are the analytic sequences for $r_0 = 200\,\mu$m, $500\,\mu$m, and $1000\,\mu$m. The filled circles are chondrule data measured by Tsuchiyama et al. (2003).

thought to be the rapidly rotating molten droplets where the deformation by the rotation dominates that by the gas drag force ($f > f_{\rm prolate}$).

10.8 Non-Steady Behavior

We derive the analytic sequences of the shape of rotating droplet exposed to the gas flow by using the analytic formalisms of Sekiya et al. (2003) and Chandrasekhar (1965); the former describes the droplet shapes exposed to the high-velocity rarefied gas flow and the latter is the equilibrium shapes of rotating droplets. We assume that the simple superposition of each deformation by the gas drag force and by the rotation gives the droplet shapes deformed by both two effects in order to derive the analytic sequence. However, in the derivation procedure, the assumption that the droplet shape can change more rapidly than its rotation is implicitly included. The reason why the major axis of the prolate droplet in Fig. 10.1 does not rotate about the rotation axis (the z-axis) is due to the rapid deformation of the droplet shape. If the rotation is much faster than the deformation of the droplet shapes, the major axis of the prolate droplet would begin to rotate and the steady state would not be established. In that case, the droplet shapes would be apart from the analytic sequences and continue to deform with time.

In the co-rotating coordinate system with the droplet, the direction of the gas flow changes with time. If the internal flow of the droplet responds to the gas flow rapidly enough, the droplet can change its shape to adopt the gas drag force. The response time scale, $t_{\rm res}$, is estimated as follows: the maximum velocity of the internal flow without rotation is analytically derived as $v_{\rm max} = 0.112 p_{\rm fm} r_0/\mu$ (Sekiya et al. 2003). Here, we define the response time scale as the time that a fluid element traverses across the diameter of the droplet with $v_{\rm max}$. Then, we obtain

$$t_{\rm res} = \frac{2\mu}{0.112\, p_{\rm fm}}. \tag{10.4}$$

On the other hand, the time scale of the rotation can be given as $t_{\rm rot} = 2\pi/\Omega$.

Figure 10.12 shows the time scales of the rotation (dashed lines) and the response of the internal flow of the droplet (solid line) as a function of the droplet radius r_0.

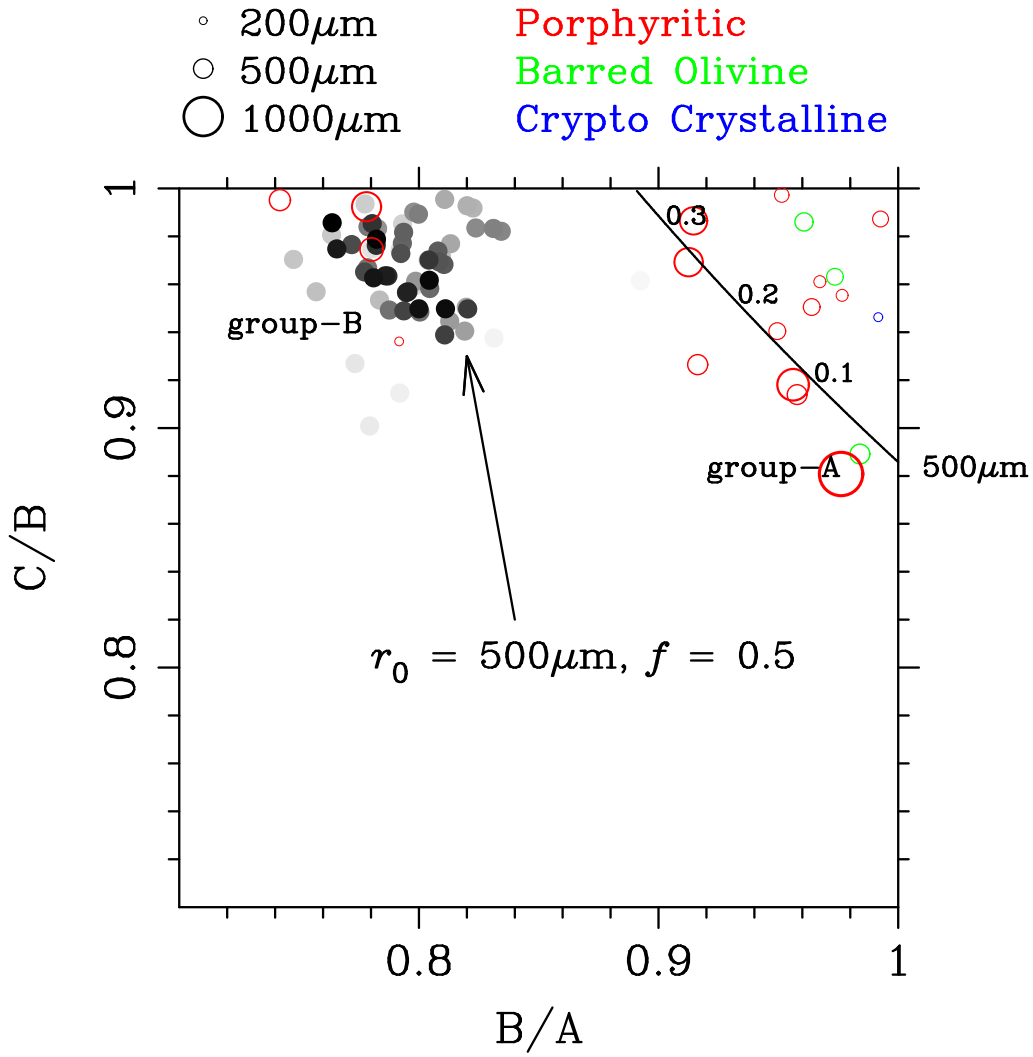

Figure 10.11: The shapes of group-B chondrules (color filled circles) and the simulation result for the case of $r_0 = 500\,\mu$m and $f = 0.5$ (black filled circles).

The left panel (a) shows the cases for various values of f, 0.1, 0.3, and 0.5. The rotation time scale $t_{\rm rot}$ becomes shorter as f increases. On the contrary, the response time scale $t_{\rm res}$ does not depend on f. We set $\mu = 1.3$ poises in the panel (a). The panel (a) indicates that the rotation time scale is shorter than the response time scale when the droplet radius is $r_0 = 200\,\mu$m. Namely, the droplets of $r_0 = 200\,\mu$m would not take the steady state during their evolutions. In fact, such small droplets seem to show the scattered distributions on the B/A-C/B diagram for considering their small magnitude of the deformation. These results might indicate that the droplet shapes do not settle into the steady state (see Fig. 10.3). On the contrary, for the droplets with $r_0 = 1000\,\mu$m, the response time scale is shorter than that of the rotation. It means that the droplets can deform rapidly enough to respond to the rotation, so the droplet shapes can settle into the steady state at the end of the time evolution.

The right panel (b) shows the cases for various values of viscous coefficient μ. The standard value of this study is $\mu = 1.3$ poises and larger values of μ indicate the droplets in the cooling phase. The rotation time scale does not depend on the viscosity and we set $f = 0.1$ in the right panel. The response time scale is proportional to the viscous coefficient μ. For the droplets with $r_0 = 500\,\mu$m, the rotation time scale when $\mu = 1.3$ poises is longer than the response time scale, so the droplets would take the steady state. However, if the viscous coefficient increases up to $\mu = 4.0$ poise (about three times larger than the standard case), the response time scale becomes longer than that of the rotation. Therefore, it can be thought that the droplet shapes continue to deform with time and do not settle into the steady state.

10.9 Conclusions

We performed the hydrodynamical simulations of rotating molten silicate dust particles exposed to the gas flow. We considered that the dust particles gain the angular momentum from the ambient gas flow before they melt. We assumed that the asymmetrical shapes of the precursor dust particles are the origin of the net torque in the

(a) different f

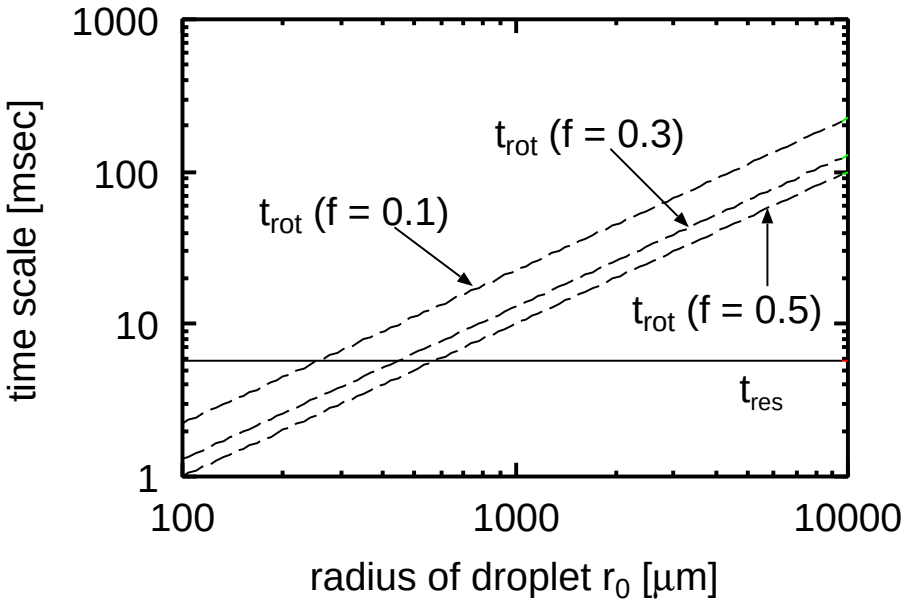

(b) different μ

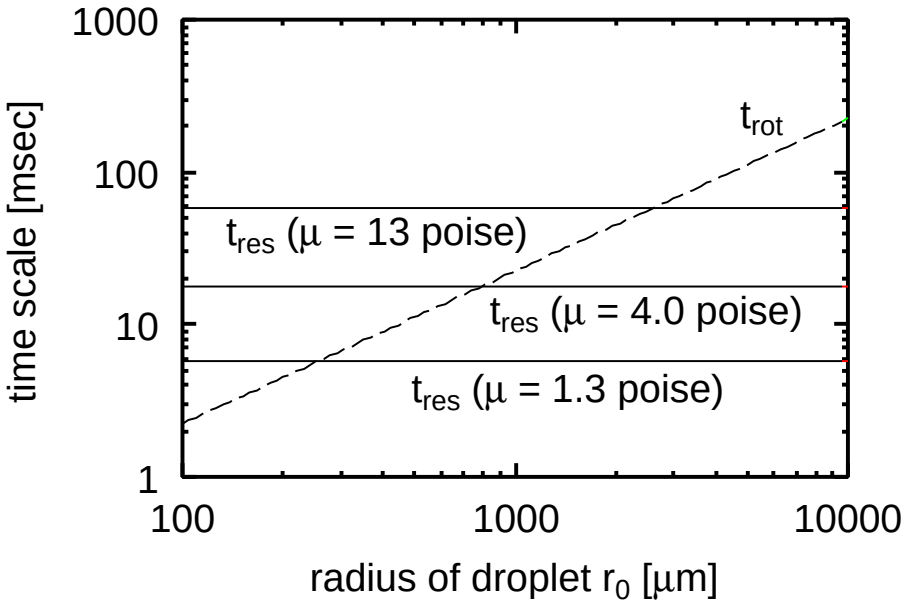

Figure 10.12: The time scales of the rotation ($t_{\rm rot}$) and the response of the internal flow of the droplet ($r_{\rm res}$). The left panel (a) shows the cases for various values of the asymmetric parameter f. $t_{\rm res}$ does not depend on f and we set $\mu = 1.3\,$poises in this panel. The right panel (b) shows the cases for various values of the viscous coefficient μ. $t_{\rm rot}$ does not depend on μ and we set $f = 0.1$ in this panel.

gas flow and the rotation axis is perpendicular to the gas flow. The ram pressure of the gas flow was assumed to be $4000\,\mathrm{dyne\,cm^{-2}}$ assuming the high-density shock waves. The standard value of the viscous coefficient was set to be 1.3 poises assuming the well-molten droplets composed of silicates. The value of the surface tension was assumed to be $\gamma = 400\,\mathrm{dyne\,cm^{-1}}$, which is the typical value for silicate melts. We also derived the analytic sequence of the droplet shapes and compared with the simulation results. We obtained following conclusions;

1. Numerical simulations showed that the rotating droplets exposed to the gas flow could take various shapes; oblate, prolate, and the general three-axial ellipsoid. The droplet shapes were determined by the rotation rate of the droplets. If there is no rotation, the droplets become the oblate shapes. As the rotation rate increases, the droplet shapes are approaching to the prolate shapes via the general three-axial ellipsoids. If the rotation rate increases after the droplet shapes become prolate, the major axis of the prolate shape elongates comparing with other shorter axes.

2. The analytic sequence of the droplet shapes showed how the droplets deform when the rotation rate changes continuously. The origin of the sequence which indicates no-rotation is at the oblate shape. As the rotation rate increases, the sequence moves toward the prolate shape via the general three-axial ellipsoid. The droplet shape becomes prolate when the magnitude of the deformation by the rotation becomes comparable to that by the gas drag force.

3. The results of numerical simulations and the analytic sequence showed a good agreement when the rotation of the droplets is not so fast as the magnitude of the deformation by the rotation does not dominate that by the gas drag force. If the rotation rate is larger than that, the simulation results were apart from the analytic sequence. The reason was thought to be due to the non-linear effects between the deformation of the droplet by the rotation and the internal flow of the droplets.

4. The origin of the group-A chondrules is thought to be rotating droplets in the gas flow, and the rotation rate should not be so large as the magnitude of the

deformation by the rotation does not dominate that by the gas drag force. According to the analytic sequence, the fraction of oblate/prolate droplets does not strongly depend on the droplet radius. The trend seems to match well with the group-A chondrule data.

5. The origin of the group-B chondrules is also thought to be rotating droplets in the gas flow, but the rotation rate should be larger than that of the group-A chondrules as the magnitude of the deformation by the rotation dominates that by the gas drag force. At the same time, the rotation rate would be small as the shape instability does not take place.

6. Non-steady behavior of the droplets would appear when the time scale of the rotation is much shorter than the time scale that the internal flow of the droplets responds to the rotation. Such situation could occur when the temperature of the droplet decreases in the cooling phase and just before the re-solidification. In these cases, the droplet shapes might be apart from the analytic sequence significantly. Therefore, the behavior for high-viscous rotating droplets in the shock-wave heating should be investigated.

Appendix A

Escape Probability

A.1 Molecular Line Coolings

In the shock-wave heating model, the optical depth effects are important in determining the net cooling rate by line emissions of gas molecules. In order to evaluate the net cooling rate, we adopt the fitting formula derived by Neufeld & Kaufman (1993), in which they numerically solved the equations of statistical equilibrium for the rotational/vibrational level populations using an escape probability method.

The equations of statistical equilibrium is given as

$$\sum_j f_j(A_{ji}\beta_{ji} + C_{ji}) - f_i \sum_j (A_{ij}\beta_{ij} + C_{ij}), \tag{A.1}$$

where f_i is the fractional population in state i, A_{ij} and C_{ij} are the spontaneous radiative rate and collisional rate for transitions from state i to state j, and β_{ij} is an angle-averaged escape probability and given by

$$\beta_{ij} \simeq \frac{1}{1 + 3\tau_{\rm S}}, \tag{A.2}$$

where the Sobolev optical depth $\tau_{\rm S}$ is given by

$$\tau_{\rm S} = \frac{hcn({\rm M})}{4\pi |dv_z/dz|}(f_j B_{ji} - f_i B_{ij}), \tag{A.3}$$

where $n({\rm M})$ is the volume density of coolant molecules, where B_{ji} and B_{ij} are the absorption and stimulated emission coefficients, and where dv_z/dz is the local

velocity gradient. Eq. (A.3) is exact in the limits of small and large $\tau_{\rm S}$, and deviates from the exact expression of Hummer & Rybicki (1982) by at most 15%. Solving the equations of statistical equilibrium is made more difficult by the fact that the escape probabilities for the emitted line photons are themselves a function of the level populations. Neufeld & Kaufman numerically solved those equations including a large number of rotational state and obtained the net cooling rates over a wide range of physical conditions.

Neufeld & Kaufman found a convenient analytic fit to express their numerical solutions. The net cooling rate Λ may be conveniently expressed as a rate coefficient, L, defined such that the cooling power per unit volume due to collisions of H_2 and species M is given by $\Lambda = Ln(H_2)n(M)$, where $n(H_2)$ and $n(M)$ are the H_2 and coolant particle densities. The cooling rate coefficient L has units of erg cm^3 s^{-1}. The analytic fit for L is written as

$$\frac{1}{L} = \frac{1}{L_0} + \frac{n(H_2)}{L_{\rm LTE}} + \frac{1}{L_0}\left[\frac{n(H_2)}{n_{1/2}}\right]^{\alpha}\left(1 - \frac{n_{1/2}L_0}{L_{\rm LTE}}\right), \tag{A.4}$$

where L_0 is a function of temperature alone and $L_{\rm LTE}$, $n_{1/2}$, α are functions of both temperature and $\tilde{N}(M)$, and $\tilde{N}(M)$ is the optical depth parameter. In a case of a static plane-parallel slab of thickness d, $\tilde{N}(M)$ is expressed as

$$\tilde{N}(M) = \frac{n(M)d}{\Delta v}, \tag{A.5}$$

where Δv is the velocity dispersion of the coolant molecules. For vibrational cooling, Neufeld & Kaufman recommended a two-parameter fit to the net cooling rate which includes only the first two terms in Eq. (A.4). The values of L_0, $L_{\rm LTE}$, $n_{1/2}$, and α are listed in Tables 2-5 of Neufeld & Kaufman (1993).

A.2 Lyman α Cooling

Regarding the Lyα cooling, we neglect the absorption by other hydrogen atoms because the optical depth for the Lyα photon is small. The absorption coefficient for the Lyα emission is given as $\alpha_\nu = \frac{h\nu}{4\pi} n_1 B_{12}\phi(\nu)$, where h is the planck constant, n_1 is

the number density of hydrogen atom in ground state ($n = 1$), B_{12} is the Einstein B-constant, and $\phi(\nu)$ is the line profile function (Rybicki & Lightman 1979). Einstein B-constant is given from the Einstein A-constant by Einstein relation. The line profile function has the maximum value of $\sim 1/\Delta\nu$ at the line center, where $\Delta\nu$ is the Doppler broadening in frequency. In the shock condition D, $n_1 \sim 10^9\,\mathrm{cm}^{-3}$ and $\Delta\nu \sim 10^{-4}\nu$ behind the shock front, so we obtain $\alpha_\nu \sim 10^{-5}\,\mathrm{cm}^{-1}$. It indicates that Ly$\alpha$ photons are not absorbed until they achieve at about $10^5\,\mathrm{cm}$ behind the shock front. However, our calculation results show that the gas cools until it reaches at that point for the shock conditions of $n_0 = 10^{11}\,\mathrm{cm}^{-3}$ and $v_\mathrm{s} = 55\,\mathrm{km\,s}^{-1}$. Moreover, the gas decelerated as it cools in the post-shock region. The relative velocity between the shocked gas immediately behind the shock front and the cooled gas far from the shock front is about $10^6\,\mathrm{cm\,s}^{-1}$ and it is comparable to the velocity dispersion of the gas molecules. Therefore, the large relative velocity does not allow the cooled gas to absorb Lyα photons emitted immediately behind the shock front.

Appendix B

Chemical Reactions

All of the 156 reactions among 28 species included in our calculation are listed in Table B.1-B.4. The reaction rates in these tables are based upon the following references: Dove et al. (1987, DRCM87), Hollenbach & McKee (1979, HM79), Hollenbach & McKee (1989, HM89), Lepp & Shull (1983, LS83), and Palla et al. (1983, PSS83). INSN included 176 reactions among 35 gas species. In this study, we neglect D- and Si-inclusive species because they do not contribute to the gas cooling processes as coolant species.

The function $R(a, b)$ used in reactions 47-49 is given by HM89 as

$$R(a,b) = (r-a)^b r e^{-r} \left(\frac{\pi}{2\phi_d}\right)^{0.5} \{1 - \mathrm{erf}[(0.5\phi_d)^{0.5}(r-a)]\}, \tag{B.1}$$

where $r = 0.5[y + (y^2 - 4a)^{0.5}]$, $y = 1 + a + b$, and $\phi_d = b/(r-a)^2 + r^{-2}$. Moreover, $T_{300} = (T/300\,\mathrm{K})$ and $T_3 = (T/1000\,\mathrm{K})$. And $c_f = 1/(1 + n_{\mathrm{cr}}/n)$ is the abundance of H_2 in excited vibrational states relative to the LTE value and we take n_{cr} to be

$$n_{\mathrm{cr}} = \frac{10^6 T^{-0.5}}{3.2y(\mathrm{H})\exp[-(400/T) - 2] + 2.8y(\mathrm{H_2})\exp[-18,100/(T + 1,200)]}\,\mathrm{cm}^{-3}, \tag{B.2}$$

where $y(i)$ is the abundance of species i.

Table B.1: Neutral-Neutral Reactions

	Reaction	Rate Coefficient ($cm^3\ s^{-1}$)	Reference
1.	$H + H \rightarrow H^+ + H + e$	$1.70 \times 10^{-13} T_{300}^{0.50} \exp(-1.58 \times 10^5\,\mathrm{K}/T)$	HM89
2.	$H + H (\rightarrow H^+ + H^-) \rightarrow H^+ + H + e$	$3.00 \times 10^{-13} T_{300}^{0.50} \exp(-1.49 \times 10^5\,\mathrm{K}/T)$	HM89
3.	$He + H \rightarrow He^+ + H + e$	$8.63 \times 10^{-14} T_{300}^{0.43} \exp(-2.85 \times 10^5\,\mathrm{K}/T)$	HM89
4.	$He + H_2 \rightarrow He^+ + H_2 + e$	$8.63 \times 10^{-14} T_{300}^{0.43} \exp(-2.85 \times 10^5\,\mathrm{K}/T)$	HM89
5.	$C + H \rightarrow C^+ + H + e$	$5.90 \times 10^{-13} T_{300}^{0.40} \exp(-1.31 \times 10^5\,\mathrm{K}/T)$	HM89
6.	$C + H_2 \rightarrow C^+ + H_2 + e$	$5.90 \times 10^{-13} T_{300}^{0.40} \exp(-1.31 \times 10^5\,\mathrm{K}/T)$	HM89
7.	$C + H_2 \rightarrow CH + H$	$4.50 \times 10^{-11} T_{300}^{0.50} \exp(-1.56 \times 10^4\,\mathrm{K}/T)$	HM89
8.	$C + OH \rightarrow CO + H$	$1.11 \times 10^{-10} T_{300}^{0.50}$	HM89
9.	$C + H_2O \rightarrow CH + OH$	$1.43 \times 10^{-10} T_{300}^{0.50} \exp(-2.40 \times 10^4\,\mathrm{K}/T)$	HM89
10.	$C + O_2 \rightarrow CO + O$	$1.80 \times 10^{-11} T_{300}^{0.50}$	HM89
11.	$O + H \rightarrow O^+ + H + e$	$3.04 \times 10^{-13} T_{300}^{0.49} \exp(-1.58 \times 10^5\,\mathrm{K}/T)$	HM89
12.	$O + H_2 \rightarrow O^+ + H_2 + e$	$3.04 \times 10^{-13} T_{300}^{0.49} \exp(-1.58 \times 10^5\,\mathrm{K}/T)$	HM89
13.	$O + CH \rightarrow CO + H$	$9.53 \times 10^{-11} T_{300}^{0.50}$	HM89
14.	$O + CH \rightarrow C + OH$	$1.73 \times 10^{-11} T_{300}^{0.50} \exp(-4.00 \times 10^3\,\mathrm{K}/T)$	HM89
15.	$O + CH_4 \rightarrow CH_3 + OH$	$3.50 \times 10^{-11} \exp(-4.55 \times 10^3\,\mathrm{K}/T)$	HM89
16.	$O + OH \rightarrow O_2 + H$	$4.33 \times 10^{-11} T_{300}^{-0.50} \exp(-3.00 \times 10\,\mathrm{K}/T)$	HM89
17.	$O + H_2O \rightarrow OH + OH$	$1.35 \times 10^{-12} T_{300}^{1.75} \exp(-7.86 \times 10^3\,\mathrm{K}/T)$	HM89
18.	$O + CO \rightarrow C + O_2$	$2.90 \times 10^{-11} T_{300}^{0.50} \exp(-6.93 \times 10^4\,\mathrm{K}/T)$	HM89
19.	$CH + H \rightarrow C + H_2$	$1.80 \times 10^{-11} T_{300}^{0.50} \exp(-4.00 \times 10^3\,\mathrm{K}/T)$	HM89
20.	$CH + H \rightarrow CH^+ + H + e$	$8.83 \times 10^{-14} T_{300}^{0.50} \exp(-1.29 \times 10^5\,\mathrm{K}/T)$	HM89
21.	$CH + H_2 \rightarrow CH_2 + H$	$3.60 \times 10^{-10} \exp(-3.90 \times 10^3\,\mathrm{K}/T)$	HM89
22.	$CH + H_2 \rightarrow CH^+ + H_2 + e$	$8.83 \times 10^{-14} T_{300}^{0.50} \exp(-1.29 \times 10^5\,\mathrm{K}/T)$	HM89
23.	$CH + OH \rightarrow H_2O + C$	1.00×10^{-10}	HM89
24.	$CH_2 + H \rightarrow CH + H_2$	$3.60 \times 10^{-10} \exp(-2.65 \times 10^3\,\mathrm{K}/T)$	HM89
25.	$CH_2 + H_2 \rightarrow CH_3 + H$	$5.30 \times 10^{-12} \exp(-3.53 \times 10^3\,\mathrm{K}/T)$	HM89
26.	$CH_3 + H \rightarrow CH_2 + H_2$	$5.30 \times 10^{-12} \exp(-1.08 \times 10^4\,\mathrm{K}/T)$	HM89
27.	$CH_3 + H_2 \rightarrow CH_4 + H$	$1.40 \times 10^{-12} \exp(-5.50 \times 10^3\,\mathrm{K}/T)$	HM89
28.	$CH_4 + H \rightarrow CH_3 + H_2$	$1.00 \times 10^{-10} \exp(-5.99 \times 10^3\,\mathrm{K}/T)$	HM89
29.	$CH_4 + OH \rightarrow CH_3 + H_2O$	$2.40 \times 10^{-12} \exp(-1.71 \times 10^3\,\mathrm{K}/T)$	HM89
30.	$OH + H \rightarrow O + H_2$	$6.60 \times 10^{-13} T_{300}^{1.53} \exp(-2.97 \times 10^3\,\mathrm{K}/T)$	HM89
31.	$OH + H \rightarrow OH^+ + H + e$	$8.83 \times 10^{-14} T_{300}^{0.50} \exp(-1.53 \times 10^5\,\mathrm{K}/T)$	HM89
32.	$OH + H_2 \rightarrow H_2O + H$	$8.80 \times 10^{-13} T_{300}^{1.95} \exp(-1.42 \times 10^3\,\mathrm{K}/T)$	HM89
33.	$OH + H_2 \rightarrow OH^+ + H_2 + e$	$8.83 \times 10^{-14} T_{300}^{0.50} \exp(-1.53 \times 10^5\,\mathrm{K}/T)$	HM89
34.	$OH + OH \rightarrow H_2O + O$	$4.20 \times 10^{-12} \exp(-2.42 \times 10^2\,\mathrm{K}/T)$	HM89
35.	$H_2O + H \rightarrow OH + H_2$	$7.44 \times 10^{-12} T_{300}^{1.57} \exp(-9.14 \times 10^3\,\mathrm{K}/T)$	HM89
36.	$H_2O + H \rightarrow H_20^+ + H + e$	$7.55 \times 10^{-14} T_{300}^{0.45} \exp(-1.47 \times 10^5\,\mathrm{K}/T)$	HM89
37.	$H_2O + H_2 \rightarrow H_20^+ + H_2 + e$	$7.55 \times 10^{-14} T_{300}^{0.45} \exp(-1.47 \times 10^5\,\mathrm{K}/T)$	HM89
38.	$CO + H \rightarrow C + OH$	$1.11 \times 10^{-10} T_{300}^{0.50} \exp(-7.77 \times 10^4\,\mathrm{K}/T)$	HM89
39.	$CO + H \rightarrow CH + O$	$9.53 \times 10^{-11} T_{300}^{0.50} \exp(-8.83 \times 10^4\,\mathrm{K}/T)$	HM89
40.	$CO + H \rightarrow CO^+ + H + e$	$1.13 \times 10^{-13} T_{300}^{0.60} \exp(-1.63 \times 10^5\,\mathrm{K}/T)$	HM89
41.	$CO + H_2 \rightarrow CO^+ + H_2 + e$	$1.13 \times 10^{-13} T_{300}^{0.60} \exp(-1.63 \times 10^5\,\mathrm{K}/T)$	HM89
42.	$O_2 + H \rightarrow OH + O$	$1.63 \times 10^{-9} T_{300}^{-0.90} \exp(-8.75 \times 10^3\,\mathrm{K}/T)$	HM89
43.	$O_2 + H \rightarrow O_2^+ + H + e$	$2.37 \times 10^{-15} T_{300}^{1.04} \exp(-1.40 \times 10^5\,\mathrm{K}/T)$	HM89
44.	$O_2 + H_2 \rightarrow O_2^+ + H_2 + e$	$2.37 \times 10^{-15} T_{300}^{1.04} \exp(-1.40 \times 10^5\,\mathrm{K}/T)$	HM89
45.	$O + H_2 \rightarrow OH + H$	$3.7 \times 10^{-12} c_f T_{300}^{1.53} \exp(-4.06 \times 10^3\,\mathrm{K}/T)$	HM89
46.	$H + H_2 \rightarrow H^- + H_2^+ \rightarrow H + H_2^+ + e$	$10^{-15} T_{300}^{1.5} (1 + 5.3 \times 10^{-3} T_{300}) \exp(-1.7 \times 10^5\,\mathrm{K}/T)$	HM89
47.	$H + H_2 \rightarrow H_2^+ + H + e$	$5.29 \times 10^{-19} T^{1.3} R[(1.789 \times 10^5/T), 0.80]$	HM89
48.	$H + H_2 \rightarrow H^+ + H_2 + e$	$5.29 \times 10^{-19} T^{1.3} R[(1.577 \times 10^5/T), 0.80]$	HM89
49.	$H_2 + H_2 \rightarrow H_2^+ + H_2 + e$	$2.39 \times 10^{-26} T^{2.54} R[(1.789 \times 10^5/T), 2.04]$	HM89
50.	$H + H_2 \rightarrow H + H + H$	$3.52 \times 10^{-9} \exp(-4.39 \times 10^4\,\mathrm{K}/T)$	LS83
51.	$H_2 + H_2 \rightarrow H_2 + H + H$	$5.48 \times 10^{-9} \exp(-5.30 \times 10^4\,\mathrm{K}/T)$	LS83
52.	$H_2 + He \rightarrow H + H + He$	$10^{-2.739 - 23474/T} \times T^{-1.75}$	DRCM87

Table B.2: Ion-Neutral Reactions

	Reaction	Rate Coefficient (cm^3 s^{-1})	Reference
53.	$He + H^+ \rightarrow He^+ + H^+ + e$	$8.63 \times 10^{-14} T_{300}^{0.43} \exp(-2.85 \times 10^5\,\mathrm{K}/T)$	HM89
54.	$C + H^+ \rightarrow C^+ + H^+ + e$	$5.90 \times 10^{-13} T_{300}^{0.40} \exp(-1.31 \times 10^5\,\mathrm{K}/T)$	HM89
55.	$CH + H^+ \rightarrow CH^+ + H^+ + e$	$8.83 \times 10^{-14} T_{300}^{0.50} \exp(-1.29 \times 10^5\,\mathrm{K}/T)$	HM89
56.	$O + H^+ \rightarrow H + O^+$	$7.00 \times 10^{-10} \exp(-2.32 \times 10^2\,\mathrm{K}/T)$	HM89
57.	$O + H^+ \rightarrow O^+ + H^+ + e$	$3.04 \times 10^{-13} T_{300}^{0.49} \exp(-1.58 \times 10^5\,\mathrm{K}/T)$	HM89
58.	$H_2 + H^+ \rightarrow H^+ + H_2^+$	$6.40 \times 10^{-10} \exp(-2.13 \times 10^4\,\mathrm{K}/T)$	HM89
59.	$CH + H^+ \rightarrow H + CH^+$	1.90×10^{-9}	HM89
60.	$OH + H^+ \rightarrow H + OH^+$	2.10×10^{-10}	HM89
61.	$OH + H^+ \rightarrow OH^+ + H^+ + e$	$8.83 \times 10^{-14} T_{300}^{0.50} \exp(-1.53 \times 10^5\,\mathrm{K}/T)$	HM89
62.	$H_2O + H^+ \rightarrow H + H_2O^+$	8.20×10^{-9}	HM89
63.	$H_2O + H^+ \rightarrow H_2O^+ + H^+ + e$	$7.55 \times 10^{-14} T_{300}^{0.45} \exp(-1.47 \times 10^5\,\mathrm{K}/T)$	HM89
64.	$CO + H^+ \rightarrow H + CO^+$	$1.90 \times 10^{-10} \exp(-4.66 \times 10^3\,\mathrm{K}/T)$	HM89
65.	$CO + H^+ \rightarrow CO^+ + H^+ + e$	$1.13 \times 10^{-13} T_{300}^{0.60} \exp(-1.63 \times 10^5\,\mathrm{K}/T)$	HM89
66.	$O_2 + H^+ \rightarrow H + O_2^+$	1.20×10^{-9}	HM89
67.	$O_2 + H^+ \rightarrow O_2^+ + H^+ + e$	$2.37 \times 10^{-15} T_{300}^{1.04} \exp(-1.40 \times 10^5\,\mathrm{K}/T)$	HM89
68.	$H + He^+ \rightarrow He + H^+$	1.90×10^{-15}	HM89
69.	$H_2 + He^+ \rightarrow H + H^+ + He$	1.10×10^{-13}	HM89
70.	$H_2O + He^+ \rightarrow H + OH^+ + He$	2.86×10^{-10}	HM89
71.	$H_2O + He^+ \rightarrow OH + H^+ + He$	2.03×10^{-10}	HM89
72.	$H_2O + He^+ \rightarrow He + H_2O^+$	6.05×10^{-11}	HM89
73.	$CO + He^+ \rightarrow O + C^+ + He$	1.70×10^{-9}	HM89
74.	$O_2 + He^+ \rightarrow O + O^+ + He$	1.10×10^{-9}	HM89
75.	$H_2 + C^+ \rightarrow CH_2^+$	$4.00 \times 10^{-16} T_{300}^{-0.20}$	HM89
76.	$H_2 + C^+ \rightarrow H + CH^+$	$2.00 \times 10^{-10} \exp(-4.64 \times 10^3\,\mathrm{K}/T)$	HM89
77.	$OH + C^+ \rightarrow H + CO^+$	7.70×10^{-10}	HM89
78.	$H_2O + C^+ \rightarrow H_2 + CO^+$	2.70×10^{-9}	HM89
79.	$O_2 + C^+ \rightarrow O + CO^+$	3.76×10^{-10}	HM89
80.	$O_2 + C^+ \rightarrow CO + O^+$	6.14×10^{-10}	HM89
81.	$H + O^+ \rightarrow O + H^+$	7.00×10^{-10}	HM89
82.	$H_2 + O^+ \rightarrow H + OH^+$	1.60×10^{-9}	HM89
83.	$H + H_2^+ \rightarrow H_2 + H^+$	1.00×10^{-10}	HM89
84.	$O + H_2^+ \rightarrow H + OH^+$	1.50×10^{-9}	HM89
85.	$H_2 + H_2^+ \rightarrow H + H_3^+$	2.10×10^{-9}	HM89
86.	$H_2 + H_2^+ \rightarrow H_2 + H^+ + H$	$4.17 \times 10^{-11} T_{300}^{0.50} \exp(-3.07 \times 10^4\,\mathrm{K}/T)$	HM89
87.	$OH + H_2^+ \rightarrow H_2 + OH^+$	7.60×10^{-10}	HM89
88.	$H_2O + H_2^+ \rightarrow H_2 + H_2O^+$	3.90×10^{-9}	HM89

Table B.2: Continue.

	Reaction	Rate Coefficient ($cm^3\ s^{-1}$)	Reference
89.	$H_2O + H_2^+ \rightarrow H + H_3O^+$	3.40×10^{-9}	HM89
90.	$O_2 + H_2^+ \rightarrow O_2^+ + H_2$	2.70×10^{-9}	HM89
91.	$CO + H_2^+ \rightarrow H_2 + CO^+$	2.80×10^{-9}	HM89
92.	$H + H_3^+ \rightarrow H_2 + H_2^+$	$2.08 \times 10^{-9} \exp(-1.88 \times 10^4\,\mathrm{K}/T)$	HM89
93.	$H_2 + H_3^+ \rightarrow H_2 + H_2^+ + H$	$3.41 \times 10^{-11} T_{300}^{0.50} \exp(-7.16 \times 10^4\,\mathrm{K}/T)$	HM89
94.	$H_2 + H_3^+ \rightarrow H_2 + H^+ + H_2$	$3.41 \times 10^{-11} T_{300}^{0.50} \exp(-5.04 \times 10^4\,\mathrm{K}/T)$	HM89
95.	$O + H_3^+ \rightarrow H_2 + OH^+$	8.00×10^{-10}	HM89
96.	$OH + H_3^+ \rightarrow H_2 + H_2O^+$	1.30×10^{-9}	HM89
97.	$H_2O + H_3^+ \rightarrow H_2 + H_3O^+$	5.90×10^{-9}	HM89
98.	$CO + H_3^+ \rightarrow H_2 + CO^+$	1.70×10^{-9}	HM89
99.	$C + H_3^+ \rightarrow H_2 + CH^+$	2.00×10^{-9}	HM89
100.	$H + OH^+ \rightarrow OH + H^+$	$2.10 \times 10^{-9} \exp(-2.80 \times 10^3\,\mathrm{K}/T)$	HM89
101.	$H + OH^+ \rightarrow O + H_2^+$	$1.60 \times 10^{-9} \exp(-2.26 \times 10^4\,\mathrm{K}/T)$	HM89
102.	$H + OH^+ \rightarrow H_2 + O^+$	$4.90 \times 10^{-10} T_{300}^{-0.03} \exp(-1.97 \times 10^3\,\mathrm{K}/T)$	HM89
103.	$H_2 + OH^+ \rightarrow OH + H_2^+$	$7.60 \times 10^{-10} \exp(-2.36 \times 10^4\,\mathrm{K}/T)$	HM89
104.	$H_2 + OH^+ \rightarrow O + H_3^+$	$8.00 \times 10^{-10} \exp(-2.90 \times 10^3\,\mathrm{K}/T)$	HM89
105.	$H_2 + OH^+ \rightarrow H + H_2O^+$	1.10×10^{-9}	HM89
106.	$H + H_2O^+ \rightarrow H_2 + OH^+$	$1.70 \times 10^{-9} T_{300}^{0.29} \exp(-1.40 \times 10^4\,\mathrm{K}/T)$	HM89
107.	$H + H_2O^+ \rightarrow H_2O + H^+$	$8.20 \times 10^{-9} \exp(-1.15 \times 10^4\,\mathrm{K}/T)$	HM89
108.	$H + H_2O^+ \rightarrow OH + H_2^+$	$7.60 \times 10^{-10} \exp(-4.00 \times 10^4\,\mathrm{K}/T)$	HM89
109.	$H_2 + H_2O^+ \rightarrow OH + H_3^+$	$1.30 \times 10^{-9} \exp(-2.03 \times 10^4\,\mathrm{K}/T)$	HM89
110.	$H_2 + H_2O^+ \rightarrow H_2O + H_2^+$	$3.90 \times 10^{-9} \exp(-3.27 \times 10^4\,\mathrm{K}/T)$	HM89
111.	$H_2 + H_2O^+ \rightarrow H + H_3O^+$	6.10×10^{-10}	HM89
112.	$H + H_3O^+ \rightarrow H_2 + H_2O^+$	$6.00 \times 10^{-9} T_{300}^{0.39} \exp(-1.98 \times 10^4\,\mathrm{K}/T)$	HM89
113.	$H + H_3O^+ \rightarrow H_2O + H_2^+$	$3.40 \times 10^{-9} \exp(-5.25 \times 10^4\,\mathrm{K}/T)$	HM89
114.	$H_2 + H_3O^+ \rightarrow H_2O + H_3^+$	$5.90 \times 10^{-9} \exp(-3.28 \times 10^4\,\mathrm{K}/T)$	HM89
115.	$H + CH^+ \rightarrow H_2 + C^+$	$6.00 \times 10^{-10} T_{300}^{-0.25}$	HM89
116.	$H_2 + CH^+ \rightarrow H + CH_2^+$	1.00×10^{-9}	HM89
117.	$H + CH_2^+ \rightarrow H_2 + CH^+$	$1.00 \times 10^{-9} \exp(-1.20 \times 10^4\,\mathrm{K}/T)$	HM89
118.	$H_2 + CH_2^+ \rightarrow CH + H_3^+$	$1.20 \times 10^{-9} \exp(-4.22 \times 10^4\,\mathrm{K}/T)$	HM89
119.	$O + CH_2^+ \rightarrow H + CO^+$	7.50×10^{-10}	HM89
120.	$H + CO^+ \rightarrow CO + H^+$	1.90×10^{-10}	HM89
121.	$H + O_2^+ \rightarrow O_2 + H^+$	$2.80 \times 10^{-10} T_{300}^{-0.04} \exp(-1.78 \times 10^4\,\mathrm{K}/T)$	HM89
122.	$H + CH^+ \rightarrow C^+ + H_2$	$2 \times 10^{-10} + 10^{-9}/(1 + T_{300})$	HM89

Table B.3: Electron Reactions

	Reaction	Rate Coefficient ($\mathrm{cm^3\ s^{-1}}$)	Reference
123.	$e + \mathrm{H^+} \rightarrow \mathrm{H}$	$3.60 \times 10^{-12} T_{300}^{-0.75}$	HM89
124.	$e + \mathrm{He^+} \rightarrow \mathrm{He}$	$8.9 \times 10^{-13} T_{300}^{-0.49} [\frac{y(\mathrm{H})+3y(\mathrm{H_2})}{y(\mathrm{H})+3y(\mathrm{H_2})+7y(\mathrm{He})}] + 2.5 \times 10^{-12} T_{300}^{-0.64}$	HM89
125.	$e + \mathrm{C^+} \rightarrow \mathrm{C}$	$1.80 \times 10^{-12} T_{300}^{-0.62}$	HM89
126.	$e + \mathrm{O^+} \rightarrow \mathrm{O}$	$1.80 \times 10^{-12} T_{300}^{-0.62}$	HM89
127.	$e + \mathrm{H_2^+} \rightarrow \mathrm{H} + \mathrm{H}$	$8.00 \times 10^{-8} T_{300}^{-0.50}$	HM89
128.	$e + \mathrm{H_3^+} \rightarrow \mathrm{H_2} + \mathrm{H}$	$5.00 \times 10^{-9} T_{300}^{-0.50}$	HM89
129.	$e + \mathrm{H_3^+} \rightarrow \mathrm{H} + \mathrm{H} + \mathrm{H}$	$5.00 \times 10^{-9} T_{300}^{-0.50}$	HM89
130.	$e + \mathrm{OH^+} \rightarrow \mathrm{O} + \mathrm{H}$	$2.00 \times 10^{-7} T_{300}^{-0.50}$	HM89
131.	$e + \mathrm{H_2O^+} \rightarrow \mathrm{OH} + \mathrm{H}$	$2.00 \times 10^{-7} T_{300}^{-0.50}$	HM89
132.	$e + \mathrm{H_2O^+} \rightarrow \mathrm{O} + \mathrm{H_2}$	$2.00 \times 10^{-7} T_{300}^{-0.50}$	HM89
133.	$e + \mathrm{H_3O^+} \rightarrow \mathrm{H_2O} + \mathrm{H}$	$1.00 \times 10^{-6} T_{300}^{-0.50}$	HM89
134.	$e + \mathrm{H_3O^+} \rightarrow \mathrm{OH} + \mathrm{H_3}$	$3.00 \times 10^{-7} T_{300}^{-0.40}$	HM89
135.	$e + \mathrm{O_2^+} \rightarrow \mathrm{O} + \mathrm{O}$	$2.00 \times 10^{-7} T_{300}^{-0.50}$	HM89
136.	$e + \mathrm{CO^+} \rightarrow \mathrm{C} + \mathrm{O}$	$1.80 \times 10^{-7} T_{300}^{-0.50}$	HM89
137.	$e + \mathrm{CH^+} \rightarrow \mathrm{C} + \mathrm{H}$	$3.00 \times 10^{-7} T_{300}^{-0.50}$	HM89
138.	$e + \mathrm{CH_2^+} \rightarrow \mathrm{C} + \mathrm{H_2}$	$2.50 \times 10^{-7} T_{300}^{-0.50}$	HM89
139.	$e + \mathrm{CH_2^+} \rightarrow \mathrm{CH} + \mathrm{H}$	$2.50 \times 10^{-7} T_{300}^{-0.50}$	HM89
140.	$e + \mathrm{H} \rightarrow \mathrm{H^+} + e + e$	$1.00 \times 10^{-9} T_{300}^{0.50} \exp(-1.58 \times 10^5\ \mathrm{K}/T)$	HM89
141.	$e + \mathrm{H_2} \rightarrow \mathrm{H_2^+} + e + e$	$6.80 \times 10^{-11} T_{300}^{0.37} \exp(-1.81 \times 10^5\ \mathrm{K}/T)$	HM89
142.	$e + \mathrm{H_2} \rightarrow \mathrm{H} + \mathrm{H} + e$	$3.20 \times 10^{-9} T_{300}^{0.35} \exp(-1.02 \times 10^5\ \mathrm{K}/T)$	HM89
143.	$e + \mathrm{He} \rightarrow \mathrm{He^+} + e + e$	$5.10 \times 10^{-10} T_{300}^{0.43} \exp(-2.85 \times 10^5\ \mathrm{K}/T)$	HM89
144.	$e + \mathrm{O} \rightarrow \mathrm{O^+} + e + e$	$1.79 \times 10^{-9} T_{300}^{0.49} \exp(-1.58 \times 10^5\ \mathrm{K}/T)$	HM89
145.	$e + \mathrm{C} \rightarrow \mathrm{C^+} + e + e$	$3.40 \times 10^{-9} T_{300}^{0.40} \exp(-1.31 \times 10^5\ \mathrm{K}/T)$	HM89
146.	$e + \mathrm{OH} \rightarrow \mathrm{OH^+} + e + e$	$5.20 \times 10^{-10} T_{300}^{0.50} \exp(-1.50 \times 10^5\ \mathrm{K}/T)$	HM89
147.	$e + \mathrm{H_2O} \rightarrow \mathrm{H} + \mathrm{OH} + e$	$9.20 \times 10^{-9} T_{300}^{-0.50} \exp(-6.96 \times 10^4\ \mathrm{K}/T)$	HM89
148.	$e + \mathrm{H_2O} \rightarrow \mathrm{H_2O^+} + e + e$	$4.40 \times 10^{-10} T_{300}^{0.45} \exp(-1.47 \times 10^5\ \mathrm{K}/T)$	HM89
149.	$e + \mathrm{O_2} \rightarrow \mathrm{O} + \mathrm{O} + e$	$2.30 \times 10^{-9} T_{300}^{-0.50} \exp(-6.96 \times 10^4\ \mathrm{K}/T)$	HM89
150.	$e + \mathrm{O_2} \rightarrow \mathrm{O_2^+} + e + e$	$1.40 \times 10^{-11} T_{300}^{1.04} \exp(-1.40 \times 10^5\ \mathrm{K}/T)$	HM89
151.	$e + \mathrm{CH} \rightarrow \mathrm{CH^+} + e + e$	$5.20 \times 10^{-10} T_{300}^{0.50} \exp(-1.50 \times 10^5\ \mathrm{K}/T)$	HM89
152.	$e + \mathrm{CO} \rightarrow \mathrm{CO^+} + e + e$	$6.70 \times 10^{-10} T_{300}^{0.60} \exp(-1.63 \times 10^5\ \mathrm{K}/T)$	HM89
153.	$e + \mathrm{CO} \rightarrow \mathrm{C} + \mathrm{O} + e$	$8.10 \times 10^{-10} T_{300}^{-0.50} \exp(-1.14 \times 10^5\ \mathrm{K}/T)$	HM89
154.	$\mathrm{H} + e\ (+\ \mathrm{H}) \rightarrow \mathrm{H_2} + e$	$8.5 \times 10^{-16} T_3^{0.8} [\frac{y(\mathrm{H})}{y(\mathrm{H})+53 T_3^{-0.4} y(\mathrm{H^+})}]$	HM79, HM89

Table B.4: Three-Body Reactions

	Reaction	Rate Coefficient ($\mathrm{cm^6\ s^{-1}}$)	Reference
155.	$\mathrm{H} + \mathrm{H} + \mathrm{H} \rightarrow \mathrm{H_2} + \mathrm{H}$	$5.5 \times 10^{-29} T^{-1}$	PSS83
156.	$\mathrm{H} + \mathrm{H} + \mathrm{H_2} \rightarrow \mathrm{H_2} + \mathrm{H_2}$	$5.5 \times 10^{-29} T^{-1}/8$	PSS83

Appendix C

Dust Rotation

In this section, we consider the rotation of irregular-shaped precursor dust particle in the gas flow. Figure C.1(a) shows the dust shape. If the gas flow gives the net torque on the dust particle, the particle begins to rotate about the mass center $y_{\rm G}$. In order to know how the rotation evolves with time, we have to solve the equation of motion for the dust rotation. The equation of the rotation is given as

$$I\frac{d^2\Theta}{dt^2} = L, \tag{C.1}$$

where I is the moment of inertia, Θ is the rotation angle (see Fig. C.1b), and L is the moment. In order to calculate that, we have to know I for the irregular-shaped particle and L acting on the irregular-shaped particle. If we perform the Legendre transformation for the dust shape as

$$r_s(\theta) = r_0 \sum_{l=0}^{l_{\rm max}} A_l P_l(\cos\theta), \tag{C.2}$$

the mass M, the moment of inertia I, and the mass center $y_{\rm G}$ of the irregular-shaped dust particle are written as

$$M = \frac{4}{3}\pi r_0^3 \rho_{\rm mat} \cdot \frac{1}{2} A_{3,1,0}, \tag{C.3}$$

$$I = \frac{8}{15}\pi r_0^5 \rho_{\rm mat} \cdot \left(\frac{3}{4}A_{5,1,0} - \frac{3}{8}A_{5,3,0}\right), \tag{C.4}$$

$$z_{\rm G} = \frac{3}{4} r_0 \frac{A_{4,1,1}}{A_{3,1,0}}, \tag{C.5}$$

where

$$A_{i,j,k} \equiv \int_0^\pi \left[\sum_{l=0}^{l_{\rm max}} A_l P_l(\cos\theta) \right]^i \sin^j\theta \cos^k\theta d\theta. \tag{C.6}$$

In our study, the gas flow is the free molecular flow because the mean free path of the gas is larger than the typical dust size. Therefore, the gas drag force acting on the dust particle can be given by the product of the ram pressure of the gas flow and the cross section of the dust particle. The cross section of the dust particle depends on not only the dust shape but also the rotation angle against the gas flow Θ (see Fig. C.1b). The procedures to obtain the radius of the projection of the dust shape are as follows. The equation of the dust surface in the coordinate of (x', y', z') is

$$(x^2+y^2+z^2)^{1/2} = r_0 \sum_{l=0}^{l_{\rm max}} A_l P_l(z/[x^2+y^2+z^2]^{1/2}), \tag{C.7}$$

where

$$x = x'\cos\Theta + z'\sin\Theta, \quad y = y', \quad z = -x'\sin\Theta + z'\cos\Theta. \tag{C.8}$$

Substituting $x' = \alpha r'_{\rm proj}$, $y' = r'_{\rm proj}\sin\beta$, and $z' = r'_{\rm proj}\cos\beta$, we obtain

$$r'_{\rm proj} = (\alpha^2+1)^{-1/2} r_0 \sum_{l=0}^{l_{\rm max}} A_l P_l([-\alpha\sin\Theta + \cos\beta\cos\Theta]/[\alpha^2+1]^{1/2}). \tag{C.9}$$

The maximum value of $r'_{\rm proj}$ for any α gives the radius of the projection of the dust shape $r_{\rm proj}$. We can calculate the gas drag force and the moment acting on the irregular-shaped dust particle as

$$F_g = p_{\rm fm} \int_0^\pi (2 r_{\rm proj}\sin\beta) \cdot (r_{\rm proj}\cos\beta d\beta), \tag{C.10}$$

$$L = p_{\rm fm} \int_0^\pi (r_{\rm proj}\cos\beta - z_{\rm G}\cos\Theta) \cdot (2 r_{\rm proj}\sin\beta) \cdot (r_{\rm proj}\cos\beta d\beta). \tag{C.11}$$

We perform the test simulation for the dust rotation. We set the dust shape as $A_0 = 1.0$, $A_1 = 0.2$, $A_3 = -0.2$, and $A_l = 0$ for other l. The shape is shown in

Fig. C.1(a). We also assume $r_0 = 500\,\mu$m and $\rho_{\rm mat} = 3\,{\rm g\,cm^{-3}}$. Figure C.2 shows the time evolutions of the angle Θ (top panel) and the angular velocity $\Omega \equiv d\Theta/dt$ (bottom panel). The initial angle is assumed to be $\Theta = 0.25\pi$. At the initial angle, the net torque by the gas flow acts to turn the particle and the particle begins to rotate clockwise in Fig. C.1. As a result, the angle Θ decreases with time. Just after $\Theta < -0.5\pi$, the net torque becomes opposite sign and the angular velocity of the particle begins to decrease. When the angle Θ takes the minimum value ($t \simeq 0.075\,{\rm s}$), the particle comes a symmetrical position of the initial position with respect to the $x'y'$-plane and the dust rotation completely stops. After that, it begins to rotate to the opposite direction. It is found that the oscillational motion continues without attenuation in the amplitude. On the other hand, the expected angular velocity estimated by the simple analysis (see Eq. 6.4) is about 300 ${\rm s^{-1}}$, where the dust shape that we assumed here roughly corresponds to the asymmetric parameter $f \simeq 0.03$ at the initial angle $\Theta = 0.25\pi$. Comparing the simulation result in Fig. C.2 with the simple estimation, it is found that the particle in the gas flow can obtain the angular velocity of the order of the simple estimation. Therefore, we thought that the simple analysis for the dust rotation is not so different with the results that we performed in this section.

The time evolution of the dust rotation depends on the initial angle Θ. Figure C.3 shows other cases that the initial angle is $\Theta = 0$ (panel a) and $\Theta = -0.25\pi$ (panel b). It is found that the angular velocity strongly depends on the initial angle Θ. As shown here, the initial angle of the dust particle against the gas flow (the direction of the shock propagation) is important for the dust rotation, but it is thought to be randomized. We could obtain the distribution of the dust angular velocity in the shock-wave heating model by the statistical treatment. It is beyond the scape of this study, so we would like to discuss it in the other paper.

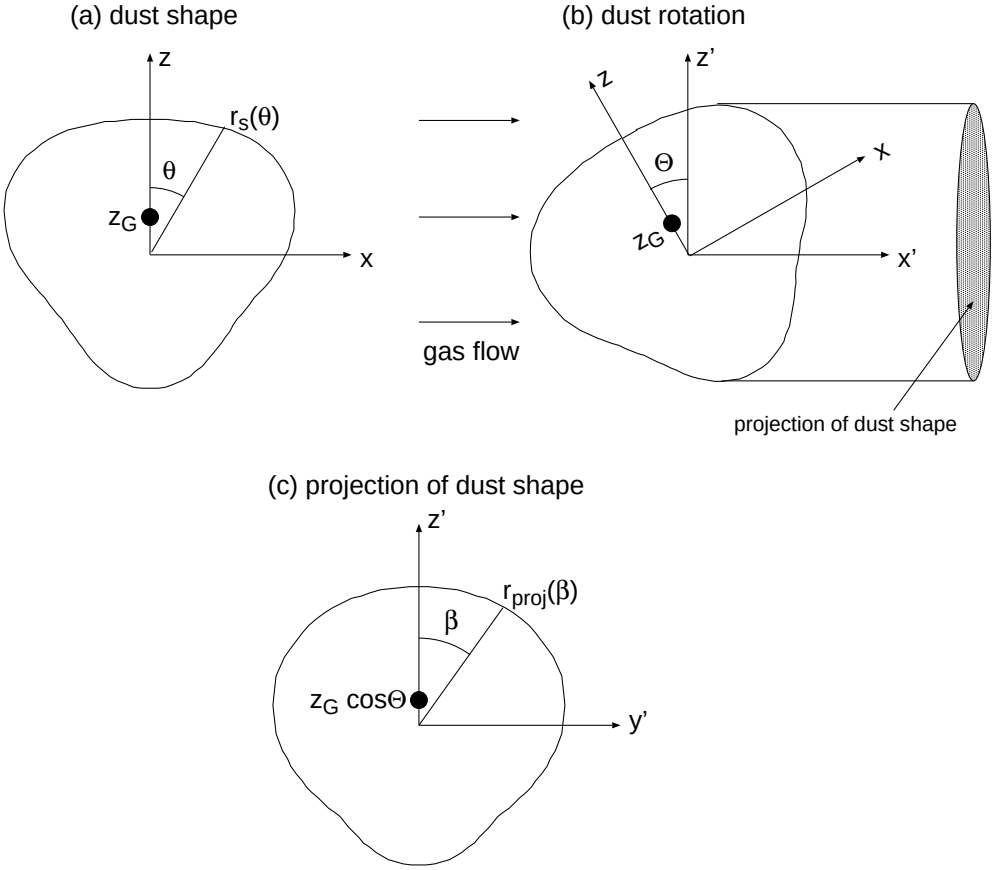

Figure C.1: The shape of precursor dust particle (a), the coordinate system for the rotating dust particle (b), and the projection of the dust shape on the $y'z'$-plane. $y_{\rm G}$ indicates the mass center.

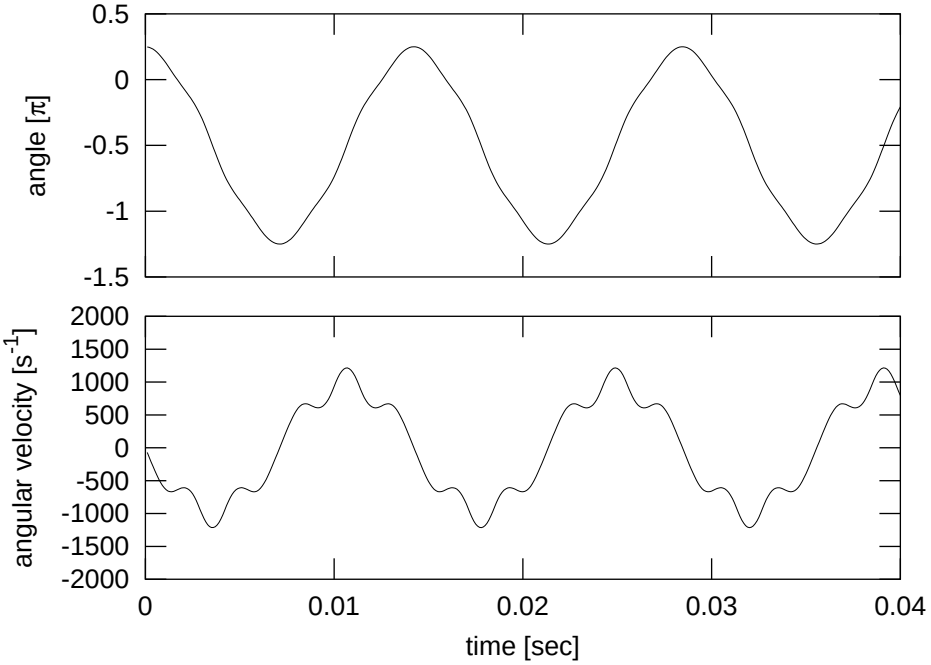

Figure C.2: Time evolution of the angle Θ (top) and the angular velocity Ω (bottom). Initial angle of the particle is set to $\Theta = 0.25\pi$.

(a) initial $\Theta = 0$ (b) initial $\Theta = -0.25\pi$

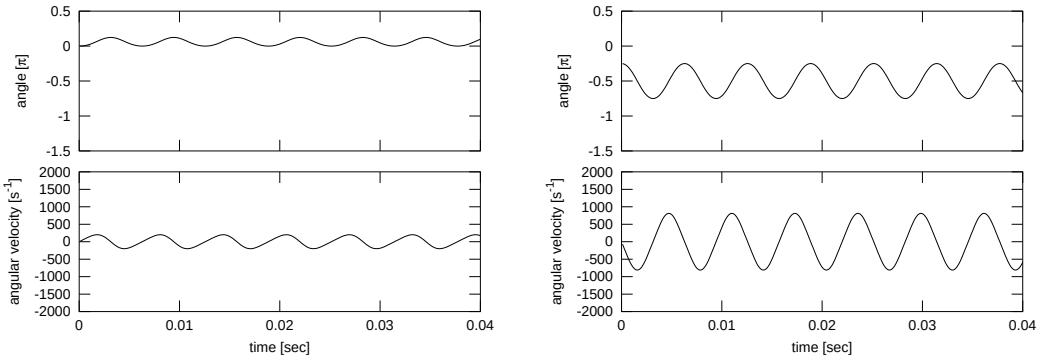

Figure C.3: Same as Fig. C.2 except for the initial angle $\Theta = 0$ (a) and $\Theta = -0.25\pi$ (b).

Bibliography

[1] Amelin, Y., Krot, A. N., Hutcheon, I. D., & Ulyanov, A. A., 2002, Science, 297, 1678

[2] Blandford, R. D., & Payne, D. G., 1982, MNRAS, 199, 883

[3] Boss, A. P., 1996, In Chondrules and the Protoplanetary Disk, ed. Hewins, R. H., Jones, R. H., & Scott, E. R. D. (Cambridge Univ. Press, Cambridge, UK), 257

[4] Boss, A. P., & Durisen, R. H., 2005, ApJ, 621, L137

[5] Brackbill, J. U., Kothe, D. B., & Zemach, C., 1992, J. Comp. Phys., 100, 335

[6] Chandrasekhar, S., 1965, Proc. Roy. Soc. London, A, 286, 1

[7] Ciesla, F. J., & Hood, L. L., 2002, Icarus, 158, 281 (CH02)

[8] Connolly, H. C., & Love, S. G., 1998, Science, 280, 62

[9] Desch, S. J., & Connolly, H. C., Jr., 2002, Meteo. Planet. Sci., 37, 183 (DC02)

[10] Dove, J. E., Rusk, A. C. M., Cribb, P. H., & Martin, P. G., 1987, ApJ, 318, 379 (DRCM87)

[11] Feigelson, E. D., Broos, P., Gaffney, J. A., III, Garmire, G., Hillenbrand, L. A., Pravdo, S. H., Townsley, L., & Tsuboi, Y., 2002, ApJ, 574, 258

[12] Finocchi, F., Gail, H. -P., & Duschl, W, J., 1997, A&A, 325, 1264

[13] Hayashi, C., Nakazawa, K., & Nakagawa, Y., 1985, In Protostars and Planets II, ed. Black, D. C., & Matthews, M. S. (Univ. of Arizona Press, Tucson), 1100

[14] Hayashi, M. R., Shibata, K., & Matsumoto, R., 1996, ApJ, 468, L37

[15] Hollenbach, D., & McKee, C. F., 1979, ApJS, 41, 555 (HM79)

[16] Hollenbach, D., & McKee, C. F., 1989, ApJ, 345, 306 (HM89)

[17] Hood, L. L., & Horanyi, M., 1991, Icarus, 93, 259

[18] Hood, L. L., & Horanyi, M., 1993, Icarus, 106, 179

[19] Hummer, D. G., & Rybicki, G. B., 1982, ApJ, 254, 767

[20] Iida, A., Nakamoto, T., Susa, H., & Nakagawa, Y., 2001, Icarus, 153, 430 (INSN)

[21] Jones, R. H., Lee, T., Connolly, H. C., Jr., Love, S. G., & Shang, H., 2000, In Protostars and Planet IV, ed. Mannings, V., Boss, A. P., & Russell, S. S. (Univ. of Arizona Press, Tucson), 927

[22] Jones, R. H., & Lofgren, G. E., 1993, Meteoritics, 28, 213

[23] Kato, T., Nakamoto, T., & Miura, H., submitted to Meteo. Planet. Sci.

[24] Kondo, M., Tsuchiyama, A., Hirai, H., & Koishikawa, A., 1997, Antarct. Meteo. Res., 10, 437

[25] Lepp, S., & Shull, J. M., 1983, ApJ, 270, 578 (LS83)

[26] Mathis, J. S., Rumpl, W., & Nordsieck, K. H., 1977, ApJ, 217, 425

[27] Miura, H., Nakamoto, T., & Susa, H., 2002, Icarus, 160, 258

[28] Miura, H., & Nakamoto, T., 2005, Icarus, 175, 289 (MN05)

[29] Miyake, K., & Nakagawa, Y., 1993, Icarus, 106, 20

[30] Murase, T., & McBirney, A. R., 1973, Geol. Soc. Am. Bull., 84, 3563

[31] Nakamoto, T., Hayashi, M. R., Kita, N. T., & Tachibana, S., 2005, Lun. Planet. Sci. Conf., abst#1256

[32] Nakamura, T., & Yabe, T., 1999, Comp. Phys. Comm., 120, 122

[33] Nakamura, T., Tanaka, R., Yabe, T., & Takizawa, K., 2001, J. Comp. Phys., 174, 171

[34] Nelson, V. E., & Rubin, A. E., 2002, Meteo. Planet. Sci., 37, 1361

[35] Neufeld, D. A., & Kaufman, M. J., 1993, ApJ, 418, 263

[36] Osterbrock, D. E., 1988, *Astrophysics of Gaseous Nebulae and Active Galactic Nuclei* (Univ Science Books)

[37] Palla, F., Salpeter, E. E., & Stahler, S. W., 1983, ApJ, 271, 632 (PSS83)

[38] Probstein, R. F., 1968, In Problems of Hydrodynamics and Continuum Mechanics, ed. Lavrent'ev, M. A. (Soc. for Industr. & Appl. Math., Philadelphia), 568

[39] Rubin, A. E., & Keil, K., 1984, Meteoritics, 19, 135

[40] Rubin, A. E., & Grossman, J. N., 1987, Meteoritics, 22, 237

[41] Rubin, A. E., 1989, Meteoritics, 24, 179

[42] Ruzmaikina, T. V., & Ip, W. H., 1994, Icarus, 112, 430

[43] Rybicki, G. B., & Lightman, A. P., 1979, *Radiative Processes in Astrophysics* (John Wiley & Sons, Inc.)

[44] Saxene, S. K., Chatterjee, N., Fei, Y., & Shen, G., 1993, *Thermodynamic Data on Oxides and Silicates* (Springer-Verlag, Berlin)

[45] Shapiro, P. R., & Kang, H., 1987, ApJ, 318, 32

[46] Sekiya, M., Uesugi, M., & Nakamoto, T., 2003, Prog. Theo. Phys., 109, 717

[47] Susa, H., Uehara, H., Nishi, R., & Yamada, M., 1998, Prog. Theo. Phys., 100, 63

[48] Susa, H., & Nakamoto, T., 2002, ApJ, 564, L57

[49] Tachibana, S., Huss, G. R., Miura, H., & Nakamoto, T., 2004, Lun. Planet. Sci. Conf., abst#1549

[50] Tachibana, S., & Huss, G. R., 2005, Geo. Cosmo. Acta, 69, 3075

[51] Tanaka, K. K., Tanaka, H., Nakazawa, K., & Nakagawa, Y., 1998, Icarus, 134, 137

[52] Tsuchiyama, A., Shigeyoshi, R., Kawabata, T., Nakano, T., Uesugi, K., & Shirono, S., 2003, Lun. Planet. Sci. Conf., abst#1271

[53] Uesugi, M., Sekiya, M., & Nakamoto, T., 2003, Earth, Planets and Space, 55, 493

[54] Wasson, J. T., & Rubin, A. E., 2003, Geo. Cosmo. Acta, 67, 2239

[55] Wasson, J. T., 2004, Workshop on Chondrites and Protoplanetary Disk, abst#9113

[56] Xiao, F., & Yabe, T., 2001, J. Comp. Phys., 170, 498

[57] Yabe, T., & Wang, P-Y., 1991, J. Phys. Soc. Japan, 60, 2105

[58] Yabe, T., Xiao, F., & Utsumi, T., 2001, J. Comp. Phys., 169, 556

[59] Yurimoto, H., & Wasson, J. T., 2002, Geo. Cosmo. Acta, 66, 4355